Numerical Modelling and Analysis of Debris Coolability using Porous Media Approach

Thesis submitted by
Aranyak Chakravarty

Doctor of Philosophy (Engineering)

DEPARTMENT OF MECHANICAL ENGINEERING
FACULTY COUNCIL OF ENGINEERING AND TECHNOLOGY
JADAVPUR UNIVERSITY
KOLKATA, INDIA

2018

JADAVPUR UNIVERSITY

KOLKATA 700032, INDIA

1. Title of the thesis:

Numerical modelling and analysis of debris coolability using porous media approach

2. Name, Designation & Institution of the Supervisor/s:

a. **Prof. Koushik Ghosh**
Professor, Department of Mechanical Engineering
Jadavpur University, Kolkata –700032

b. **Prof. Swarnendu Sen**
Professor, Department of Mechanical Engineering
Jadavpur University, Kolkata –700032

3. List of publications:

Journal Publications

1. Aranyak Chakravarty, Priyankan Datta, Koushik Ghosh, Swarnendu Sen, Achintya Mukhopadhyay: **Numerical analysis of a heat-generating, truncated conical porous bed in a fluid-filled enclosure.** *Energy*, 106, 646-661, 2016.
2. Aranyak Chakravarty, Priyankan Datta, Koushik Ghosh, Swarnendu Sen, Achintya Mukhopadhyay: **Thermal non-equilibrium heat transfer and entropy generation due to natural convection in an enclosure with a truncated conical, heat-generating porous bed**. *Transport in Porous Media*, 116, 353-377, 2017.
3. Aranyak Chakravarty, Priyankan Datta, Koushik Ghosh, Swarnendu Sen, Achintya Mukhopadhyay: **Mixed convective heat transfer in an enclosure containing a heat-generating porous bed under the influence of bottom injection.** *International Journal of Heat and Mass Transfer*, 117, 645-657, 2018.
4. Aranyak Chakravarty, Priyankan Datta, Koushik Ghosh, Swarnendu Sen: **Pressure dependence of dryout in a heat-generating porous debris bed** (under Review)
5. Aranyak Chakravarty, Priyankan Datta, Koushik Ghosh, Swarnendu Sen, Achintya Mukhopadhyay: **Coolability assessment of a heap-shaped heat generating porous bed** (under preparation)
6. Aranyak Chakravarty, Priyankan Datta, Koushik Ghosh, Swarnendu Sen, Achintya Mukhopadhyay: **Mixed convection in an enclosure containing a bottom-flooded, heat-generating porous bed: A comparative analysis using LTE and LTNE approaches** (under preparation)

Book Chapters

1. Aranyak Chakravarty, Priyankan Datta, Koushik Ghosh, Swarnendu Sen, Achintya Mukhopadhyay: **Coolability of heat-generating porous debris beds in severe accident situations**. In: Kaushik Saha, Avinash Kumar Agarwal, Koushik Ghosh, Sibendu Som (Eds.): *Two-Phase Flow for Automotive and Power Generation Sectors*, pp. 305 – 336, Springer, Singapore, 2019

International Conference Publications

1. Aranyak Chakravarty, Priyankan Datta, Koushik Ghosh, Swarnendu Sen, Achintya Mukhopadhyay: **Analysis of a heat-generating stratified porous debris bed in a fluid-filled enclosure**. *Proc. 23rd National and 1st International ISHMT-ASTFE Heat Mass Transfer Conference*, Thiruvananthapuram, India, Paper No. IHMTC2015-312, December 17-20, 2015.
2. Aranyak Chakravarty, Priyankan Datta, Koushik Ghosh, Swarnendu Sen, Achintya Mukhopadhyay: **Numerical analysis of a bottom-flooded porous bed in a ventilated enclosure**. *Proc. National Conference on Advances in Thermal Engineering*, Jadavpur University, Kolkata, India, Paper No. ATE2016-023, September 23-24, 2016.
3. Aranyak Chakravarty, Akash Swarnakar, Priyankan Datta, Koushik Ghosh, Swarnendu Sen, Achintya Mukhopadhyay: **Effect of porosity distribution on heat transfer characteristics of a heat generating porous enclosure**. *Proc. 6th International and 43rd National Conference on Fluid Mechanics and Fluid Power*, MNNITA, Allahabad, India, Paper No. FMFP2016-219, December 15-17, 2016.
4. Aranyak Chakravarty, Priyankan Datta, Koushik Ghosh, Swarnendu Sen, Achintya Mukhopadhyay: **Development and Validation of a CFD model for simulating dryout phenomena in corium debris beds**. *Proc. International Conference on Sustainable Energy and Environmental Challenges (SEEC-2017)*, Mohali, India, Paper No. 135, February 26-28, 2017.
5. Aranyak Chakravarty, Priyankan Datta, Koushik Ghosh, Swarnendu Sen, Achintya Mukhopadhyay: **Natural Convective Heat Removal from a Heat-generating Corium Debris Bed.** *Proc. 24th National and 2nd International ISHMT-ASTFE Heat Mass Transfer Conference*, BITS Pilani, Hyderabad, India, Paper No. IHMTC2017-11-0131, December 28-30, 2017.
6. Aranyak Chakravarty, Priyankan Datta, Koushik Ghosh, Swarnendu Sen: **Pressure dependence of dryout in a heat-generating porous debris bed**. *Proc. 1st International Conference on Mechanical Engineering (INCOM18)*, Jadavpur University, Kolkata, India, Paper No. INCOM18-065, January 4-6, 2018.

National Conference Publications

1. Aranyak Chakravarty, Priyankan Datta, Koushik Ghosh, Swarnendu Sen, Achintya Mukhopadhyay: **Numerical analysis of a bottom-flooded porous bed in a ventilated enclosure**. *Proc. National Conference on Advances in Thermal Engineering*, Jadavpur University, Kolkata, India, Paper No. ATE2016-023, September 23-24, 2016

4. List of Patents: NIL

5. List of Presentation in National / International Conferences/Workshops:

1. Aranyak Chakravarty, Priyankan Datta, Koushik Ghosh, Swarnendu Sen, Achintya Mukhopadhyay: **Analysis of a heat-generating stratified porous debris bed in a fluid-filled enclosure**. *Proc. 23rd National and 1st International ISHMT-ASTFE Heat Mass Transfer Conference*, Thiruvananthapuram, India, Paper No. IHMTC2015-312, December 17-20, 2015.
2. Aranyak Chakravarty, Priyankan Datta, Koushik Ghosh, Swarnendu Sen, Achintya Mukhopadhyay: **Numerical analysis of a bottom-flooded porous bed in a ventilated enclosure**. *Proc. National Conference on Advances in Thermal Engineering*, Jadavpur University, Kolkata, India, Paper No. ATE2016-023, September 23-24, 2016.
3. Aranyak Chakravarty, Priyankan Datta, Koushik Ghosh, Swarnendu Sen, Achintya Mukhopadhyay: **Natural Convective Heat Removal from a Heat-generating Corium Debris Bed.** *Proc. 24th National and 2nd International ISHMT-ASTFE Heat Mass Transfer Conference*, BITS Pilani, Hyderabad, India, Paper No. IHMTC2017-11-0131, December 28-30, 2017.
4. Aranyak Chakravarty, Priyankan Datta, Koushik Ghosh, Swarnendu Sen. **Pressure dependence of dryout in a heat-generating porous debris bed:** *Proc. 1st International Conference on Mechanical Engineering (INCOM18)*, Jadavpur University, Kolkata, India, Paper No. INCOM18-065, January 4-6, 2018.
5. Aranyak Chakravarty, Koushik Ghosh, Swarnendu Sen: **Modelling and analysis of debris coolability**. *Humboldt Kolleg on Energy Sustainability: A Roadmap for the future*, Kolkata, India, February 2-4, 2018.

JADAVPUR UNIVERSITY
FACULTY OF ENGINEERING AND TECHNOLOGY

CERTIFICATE FROM THE SUPERVISOR/S

This is to certify that the thesis entitled **'Numerical modelling and analysis of debris coolability using porous media approach'** submitted by Shri Aranyak Chakravarty who got his name registered on 11th April, 2016 for the award of Ph. D. (Engineering) degree of Jadavpur University, is absolutely based upon his own work under the supervision of Prof. Koushik Ghosh and Prof. Swarnendu Sen and that neither his thesis nor any part of the thesis has been submitted for any degree/diploma or any other academic award anywhere before.

1._____
Signature of the Supervisor
with date and Office Seal

2._____
Signature of the Supervisor
with date and Office Seal

Dedicated to the memory of my father and to my immediate family

ACKNOWLEDGEMENTS

I am sincerely grateful to my supervisors, Prof. Koushik Ghosh and Prof. Swarnendu Sen, for their extensive support, encouragement and unparalleled guidance. It would have been difficult to bring this research to completion without their active involvement.

I would also like to take this opportunity to extend my sincere gratitude to Prof. Achintya Mukhopadhyay for his insightful guidance during all phases of this research. The support extended by Dr. Pallab Sinha Mahapatra – whenever needed – deserves a special mention in this regard.

My sincere regards to other senior faculty members associated with Project Neptune – Prof. Kamalesh Majumder, Prof. Sankar Dhar, Prof. Dipankar Sanyal, Prof. Sanjib Acharyya, Prof. Saikat Mookherjee, Prof. Rana Saha, Prof. Nirmal Kumar Manna and Dr. Pranibesh Mandal.

I consider myself extremely fortunate for having the opportunity to simultaneously work on some other interesting projects alongside my Ph.D. research topic. This would not have been possible without the support and co-operation of other researchers, past and present, of our group – Priyankan Datta, Ritabrata Saha, Sourav Sarkar, Uddalok Sen, Chandrachur Bhattacharya, and Dr. Nirmalendu Biswas. I thank them all.

My sincere thanks also goes to the rest of my colleagues particularly Shouvik Chaudhuri, Nitesh Mondal, Krishnendu Maji, Somnath De, Arijit Banerjee, Amlam Garai, Sukalpa Chowdhury, Snehashish Bhattacharjee and Aayush Sharma who created a friendly and pleasant atmosphere and helped me with little but essential things during the course of my work. The contributions of my seniors – Dr. Souvick Chatterjee, Dr. Sirshendu Mondal, Dr. Dipak Chandra Das, Dr. Nripen Mondal, Dr. Nimai Mondal, Shibsankar Das Mahapatra – are no less in this regard.

I must separately thank Prof. (Dr.) Amitava Gupta, Director, School of Nuclear Studies & Application, Jadavpur University, without whose initiative and support it would not have been possible to bring the thesis to completion.

I must acknowledge the contribution of my parents, brother and wife, without whose support and motivation this work would certainly remain incomplete.

I would like to acknowledge the financial support extended by AREVA (now rechristened as FRAMATOME) for conducting this research. I must also acknowledge the help extended by Reactor Safety Division, Bhabha Atomic Research Centre (BARC) for carrying out experiments invaluable to this thesis.

Aranyak Chakravarty

May 2018

SYNOPSIS

The present thesis is devoted to the development and application of a computational fluid dynamics model in simulating fluid flow and associated heat and mass transfer phenomena in situations involving heat-generating porous debris beds. This is relevant to coolability assessment of decay heat-generating debris beds formed due to molten fuel-coolant interactions in the aftermath of a core meltdown accident in nuclear reactors. The necessity of assessing coolability of such debris beds is due to possible progression of the accident to situations involving radioactive releases to the environment. Fluid flow and heat transfer involving typical debris beds are investigated in this thesis using the developed numerical model considering both single phase flow and multiphase flow with phase change. The developed numerical model is implemented within the framework of the finite volume based computational fluid dynamics platform ANSYS FLUENT with extensive use of user-defined functions.

Literature survey indicates that development of the computational model requires proper modelling of multiphase heat and mass transfer mechanisms in addition to the effects of porous media on fluid flow. The latter is first implemented by considering a single phase flow situation and local thermal equilibrium (LTE) within porous media, and validated extensively with existing experimental as well as numerical data (Figs. 1a, 1b, 1d). The issue of interfacial heat transfer between the heat-generating solid phase and the saturating fluid(s) is next addressed by considering local thermal non-equilibrium (LTNE) within the porous media components. The correlation of Ranz and Marshall (1952) is utilised to determine heat transfer from the heat-generating solid phase to the saturating fluid(s). This is also validated with existing numerical data for a single phase flow situation (Fig. 1c). The LTNE model is then extended to a multiphase flow situation by appropriate inclusion of interfacial momentum, heat and mass transfer terms. Interfacial drag between the co-existing fluid phases in the clear fluid region is modelled using the Schiller and Naumann (1935) while interfacial drag between the fluid phases and the solid phase within the porous debris is modelled using the correlations proposed by Reed (1982), Schulenberg and Müller (1987) and Schmidt (2004). Interfacial heat transfer between the co-existing fluid phases is modelled using the Ranz and Marshall (1952) correlation while boiling heat transfer within the porous debris bed is modelled using the correlations of Rhosenow (1952) and Bromley (1950). The applicability of the multiphase model is also validated with reported experimental data (Fig. 1e and Table 1). All the models and correlations utilised in the computational model are implemented in ANSYS FLUENT using user-defined functions.

The first problem investigated in this thesis involves single phase laminar natural convection in a cylindrical enclosure. A heat-generating porous debris bed is assumed to be located in a central position on the base of the enclosure (Fig. 2). The problem is solved in a dimensionless manner following both LTE and LTNE approaches. In the LTE approach, the side wall of the enclosure is assumed to be in a cold isothermal state and all other walls are assumed to be adiabatic (Fig. 2a). In the LTNE approach, the top wall and

the side wall are assumed to be in a cold isothermal state while the bottom wall is assumed to be adiabatic (Fig. 2b).

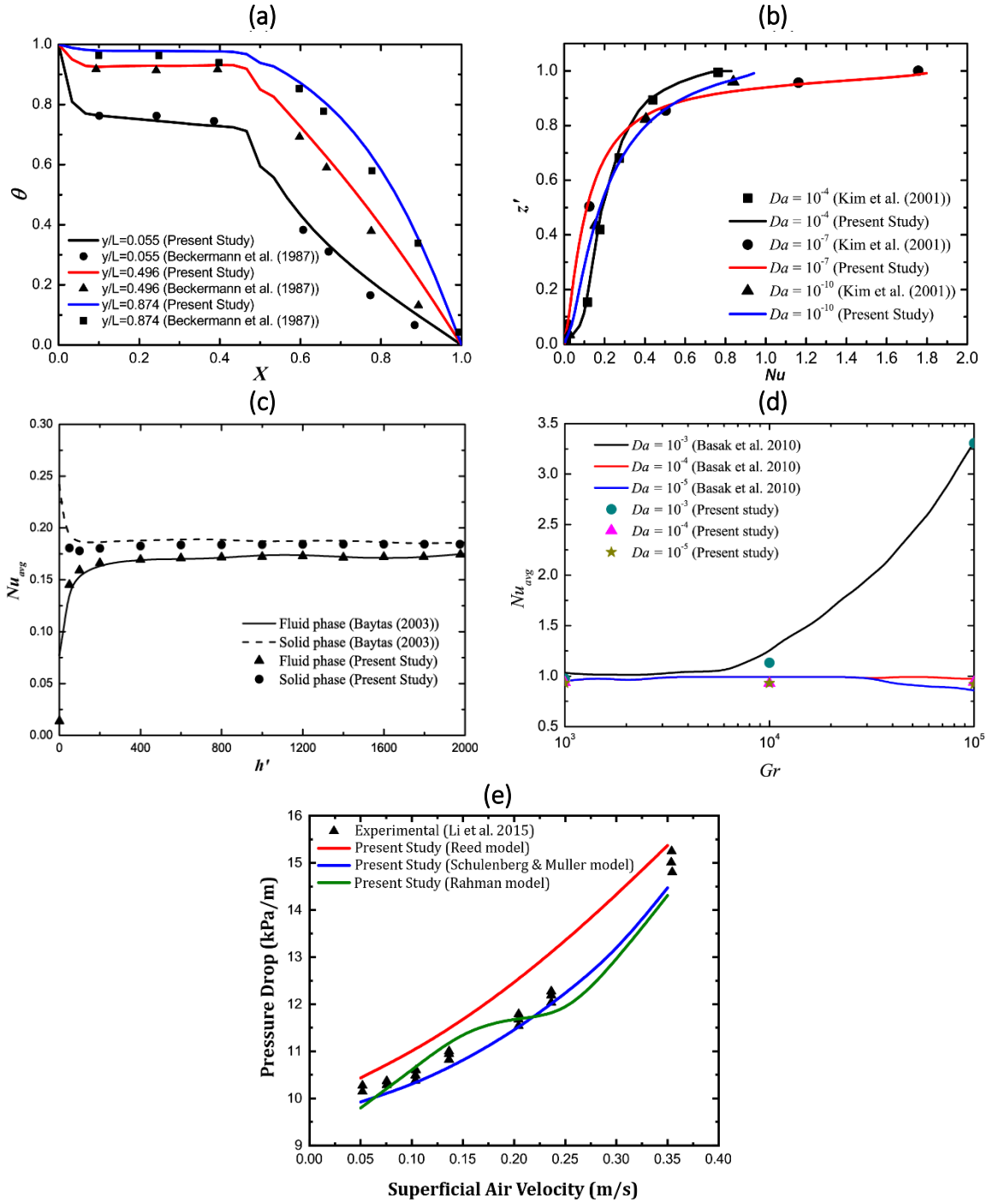

Figure 1 Validation of the numerical model with (a) experimental data for single phase LTE model (b) numerical data for single phase LTE model with internal heat generation (c) numerical data for single phase LTNE model with internal heat generation (d) numerical data for single phase LTE model in mixed convective situation (e) experimental data for porous media drag models in two-phase flow situation

Results indicate that heat transfer takes place from the heat-generating porous bed to the working fluid which establishes a buoyancy-driven counter-clockwise fluid motion within the enclosure, irrespective of the approach followed. The heated fluid first comes

in contact with the top wall where heat transfer takes place from the fluid to the wall depending upon the imposed boundary condition. No energy transfer takes place in case of the adiabatic wall and as such, entire thermal energy is transferred to the side wall of the enclosure in the LTE approach (Fig. 3). In the LTNE approach, however, the major amount of heat transfer takes place at the cold top wall and only the residual energy is transferred to the side wall of the enclosure (Fig. 4).

Table 1 Comparison of experimental and numerical prediction of dryout

Bed Configuration	**Dryout Assessment Study**	**Dryout Power (kW)**	**Dryout Power Density (kW/m^3)**
Truncated Conical	COOLOCE Experiment (Takasuo 2016)	39.2	2602.0
	Present Study with Reed model	40.0	2655.16
	Present Study with Schulenberg & Müller model	39.0	2588.78
	Present Study with Rahman model	45.0	2987.05
Conical	COOLOCE Experiment (Takasuo 2016)	36	2349.87
	Present Study with Schulenberg & Müller model	37	2415.14
Fully-flooded Cylindrical	COOLOCE Experiment (Takasuo 2016)	40.1	2617.49
	Present Study with Schulenberg & Müller model	40	2610.96
Top-flooded Cylindrical	COOLOCE Experiment (Takasuo 2016)	20.4	1331.59
	Present Study with Schulenberg & Müller model	21	1370.75

The effects of bed permeability, bed heat generation, thermal conductivity ratio, bed geometry and bed stratification on the natural convective fluid flow and heat transfer characteristics of the system are analysed in this investigation. It is observed from this analysis that stratification of the debris bed has a minimal effect on the heat transfer characteristics of the system. All the other parameters investigated, however, are observed to significantly influence the fluid flow mechanism and hence, the heat transfer characteristics. Figure 5 represents the heat transfer characteristics obtained with the LTE approach and LTNE approaches, in terms dimensionless Nu_{avg}, with variations in bed

heat generation (in terms of dimensionless Ra) and bed permeability (in terms of dimensionless Da). The impacts of bed geometry and thermal conductivity ratio on the heat transfer characteristics are evident from Fig. 6 and Table 2, respectively.

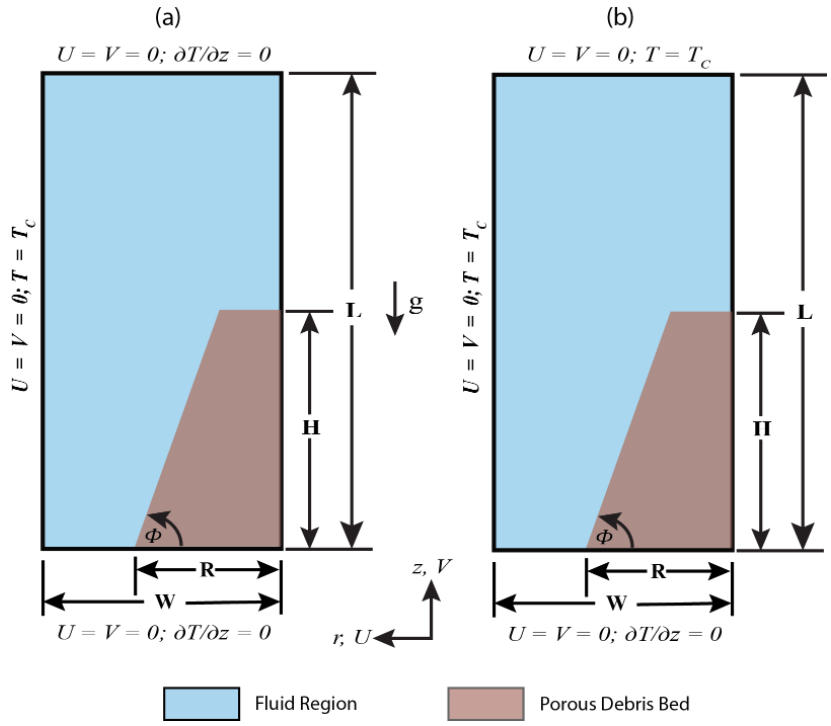

Figure 2 Schematic representation of the problem geometry utilised for analysing single phase natural convection using (a) LTE approach and (b) LTNE approach

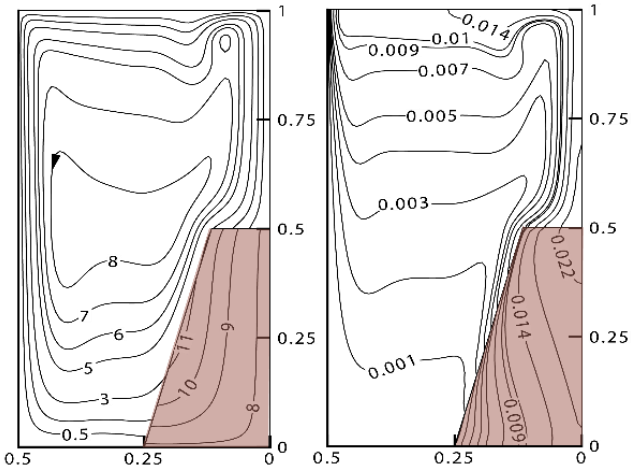

Figure 3 Stream function (left) and Isotherm (right) contour within the domain using the LTE approach

The aforementioned analysis also reveals information regarding the dominant heat transfer mechanism. The dominant mode of heat transfer from the porous bed to the fluid region is observed to depend on the associated heat generation rate as well as bed permeability. At a constant heat generation, convective heat transfer dominates in a highly permeable bed while conductive heat transfer is observed to have the major contribution when permeability decreases. At a certain bed permeability, increase in heat generation strengthens the convective flow and vice-versa. This change is observed to

happen at a specific bed permeability for a given bed heat generation and is characterised in terms of *RaDa*. In the LTE approach, this change is observed to occur at $RaDa = 10^3$ when $Ra < 10^8$ and at $RaDa = 10^4$ when $Ra > 10^8$. In contrast, this magnitude of *RaDa* is observed to be 100 in the analysis using LTNE approach.

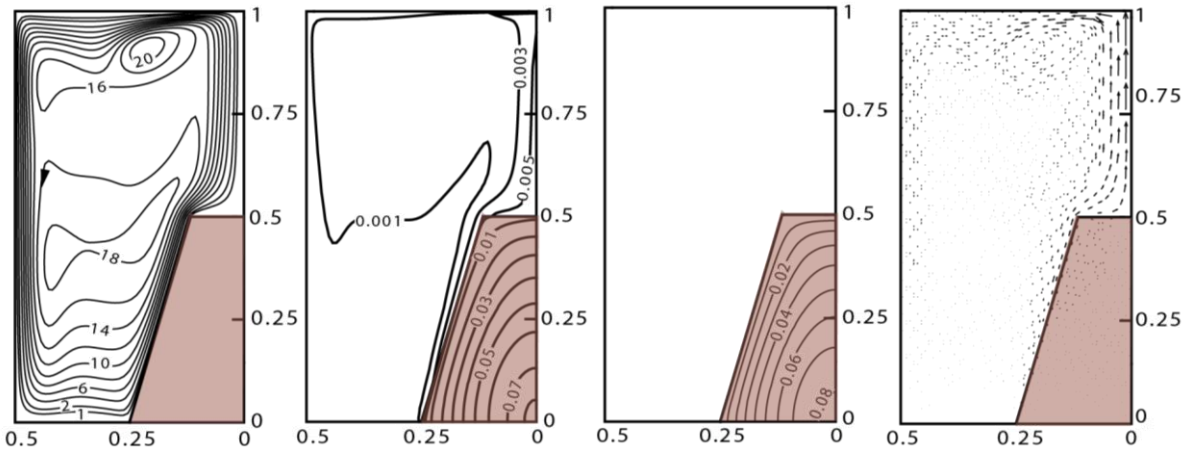

Figure 4 Stream function, Fluid isotherm, Solid isotherm and Energy flux vectors within the domain using the LTNE approach

The second problem investigated in this thesis is motivated from the concept of injecting cold fluid from the bottom of the debris bed with the objective of augmenting the coolability of the bed. This creates a mixed convective flow situation within the cavity containing the heat-generating debris bed. Analysis is carried out for this configuration in a dimensionless manner following both LTE and LTNE approaches considering single phase laminar flow. Figure 7 represents the problem geometry analysed in this study. The bounding walls of the cavity, except the bottom wall, are considered to be in an isothermal cold state. The bottom wall is assumed to be adiabatic.

Table 2 Variation in Nu_{avg} with changing thermal conductivity ratio (λ)

$\boldsymbol{\lambda}$	$\boldsymbol{Nu_{avg}}$
1.0	0.14988
5.0	0.69978
10.0	1.39957

Analysis shows that the fluid flow within the system is governed mainly by the combined effects of bed permeability, buoyancy-induced flow due to heat generation within the porous bed and inertial flow due to additional fluid injection from bottom of the bed. The buoyancy-induced and inertial flow mechanisms, coupled with each other, transfers thermal energy from the heat-generating porous bed to the cold enclosure walls and towards the system outlet. The relative dominancy of these flow mechanisms is denoted by the dimensionless Richardson number (Ri) such that the flow mechanism evolves from a strongly inertial flow at very low Ri to a buoyancy-driven flow at very high Ri. Heat transfer characteristics at the cold walls are comprehended by means of Nu_{avg} for different situations. Stronger fluid injection at low Ri enables greater heat removal from the heat-generating bed leading to a lower bed temperature rise.

Establishment of a weak temperature gradient results in a smaller Nu_{avg} at low Ri (see Fig. 8). The strength of fluid injection decreases as Ri is increased and as such, relatively less heat is removed from the bed leading to a very high temperature rise. This also results in a larger temperature gradient within the enclosure and a consequent increase in Nu_{avg}, as evident from Fig. 8.

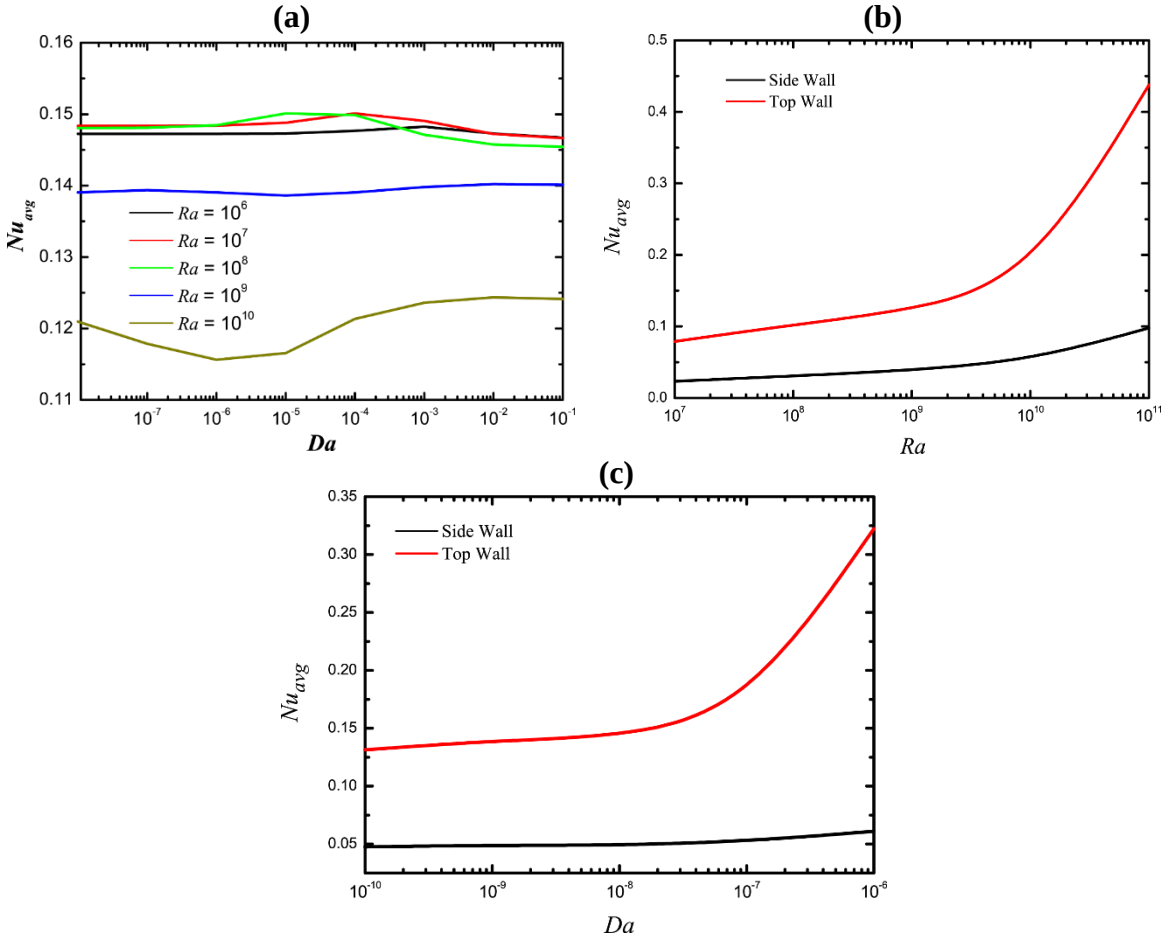

Figure 5 Variations of (a) Nu_{avg} with *Da* for different *Ra* using LTE approach (b) Nu_{avg} for top wall and side wall with *Ra* at *Da* = 10^{-7} using LTNE approach and (c) Nu_{avg} for top wall and side wall with *Da* at *Ra* = 10^{10} using LTNE approach

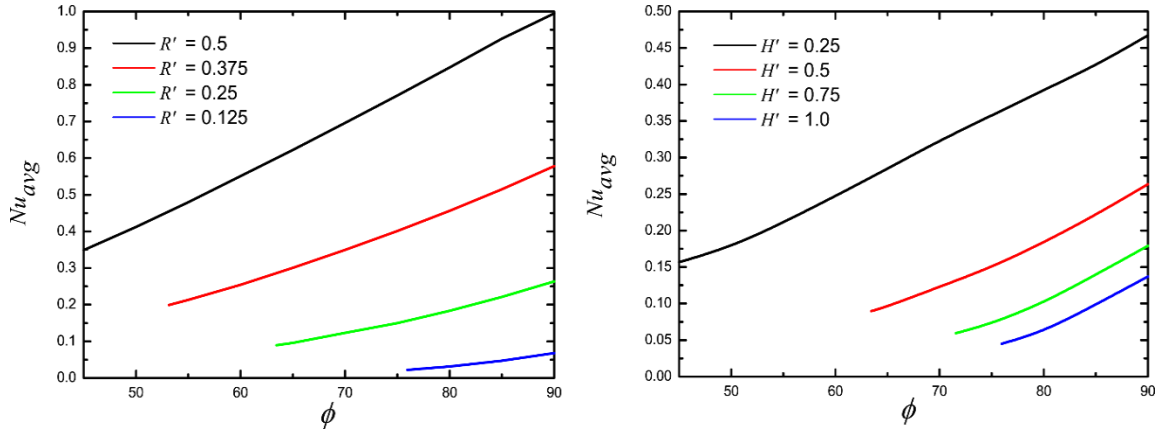

Figure 6 Variation of Nu_{avg} with bed angle (ϕ) at *Ra* = 10^8, *Da* = 10^{-4} for (a) different bed radii at H' = 0.5 (b) different bed height at R' = 0.25

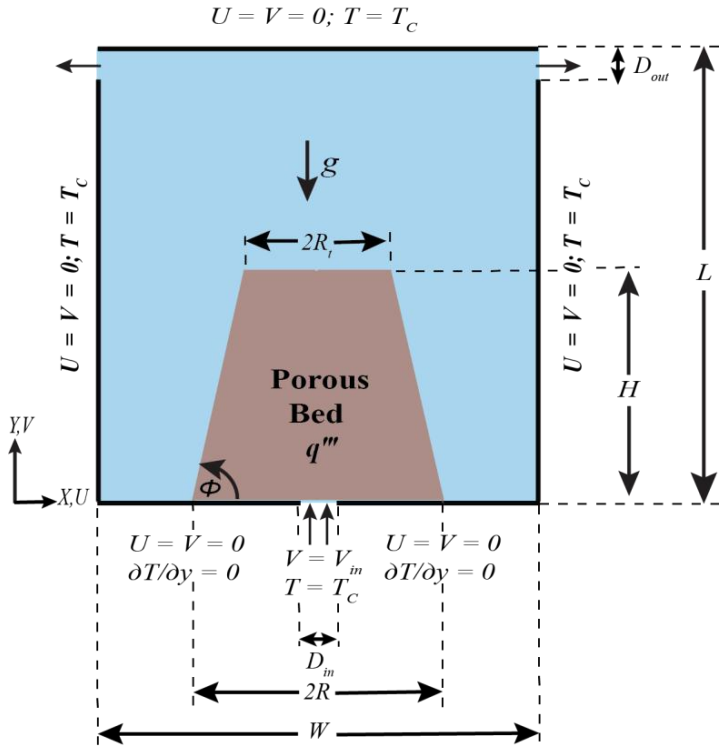

Figure 7 Schematic representation of the problem geometry utilised for analysing single phase mixed convection

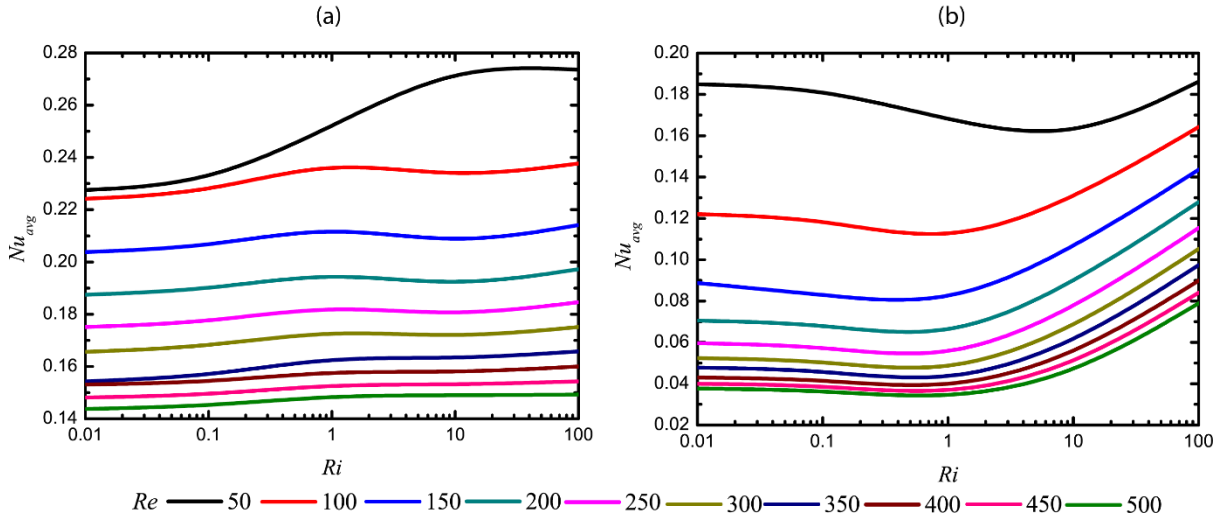

Figure 8 Nu_{avg} variation with Ri at different Re at a constant Da at (a) top wall and (b) side walls

A significant effect of the porous medium is the spreading of flow near the fluid inlet as bed permeability reduces i.e. Da becomes smaller. This effect blocks the cold injected fluid from reaching the upper region of the bed and as such, maximum temperature is found in this region of the bed and the adjoining fluid region. Heat transfer at the top wall increases while that at the side walls decrease as Da is reduced. However, the effect of flow spreading increases the heat transfer at the side walls with a

corresponding decrease at the top wall in situations with low *Ri* and low *Re*, as can be seen from Fig. 9.

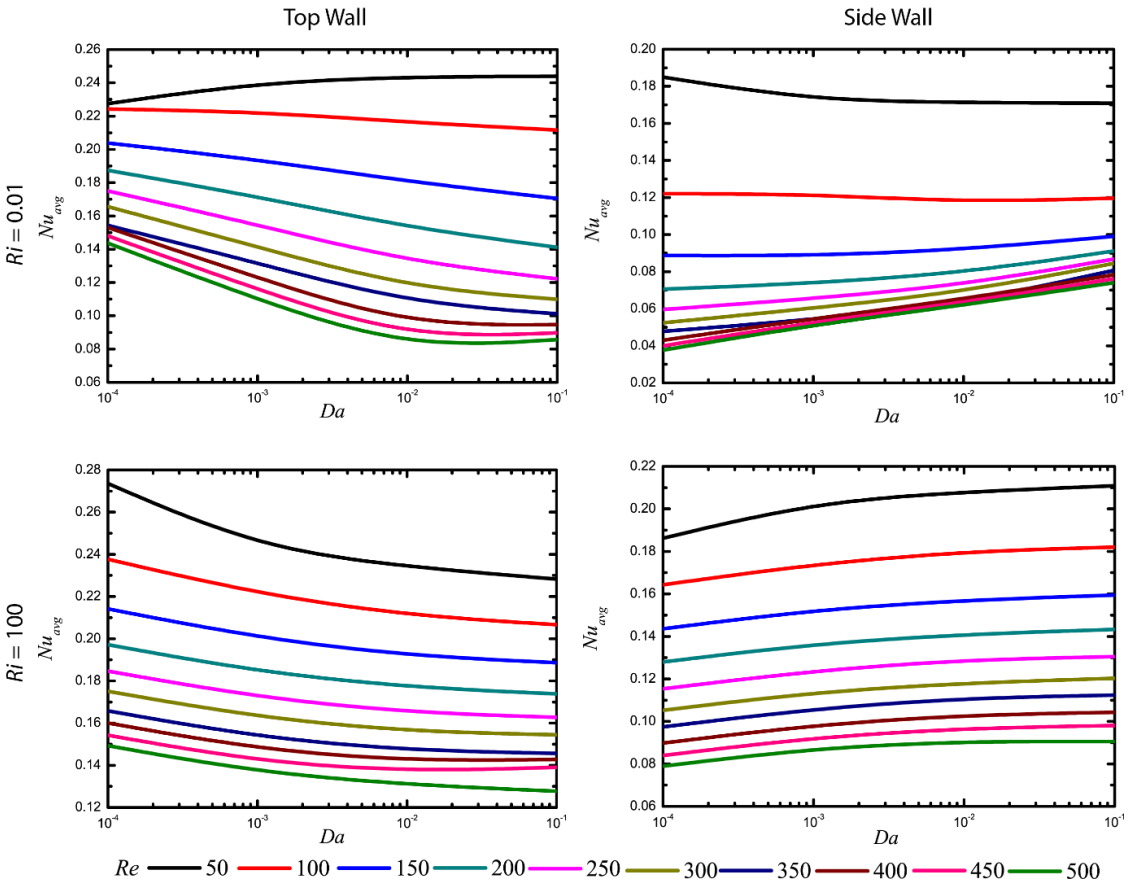

Figure 9 Nu_{avg} variation with Da at different Re and Ri

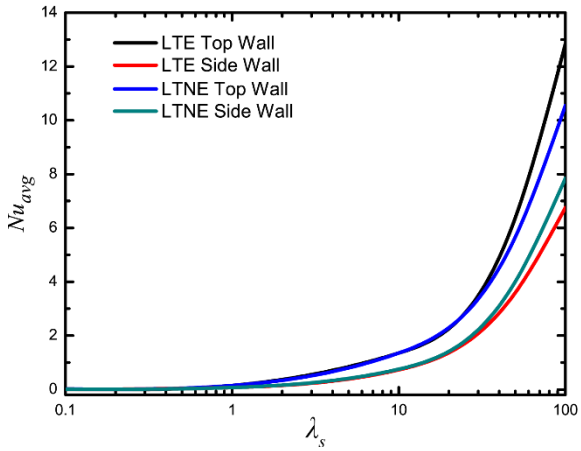

Figure 10 Nu_{avg} variation with λ_s with LTE and LTNE approaches

It is also seen from the analyses that predictions of the LTE and LTNE approaches in the mixed convective situation are qualitatively similar to each other. However, quantitative differences are observed between these models especially in situations with a high thermal conductivity ratio as shown in Fig. 10. It is further observed that irrespective of the flow situation, fluid circulation is symmetric within the enclosure and heat transfer at the top wall significantly exceeds that at the side walls. The symmetric nature of flow

is evident from the contours of stream function, isotherms and energy flux vector for various cases (Fig. 11). Another feature observed is the location of the maximum temperature zone near the top of the bed and the adjoining fluid region. This occurs due to the effect of cold fluid injection from the bottom of the bed and is in stark contrast to that observed in natural convective situations where maximum temperature is observed in the inner regions of the bed (see Figs. 3 and 4).

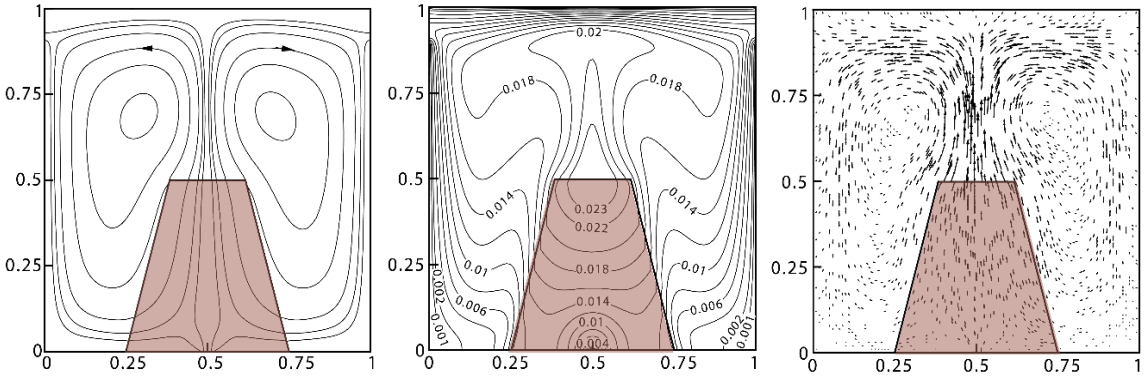

Figure 11 Stream function, Isotherm and Energy flux vectors within the domain

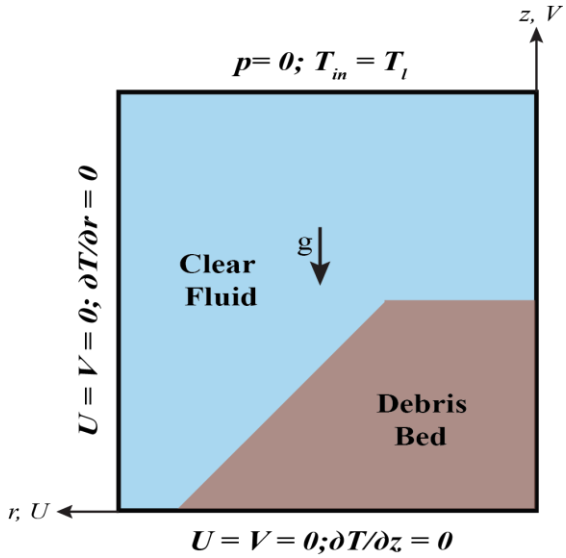

Figure 12 Schematic representation of the problem geometry utilised for analysing multiphase flow and dryout phenomena

The final problem analysed in this thesis involves multiphase flow, heat and mass transfer in a cavity containing a typical debris bed. The top boundary of the domain is considered to be maintained at a constant pressure allowing fluid movement across the boundary, with the constraint that only the liquid phase can enter the domain while both fluid phases can exit. The bottom and side walls of the cavity are assumed to be impermeable and adiabatic. The entire system is symmetric about the z-axis. Figure 12 represents the physical configuration assumed for analysis. The main objective of this study is to achieve an accurate prediction of dryout phenomena in such debris beds and to investigate the effects of the pertinent parameters on dryout occurrence. Dryout occurs in a debris bed if a region of the bed becomes devoid of any liquid and a significant temperature rise occurs in that region. This is identified in the present analysis by tracking

the minimum magnitude of liquid volume fraction and maximum magnitude of solid phase temperature within the debris bed.

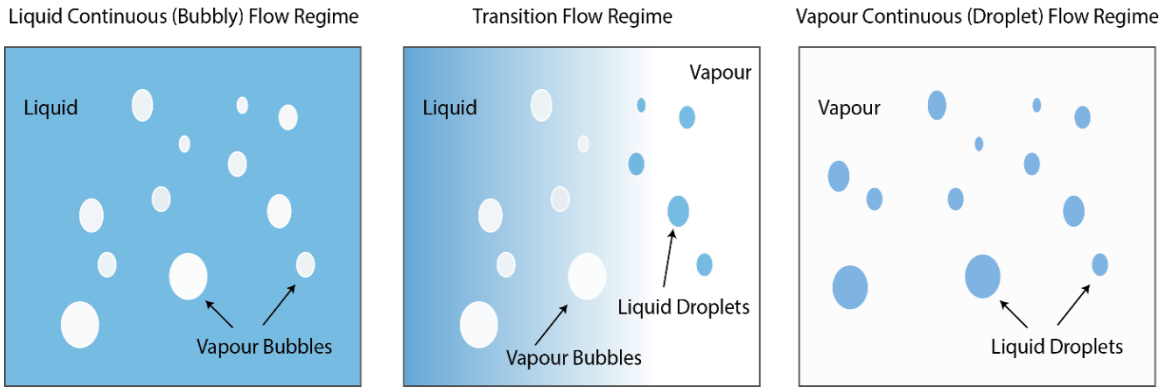

Figure 13 Schematic representation of the various flow regimes

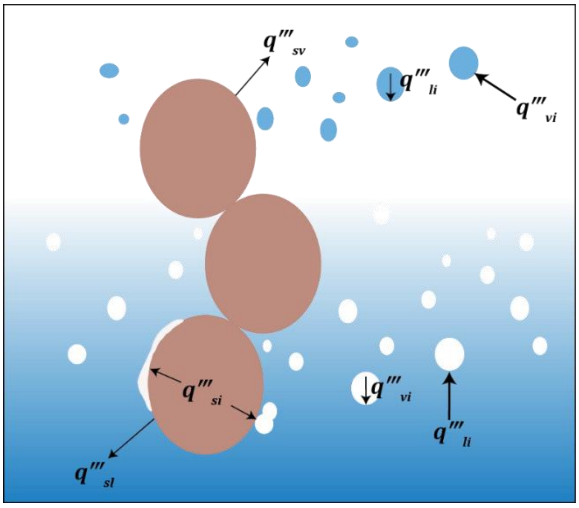

Figure 14 Heat transfer mechanisms considered between the heat-generating solid particles (brown colour), liquid phase (blue colour) and vapour phase (white colour)

Analysis of multiphase flow and the associated heat and mass transfer requires proper characterisation of the flow regime as well as heat transfer regimes, in addition to the various models and correlations. Figure 13 represents the various flow considered in this analysis. The liquid continuous or bubbly flow regime is assumed to exist within the debris bed and the clear fluid region if $\alpha_l \geq 0.7 (\alpha_v \leq 0.3)$ following standard practice (Rahman 2013; Mahapatra et al. 2015). The vapour bubbles are considered to be dispersed in the continuous liquid phase in this flow regime. The vapour continuous or droplet flow regime is considered when $\alpha_l \leq 0.01 (\alpha_v \geq 0.99)$ following the work of Bachrata (2012). In this flow regime, the liquid droplets are assumed to be dispersed in the continuous vapour phase. A transition flow regime is considered between the liquid continuous and vapour continuous regimes when $0.01 < \alpha_l < 0.7 (0.99 > \alpha_v > 0.3)$. The diameter of vapour bubbles (D_v) in the liquid continuous regime and of liquid droplets (D_l) in the vapour continuous regime is assumed to be 0.1 mm throughout this analysis (Raverdy et al. 2017). Figure 14 schematically represents the various heat transfer regimes considered. Convective heat transfer takes place from the solid particles to the fluid phases i.e. liquid or vapour depending on which phase is continuous. Interfacial heat transfer between liquid and vapour phases is also considered in this

analysis. In addition, boiling heat transfer takes place due to heat generation in the solid particles when the temperature of the solid phase exceeds the saturation temperature. Boiling heat transfer is again demarcated into a pure nucleate boiling, pure film boiling and a transition regime depending on the solid phase temperature.

Figure 15 represents the liquid saturation and solid temperature distribution within the system in a dryout situation. It can be observed that vapour accumulation takes place in a small region of the debris bed and a localised hotspot is formed in that region while the surrounding region of the bed remains at a much lower temperature. The effect of several pertinent parameters on dryout are also investigated in this analysis. These include bed composition, bed geometry, liquid subcooling, system pressure and flooding modes – all of which are observed to have a substantial impact on dryout occurrence. These are represented in Fig. 16.

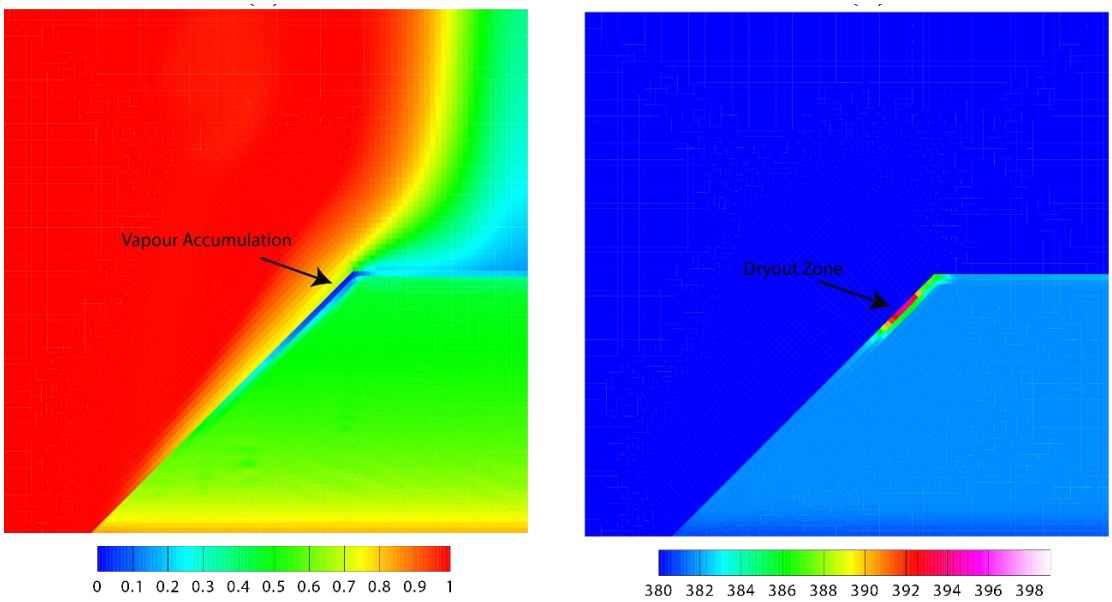

Figure 15 Liquid saturation and Solid temperature distribution in a dryout situation

Additionally, the problem of natural convective heat removal considering phase change of the working fluid is also studied in this thesis. The problem configuration is assumed to be similar to that depicted in Fig. 12 except that the top and side boundaries of the domain are considered to be maintained at a constant temperature. The temperature difference between the heat-generating bed and the cold walls drive the circulation. The effect of wall temperature on the heat transfer characteristics is analysed in this study. It is observed that dryout does not occur within the debris bed if the walls are maintained at a certain temperature lower than the saturation temperature. Natural convection can, thus, potentially be utilised to ensure long term coolability of a debris bed.

The major findings and contributions of the thesis are summarised below –

a. Qualitatively similar results are predicted by the LTE and LTNE models for the single phase scenarios. Heat transfer from the heat-generating debris bed to the cold walls occur by means of a buoyancy-driven counter-clockwise fluid circulation in a natural convective situation. Similar type of fluid circulation is observed in single phase as

well as multiphase situations. This flow pattern gets modified on injection of coolant from the bottom of the debris bed such that maximum temperature rise is observed to occur near the top of the bed. This is in stark contrast to the natural convective situation where maximum temperature rise is found in the inner regions of the bed (see Figs. 3, 4 and 11). Further, flow spreading is observed within the debris bed near the fluid inlet in the bottom flooding situation.

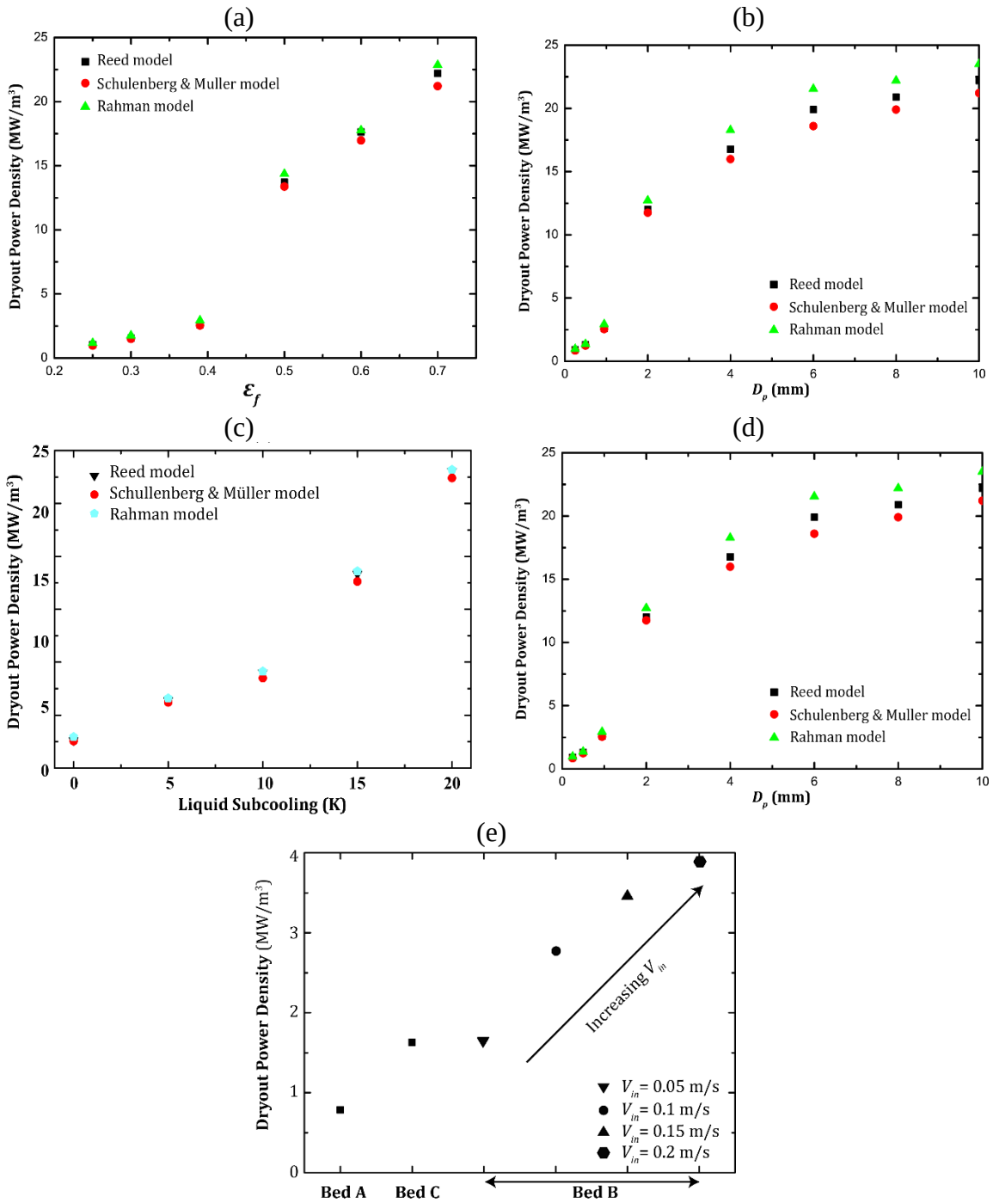

Figure 16 Variation in dryout power density with (a) bed porosity (b) particle size (c) liquid subcooling (d) system pressure for different geometries and (e) flooding modes

b. Quantitative differences between the predictions of the LTE and LTNE approaches are, however, observed especially when there is appreciable convection within the debris bed (*RaDa* > 100) and at large solid to fluid thermal conductivity ratios ($k_s/k_f > 10$) (see Tables 3 and 4). This necessitates the use of the LTNE approach in multiphase situations.

Table 3 Comparison of maximum temperature rise with reducing bed permeability in the single phase natural convective situation

Solution approach	***Ra***	***Da***	***RaDa***	$\theta_{f,max}$	$\theta_{s,max}$
LTNE	10^{10}	10^{-6}	10^{4}	0.02807	0.06069
		10^{-7}	10^{3}	0.0618	0.06938
		10^{-8}	10^{2}	0.07915	0.08107
		10^{-9}	10	0.0812	0.0818
		10^{-10}	1	0.08162	0.0818
LTE	10^{8}	10^{-1}	10^{7}	0.00908	n/a
		10^{-5}	10^{3}	0.05619	
		10^{-8}	1	0.10845	

Table 4 Comparison between the LTE and LTNE approaches in terms of the predicted maximum temperature rise for the single phase mixed convective situation

Ri	***Re***	λ_s	**LTNE**		**LTE**
			$\theta_{s,max}$	$\theta_{f,max}$	θ
0.01	100	0.1	0.003323	0.002833	0.002824
		1	0.030553	0.027053	0.026304
		10	0.241422	0.21548	0.203255
		50	0.971435	0.88473	0.74999
		100	1.84147	1.68529	1.33195

c. Additional fluid injection from the bottom of the debris bed increases heat transfer from the heat-generating debris to the coolant. It is observed from the single phase analysis that maximum temperature rise within the debris progressively decreases as the injection strength is increased signifying enhanced heat transfer (see Table 5). Similar observations are obtained from the multiphase analysis. Greater heat transfer resists vapour accumulation within the debris bed and hence, a significantly larger power density is required for dryout occurrence under bottom flooding situations. The dryout power density is observed to increase from 0.78 MW/m^3 under top-flooding situation to 1.6 MW/m3 with bottom-flooding at an injection velocity of 0.05 m/s. This continues to increase with further increase in injection velocity to 3.9 MW/m^3 at 0.2 m/s (see Fig. 16e).

Table 5 Change in maximum bed temperature rise with increasing injection strength (in terms of *Re*)

Ri	Gr	Re	θ_{max}
0.01	10^5	3162.278	0.00205
0.1		1000	0.00562
1		316.278	0.01251
10		100	0.01508
100		31.6278	0.03204

Table 6 Comparison of maximum bed temperature rise with reducing bed permeability in single phase mixed convective situation

Ri	Re	Da	θ_{max}
0.01	50	10^{-1}	0.04618
		10^{-4}	0.05395
	500	10^{-1}	0.00689
		10^{-4}	0.01001

d. Analysis shows that one of the main factors influencing coolability of debris beds is its permeability. Permeability determines the strength of fluid flow through porous media and hence, also affects heat transfer from porous media to the fluid phases. It is observed from the single phase analyses that a reduction in permeability lowers the heat transfer from the debris bed and leads to a larger temperature rise within the bed (see Tables 3 and 6). In the single phase natural convective situation, this is accompanied by a gradual shift in the location of the maximum temperature zone towards the interior of the bed as the permeability reduces. The maximum temperature zone, in contrast, remains unaltered near the top of the debris bed with change in permeability under bottom-flooding conditions. This effect of reduced heat transfer from the debris bed with decreasing permeability results in easier vapour accumulation within the bed in a multiphase flow situation. Dryout of a debris bed, therefore, occurs at a much lower power density at reduced permeabilities. The dryout power density increases from 21 MW/m^3 to 0.85 MW/m^3 when the permeability of the bed is reduced from 10^{-7} to 10^{-11} from (see Fig. 16a, 16b). Further, it is observed that the dryout zone shifts from the upper central region to upper peripheral regions of the bed as the permeability is reduced.

e. Bed configuration and the available fluid flow passage is observed to play a major role in determining heat transfer and hence, coolability of a debris bed. A comparison of the maximum temperature rise in natural convection situation for three different bed configurations – cylindrical, truncated conical and conical – reveals that the largest and smallest temperature rise occurs in the conical and the cylindrical configuration, respectively. The dimensionless maximum temperatures obtained for these configurations – 0.02128, 0.02341 and 0.0303 for the cylindrical, truncated

conical and conical, respectively – indicate a wide variation (~ 29%). The effect of bed configuration is more pronounced in a multiphase situation. It is observed that the availability of an additional flow passage in a laterally flooded bed modifies the fluid flow pattern within the bed and increases the dryout power density to 1.6 MW/m^3 from 0.78 MW/m^3 in a top-flooded bed (see Fig. 16e). The change in dryout power density in differing bed configurations is determined by the combined effects of available surface area of the bed for coolant infiltration and height of the bed. The truncated conical bed configuration, with a large coolant infiltration area and an intermediate height, is observed to have the largest dryout power density (1.8 MW/m^3 at 1 bar pressure). Interestingly, the lowest dryout power density (1.5 MW/m^3 at 1 bar) is obtained for the conical configuration which has the largest coolant infiltration area (see Fig. 16d). This happens due to a counter-current flow mechanism existing across the lateral surface of the bed leading to easier vapour accumulation and consequent dryout of the bed.

f. Coolant subcooling is observed to significantly affect the heat transfer dynamics. Greater heat transfer takes place from the heat-generating solid phase to the coolant due to its subcooled state. This enables greater condensation of the vapour generated and as such, a significantly higher power density becomes necessary for dryout to occur. The dryout power density increases from 2.5 MW/m^3 for saturated water to 6.2 MW/m^3 for water at 5K subcooling and thereafter, increases further to 27 MW/m^3 for 20 K subcooling (see Fig. 16c). In addition, it is observed that the dryout zone progressively shifts towards the inner regions of the bed when liquid subcooling is considered.

g. A change in system pressure is observed to have a substantial impact on dryout power density. The dryout power density increases from 1.8 MW/m^3 at 1 bar to 6.2 MW/m^3 at 10 bar for the truncated conical configuration. Similar variation in dryout power density with pressure is obtained for all bed configurations studied in this analysis (see Fig. 16d).

h. It is observed from the analysis of natural convection in a multiphase situation that if the enclosure walls are maintained at a definite subcooling (~5 K) below the saturation temperature, the debris bed can be maintained in a coolable condition. Thus, if the requisite amount of energy can be removed from the enclosure walls such that the walls are maintained at a subcooled temperature, dryout of a debris bed can be avoided. This is especially relevant in view of long-term coolability of a debris bed.

TABLE OF CONTENTS

LIST OF FIGURES

Chapter 4

Chapter 5

LIST OF TABLES

NOMENCLATURE

English alphabets

a_i	Interfacial area density, m^{-1}	$\boldsymbol{n}$	Unit normal vector
A	Area, m^2	Nu	Nusselt number
c_p	Specific heat capacity, J/kg.K	p	Pressure, Pa
D	Diameter, m	Pr	Prandtl number
D_l	Droplet diameter, m	q	Volumetric heat transfer rate, $W.m^{-3}$
D_p	Particle size, m	$\boldsymbol{q}$	Heat flux, $W.m^{-2}$
D_v	Bubble diameter, m	r	Radial co-ordinate
Da	Darcy number	R	Interfacial momentum exchange coefficient, $kg.m^{-3}.s^{-1}$
$\boldsymbol{E}$	Energy flux vector		Bed radius, m
f	Drag function	R_t	Radius of top surface of the bed, m
$\boldsymbol{F}$	Solid-fluid drag force, $kg.m^{-2}.s^{-2}$	Ra	Rayleigh number
F_c	Forchheimer Co-efficient	Re	Reynolds number
$\boldsymbol{g}$	Acceleration due to gravity, m/s^2	Ri	Richardson number
Gr	Grashof number	T	Temperature, K
h	Enthalpy, J/kg (Chapter 5) Heat transfer coefficient, $W/m^2.K$ (Chapter 3,4)	U	Radial velocity, $m.s^{-1}$
		V	Axial velocity, $m.s^{-1}$
$h_{i,j}$	Interfacial heat transfer coefficient, $W/m^2.K$	$\boldsymbol{V}$	Velocity, $m.s^{-1}$
H	Bed height, m	$\mathcal{V}$	Volume, m^3
Ja	Jakob number	W	Weighing function Domain width, m
k	Thermal conductivity, W/m.K (Chapter 3, 4) Turbulent kinetic energy, m^2/s^2 (Chapter 5)	X	X co-ordinate
K	Permeability, m^2	$\boldsymbol{X}$	Body force per unit volume, $N.m^{-3}$
K_r	Relative permeability	Y	Y co-ordinate
L	Domain height, m	z	Axial co-ordinate
m	Mass transfer rate, $kg.s^{-1}$		

Greek characters

α	Volume fraction Thermal diffusivity, $m^2.s^{-1}$
β	Thermal expansion coefficient, K^{-1}
γ	Porosity-scaled thermal conductivity ratio
ε	Turbulent kinetic energy dissipation rate
ε_f	Porosity
η	Passability, m
η_r	Relative passability
θ	Dimensionless temperature
λ	Thermal conductivity, $W.m^{-1}.K^{-1}$ (Chapter 5) Thermal conductivity ratio (Chapter 3, 4)
μ	Dynamic viscosity, $kg.m^{-1}.s^{-1}$
μ_t	Turbulent viscosity
ν	Kinematic viscosity, $m^2.s^{-1}$
ρ	Density, $kg.m^{-3}$
σ	Surface tension coefficient, $N.m^{-1}$
$\sigma_k, \sigma_\varepsilon$	Turbulent Prandtl number
τ	Stress, $N.m^{-2}$
ϕ	Bed angle, $^\circ$
ψ	Stream function (Chapter 3, 4) Sphericity or Shape factor (Chapter 2, 5)
Π	Heat function
Φ	Generalised property

Subscripts/Superscripts and others

avg	Average value
A	Annular flow regime
BST	Bubbly to Slug Transition regime
eff	Effective value
f	Fluid phase
fb	Film boiling regime
HVB	High Void Bubbly regime
i	Liquid-Vapour Interface
in	Domain inlet
j	Primary phase index
k	Dispersed phase index
l	Liquid phase
LC	Liquid Continuous regime
LVB	Low Void Bubbly regime
m	Mixture phase
max	Maximum value
min	Minimum value
nb	Nucleate boiling regime
out	Domain outlet
p	Porous medium
ref	Reference value
s	Solid phase
S	Slug flow regime
sat	Saturation value
sub	Subcooling
v	Vapour phase
VC	Vapour continuous regime
$'$	Dimensionless quantities
$'''$	Volumetric quantities
$\langle \quad \rangle$	Eulerian volume-averaged quantities

Chapter 1

INTRODUCTION

This chapter introduces the phenomena of debris bed formation and the need for ensuring its coolability under severe accident situations in nuclear reactors. This is followed by a survey of existing works on debris coolability, challenges faced in this regard and the outstanding issues. The overall objectives of this thesis and its organisation are also discussed in this chapter.

1.1. Background

The major drawback of any nuclear reactor is the continued generation of substantial amount of decay heat within the radioactive fuel even after termination of the nuclear fission reaction. The decay heat generated is estimated to be approximately 6% of the reactor thermal power just after reactor shutdown and decreases exponentially to about 1% of the thermal power after 1 hour (Schmidt 2004). Continuous removal of the decay heat is, therefore, necessary in order to prevent temperature rise within the reactor core and thereby, melting of the core. This is the basic premise of safety in nuclear power reactors.

Severe accidents in nuclear reactors are characterised by the absence of adequate heat removal mechanism from the reactor core due to the failure of normal as well as emergency cooling systems. Although emergency shutdown of the reactor takes place and the fission chain reaction stops immediately post a severe accident, decay heat generation and its inadequate removal leads to tremendous heating of the reactor core. This causes the residual cooling water to evaporate which decreases the water level within the core and as a result, exposes the decay heat-generating fuel rods to water vapour. This decreases the heat removal rate from the fuel rods and results in rapid temperature rise which may cause melting of the fuel rods in an extreme situation.

The melt pool formed, if the core melts down, is a mixture of fuel and support structure material (typically termed as *corium*), and it relocates to the lower regions of the reactor pressure vessel (RPV) due to gravitational action (see Fig. 1.1). This usually takes place in the form of jets or drops of the melt depending on the severity of the meltdown and core breach. The relocating molten mass impinges directly on the RPV wall if the latter is devoid of any residual water and forms a melt pool in the lower head of the RPV in such a situation (see Fig. 1.1a). The superheated molten mass comes in contact with subcooled water if the RPV contains some residual water. During the descent of the molten mass through the water pool, it is subjected to hydrodynamic forces and it fragments into smaller droplets (Mahapatra et al. 2018). This action is typically termed as *hydrodynamic fragmentation*. At the same time, film boiling of water occurs since the temperature of the molten mass is much higher than the Leidenfrost temperature. A meta-stable mixture is thereby formed comprising of water, vapour and fragmented material. In certain situations, the vapour film enveloping the fragments may destabilise and result in direct contact of water with the superheated molten mass. The thermal stress generated as

a result of this interaction causes local pressurisation and can lead to secondary fragmentation of the fragmented molten mass. Such temperature-induced fragmentation is typically termed as *thermal fragmentation*. The fragmented material eventually quenches and settles down on the base of the RPV as a mass of decay heat-generating debris (see Fig. 1.1b). The above-described phenomena is referred to in literature as *Molten Fuel-Coolant Interactions* (MFCI).

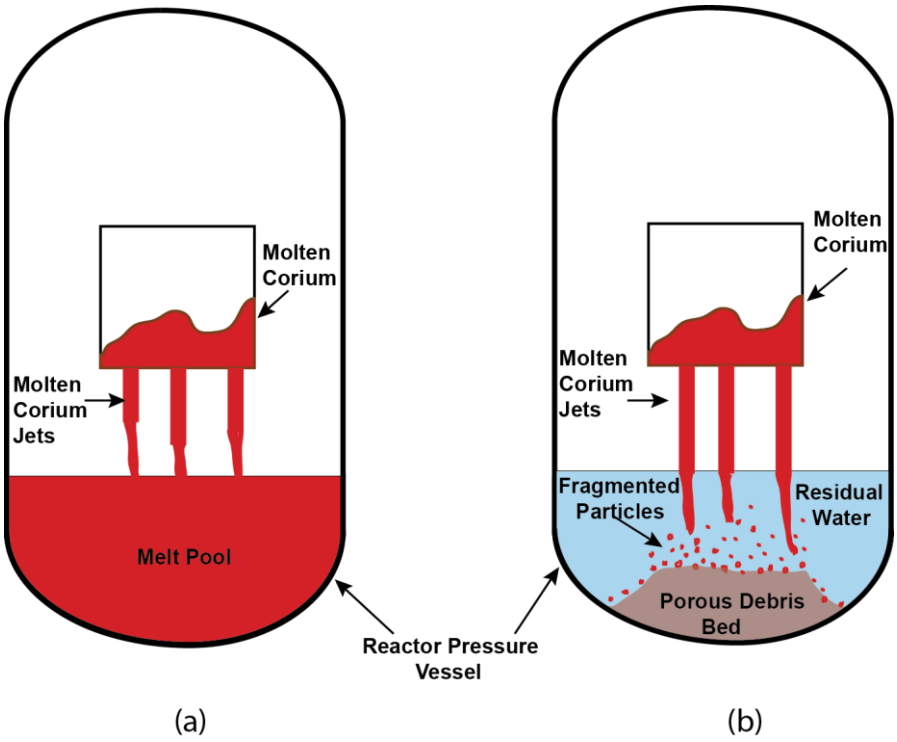

Figure 1.1 Schematic representation of formation of melt pool and debris bed in the RPV due to melt relocation

Estimation of the decay heat generated within the debris yields a specific power ranging between 100 W/kg to 300 W/kg and an equivalent power density between 0.5 to 1.5 MW/m^3, depending on reactor type and corium composition. Such large heat generation can only be removed by boiling heat transfer using cooling water. In order to establish a stable and coolable condition, the evaporated water must be replaced continually – either by external injection of additional water or by condensation and recirculation of the evaporated water. Also, the vapour generated within the debris must be able to escape the debris mass and the cooling water must be able to penetrate into the debris. Any failure to maintain the debris mass in a coolable state will lead to localised dryout and a consequent temperature rise in the debris. This creates a possibility where the debris might re-melt and again form a molten pool in the RPV lower head. The melt pool interacts with the RPV wall and in an extreme situation will result in failure of the RPV and subsequent transport of the molten mass into the containment. This scenario is termed as the *In-Vessel phase* in the accident progression sequence wherein the entire phenomena is confined within the RPV.

The molten mass relocates to the reactor containment due to RPV rupture and is subjected to similar actions as in the in-vessel scenario. Failure to terminate the accident

progression at this stage, however, can lead to steam explosion, failure of the containment building and the imperative release of radioactivity to the environment. This phase of the accident sequence is termed as the *Ex-Vessel phase* since the phenomena occurs outside the RPV. The accident progression sequence, described above, is schematically represented in Fig. 1.2.

It can, thus, be seen that ensuring adequate heat removal from the heat-generating debris and maintaining it in a coolable condition is critical to terminating the accident progression sequence. In this context, it becomes imperative to have an assessment of the limit beyond which the debris cannot be maintained in a coolable condition. This limit is typically termed as the *dryout* condition and is represented in literature in terms of the corresponding heating power (*dryout power*) or the heat flux that can be removed through the upper surface of the bed (*dryout heat flux*).

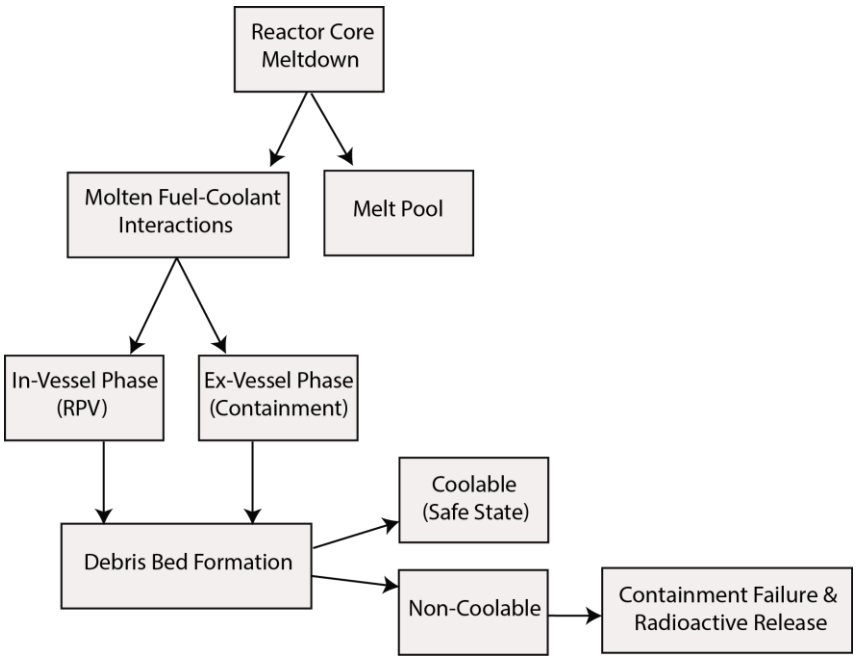

Figure 1.2 Schematic of accident progression sequence considering molten fuel-coolant interactions

1.2. Literature Review

The occurrence of dryout in debris beds is governed by the associated multiphase fluid flow as well as heat and mass transfer characteristics. These are significantly influenced by system thermal hydraulic parameters (such as system pressure, coolant temperature, coolant flooding mechanism etc.) as well as debris bed characteristics (composition, structure etc.).

1.2.1. Debris bed characteristics

Debris bed characteristics i.e. its composition and structure are primarily determined by the preceding molten fuel-coolant interactions (MFCI). The phenomena of MFCI is itself dependent on several parameters such as size of the breach, mass flux of the relocating melt, temperature of the melt and water pool etc. Therefore, it becomes

necessary to have a proper assessment of the MFCI phenomena and its outcomes in order to carry out subsequent studies on debris coolability.

(a)

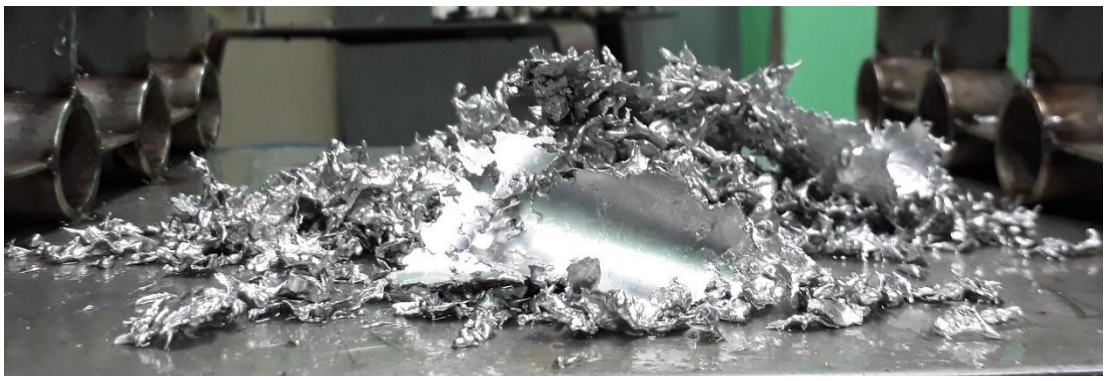

(b)

(c)

Figure 1.3 A typical debris bed formed as a result of MFCI in (a) DEFOR experiment (Karbojian et al. 2009) (b-c) in-house experiment at Jadavpur University

Several experimental studies have been carried out over the years with focus on characterising the composition of the debris. Experiments conducted in the FARO and KROTOS facilities investigated debris formation over a wide range of parameters (Magallon and Huhtiniemi 2001; Magallon 2006). Parameters analysed include melt

mass, water pool depth, melt jet diameter and system pressure. Significant fragmentation was observed to occur irrespective of the parametric conditions. The DEFOR experiments provided additional information regarding the effect of water pool subcooling on the fragmentation process. Similar investigations have been carried out in TROI facility (Song et al. 2003) as well as the MISTEE-Jet facility (Manickam et al. 2016, 2017).

Table 1.1 Debris bed composition observed (debris formation experiments) and adopted (debris coolability experiments) in different experimental programmes

Experiment type	Experimental Programme	Particle Size Range (mm)	Average Porosity
Debris Formation	KROTOS (Huhtiniemi and Magallon 2001)	< 2	N/A
	FARO (Magallon 2006)	< 6	0.5 – 0.6
	TROI (Song et al. 2003)	< 6.35	N/A
	DEFOR (Kudinov et al. 2008; Karbojian et al. 2009)	< 10	0.46 – 0.7
	COMECO (Singh et al. 2015)	< 10 (without decay heat) < 50 (with decay heat)	0.51
Debris Coolability	COOLOCE (Takasuo et al. 2012; Takasuo 2016)	0.8 – 1.07	0.38
	DEBRIS (Schäfer and Lohnert 2006, Schäfer et al. 2006)	3- 6	0.36 – 0.38
	STYX (Lindholm et al. 2006; Takasuo et al. 2011)	0.25 – 10	0.34 – 0.37
	POMECO (Nayak et al. 2006; Thakre et al. 2014)	< 5	0.26 – 0.38
	SILFIDE (Atkhen and Berthoud 2006)	2 – 7.18	0.4
	PEARL, PRELUDE (Bachrata et al. 2012)	0.5 – 8	0.3 – 0.4

The above mentioned experimental investigations reveal that the fragmented mass of debris formed as a result of MFCI has an irregular and heterogeneous porous composition which allows fluid movement through the inter-connected void between the constituent particles. Significant uncertainty is, however, evident from the reported data on bed porosity and particle size from these experiments. The average porosity in the debris have been reported to vary between 0.25 and 0.7. The size of the fragments have been observed to range from a few hundred microns to large chunks (~50 mm). Table 1.1 summarises the observations reported from various experimental programs on debris bed

characterisation. These data have been used in recreating debris beds for the purpose of investigation on debris coolability.

Along with bed composition, a significant uncertainty also exists with regard to the structure a debris bed will have on its formation. It is expected that the resulting debris bed will be a heap-like structure similar to that formed on pouring of granular material on a surface. Karbojian et al. (2009) observed a heap-like debris bed to be formed in cases when the melt jet is completely fragmented into very fine particles (Fig. 1.3a). More recently, Lin et al. (2017) characterised the structure of a debris bed in terms of the particle size. A flat-topped cylindrical bed was observed for very fine particles (< 0.25 mm) while the bed structure changed from a concave shaped to a convex shaped conical heap as the particle size was increased to ~ 2.5 mm and beyond. Observations from an in-house experiment carried out on MFCI also confirm the formation of heap-like debris beds (Fig. 1.3b). Figure 1.3c represents the fragmented particle sizes obtained as a result of the in-house MFCI experiments.

1.2.2. Dryout estimation

The key parameter of interest in studies involving coolability assessment of corium debris beds is the dryout phenomena and the corresponding dryout heat flux (DHF) or dryout power. Several experimental as well as numerical studies have been carried out over the years to quantify the dryout phenomena in typical debris beds and to understand the impacts of various parameters affecting the phenomena. These are discussed in the following sections.

1.2.2.1. Experimental Investigations

Observations from the various experimental studies have led to identification of the root cause of dryout occurrence in heat-generating debris beds. As mentioned in *Section 1.1,* heat transfer from the heat-generating solid particles is achieved by flooding the debris bed with cooling water. The large power density within the debris bed results in evaporation and boiling of the flooding water and leads to substantial vapour generation. The vapour generated, along with the heated water, flows upwards due to buoyancy and ideally leaves the bed through its top surface. The vapour and heated water leaving the bed is replaced by additional cooling water which penetrates into the bed through its surfaces. A counter-current flow situation is, thus, encountered in the upper regions of the bed near the top surface (see Fig. 1.4). The downward moving cooling water, as such, is resisted by the upward moving vapour and at a critical value of vapour mass flux, water would not be able to penetrate into the bed any further. The vapour present, therefore, accumulates within the bed leading to subsequent dryout of the bed. This leads to the conclusion that counter-current fluid flow mechanism within the bed is the major reason behind dryout of the bed.

Dryout in debris beds is expected to be significantly influenced by the system pressure. One of the earliest reported works on the impact of pressure on debris dryout is by Squarer et al. (1982). Reed et al. (1986) determined the effect of system pressure on

dryout, in experiments as part of the Degraded Core Coolability (DCC) program, by varying the system pressure in the range of 1 to 170 atmospheres for various particle sizes. The pressure dependence of dryout was also determined by Miyazaki et al. (1986), DEBRIS experiments (Schäfer and Lohnert 2006, Schäfer et al. 2006) and STYX experiments (Lindholm et al. 2006). In all these experimental investigations, the DHF was observed to substantially increase with system pressure. However, above a system pressure of approximately 10 bar, the DHF was found to decrease with further increase in system pressure.

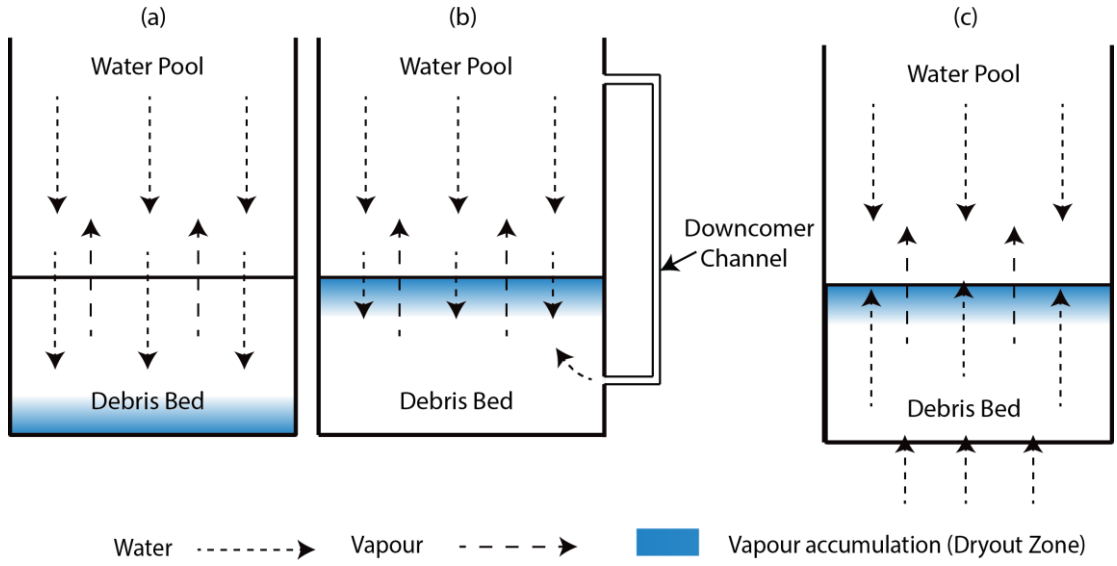

Figure 1.4 Schematic representation of (a) Top-flooding and Counter-current flow of water and vapour (b) Lateral flooding and (c) Bottom flooding in one-dimensional debris beds

Dryout has also been observed to be significantly influenced by the composition of the porous debris bed. Squarer et al. (1982) investigated the effects of particle size and its distribution within the debris bed on DHF. Experiments conducted under the Degraded Core Coolability (DCC) program (Reed et al. 1986) considered particle size varying between 75 micron to 11.2 mm. Cha and Chung (1986) reported the DHF as a function of mass flux of water for a particle size ranging between 1.5 – 4.0 mm in a forced convective situation over an inductively heated porous bed. The impact of particle size has also been studied in the STYX (Lindholm et al. 2006) and DEBRIS (Schäfer and Lohnert 2006, Schäfer et al. 2006) experimental programs. Results obtained from the experimental investigations suggest that the DHF becomes larger as the particle size is progressively increased. Porosity of the debris bed was also found to have a substantial impact on DHF (Ma and Dinh 2010). These observations suggest that the occurrence of dryout is strongly influenced by the composition of the porous medium.

In a realistic situation, the debris bed is expected to be heterogeneous and the particles constituting the bed are expected to be highly irregular. This can be visualised from the photographs of an experimentally obtained debris in Fig. 1.3. The effect of a varying bed composition was studied by Tung and Dhir (1987). They considered a

varying bed permeability in both axial and radial directions, and performed quenching as well as dryout experiments in an inductively heated particle bed. The influence of heterogeneous composition of a debris bed was investigated in the DEBRIS experimental program (Schäfer and Lohnert 2006, Schäfer et al. 2006). Stratified beds were considered in the experimental programs at STYX (Lindholm et al. 2006) and POMECO (Nayak et al. 2006). Significant reduction in DHF was observed in case of an axially stratified bed, with finer particles in the top layer, in the STYX facility (Lindholm et al. 2006). Micro-inhomogeneity in the constituent solid particles results in a localised high porosity zone. This has been observed by Ma and Dinh (2010) to enhance the DHF of the bed by up to 50% when compared to a bed without such inhomogeneity. Particle morphology has also been observed to significantly affect the dryout limit (Ma and Dinh 2010).

Since fluid flow mechanism is the main parameter affecting the dryout phenomena, it can be expected that the dryout limit in a debris bed can be augmented with appropriate modification of the fluid flow mechanism within the debris bed. Extensive investigations have been carried out in this regard. Liquid-vapour flow within the porous bed can be effectively altered from counter-current mode (in a purely *top-flooding* situation) to co-current mode if additional coolant is injected from the bottom of the bed (*bottom-flooding*) or across the lateral surface of the bed (*lateral-flooding*). This is represented in Fig. 1.4 and is expected to substantially enhance the dryout limit of the bed.

One of the earliest works on investigation of multidimensional flooding effects on coolability of debris beds was carried out by Wang & Dhir (1988). They studied the effects of bottom flooding on quenching characteristics of a heated particulate bed. Atkhen and Berthoud (2006) investigated the effects of bottom flooding in the SILFIDE experimental facility. Observations reveal that coolant injection from bottom of the bed, in addition to top flooding, is substantially more efficient than top flooding mechanism only. Similar observations from experiments carried out in the DEBRIS facility has been reported by Schafer et al. (2006) and Rashid et al. (2011). Ma and Dinh (2010) reported a DHF augmentation of about 40%, from experiments in DEFOR, in bottom-flooding situations when compared to top-flooding conditions. Emphasis on bottom injection of coolant as possible means of augmenting the dryout limit can be found in several other works (Paladino et al. 2002, Miscevic et al. 2006, Cho et al. 2006, Bang and Kim 2010). The concept of bottom-flooding of debris bed has been extended to the development of a core catcher device (Widmann et al. 2006, Kang et al. 2007; Fischer et al. 2005, Jasmin Sudha et al. 2015).

The concept of lateral-flooding of debris beds was addressed by the POMECO experiments (Kazachkov and Konovalikhin 2002, Nayak et al. (2006)) which utilised the concept of downcomers for recirculating the condensing vapour. A unique feature of the POMECO debris bed is its sand-based composition with different particle size distributions. The magnitude of DHF was observed to be augmented with the application of downcomers. The effect of lateral flooding on coolability of debris beds, by means of downcomers, has also been investigated by Takasuo et al. (2011) in the STYX

experimental facility considering an irregular core debris bed. It was observed that the use of lateral flooding increased the DHF by 22-25% in case of homogeneous beds. However, in case of stratified beds with a fine particle layer on top of the bed, only a marginal increase was found in the DHF with the use of lateral flooding. Also, the observed increases in DHF for the latter case were found to be inconsistent. Similar effects of DHF enhancement with lateral flooding, using downcomers, has been observed by Rashid et al. (2012) in the DEBRIS experimental facility.

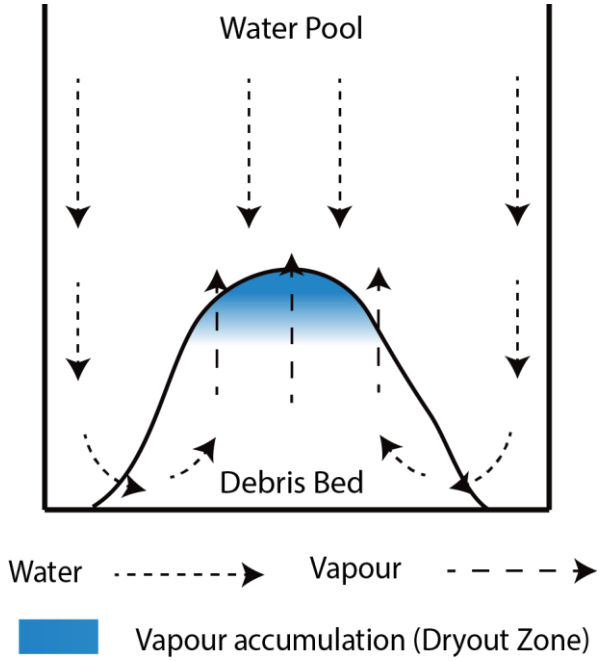

Figure 1.5 Inherent multidimensionality associated with heap-like beds

As discussed in *Section 1.2.1*, the quenched debris as a result of MFCI settle down in the RPV as a heap-like mass. However, it becomes difficult to predict the exact shape of the debris bed due to the uncertain nature of the parameters affecting it. Therefore, it is necessary to carry out investigations into the effects of bed configuration on dryout occurrence. Surprisingly, all the experimental investigations discussed above considered one-dimensional beds and as such, do not appreciate the multidimensional effects associated with heap-like beds (see Fig. 1.5). This has led to investigations into the effects of bed geometry in the past few years. Takasuo et al. (2012) compared the dryout behaviour of conical and top-flooded cylindrical debris bed configurations in the COOLOCE experimental facility. A better coolability was observed in case of the conical bed geometry when the two beds had the same height. However, if the two beds had the same volume with equal bed diameter, the conical bed was observed to have a lower dryout power density. This is due to a higher bed height in case of the conical bed which results in greater heat flux in upper parts of the bed. Thakre et al. (2014) compared the dryout power density of a triangular and a cylindrical bed in their study. The dryout power density in triangular beds was observed to increase by 69% and was attributed to the effects of multi-dimensional coolant infiltration in the triangular bed. Takasuo (2016) considered the following different bed configurations for analysis in the COOLOCE facility – conical, top-flooded cylinder, fully-flooded cylinder, laterally-flooded cylinder,

cone on a cylindrical base and a truncated cone. It was observed that the DHF increased by about 47% - 73% in bed configuration with multidimensional flooding effects.

Experimental investigations have also focused on developing correlations for prediction of frictional pressure drop in two-phase flow situation through porous media. Frictional pressure drop determines the onset of counter-current flow limit for the liquid-vapour flow which contributes to dryout occurrence. These correlations have been extensively used in numerical modelling of the debris coolability problem. The correlations proposed by Reed (1982), Lipinski (1981), and Hu and Theofanous (1991) do not take into account interfacial drag between liquid and vapour. The correlations proposed by Schulenberg and Muller (1987), and Tung and Dhir (1988), however, considers the interfacial drag in their models. Experimental studies in the DEBRIS facility (Schafer et al. 2006) have established that the correlations which do not consider interfacial drag are inadequate to predict the trends of pressure drop across a wide range of conditions. However, the Reed model was observed to give a good representation of the pressure drop characteristics for bottom-flooding conditions at high flow rates. A better representation of the qualitative behaviour of pressure drop were achieved with the use of correlations considering interfacial drag. The Tung and Dhir model has undergone modifications with respect to consideration of smaller particles (Schmidt 2007) and the annular flow regime (Schmidt 2007, Taherzadeh and Saidi 2015, Li et al. 2018b).

The issue of identification of an effective diameter of the constituent particles is important in the perspective of numerical modelling of the frictional pressure drop. Li and Ma (2011a) worked on quantifying the effective particle diameter of a particulate bed composed of multi-diameter spheres. It was found that at very low flow rates ($Re < 7$) the effective particle diameter can be represented by the area mean diameter of the particles present in the bed, while at higher flow rates it is closer to length mean diameters. In case of a particulate bed composed of non-spherical irregular particles, the effective particle diameter was represented by a product of Sauter mean diameter and sphericity of the constituent particles (Li and Ma 2011b, Li et al. 2012). This has been extended to situations involving very fine particles (Li et al. 2015), coarse particles (Li et al. 2017) and stratified configurations (Li et al. 2018a). Based on these observations, a modified pressure drop correlation has been proposed by Li et al. (2018b). Similar attempts at estimation of an effective particle diameter in different situations has been made by Chikhi et al. (2014), Clavier et al. (2015), Chikhi et al. (2016) and Clavier et al. (2017).

1.2.2.2. Numerical studies

It is evident from the experimental studies on debris formation (see *Section 1.2.1* and Fig. 1.3) that a typical debris bed is composed of solid particles and interconnected voids. This gives it a porous structure and as a result, the numerical models developed for porous media can be utilised in modelling flow through a debris bed. The earliest attempts at numerical predictions of dryout resulted in development of empirical correlations and simplified models for DHF estimation in one-dimensional beds. These include the correlations proposed by Theofanous and Saito (1981), Lipinski (1984) and

Shrock et al. (1986). The correlation proposed by Theofanous and Saito (1981) evaluated the DHF as follows –

$$q = 0.0707\rho_l h_{lv}\sqrt{\frac{gD_p{\varepsilon_f}^3}{\psi(1-\varepsilon_f)}}\left(\frac{\rho_v}{\rho_l}\right)^{3/8}\left(\frac{\mu_v}{\mu_l}\right)^{0.1} \tag{1.1}$$

The correlation proposed by Lipinski (1984) evaluated the DHF as follows –

$$q = \left(\frac{{q_T}^4}{4{q_L}^2} + {q_T}^2\right) - \frac{{q_T}^2}{4q_L} \tag{1.2}$$

where, the terms q_L and q_T denote the heat flux at the laminar and turbulent limits, respectively. These are expressed as –

$$q_L = \frac{(\rho_l - \rho_v)g{D_p}^2{\varepsilon_f}^3 h_{lv}}{150(1-\varepsilon_f)^2}\left[\frac{\mu_v}{\rho_v{\alpha_v}^n} + \frac{\mu_l}{\rho_l{\alpha_l}^n}\right]^{-1}\left(1+\frac{\lambda_c}{L}\right) \tag{1.3}$$

$$q_T = \left[\frac{(\rho_l - \rho_v)gD_p{\varepsilon_f}^3 h_{lv}}{1.75(1-\varepsilon_f)}\left[\frac{1}{\rho_v{\alpha_v}^m} + \frac{1}{\rho_l{\alpha_l}^m}\right]^{-1}\left(1+\frac{\lambda_c}{L}\right)\right]^{1/2} \tag{1.4}$$

Shrock et al. (1986) evaluated the DHF using the following correlation –

$$q = C^2\rho_l h_{lv}\sqrt{\frac{gD_p{\varepsilon_f}^3}{6(1-\varepsilon_f)}}\left[2.18 + \left(\frac{\rho_l}{\rho_v}\right)^{1/4}\right]^{-2}\left(1-\frac{\rho_v}{\rho_l}\right)^{1/2} \tag{1.5}$$

These correlations, however, cannot be utilised for DHF prediction in multidimensional situations. Multidimensional numerical models must be developed to predict the dryout occurrence in such situations. Such numerical models must take into account the existence of three distinct phases – solid particles, liquid water and water vapour – and must also consider the hydrodynamic as well as thermal interactions between the phases. The complex transport processes of two-phase flow and boiling heat transfer must also be considered in such models. Several attempts have been made at development of such multidimensional numerical models which is capable of assessing debris coolability.

The debris coolability module in the severe accident analysis code SAMPSON provides a good tool for prediction of reactor safety margin following a severe accident by analysis of three-dimensional natural convection in a debris bed with simultaneous spreading, melting and solidification (Hidaka and Ujita 2001, Ujita and Hidaka 2001). In addition to this, the code also calculates temperature distribution of the vessel wall and evaluates wall failure.

Berthoud (2006) attempted to model the dryout of a debris bed with MC3D by implementing proper modifications to account for the complex processes associated with boiling in porous media, including the presence of non-condensable gases. The modified code – MC3D-REPO – was validated with analytical solutions of various simplified problems as well as with two different experiments. Although the code could properly

tackle the multidimensionality of the problem, application of the code is limited due to its assumption of thermal equilibrium in a representative elementary volume and as such, cannot be applied for modelling post-dryout heat transfer from debris beds. Raverdy et al. (2017) reported the development made in MC3D with respect to tackling of the thermal non-equilibrium aspect of the problem.

Fichot et al. (2006) presented a multidimensional numerical model, considering thermal non-equilibrium, for two phase flow in debris beds that is implemented in ICARE/CATHARE. Reasonable agreement was obtained in prediction of DHFs, as available in literature, in one-dimensional situations. Results of one-dimensional reflooding show the importance of using a thermal non-equilibrium model and further indicate that the effects of channelling within the debris bed should be taken into account for more accurate modelling. The two-dimensional results presented highlight the influence of porous medium characteristics of a debris bed. As expected, water circulation is improved by considering multi-dimensional flow in the bed and the dryout heat flux is larger than predicted by 1D modelling. This leads to a flow pattern where steam can exit the debris bed in preferential channels and there is less limitation by counter-current flow. An improved model of heat transfer was implemented in ICARE/CATHARE by Bachrata (2012) and utilised to model reflooding situations in debris beds.

The numerical code WABE-2D (Bürger et al. 2006) was developed at IKE, University of Stuttgart, to simulate boil-offs and quenching of debris bed pertaining to debris coolability. The multidimensional effects along with top and bottom injection of coolants were discussed with proper constitutive laws for drag and interfacial friction. Experimental data from SILFIDE facility was used for the validation of the code. A different code developed at the same institute is MEWA. Takasuo et al. (2011) analysed the effects of lateral flooding in irregular debris bed using MEWA. Rahman (2013) utilised the MEWA code to perform extensive analysis on quenching as well as coolability of debris beds. Huang and Ma (2018) utilised the MEWA code to study the dryout phenomena in multidimensional heap-like beds. Numerical models have also been implemented in the framework of PORFLO (Takasuo 2015) and THERMOUS (Taherzadeh and Saidi 2015) programs.

All the above mentioned models and codes, however, have been sparingly used in addressing coolability in multidimensional heap-like beds. Also, no reported studies exist which have utilised commercially available computational fluid dynamics tools for modelling the problem of debris coolability.

1.3. Outstanding issues

It is evident from the literature survey presented in *Section 1.2* that a substantial amount of work has been carried out on understanding the physics of debris bed formation, and also on the fluid flow and the associated heat transfer mechanism governing the coolability of a debris bed. However, several issues related to debris coolability still needs to be addressed. These are summarised below –

a. Most of the experimental investigations as well as numerical studies adopted a simplified structure of debris bed for analysis. This serves the purpose of developing the basic premise of understanding and modelling heat transfer from the debris beds. However, studies need to be carried out with a more realistic debris bed structure (for e.g. a conical heap) in order to properly appreciate the effects of multidimensionality of the bed configuration.

b. It can be expected from a practical perspective that the coolant flooding the debris bed will be at a substantially subcooled state. Surprisingly, none of the experiments or numerical studies address this important issue.

c. It is an experimentally established fact that bed composition significantly affects the fluid flow through the porous debris bed and hence, also influences the dryout phenomena. Investigations in this regard have mostly focused on the effects of particle size. Some studies have also estimated the effects of bed heterogeneity, variable permeability, bed stratification and particle morphology. However, the effects of bed porosity on dryout has not been properly documented in the literature.

d. Only a handful of studies have been carried out on natural convective heat removal from a typical debris bed (Yakush et al. 2008; Kim et al. 2016).

e. Although the expected power density in a typical debris bed warrants phase change of the cooling water, the exponentially decreasing characteristic of decay heat generation would eventually result in a low power density. This type of situation is likely to be encountered while ensuring long-term bed coolability. In such situations, the cooling water may not undergo phase change due to the low power density. In view of this situation, heat transfer from the debris bed must be characterised in absence of phase change as well. However, only limited studies have been carried out in this regard and almost none involving a realistic heap-like bed configuration.

1.4. Scope and Objectives of the thesis

The overall objective of the present Ph.D. thesis is to address the issues highlighted in *Section 1.3*. An Eulerian-Eulerian numerical model is developed in this respect which is capable of handling single phase as well as multiphase flow in heat-generating porous media and in clear fluid region. The model is also equipped to take into account boiling heat transfer, and phase change of liquid into vapour and vice-versa. The numerical model solves the mass, momentum and energy transport equations for the three different phases encountered in debris coolability problem – solid particles in the porous debris, liquid water and water vapour. Appropriate correlations are utilised to achieve proper closure of the equations. The developed numerical model is implemented in the framework of the commercial CFD platform ANSYS FLUENT with extensive use of user-defined functions. Three different problems have been addressed using this model.

The first two problems studied are relevant in a very low decay power density situation when the cooling water is not expected to undergo phase change. The first problem characterises natural convective heat transfer from a heat-generating heap-

shaped porous bed present within a fluid filled enclosure. Phase change of the working fluid is not considered in this problem. Analysis of this problem has been carried out in a dimensionless manner using two different approaches of energy transport modelling in porous media – the local thermal equilibrium (LTE) approach and the local thermal non-equilibrium (LTNE) approach. The effects of bed heat generation, bed permeability, thermal conductivity ratio, bed configuration and bed stratification on fluid flow and associated heat transfer characteristics has been studied in this analysis.

The second problem analyses mixed convection in an enclosure containing a bottom flooded heat-generating porous bed. The porous bed is assumed to have a heap-like shape. Phase change of the working fluid is not considered in this problem. This problem has also been solved in a dimensionless manner and using the LTE as well as the LTNE approaches. The effects of Richardson number, bed heat generation, fluid injection strength, bed permeability and thermal conductivity ratio on fluid flow and heat transfer characteristics has been studied in this analysis.

The third problem is relevant in a high decay power density situation when heat removal from the debris is achieved primarily by phase change of the cooling water. Heat transfer from a typical heap-shaped debris bed is analysed considering phase change following a dimensional approach and utilising the LTNE model of energy transport equation. A close prediction of dryout power density is achieved with reported experimental data. The effects of bed composition, coolant subcooling, system pressure, bed configurations and coolant flooding modes on dryout occurrence have been characterised in this problem. In addition, dryout occurrence considering natural convection only has been analysed in this study in order to highlight the applicability of natural convective heat removal in ensuring long-term coolability of a debris bed.

1.5. Organisation of the thesis

The thesis is organised in the following sequence –

a. *Chapter 1*: This chapter discusses the phenomena of dryout in heat-generating debris beds encountered in severe accident situations. This is followed by an extensive literature survey, identification of the un-addressed issues, scope and objectives of the thesis, and organisation of the thesis.

b. *Chapter 2*: Eulerian averaging techniques and details the derivation of the governing equations utilised for development of the numerical model are discussed in this chapter.

c. *Chapter 3*: This chapter is devoted to the problem of natural convection heat transfer from a heap-shaped and heat-generating porous bed without considering phase change.

d. *Chapter 4*: Mixed convection heat transfer from a heap-shaped and heat-generating porous bed, as a result of bottom flooding of the bed, is discussed in this chapter. Phase change of the working fluid is not considered in this analysis.

e. *Chapter 5*: Heat transfer, considering phase change, from a typical heap-shaped debris bed is analysed in this chapter. Dryout occurrence in such debris beds is predicted in terms of the dryout power density.

f. *Chapter 6*: The overall contributions from this thesis are outlined in this chapter.

Chapter 2

FORMULATION OF THE GOVERNING EQUATIONS

Numerical solution of debris coolability problem in the context of the present thesis involves solving the mass, momentum and energy transport equations in porous media as well as clear fluid medium for liquid water and water vapour, and the energy equation for solid particles constituting the porous medium. Solution of the transport equations are obtained in the present thesis using the finite volume approach based commercial computational fluid dynamics (CFD) tool ANSYS FLUENT. The Eulerian multiphase model is used for handling the fluid transport equations while the solid energy transport equation is solved separately as a user-defined scalar (UDS) transport equation. Therefore, it becomes necessary to derive the transport equations for the indivual phases from the first principles following the Eulerian volume-averaging technique.

Various averaging techniques and the principles of Eulerian averaging are discussed in *Section 2.1*. The fluid transport equations are derived in *Section 2.2* following the Eulerian volume averaging technique. These equations are extended to incorporate the effects of porous media and the equations thus derived are discussed in *Section 2.3*.

2.1 Principles of averaging

The averaging techniques used in formulation of multiphase transport phenomena can be classified into the following three major groups, based on the physical concepts used (Faghri and Zhang 2006) –

1. *Eulerian Averaging*: It is the most widely-used and important concept of averaging, and is applicable to the most common techniques of experimental observations. The concept is based on the description of physical phenomena in the time-space domain. Changes in the various dependent variables such as pressure, velocity and temperature are expressed as functions of time and space co-ordinates, both of which are considered to be independent variables.
2. *Lagrangian Averaging*: In this technique of averaging, the motion of a specific particle of interest is observed over a certain time-interval. This is useful when the dynamics of individual particles are of interest.
3. *Molecular Statistical Averaging*: This concept is useful when the collective mechanics of a large number of particles is of interest. To describe the behaviour of each particle, it is necessary to track the motion resulting from the random collisions of each particle – which is an impractical task. Although the behaviour of each particle is random, the collection of particles may follow some statistical behaviour and when the collection of particles become large enough, the statistical average value becomes independent of the number of particles involved. Then this

statistically averaged value of the microscopic properties may be correlated to the macroscopic properties of the system.

In the present thesis, the Eulerian averaging technique has been used in formulating the multiphase transport equation in porous media. Hence, this technique is discussed in further detail.

2.1.1 Eulerian averaging technique

The Eulerian time-average for a generalised function $\Phi = \Phi(x, y, z, t)$, is obtained by averaging the flow properties over a time period Δt at a fixed point in the reference frame i.e.

$$\bar{\Phi} = \frac{1}{\Delta t}\int_{\Delta t} \Phi(x, y, z, t)dt \tag{2.1}$$

The time period Δt is chosen such that it is larger than the largest time scale of fluctuation of the local properties, yet small enough in comparison to the macroscopic time scale of the process.

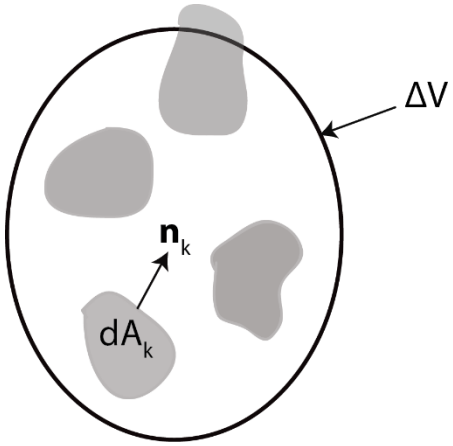

Figure 2.1 Schematic representation of control volume for volume averaging

Eulerian volume averaging is performed over an elemental volume ΔV around a spatial coordinate(x, y, z) as represented in Fig. 2.1. For a multiphase system involving Π different phases, the total elemental volume equals the summation of the individual phasic volumes (ΔV_k) i.e.

$$\Delta V = \sum_{k=1}^{\Pi} \Delta V_k \tag{2.2}$$

The volume fraction of the k^{th} phase is defined as the ratio of the elemental volume of the k^{th} phase to the total elemental volume of all phases combined i.e.

$$\varepsilon_k = \frac{\Delta V_k}{\Delta V} \tag{2.3}$$

Subject to the constraint that

$$\sum_{k=1}^{\Pi} \varepsilon_k = 1 \tag{2.4}$$

The Eulerian volume-average of a property Φ is expressed as –

$$\langle \Phi \rangle = \frac{1}{\Delta V} \sum_{k=1}^{\Pi} \int_{\Delta V_k} \Phi_k(x, y, z, t) dV \tag{2.5}$$

It is important to keep in mind that the volume element ΔV must be much smaller than the total volume of the multiphase system such that the averaging can provide a local value of Φ in the flow field.

The phase-averaged value of any variable or property is obtained in two different manner, namely – *Intrinsic phase average* and *Extrinsic phase average*. The difference between the two techniques is in the consideration of the phasic volumes during averaging. Intrinsic phase averaging is carried out only over ΔV_k and hence, does not take into account the interaction of k^{th} phase with the co-existing phases in the control volume. In contrast, Extrinsic phase averaging considers the various phasic interactions which necessitates the averaging to be carried out over the entire control volume ΔV. Eqs. (2.6) and (2.7) represents the Intrinsic and Extrinsic phase averaging, respectively.

$$\langle \Phi_k \rangle^k = \frac{1}{\Delta V_k} \int_{\Delta V_k} \Phi_k dV \tag{2.6}$$

$$\langle \Phi_k \rangle = \frac{1}{\Delta V} \int_{\Delta V_k} \Phi_k dV \tag{2.7}$$

The two phase-averages can, thus, be related using Eq. (2.3) as –

$$\langle \Phi_k \rangle = \varepsilon_k \langle \Phi_k \rangle^k \tag{2.8}$$

The phase averages can also be related to $\langle \Phi \rangle$ as –

$$\langle \Phi \rangle = \sum_{k=1}^{\Pi} \langle \Phi_k \rangle = \sum_{k=1}^{\Pi} \varepsilon_k \langle \Phi_k \rangle^k \tag{2.9}$$

The deviation of a property from its intrinsic phase-average value is expressed as –

$$\widehat{\Phi}_k = \Phi_k - \langle \Phi_k \rangle^k \tag{2.10}$$

The following two relations are particularly useful when the products of two variables (Φ, Ψ) are phase-averaged –

$$\langle \Phi_k \Psi_k \rangle^k = \langle \Phi_k \rangle^k \langle \Psi_k \rangle^k + \langle \widehat{\Phi}_k \widehat{\Psi}_k \rangle^k \tag{2.11}$$

$$\langle \Phi_k \Psi_k \rangle = \varepsilon_k \langle \Phi_k \rangle^k \langle \Psi_k \rangle^k + \langle \widehat{\Phi}_k \widehat{\Psi}_k \rangle \tag{2.12}$$

The volume average of the partial derivative with respect to time, gradient and divergence are also required, especially when the volume-averaged form of the transport equations are required. These are expressed in Eqs. (2.13), (2.14) and (2.15), respectively.

$$\langle\frac{\partial\Phi_k}{\partial t}\rangle = \frac{\partial\langle\Phi_k\rangle}{\partial t} - \frac{1}{\Delta V}\int_{A_k}\Phi_k \boldsymbol{V}_I.\boldsymbol{n}_k dA_k \tag{2.13}$$

$$\langle\nabla\Phi_k\rangle = \nabla\langle\Phi_k\rangle + \frac{1}{\Delta V}\int_{A_k}\Phi_k \boldsymbol{n}_k dA_k \tag{2.14}$$

$$\langle\nabla.\Phi_k\rangle = \nabla.\langle\Phi_k\rangle + \frac{1}{\Delta V}\int_{A_k}\Phi_k.\boldsymbol{n}_k dA_k \tag{2.15}$$

In the above equations, A_k is the interfacial area surrounding the k^{th} phase within the control volume, $\boldsymbol{V}_I$ is the interfacial velocity and $\boldsymbol{n}_k$ is the unit normal vector at the interface directed outward from k^{th} phase.

2.2 Eulerian averaging of the transport equations

The transport equations of mass, momentum and energy for a specific phase are derived in this section taking into account the interactions with other phases.

2.2.1 Mass conservation

The mass conservation equation for the k^{th} phase in its partial derivative form can be expressed as (Faghri and Zhang 2006) –

$$\frac{\partial\rho_k}{\partial t} + \nabla.(\rho_k \boldsymbol{V}_k) = 0 \tag{2.16}$$

The volume average of the above equation is obtained by taking extrinsic phase averaging of Eq. (2.16) –

$$\langle\frac{\partial\rho_k}{\partial t}\rangle + \langle\nabla.(\rho_k \boldsymbol{V}_k)\rangle = 0 \tag{2.17}$$

The individual terms of Eq. (2.17) are expressed as follows –

$$\langle\frac{\partial\rho_k}{\partial t}\rangle = \frac{\partial\langle\rho_k\rangle}{\partial t} - \frac{1}{\Delta V}\int_{A_k}\rho_k \boldsymbol{V}_I.\boldsymbol{n}_k dA_k \tag{2.18}$$

$$\langle\nabla.(\rho_k \boldsymbol{V}_k)\rangle = \nabla.\langle\rho_k \boldsymbol{V}_k\rangle + \frac{1}{\Delta V}\int_{A_k}\rho_k \boldsymbol{V}_k.\boldsymbol{n}_k dA_k \tag{2.19}$$

Substituting the above expressions into Eq. (2.17), the volume-averaged continuity equation becomes –

$$\frac{\partial\langle\rho_k\rangle}{\partial t} + \nabla.\langle\rho_k \boldsymbol{V}_k\rangle = -\frac{1}{\Delta V}\int_{A_k}\rho_k(\boldsymbol{V}_k - \boldsymbol{V}_I).\boldsymbol{n}_k dA_k \tag{2.20}$$

The terms on right hand side of Eq. (2.20) represents mass transfer per unit volume from all other phases to the k^{th} phase due to phase change. This is re-written as –

$$-\frac{1}{\Delta V}\int_{A_k}\rho_k(\boldsymbol{V}_k-\boldsymbol{V}_I).\boldsymbol{n}_k dA_k=\sum_{j=1(j\neq k)}^{\Pi} {m_{jk}}''' \tag{2.21}$$

In Eq. (2.21), ${m_{jk}}'''$ represents mass transfer per unit volume from the j^{th} phase to the k^{th} phase due to phase change. It is to be noted that the principle of conservation of mass requires that ${m_{jk}}''' = -{m_{kj}}'''$. Substituting Eq. (2.21) into Eq. (2.20) and using Eqs. (2.8) and (2.12), the mass conservation equation for the k^{th} phase becomes –

$$\frac{\partial}{\partial t}(\varepsilon_k\langle\rho_k\rangle^k)+\nabla.\left(\varepsilon_k\langle\rho_k\rangle^k\langle\boldsymbol{V}_k\rangle^k+\langle\widehat{\rho_k}\widehat{\boldsymbol{V}_k}\rangle\right)=\sum_{j=1(j\neq k)}^{\Pi} {m_{jk}}''' \tag{2.22}$$

The dispersive term in Eq. (2.22) is usually very small and is therefore, neglected. The continuity equation for the k^{th} phase, thus, can be written as –

$$\frac{\partial}{\partial t}(\varepsilon_k\langle\rho_k\rangle^k)+\nabla.(\varepsilon_k\langle\rho_k\rangle^k\langle\boldsymbol{V}_k\rangle^k)=\sum_{j=1(j\neq k)}^{\Pi} {m_{jk}}''' \tag{2.23}$$

2.2.2 Momentum conservation

The momentum conservation equation for the k^{th} phase in its partial derivative form can be expressed as (Faghri and Zhang 2006) –

$$\frac{\partial(\rho_k\boldsymbol{V}_k)}{\partial t}+\nabla.(\rho_k\boldsymbol{V}_k\boldsymbol{V}_k)=\nabla.\tau_k+\rho_k\boldsymbol{X}_k \tag{2.24}$$

Here, $\boldsymbol{X}_k$ represents the body force per unit volume acting on the k^{th} phase. The volume-averaged momentum equation for the k^{th} phase is obtained by performing extrinsic phase-averaging on Eq. (2.24) and is expressed as –

$$\langle\frac{\partial(\rho_k\boldsymbol{V}_k)}{\partial t}\rangle+\langle\nabla.(\rho_k\boldsymbol{V}_k\boldsymbol{V}_k)\rangle=\langle\nabla.\boldsymbol{\tau}_k\rangle+\langle\rho_k\boldsymbol{X}_k\rangle \tag{2.25}$$

Using the techniques of Eulerian averaging (as detailed in Section 2.1.1), the individual terms of Eq. (2.25) are expressed as follows –

$$\langle\frac{\partial(\rho_k\boldsymbol{V}_k)}{\partial t}\rangle=\frac{\partial\langle\rho_k\boldsymbol{V}_k\rangle}{\partial t}-\frac{1}{\Delta V}\int_{A_k}\rho_k\boldsymbol{V}_k(\boldsymbol{V}_I.\boldsymbol{n}_k)dA_k \tag{2.26}$$

$$\langle\nabla.(\rho_k\boldsymbol{V}_k\boldsymbol{V}_k)\rangle=\nabla.\langle\rho_k\boldsymbol{V}_k\boldsymbol{V}_k\rangle+\frac{1}{\Delta V}\int_{A_k}\rho_k\boldsymbol{V}_k\boldsymbol{V}_k.\boldsymbol{n}_k dA_k \tag{2.27}$$

$$\langle\nabla.\boldsymbol{\tau}_k\rangle=\nabla.\langle\boldsymbol{\tau}_k\rangle+\frac{1}{\Delta V}\int_{A_k}\boldsymbol{\tau}_k.\boldsymbol{n}_k dA_k \tag{2.28}$$

$$\langle\rho_k\boldsymbol{X}_k\rangle=\langle\rho_k\rangle\boldsymbol{X}_k \tag{2.29}$$

In the expression of Eq. (2.29), it is assumed that the volumetric body force ($\boldsymbol{X}_k$) is uniform over the entire control volume i.e. $\langle \boldsymbol{X}_k \rangle = \boldsymbol{X}_k$. Substituting the above expressions into Eq. (2.25), we obtain –

$$\frac{\partial \langle \rho_k \boldsymbol{V}_k \rangle}{\partial t} + \nabla . \langle \rho_k \boldsymbol{V}_k \boldsymbol{V}_k \rangle = \nabla . \langle \boldsymbol{\tau}_k \rangle - \frac{1}{\Delta V} \int_{A_k} \rho_k \boldsymbol{V}_k \big((\boldsymbol{V}_k - \boldsymbol{V}_I) . \boldsymbol{n}_k \big) dA_k + \frac{1}{\Delta V} \int_{A_k} \boldsymbol{\tau}_k . \boldsymbol{n}_k dA_k + \langle \rho_k \rangle \boldsymbol{X}_k \quad (2.30)$$

Using Eqs. (2.8) as well as (2.12) and neglecting the product of the deviations, Eq. (2.30) is re-written as follows –

$$\frac{\partial}{\partial t} (\varepsilon_k \langle \rho_k \rangle^k \langle \boldsymbol{V}_k \rangle^k) + \nabla . (\varepsilon_k \langle \rho_k \rangle^k \langle \boldsymbol{V}_k \boldsymbol{V}_k \rangle^k) = \nabla . (\varepsilon_k \langle \boldsymbol{\tau}_k \rangle^k) - \frac{1}{\Delta V} \int_{A_k} \rho_k \boldsymbol{V}_k \big((\boldsymbol{V}_k - \boldsymbol{V}_I) . \boldsymbol{n}_k \big) dA_k + \frac{1}{\Delta V} \int_{A_k} \boldsymbol{\tau}_k . \boldsymbol{n}_k dA_k + \varepsilon_k \langle \rho_k \rangle^k \boldsymbol{X}_k \quad (2.31)$$

The phase-averaged stress tensor ($\langle \boldsymbol{\tau}_k \rangle^k$) is expressed as –

$$\langle \boldsymbol{\tau}_k \rangle^k = -\langle p_k \rangle^k \boldsymbol{I} + \mu_k [\nabla \langle \boldsymbol{V}_k \rangle^k + (\nabla \langle \boldsymbol{V}_k \rangle^k)^T] - \frac{2}{3} \mu_k (\nabla \langle \boldsymbol{V}_k \rangle^k) \boldsymbol{I} \quad (2.32)$$

The second and third terms on the right-hand side of Eq. (2.31) represent the momentum exchanges and interactive forces between all other phases and the k^{th} phase. These are written as –

$$-\frac{1}{\Delta V} \int_{A_k} \rho_k \boldsymbol{V}_k \big((\boldsymbol{V}_k - \boldsymbol{V}_I) . \boldsymbol{n}_k \big) dA_k = \sum_{j=1 (j \neq k)}^{\Pi} m_{jk}''' \langle \boldsymbol{V}_{k,I} \rangle^k \quad (2.33)$$

$$\frac{1}{\Delta V} \int_{A_k} \boldsymbol{\tau}_k . \boldsymbol{n}_k dA_k = \sum_{j=1 (j \neq k)}^{\Pi} \langle \boldsymbol{F}_{jk} \rangle \quad (2.34)$$

$\langle \boldsymbol{V}_{k,I} \rangle^k$ represents the phase-averaged velocity of the k^{th} phase at the phasic interface. $\langle \boldsymbol{F}_{jk} \rangle$ is an interactive force acting between the k^{th} phase and all other phases, and depends on friction, pressure and cohesion between the phases. In accordance to Newton's third law of motion, $\langle \boldsymbol{F}_{jk} \rangle = -\langle \boldsymbol{F}_{kj} \rangle$. This interactive force is usually expressed as a function of the relative velocity between the phases with the use of a momentum exchange coefficient (K_{jk}) as follows –

$$\langle \boldsymbol{F}_{jk} \rangle = K_{jk} \big(\langle \boldsymbol{V}_j \rangle^j - \langle \boldsymbol{V}_k \rangle^k \big) \quad (2.35)$$

Combining the above expressions, the phase-averaged momentum equation can thus be written as –

$$\frac{\partial}{\partial t}(\varepsilon_k\langle\rho_k\rangle^k\langle\boldsymbol{V}_k\rangle^k)+\nabla.(\varepsilon_k\langle\rho_k\rangle^k\langle\boldsymbol{V}_k\boldsymbol{V}_k\rangle^k)$$
$$=\nabla.\left[\varepsilon_k\left(-\langle p_k\rangle^k\boldsymbol{I}+\mu_k[\nabla\langle\boldsymbol{V}_k\rangle^k+(\nabla\langle\boldsymbol{V}_k\rangle^k)^T]-\frac{2}{3}\mu_k(\nabla\langle\boldsymbol{V}_k\rangle^k)\boldsymbol{I}\right)\right]$$
$$+\sum_{j=1(j\neq k)}^{\Pi}\left(\dot{m_{jk}}'''\langle\boldsymbol{V}_{k,I}\rangle^k+K_{jk}\left(\langle\boldsymbol{V}_j\rangle^j-\langle\boldsymbol{V}_k\rangle^k\right)\right)+\varepsilon_k\langle\rho_k\rangle^k\boldsymbol{X}_k \quad (2.36)$$

2.2.3 Energy conservation

The partial derivative form of the energy equation, in terms of phasic enthalpy (h_k), can be written as (Faghri and Zhang 2006) –

$$\frac{\partial(\rho_k h_k)}{\partial t}+\nabla.(\rho_k\boldsymbol{V}_k h_k)=\frac{\partial p_k}{\partial t}+(\boldsymbol{V}_k.\nabla p_k)+(\nabla\boldsymbol{V}_k:\boldsymbol{\tau}_k)-\nabla.\boldsymbol{q}_k''+q_k''' \quad (2.37)$$

Extrinsic phase-averaging of Eq. (2.37) yields –

$$\langle\frac{\partial(\rho_k h_k)}{\partial t}\rangle+\langle\nabla.(\rho_k\boldsymbol{V}_k h_k)\rangle$$
$$=\langle\frac{\partial p_k}{\partial t}\rangle+\langle\boldsymbol{V}_k.\nabla p_k\rangle+\langle\nabla\boldsymbol{V}_k:\boldsymbol{\tau}_k\rangle-\langle\nabla.\boldsymbol{q}_k''\rangle+\langle q_k'''\rangle \quad (2.38)$$

The individual terms of Eq. (2.38) can be expressed in the following forms using the principles of Eulerian averaging (as detailed in Section 2.1.1) –

$$\langle\frac{\partial(\rho_k h_k)}{\partial t}\rangle=\frac{\partial\langle\rho_k h_k\rangle}{\partial t}-\frac{1}{\Delta V}\int_{A_k}\rho_k h_k(\boldsymbol{V}_I.\boldsymbol{n}_k)dA_k \quad (2.39)$$

$$\langle\nabla.(\rho_k\boldsymbol{V}_k h_k)\rangle=\nabla.\langle\rho_k\boldsymbol{V}_k h_k\rangle+\frac{1}{\Delta V}\int_{A_k}\rho_k h_k(\boldsymbol{V}_k.\boldsymbol{n}_k)dA_k \quad (2.40)$$

$$\langle\frac{\partial p_k}{\partial t}\rangle=\frac{\partial\langle p_k\rangle}{\partial t}-\frac{1}{\Delta V}\int_{A_k}p_k(\boldsymbol{V}_I.\boldsymbol{n}_k)dA_k \quad (2.41)$$

$$\langle\boldsymbol{V}_k.\nabla p_k\rangle\simeq\langle\boldsymbol{V}_k\rangle.\langle\nabla p_k\rangle=\langle\boldsymbol{V}_k\rangle.\left(\nabla\langle p_k\rangle+\frac{1}{\Delta V}\int_{A_k}p_k\boldsymbol{n}_k dA_k\right) \quad (2.42)$$

$$\langle\nabla\boldsymbol{V}_k:\boldsymbol{\tau}_k\rangle\simeq\langle\nabla\boldsymbol{V}_k\rangle:\langle\boldsymbol{\tau}_k\rangle=\nabla\langle\boldsymbol{V}_k\rangle:\langle\boldsymbol{\tau}_k\rangle+\frac{1}{\Delta V}\left(\int_{A_k}\boldsymbol{V}_k\boldsymbol{n}_k dA_k\right):\langle\boldsymbol{\tau}_k\rangle \quad (2.43)$$

$$\langle\nabla.\boldsymbol{q}_k''\rangle=\nabla.\langle\boldsymbol{q}_k''\rangle+\frac{1}{\Delta V}\int_{A_k}\boldsymbol{q}_k''.\boldsymbol{n}_k dA_k \quad (2.44)$$

Neglecting the product of the deviations, Eq. (2.38) is re-written using Eqs. (2.39-2.44) as follows –

$$\left\langle\frac{\partial(\rho_k h_k)}{\partial t}\right\rangle + \langle\nabla.(\rho_k \boldsymbol{V}_k h_k)\rangle = \frac{\partial\langle p_k\rangle}{\partial t} + \langle\boldsymbol{V}_k\rangle.\nabla\langle p_k\rangle + \nabla\langle\boldsymbol{V}_k\rangle:\langle\boldsymbol{\tau}_k\rangle - \nabla.\langle\boldsymbol{q}_k{}''\rangle + \langle q_k{}'''\rangle$$
$$+\frac{1}{\Delta V}\left[-\int_{A_k} p_k(\boldsymbol{V}_I.\boldsymbol{n}_k)dA_k + \langle\boldsymbol{V}_k\rangle\int_{A_k} p_k\boldsymbol{n}_k dA_k + \left(\int_{A_k}\boldsymbol{V}_k\boldsymbol{n}_k dA_k\right):\langle\boldsymbol{\tau}_k\rangle\right]$$
$$-\frac{1}{\Delta V}\int_{A_k}\rho_k h_k(\boldsymbol{V}_k - \boldsymbol{V}_I).\boldsymbol{n}_k dA_k - \frac{1}{\Delta V}\int_{A_k}\boldsymbol{q}_k{}''.\boldsymbol{n}_k dA_k \tag{2.45}$$

The terms in the square bracket on the right-hand side of Eq. (2.45) represent the work done per unit volume by pressure and shear stress at the phasic interface. These quantities reflect conversion of mechanical energy to thermal energy at the interface and are usually negligible as compared to the other terms. As such, these quantities are neglected.

The sixth term on the right-hand side of Eq. (2.45) represents the interphase enthalpy exchange between the k^{th} phase and all other phases due to phase change. This is expressed as –

$$-\frac{1}{\Delta V}\int_{A_k}\rho_k h_k(\boldsymbol{V}_k - \boldsymbol{V}_I).\boldsymbol{n}_k dA_k = \sum_{j=1(j\neq k)}^{\Pi} m_{jk}{}'''\langle h_{k,I}\rangle^k \tag{2.46}$$

Here, $\langle h_{k,I}\rangle^k$ is the intrinsic phase-averaged enthalpy of the k^{th} phase at the phasic interface. The seventh term on the right-hand side of Eq. (2.45) takes into account heat transfer between all other phases and the k^{th} phase, and is written as –

$$-\frac{1}{\Delta V}\int_{A_k}\boldsymbol{q}_k{}''.\boldsymbol{n}_k dA_k = \sum_{j=1(j\neq k)}^{\Pi}\langle q_{jk}{}'''\rangle \tag{2.47}$$

Here, $\langle\boldsymbol{q}_{jk}{}'''\rangle$ is the intensity of heat exchange between the phases. It is usually determined using Newton's law of cooling as follows –

$$\langle q_{jk}{}'''\rangle = \frac{h_c\Delta A_j\left(\langle T_j\rangle^j - \langle T_k\rangle^k\right)}{\Delta V_j} \tag{2.48}$$

Here, h_c is the convective heat transfer coefficient, ΔA_j is the interfacial area between the phases and ΔV_j is the volume of the secondary phase in the elemental volume ΔV.

As in case of the continuity and momentum equations, the extrinsically phase-averaged energy equation can also be written in intrinsically phase-averaged form taking into account the above considerations as below –

$$\frac{\partial}{\partial t}(\varepsilon_k\langle\rho_k\rangle^k\langle h_k\rangle^k) + \nabla.(\varepsilon_k\langle\rho_k\rangle^k\langle\boldsymbol{V}_k h_k\rangle^k) = \frac{\partial(\varepsilon_k\langle p_k\rangle^k)}{\partial t} + \langle\boldsymbol{V}_k\rangle.\nabla(\varepsilon_k\langle p_k\rangle^k)$$

$$+\nabla\langle \boldsymbol{V}_k\rangle:\langle \boldsymbol{\tau}_k\rangle - \nabla.\langle \boldsymbol{q}_k{}''\rangle + \langle q_k{}'''\rangle + \sum_{j=1(j\neq k)}^{\Pi}\left(m_{jk}{}'''\langle h_{k,I}\rangle^k + \langle q_{jk}{}'''\rangle\right) \quad (2.49)$$

2.3 Extension of the averaged transport equations to porous media

A solid matrix with several interconnected voids or pores is usually termed as Porous Medium. The voids are filled with one or more fluids and the interconnected network of the voids allow fluid movement through the material.

The volume fraction of voids within the porous medium is referred to as the void fraction or more frequently as the porosity of the medium (ε_f). This is defined in a similar manner as phasic volume fraction in Eq. (2.3) and is expressed as –

$$\varepsilon_f = \frac{V_f}{V} = \frac{V_f}{V_f + V_s} \quad (2.50)$$

The volume fraction of the solid particles in the porous medium is defined subject to the constraint that the volume fraction of the voids and the solid in the porous medium sums up to 1 i.e.$\varepsilon_s + \varepsilon_f = 1$. This leads to the following expression of solid volume fraction –

$$\varepsilon_s = 1 - \varepsilon_f = \frac{V_s}{V} = \frac{V_s}{V_f + V_s} \quad (2.51)$$

The most important characteristic of a porous medium is the existence of multiple length scales which can be used in modelling the transport phenomena. The first scale is the particle or void length scale (d) and the second scale is the system or porous zone length scale (L). If d is of the order of L, such as in a very thin porous layer, the transport phenomena can be directly modelled with minimal assumptions. However, if $d \ll L$ and the bulk properties are more important, as is the case in most practical situations, direct simulation of transport characteristics in a single pore is not feasible. In such cases, Eulerian volume averaging is used to describe the transport phenomena in a porous system.

In the following sections, the transport equations derived in Section 2.2 will be used in obtaining governing equations for transport in porous media assuming that only a single fluid saturates the porous media and without taking into account phase change. These will then be extended for situations involving phase change.

2.3.1 Mass conservation

Using the volume-averaged mass conservation equation (Eq. 2.23), the mass conservation equation for the fluid phase in the porous media can be written as –

$$\frac{\partial}{\partial t}\left(\varepsilon_f\langle\rho_f\rangle^f\right) + \nabla.\left(\varepsilon_f\langle\rho_f\rangle^f\langle \boldsymbol{V}_f\rangle^f\right) = 0 \quad (2.52)$$

Utilising Eq. (2.8), the Intrinsic average velocity or the physical velocity ($\langle \boldsymbol{V}_f \rangle^f$) can be expressed in terms of the extrinsic average velocity or the superficial velocity ($\langle \boldsymbol{V}_f \rangle$). This is termed as the Dupuit-Forchheimer relationship and expressed as follows –

$$\langle \boldsymbol{V}_f \rangle = \varepsilon_f \langle \boldsymbol{V}_f \rangle^f \tag{2.53}$$

The mass conservation equation in terms of extrinsic average velocity or superficial velocity is as follows –

$$\frac{\partial}{\partial t}\left(\varepsilon_f \langle \rho_f \rangle^f\right) + \nabla.\left(\langle \rho_f \rangle^f \langle \boldsymbol{V}_f \rangle\right) = 0 \tag{2.54}$$

2.3.2 Momentum conservation

In order to macroscopically model transport through the porous medium, the bulk resistance of the porous media to fluid flow must be appropriately modelled. In 1856, Henry Darcy experimentally measured the resistance offered by an unconsolidated, uniform, rigid and isotropic solid matrix in a one-dimensional, gravity driven flow at steady state and proposed the well-known Darcy's Law for flow through porous media. This is expressed as (Nield and Bejan 2017) –

$$\rho_f \boldsymbol{g} - \frac{1}{\varepsilon_f} \nabla \langle \varepsilon_f p \rangle = \frac{\mu_f}{\boldsymbol{K}} \langle \boldsymbol{V}_f \rangle \tag{2.55}$$

In the above equation, $\boldsymbol{K}$ represents permeability of the medium which signifies the resistance to fluid flow through the porous medium. It is a second-order symmetric tensor and has a unit of m^2. The term on the right hand side of Eq. (2.55) is referred to in literature as the Darcy term (Nield and Bejan 2017).

The validity of Darcy's Law is, however, limited to the creeping flow regime where the viscous forces dominate i.e. $Re < 1$. The wall effects are confined to one or two particle diameters from the wall, while the entrance region is approximately within three particle diameters. As such, fluid flow becomes very closely uniform in the main direction and the walls have a minimal effect on the fluid flow. The Reynolds number (Re) referred to above is defined in terms of the extrinsic average velocity ($\langle \boldsymbol{V}_f \rangle$) and the characteristic length scale of the voids (D) i.e.

$$Re = \frac{\rho_f \langle \boldsymbol{V}_f \rangle^f D}{\mu_f} \tag{2.56}$$

As the flow moves from a creeping flow regime to the laminar flow regime i.e. $1 < Re < 10$, the drag force acting smoothly transitions into a non-linear function. This non-linearity was accounted for by Forchheimer who proposed a quadratic drag term as follows (Nield and Bejan 2017) –

$$\rho_f \boldsymbol{g} - \frac{1}{\varepsilon_f} \nabla \langle \varepsilon_f p \rangle = \frac{\mu_f}{\boldsymbol{K}} \langle \boldsymbol{V}_f \rangle + \frac{\rho_f}{\eta} \left|\langle \boldsymbol{V}_f \rangle\right| \langle \boldsymbol{V}_f \rangle \tag{2.57}$$

The effect of neighbouring spheres on the drag force exerted by a single sphere in an infinite domain is taken into account with the Stokes drag force, as proposed by Brinkman, in the following manner (Nield and Bejan 2017) –

$$\rho_f \boldsymbol{g} - \frac{1}{\varepsilon_f}\nabla\langle\varepsilon_f p\rangle = \frac{\mu_f}{\boldsymbol{K}}\langle \boldsymbol{V}_f\rangle + \frac{\rho_f}{\eta}\left|\langle \boldsymbol{V}_f\rangle\right|\langle \boldsymbol{V}_f\rangle - \mu_f\nabla^2\langle \boldsymbol{V}_f\rangle \tag{2.58}$$

Considering the above expressions and assuming the fluid to be incompressible i.e. $\langle\rho_f\rangle^f = \rho_f$, the volume-averaged momentum conservation equation can be written using Eq. (2.36) as (Faghri and Zhang 2006) –

$$\frac{\partial}{\partial t}\left(\varepsilon_f\rho_f\langle \boldsymbol{V}_f\rangle^f\right) + \nabla.\left(\varepsilon_f\rho_f\langle \boldsymbol{V}_f\boldsymbol{V}_f\rangle^f\right) = \nabla.\left[\varepsilon_f\left(-\langle p_f\rangle^f\boldsymbol{I} + \mu_f\left[\nabla\langle \boldsymbol{V}_f\rangle^f + \left(\nabla\langle \boldsymbol{V}_f\rangle^f\right)^T\right]\right)\right] + \varepsilon_f\rho_f\boldsymbol{X}_f + \langle \boldsymbol{F}_{s,f}\rangle \tag{2.59}$$

Neglecting the deviation of the intrinsically phase-averaged velocity and pressure, Eq. (2.59) can be re-written as –

$$\frac{\partial}{\partial t}\left(\varepsilon_f\rho_f\langle \boldsymbol{V}_f\rangle^f\right) + \nabla.\left(\varepsilon_f\rho_f\langle \boldsymbol{V}_f\rangle^f\langle \boldsymbol{V}_f\rangle^f\right) = -\nabla\left(\varepsilon_f p\right) + \mu_f\nabla^2\left[\varepsilon_f\langle \boldsymbol{V}_f\rangle^f\right] + \varepsilon_f\rho_f\boldsymbol{X}_f + \langle \boldsymbol{F}_{s,f}\rangle \tag{2.60}$$

The mass conservation equation in terms of extrinsically averaged velocity can be obtained using the Dupuit-Forchheimer relationship (Eq. 2.53). It is expressed as –

$$\frac{\partial}{\partial t}\left(\rho_f\langle \boldsymbol{V}_f\rangle\right) + \nabla.\left(\frac{\rho_f\langle \boldsymbol{V}_f\rangle\langle \boldsymbol{V}_f\rangle}{\varepsilon_f}\right) = -\nabla\left(\varepsilon_f p\right) + \mu_f\nabla^2\left[\langle \boldsymbol{V}_f\rangle\right] + \varepsilon_f\rho_f\boldsymbol{X}_f + \langle \boldsymbol{F}_{s,f}\rangle \tag{2.61}$$

In the above equations, the term $\langle \boldsymbol{F}_{s,f}\rangle$ represents the momentum interaction between the solid matrix and the fluid phase. It is a combination of the Darcy and Forchheimer terms as shown in Eq. (2.62).

$$\langle \boldsymbol{F}_{s,f}\rangle = -\varepsilon_f\left(\frac{\mu_f}{\boldsymbol{K}}\langle \boldsymbol{V}_f\rangle + \frac{\rho_f}{\eta}\left|\langle \boldsymbol{V}_f\rangle\right|\langle \boldsymbol{V}_f\rangle\right) \tag{2.62}$$

The permeability ($\boldsymbol{K}$) and passability (η) of porous medium, as referred to in the above expressions, is represented mathematically as –

$$\boldsymbol{K} = \frac{\psi^2 {D_p}^2 {\varepsilon_f}^3}{150\left(1-\varepsilon_f\right)^2} \tag{2.63}$$

$$\eta = \frac{\psi D_p {\varepsilon_f}^3}{1.75\left(1-\varepsilon_f\right)} \tag{2.64}$$

where,D_p is the particle diameter and ψ is the sphericity or shape factor of the particles. The latter is defined as the ratio between the area of an equivalent-volume sphere and the surface area of the particle.

2.3.3 Energy conservation

The energy conservation equation for the fluid phase is derived in a similar manner as the continuity and momentum equations, by assuming the fluid to be incompressible and neglecting the viscous dissipation –

$$\frac{\partial}{\partial t}\left(\varepsilon_f \rho_f \langle h_f \rangle^f\right) + \nabla.\left(\varepsilon_f \rho_f \langle \boldsymbol{V}_f \rangle^f \langle h_f \rangle^f\right) = -\nabla.\langle \boldsymbol{q}_f{}'' \rangle + \langle q_f{}''' \rangle + \langle q_{s,f}{}''' \rangle \tag{2.65}$$

The energy equation for the solid matrix is expressed as –

$$\frac{\partial}{\partial t}\left(\varepsilon_s \rho_s \langle h_s \rangle^s\right) = -\nabla.\langle \boldsymbol{q}_s{}'' \rangle + \langle q_s{}''' \rangle - \langle q_{s,f}{}''' \rangle \tag{2.66}$$

In the above equations, $\langle \boldsymbol{q}_{s,f}{}''' \rangle$ represents the interfacial heat transfer between the solid matrix and the fluid phase. This is evaluated as follows –

$$\langle \boldsymbol{q}_{s,f}{}''' \rangle = h a_i \left(T_s - T_f\right) \tag{2.67}$$

In the above equation, h represents the interfacial heat transfer coefficient while a_i represents the interfacial area density. If the fluid and solid matrix are considered to be in local thermal equilibrium i.e. $\langle T_f \rangle = \langle T_s \rangle = T$, the energy equations for the solid and fluid phases can be combined to give –

$$\frac{\partial}{\partial t}\left(\left(\varepsilon_f \rho_f \langle h_f \rangle^f\right) + \varepsilon_s \rho_s \langle h_s \rangle^s\right) + \nabla.\left(\varepsilon_f \rho_f \langle \boldsymbol{V}_f \rangle^f \langle h_f \rangle^f\right) = -\nabla.\langle \boldsymbol{q}_f{}'' \rangle - \nabla.\langle \boldsymbol{q}_s{}'' \rangle + \langle q_f{}''' \rangle + \langle q_s{}''' \rangle \tag{2.68}$$

Assuming that enthalpy is a function of temperature only and considering a constant specific heat capacity as well as utilising the mass conservation equations, Eq. (2.68) is represented in terms of intrinsic average velocity ($\langle \boldsymbol{V}_f \rangle$) as –

$$\left(\rho c_p\right)_{eff} \frac{\partial T}{\partial t} + \left(\rho c_p\right)_{eff} \langle \boldsymbol{V}_f \rangle \nabla.T = \nabla.\langle k_{eff} \nabla T \rangle + \langle q_{eff}{}''' \rangle \tag{2.69}$$

The effective heat capacity, thermal conductivity and heat generation rates in Eq. (2.69) are defined by the following equations –

$$\left(\rho c_p\right)_{eff} = \varepsilon_f \left(\rho c_p\right)_f + \varepsilon_s \left(\rho c_p\right)_s \tag{2.70}$$

$$k_{eff} = \varepsilon_f k_f + \varepsilon_s k_s \tag{2.71}$$

$$\langle \boldsymbol{q}_{eff}{}''' \rangle = \varepsilon_f \langle \boldsymbol{q}_f{}''' \rangle + \varepsilon_s \langle \boldsymbol{q}_s{}''' \rangle \tag{2.72}$$

2.3.4 Multiphase transport in porous media

In case the porous media is saturated with more than one fluid phase (such as liquid water and water vapour), the governing equations for either phase must be specified in addition to that of the solid matrix.

The volume fraction of liquid (α_l) and vapour (α_v) phases in the total fluid phase volume can be represented using Eq. (2.3) as –

$$\alpha_l = \frac{\Delta V_l}{\Delta V_f} \tag{2.73}$$

$$\alpha_v = \frac{\Delta V_v}{\Delta V_f} \tag{2.74}$$

Taking into account the liquid and vapour volume fractions, the mass conservation equations in terms of extrinsic average velocity or superficial velocity are expressed as –

$$\frac{\partial}{\partial t}\left(\varepsilon_f \alpha_v \rho_v\right) + \nabla.\left(\alpha_v \rho_v \langle \boldsymbol{V}_v \rangle\right) = \langle {m_{lv}}''' \rangle \tag{2.75}$$

$$\frac{\partial}{\partial t}\left(\varepsilon_f \alpha_l \rho_l\right) + \nabla.\left(\alpha_l \rho_l \langle \boldsymbol{V}_l \rangle\right) = -\langle {m_{lv}}''' \rangle \tag{2.76}$$

In Eqs. (2.75-2.76), $\langle {m_{lv}}''' \rangle$ represents the volumetric mass transfer rate from the liquid to the vapour phase such that $\langle {m_{lv}}''' \rangle = -\langle {m_{vl}}''' \rangle$. By definition, it is positive for mass transfer from liquid to vapour (i.e. evaporation) and negative for vapour to liquid (i.e. condensation).

The momentum conservation equations are expressed in terms of intrinsic average velocity or physical velocity using Eq. (2.61) as follows –

$$\frac{\partial}{\partial t}\left(\varepsilon_f \alpha_v \rho_v \langle \boldsymbol{V}_v \rangle^v\right) + \nabla.\left(\varepsilon_f \alpha_v \rho_v \langle \boldsymbol{V}_v \boldsymbol{V}_v \rangle^v\right) = -\nabla\left(\varepsilon_f \alpha_v p\right) + \mu_v \nabla^2\left(\varepsilon_f \langle \boldsymbol{V}_v \rangle^v\right) + \varepsilon_f \alpha_v \rho_v \boldsymbol{g} + \left({m_{lv}}''' \langle \boldsymbol{V}_{v,I} \rangle^v + K_{lv}(\langle \boldsymbol{V}_l \rangle^l - \langle \boldsymbol{V}_v \rangle^v)\right) + \langle \boldsymbol{F}_{s,v} \rangle \tag{2.77}$$

$$\frac{\partial}{\partial t}\left(\varepsilon_f \alpha_l \rho_l \langle \boldsymbol{V}_l \rangle^l\right) + \nabla.\left(\varepsilon_f \alpha_l \rho_l \langle \boldsymbol{V}_l \boldsymbol{V}_l \rangle^l\right) = -\nabla\left(\varepsilon_f \alpha_l p\right) + \mu_l \nabla^2\left(\varepsilon_f \langle \boldsymbol{V}_l \rangle^l\right) + \varepsilon_f \alpha_l \rho_l \boldsymbol{g} + \left({m_{vl}}''' \langle \boldsymbol{V}_{l,I} \rangle^l + K_{vl}(\langle \boldsymbol{V}_v \rangle^v - \langle \boldsymbol{V}_l \rangle^l)\right) + \langle \boldsymbol{F}_{s,l} \rangle \tag{2.78}$$

Alternatively, Eqs. (2.77-2.78) can be re-written in terms of extrinsically-averaged or superficial velocity using Eq. (2.62) as –

$$\frac{\partial}{\partial t}\left(\alpha_v \rho_v \langle \boldsymbol{V}_v \rangle\right) + \nabla.\left(\frac{\alpha_v \rho_v \langle \boldsymbol{V}_v \rangle \langle \boldsymbol{V}_v \rangle}{\varepsilon_f}\right) = -\nabla\left(\varepsilon_f \alpha_v p\right) + \mu_v \nabla^2 \langle \boldsymbol{V}_v \rangle + \frac{1}{\varepsilon_f}\left({m_{lv}}''' \langle \boldsymbol{V}_{v,I} \rangle + K_{lv}(\langle \boldsymbol{V}_l \rangle - \langle \boldsymbol{V}_v \rangle)\right) + \varepsilon_f \alpha_v \rho_v \boldsymbol{g} + \langle \boldsymbol{F}_{s,v} \rangle \tag{2.79}$$

$$\frac{\partial}{\partial t}\left(\alpha_l \rho_l \langle \boldsymbol{V}_l \rangle\right) + \nabla.\left(\frac{\alpha_l \rho_l \langle \boldsymbol{V}_l \rangle \langle \boldsymbol{V}_l \rangle}{\varepsilon_f}\right) = -\nabla\left(\varepsilon_f \alpha_l p\right) + \mu_l \nabla^2 \langle \boldsymbol{V}_l \rangle + \frac{1}{\varepsilon_f}\left({m_{vl\,m}}''' \langle \boldsymbol{V}_{l,I} \rangle + K_{vl}(\langle \boldsymbol{V}_v \rangle - \langle \boldsymbol{V}_l \rangle)\right) + \varepsilon_f \alpha_l \rho_l \boldsymbol{g} + \langle \boldsymbol{F}_{s,l} \rangle \tag{2.80}$$

The solid-fluid interfacial drag terms are suitably modified to account for the existence of multiple phases. This is achieved by introducing the concepts of relative

permeability ($\boldsymbol{K_r}$) and relative passability (η_r) as functions of the phasic volume fractions. The drag terms are expressed as follows –

$$\langle \boldsymbol{F}_{s,v} \rangle = -\varepsilon_f \alpha_v \left(\frac{\mu_v}{\boldsymbol{K K_{r,v}}} \langle \boldsymbol{V}_v \rangle + \frac{\rho_v}{\eta \eta_{r,v}} |\langle \boldsymbol{V}_v \rangle| \langle \boldsymbol{V}_v \rangle \right) \tag{2.81}$$

$$\langle \boldsymbol{F}_{s,l} \rangle = -\varepsilon_f \alpha_l \left(\frac{\mu_l}{\boldsymbol{K K_{r,l}}} \langle \boldsymbol{V}_l \rangle + \frac{\rho_l}{\eta \eta_{r,l}} |\langle \boldsymbol{V}_l \rangle| \langle \boldsymbol{V}_l \rangle \right) \tag{2.82}$$

The fluid energy transport equations are derived utilising Eq. (2.65) and that for the solid matrix is derived utilising Eq. (2.66). These are expressed as follows –

$$\frac{\partial}{\partial t}\left(\varepsilon_f \alpha_v \rho_v \langle h_v \rangle^v\right) + \nabla.\left(\alpha_v \rho_v \langle \boldsymbol{V}_v \rangle \langle h_v \rangle^v\right) = -\nabla.\langle \boldsymbol{q}_v{}'' \rangle + \langle {q_v}''' \rangle + \langle {q_{s,v}}''' \rangle + \langle {q_{l,v}}''' \rangle + \dot{m_{lv}}''' \langle h_{v,I} \rangle^v \tag{2.83}$$

$$\frac{\partial}{\partial t}\left(\varepsilon_f \alpha_l \rho_l \langle h_l \rangle^l\right) + \nabla.\left(\alpha_l \rho_l \langle \boldsymbol{V}_l \rangle \langle h_l \rangle^l\right) = -\nabla.\langle \boldsymbol{q}_l{}'' \rangle + \langle {q_l}''' \rangle + \langle {q_{s,l}}''' \rangle + \langle {q_{v,l}}''' \rangle + \dot{m_{vl}}''' \langle h_{l,I} \rangle^l \tag{2.84}$$

$$\frac{\partial}{\partial t}\left(\varepsilon_s \rho_s \langle h_s \rangle^s\right) = -\nabla.\langle \boldsymbol{q}_s{}'' \rangle + \langle {q_s}''' \rangle - \langle {q_{s,l}}''' \rangle - \langle {q_{s,v}}''' \rangle - \langle {q_{s,i}}''' \rangle \tag{2.85}$$

Chapter 3

SINGLE PHASE NATURAL CONVECTION IN AN ENCLOSURE CONTAINING A HEAT-GENERATING POROUS DEBRIS BED

This chapter reports the numerical analysis that has been carried out in order to characterise the natural convective heat phenomena in enclosures containing heat-generating porous media. Phase change of the working fluid has not been considered in this analysis. Analysis has been carried out using both the local thermal equilibrium (LTE) and the local thermal non-equilibrium (LTNE) approaches in a dimensionless form. The effects of bed heat generation, bed permeability, thermal conductivity, bed configuration and bed stratification have been studied in this analysis.

Section 3.1 gives a brief review of the existing works on heat-generating porous media. *Section 3.2* gives a description of the problem that has been considered for analysis and the modelling assumptions made. *Section 3.3* and *Section 3.4* are devoted to the local thermal equilibrium (LTE) and the local thermal non-equilibrium (LTNE) approaches, respectively. *Section 3.5* summarises the observations from these analyses.

3.1 Literature review and Objectives

Substantial research has been carried out in the last few decades with focus on fluid flow and heat transfer involving heat-generating porous media. This is primarily due to the occurrence of heat-generating porous materials in various important applications. One such application is the heat removal from decay heat generating debris beds that are formed in the aftermath of core meltdown in nuclear reactors. Other examples include cooling of self-igniting coal stockpiles, removal of heat generated due to grain metabolism in agricultural storages etc.

Fundamental studies have been carried out over the last few decades with the objective of characterising the natural convective fluid flow and the associated heat transfer mechanisms in heat generating porous media following the local thermal equilibrium (LTE) approach. Analysis was carried out by Haajizadeh et al. (1984) as well as Prasad (1987) for a vertical enclosure filled with heat generating porous media, and bounded by adiabatic horizontal walls and isothermal vertical walls. The effect of Rayleigh number (*Ra*), Darcy number (*Da*) and aspect ratio of the cavity was well established in their study. Prasad (1987) also analysed the situation with isothermal horizontal walls in his study. Du and Bilgen (1992) observed a change in the flow pattern and the corresponding temperature distribution from symmetric to asymmetric in a similar geometry. The asymmetry was found to increase with increase in heat generation. It was also found that heat transfer at the enclosure walls are highly dependent on Rayleigh number (*Ra*), aspect ratio and heating asymmetry. Das and Sahoo (1999) attempted to establish the effects of Darcy number (*Da*), fluid Rayleigh number (*Ra*) and a specially defined heat generation parameter on natural convection in a square enclosure

filled with heat-generating porous media with the use of Brinkmann-extended Darcy model. Jue (2003) carried out a transient analysis of thermal convection in a square cavity with external side-wall heating. He concluded that porosity of the medium has a greater influence heat transfer at high Darcy numbers while permeability has a dominating effect at relatively lower Darcy numbers. It was also observed that permeability of the medium significantly influences the time taken to reach a steady state. Several other physical configurations containing heat generating porous media have also been considered for analysis by various researchers (Nield 1977; Poulikakos and Bejan 1983; Das and Morsi 2005; Reddy and Narasimhan 2010; Sivasankaran et al. 2011; Tian et al. 2014).

The local thermal equilibrium (LTE) approach assumes all the component phases of the porous media to be at the same temperature and as such, neglects the interfacial heat transfer between the component phases. In certain situations (such as in case of internal heat generation), however, the component phases may be far from thermal equilibrium and the use of the LTE approach in such situations can lead to erroneous predictions (Minkowycz et al. 1999; Bortolozzi and Deiber 2001; Rees and Pop 2005). This necessitates the use of the local thermal non-equilibrium (LTNE) approach which assumes a finite temperature difference between the component phases leading to interfacial heat transfer. A more accurate modelling of the thermal conditions can, thus, be expected with use of the LTNE approach.

However, only a limited number of studies have been carried out on natural convection involving heat-generating porous media using the LTNE approach. Baytaş (2003) modelled steady natural convection in a square enclosure bounded on all sides with isothermal walls. The validity of LTE approach was observed to hold for large values of the dimensionless solid-fluid heat transfer coefficient and porosity-scaled thermal conductivity ratio, while at smaller values of these parameters the use of LTNE was found to be indispensable. Nouri-Borujerdi et al. (2007b) and Saravanan (2009) performed linear stability analyses to determine the onset of natural convection in a fluid-saturated porous medium with uniform heat generation. Nouri-Borujerdi et al. (2007a) also analysed conduction in a heat generating porous layer using the LTNE approach and determined the exact solutions of temperature profiles within the channel. Convective instability was studied by Saravanan and Senthil Nayaki (2014) in a horizontal heat generating porous layer, with temperature dependent fluid viscosity, and heated from below. Kuznetsov and Nield (2014) analytically studied the effect of LTNE on the onset of convection in two internally heated horizontal porous layers. A similar work by Kuznetsov and Nield (2015) studies vertical flow through internally heated horizontal porous layers. Mahmoudi (2015) carried out an analysis on forced convection in a micro-channel filled with heat generating porous material and saturated with rarefied gas under a constant heat flux boundary condition. A numerical study was carried out by Wu et al. (2015a) with focus on steady non-Darcy natural convection in a square enclosure filled with heat-generating porous medium and having partially cooled walls. Analysis of different cooling configurations with both LTE and LTNE models showed that a partially cooled wall leads to augmentation of wall heat transfer as compared to a completely

cooled wall. A different study by Wu et al. (2015b), with adiabatic horizontal walls and sinusoidal temperature distribution on the side walls, also reported heat transfer enhancement as compared to uniform temperature distribution.

In all the above mentioned studies, following both LTE and LTNE approaches, geometries have been considered to be completely filled with porous media. In a realistic situation, however, it is more reasonable to accept that enclosures may not be completely filled with porous media. Heat removal from heat-generating debris beds is one such situation (see Fig. 1.1). Cooling of self-igniting coal stockpiles (Ejlali and Hooman 2011) and agricultural storages (Beukema 1983) are other typical examples. Several studies have been reported on partially porous configurations, with LTE as well as LTNE approaches (Nield 1977; Poulikakos and Bejan 1983; Nishimura et al. 1986; Beckermann et al. 1987; Kim and Choi 1996). However, only a few works have been carried out for partially porous configurations considering heat-generating porous media.

Schulenberg and Müller (1984) attempted to model natural convective heat transfer following the LTE approach in a heat-generating porous layer superposed by a clear fluid layer. Turbulence was considered within the clear fluid layer but not within the porous layer. Comparison of experimental data with numerical results led to the development of a 1-D asymptotic correlation in terms of Nusselt number. Chen and Lin (1997) highlighted the effect of inclination of the enclosure for a similar configuration using the LTE approximation, and with all the bounding walls maintained at the same isothermal temperature. They reported multiple steady state solutions with different flow patterns and heat transfer performance depending upon the tilt angle as well as the aspect ratio of the enclosure. It was further concluded that the global Nusselt number has an increasing trend with increasing aspect ratio in case of flows with similar pattern. The LTE approach was also utilised by Du and Bilgen (1990). They assumed a vertical cavity in their analysis, having adiabatic horizontal walls and differentially heated vertical walls. It was observed that, in addition to *Da* and *Ra*, heat transfer is significantly affected by position of the porous layer, aspect ratio, filling factor as well as cooling asymmetry from the side walls. Kim et al. (2001) carried out a scale analysis as well as numerical computations, following the LTE approach, for an identical geometry but with isothermal vertical walls. Three distinct regimes of heat transfer could be identified from their analysis depending on the relative magnitudes of *Ra* and *Da*. Results also revealed a substantial influence of thermal conductivity ratio in the intermediate heat transfer regime as compared to convection-dominated and conduction-dominated regimes. In contrast to the LTE approach, no significant studies yet exist on natural convection involving heat-generating porous media following the LTNE approach.

It can, thus, be inferred from the above discussion that several fundamental studies have been carried out on natural convective heat transfer involving heat generating porous media utilising the LTE as well as the LTNE approximations. In contrast, there is a dearth of studies on situations having a partially porous configuration and with internal heat generation. In this regard, the present analysis focuses on natural convection induced by heat-generating porous media in a cylindrical enclosure. The shape of the porous region is

assumed to be truncated conical in order to approximate the heap-like mass of debris formed consequent to severe accidents. Analysis has been carried out following the LTE approach as well as the LTNE approach.

3.2 Problem statement

Figure 3.1 is a schematic representation of the geometric configurations considered for analysis. The truncated conical porous bed is assumed to be placed centrally on the base of the cylindrical enclosure. All walls of the enclosure are assumed to be impermeable to fluid flow. Adiabatic condition is imposed on the bottom wall of the enclosure while an isothermal condition is assumed for the side wall. The top wall is assumed to be adiabatic in the analysis using the LTE approach (*Section 3.3*, Fig. 3.1(a)) while it is considered as an isothermal wall in case of analysis using the LTNE approach (*Section 3.4*, Fig, 3.1(b)). Other important assumptions are summarised as follows –

1. Steady incompressible fluid flow and heat transfer takes place in a 2D cylindrical co-ordinate system.
2. Fluid flow remains in the laminar regime.
3. Newtonian fluid is considered.
4. Barring density, which is modelled using Boussinesq approximation, all other thermos-physical properties are constant.
5. Porous medium is fluid saturated and is homogeneous as well as isotropic.
6. Heat generation is uniform and does not cause phase change of the working fluid.
7. The solid particles comprising the porous media are perfectly spherical i.e. $\psi = 1$ in the expression for permeability (Eq. 2.64).
8. The problem is symmetric about the z axis.

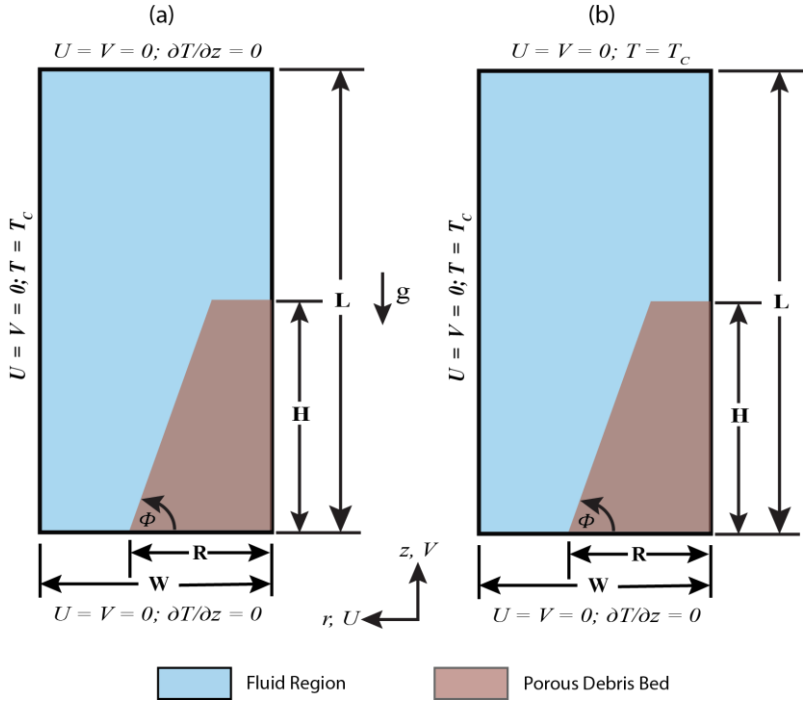

Figure 3.1 Schematic representation of the configurations assumed for analysis using (a) LTE approach and (b) LTNE approach

Properties of the porous material considered are based on the reported experimental data for debris beds in this regard (see *Chapter 1*). Porosity of the porous material is assumed to be 0.4 (Schmidt 2004) while the dimensionless parameter characterising permeability is assumed such that it is in accordance with the reported permeability for debris beds (see *Chapter 1*).

3.3 Local Thermal Equilibrium (LTE) approach

3.3.1 Governing equations

The governing equations for the clear fluid region and the heat-generating porous bed are derived, in terms of extrinsic average velocity, from the generalised transport equations formulated in *Chapter 2* taking into account the above stated assumptions. In addition, it is assumed that the component phases of the porous medium are in thermal equilibrium with each other. The mass, momentum and energy transport equations for the clear fluid region are derived from Eqs. 2.23, 2.36 and 2.49, respectively, while that for the porous bed are derived from Eqs. 2.54, 2.62 and 2.69, respectively. These are stated below –

Clear Fluid Region:

$$\nabla.\left(\rho_f\langle \boldsymbol{V}_f\rangle\right) = 0 \tag{3.1}$$

$$\nabla.\left(\rho_f\langle \boldsymbol{V}_f\rangle\langle \boldsymbol{V}_f\rangle\right) = -\nabla p + \mu_f\nabla^2\langle \boldsymbol{V}_f\rangle + \rho_f \boldsymbol{g}\beta\Delta T \tag{3.2}$$

$$\rho_f c_{p,f}\langle \boldsymbol{V}_f\rangle\nabla.T = k_f\nabla^2 T \tag{3.3}$$

Porous Region:

$$\nabla.\left(\rho_f\langle \boldsymbol{V}_f\rangle\right) = 0 \tag{3.4}$$

$$\frac{1}{\varepsilon_f}\nabla.\left(\frac{\rho_f\langle \boldsymbol{V}_f\rangle\langle \boldsymbol{V}_f\rangle}{\varepsilon_f}\right) = -\nabla p + \frac{\mu_f}{\varepsilon_f}\nabla^2\langle \boldsymbol{V}_f\rangle - \left(\frac{\mu_f}{\boldsymbol{K}}\langle \boldsymbol{V}_f\rangle + \frac{\rho_f}{\eta}\left|\langle \boldsymbol{V}_f\rangle\right|\langle \boldsymbol{V}_f\rangle\right) + \rho_f \boldsymbol{g}\beta\Delta T \tag{3.5}$$

$$\left(\rho c_p\right)_{eff}\langle \boldsymbol{V}_f\rangle\nabla.T = k_{eff}\nabla^2 T + {q_{eff}}''' \tag{3.6}$$

The dimensional equations stated above are converted into a dimensionless form by appropriate choice of the following dimensionless parameters –

$$r' = \frac{r}{L}, z' = \frac{z}{L}, H' = \frac{H}{L}, R' = \frac{R}{L}, \alpha_f = \frac{k_f}{\rho_f c_{p,f}}, \alpha_{eff} = \frac{k_{eff}}{\left(\rho c_p\right)_{eff}}, U' = \frac{UL}{\alpha_f}, V' = \frac{VL}{\alpha_f},$$
$$p' = \frac{pL^2}{\rho_f {\alpha_f}^2}, Pr = \frac{\nu_f}{\alpha_f}, Da = \frac{K}{L^2}, F_c = \frac{1.75}{\sqrt{150}}, \theta = \frac{T - T_c}{\Delta T_{ref}}, \Delta T_{ref} = \frac{{q_{eff}}''' H^2}{2k_{eff}},$$
$$\lambda = \frac{\alpha_{eff}}{\alpha_f}, Ra = \frac{g\beta\Delta T_{ref} H^3}{\nu_f \alpha_f} \tag{3.7}$$

The dimensionless equations thus obtained are stated below. It should be noted that the symbol for averaged quantities and vectors are not used in Eq. 3.7 and the subsequent equations for simplification of notations.

Clear Fluid Region:

$$\frac{1}{r'}\frac{\partial(r'U')}{\partial r'}+\frac{\partial V'}{\partial z'}=0 \tag{3.8}$$

$$U'\frac{\partial U'}{\partial r'}+V'\frac{\partial U'}{\partial z'}=-\frac{\partial p'}{\partial r'}+Pr\left[\frac{1}{r'}\frac{\partial}{\partial r'}\left(r'\frac{\partial U'}{\partial r'}\right)-\frac{U'}{r'^2}+\frac{\partial^2 U'}{\partial z'^2}\right] \tag{3.9}$$

$$U'\frac{\partial V'}{\partial r'}+V'\frac{\partial V'}{\partial z'}=-\frac{\partial p'}{\partial z'}+Pr\left[\frac{1}{r'}\frac{\partial}{\partial r'}\left(r'\frac{\partial V'}{\partial r'}\right)+\frac{\partial^2 V'}{\partial z'^2}\right]+\frac{RaPr}{H'^3}\theta \tag{3.10}$$

$$U'\frac{\partial \theta}{\partial r'}+V'\frac{\partial \theta}{\partial z'}=\frac{1}{r'}\frac{\partial}{\partial r'}\left(r'\frac{\partial \theta}{\partial r'}\right)+\frac{\partial^2 \theta}{\partial z'^2} \tag{3.11}$$

Porous Region:

$$\frac{1}{r'}\frac{\partial(r'U')}{\partial r'}+\frac{\partial V'}{\partial z'}=0 \tag{3.12}$$

$$\frac{1}{{\varepsilon_f}^2}\left(U'\frac{\partial U'}{\partial r'}+V'\frac{\partial U'}{\partial z'}\right)=-\frac{\partial p'}{\partial r'}+\frac{Pr}{\varepsilon_f}\left[\frac{1}{r'}\frac{\partial}{\partial r'}\left(r'\frac{\partial U'}{\partial r'}\right)-\frac{U'}{r'^2}+\frac{\partial^2 U'}{\partial z'^2}\right]$$
$$-\frac{Pr}{DaH'^2}U'-\frac{F_c}{\sqrt{Da}H'{\varepsilon_f}^{3/2}}|U'|U' \tag{3.13}$$

$$\frac{1}{{\varepsilon_f}^2}\left(U'\frac{\partial V'}{\partial r'}+V'\frac{\partial V'}{\partial z'}\right)=-\frac{\partial p'}{\partial z'}+\frac{Pr}{\varepsilon_f}\left[\frac{1}{r'}\frac{\partial}{\partial r'}\left(r'\frac{\partial V'}{\partial r'}\right)+\frac{\partial^2 V'}{\partial z'^2}\right]-\frac{Pr}{DaH'^2}V'$$
$$-\frac{F_c}{\sqrt{Da}H'{\varepsilon_f}^{3/2}}|V'|V'+\frac{RaPr}{H'^3}\theta \tag{3.14}$$

$$U'\frac{\partial \theta}{\partial r'}+V'\frac{\partial \theta}{\partial z'}=\lambda\left(\frac{1}{r'}\frac{\partial}{\partial r'}\left(r'\frac{\partial \theta}{\partial r'}\right)+\frac{\partial^2 \theta}{\partial z'^2}\right)+\frac{2\lambda}{H'^2} \tag{3.15}$$

3.3.2 Boundary conditions and Interfacial conditions

The associated boundary conditions in dimensionless form are expressed as follows –

$$U'=V'=0,\theta=0\ at\ r'=0.5,0<z'\leq 1$$
$$U'=V'=0,\frac{\partial\theta}{\partial z'}=0\ at\ z'=0{,}1\ and\ 0<r'\leq 0.5 \tag{3.16}$$

In addition to the above stated boundary conditions, it is also necessary to properly model the interface conditions at the porous-fluid interface. This is done by ensuring a continuity of variables and fluxes at the interface. These are stated as follows –

$$U'|_f=U'|_p;Pr\left[\frac{1}{r'}\frac{\partial}{\partial r'}\left(r'\frac{\partial U'}{\partial r'}\right)-\frac{U'}{r'^2}+\frac{\partial^2 U'}{\partial z'^2}\right]\Bigg|_f=\frac{Pr}{\varepsilon_f}\left[\frac{1}{r'}\frac{\partial}{\partial r'}\left(r'\frac{\partial U'}{\partial r'}\right)-\frac{U'}{r'^2}+\frac{\partial^2 U'}{\partial z'^2}\right]\Bigg|_p$$

$$V'|_f = V'|_p;\ Pr\left[\frac{1}{r'}\frac{\partial}{\partial r'}\left(r'\frac{\partial V'}{\partial r'}\right)+\frac{\partial^2 V'}{\partial z'^2}\right]\Bigg|_f = \frac{Pr}{\varepsilon_f}\left[\frac{1}{r'}\frac{\partial}{\partial r'}\left(r'\frac{\partial V'}{\partial r'}\right)+\frac{\partial^2 V'}{\partial z'^2}\right]\Bigg|_p$$

$$\theta|_f = \theta|_p;\ \frac{1}{r'}\frac{\partial}{\partial r'}\left(r'\frac{\partial \theta}{\partial r'}\right)+\frac{\partial^2 \theta}{\partial z'^2}\Bigg|_f = \lambda\left(\frac{1}{r'}\frac{\partial}{\partial r'}\left(r'\frac{\partial \theta}{\partial r'}\right)+\frac{\partial^2 \theta}{\partial z'^2}\right)\Bigg|_p \qquad (3.17)$$

3.3.3 Wall heat transfer assessment

Heat transfer due to natural convection is assessed at the cold enclosure wall in terms of the dimensionless Nusselt number (Nu). This is calculated as follows –

$$Nu = -\frac{\partial \theta}{\partial r'} \qquad (3.18)$$

$$Nu_{avg} = \int_0^1 Nu dz' \Big/ \int_0^1 dz' \qquad (3.19)$$

3.3.4 Numerical procedure

The pressure-based solver of ANSYS FLUENT is used for obtaining solution of the aforementioned dimensionless governing equations (Eqs. 3.8 – 3.15). Numerical schemes utilised in solving are listed in Table 3.1. A convergence criterion of all residuals below 10^{-8} is followed in this analysis. The entire analysis is carried out with a mesh comprising 17345 nodes and 16929 elements.

Table 3.1 Numerical schemes adopted for simulation

Parameter	Numerical Scheme
Pressure-Velocity Coupling	SIMPLE
Pressure	PRESTO
Momentum	QUICK
Energy	QUICK

3.3.4.1 Model validations

The numerical model, thus developed, is validated with experimental as well as numerical results reported in literature. Beckermann et al. (1987) carried out an experimental study using water and glass beads in a partial porous rectangular enclosure having differentially heated vertical walls and insulated horizontal walls. Figure 3.2(a) compares the experimentally obtained distribution of dimensionless temperature (θ) along the dimensionless x-coordinate (X) at three different locations within the enclosure with the numerical predictions using the present model. Figure 3.2(b) represents the comparison of solutions obtained by Kim et al. (2001) and the present model in a rectangular enclosure half-filled with heat-generating porous material in terms of local Nusselt number (Nu) along the cold side wall of the enclosure for $Ra = 10^{10}$ and $Pr = 7.0$, with three different values of Da (10^{-4}, 10^{-7}, 10^{-10}). It can be observed that a very good agreement is achieved between the predictions of the present numerical model and

previously reported data. The developed numerical model can, thus, be used for further investigations.

3.3.4.2 Grid independence study

The accuracy of solution obtained using the present model is assessed by performing computations with three different configurations of the computational grid. Table 3.2 summarises the values of Nu_{avg} obtained using the different configurations for two different values of *Ra* (10^6, 10^{10}) and *Da* of 10^{-4}. It is evident that when the grid is refined beyond 17345 nodes, the percentage change in Nu_{avg} becomes negligible. Therefore, this configuration has been utilised for carrying out further numerical simulations.

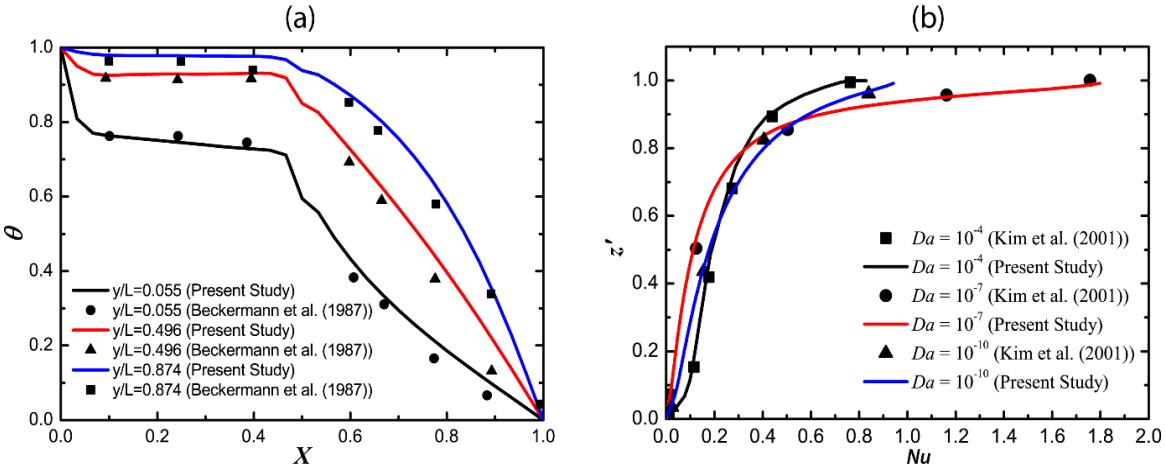

Figure 3.2 Validation of the numerical model using LTE approach with (a) experimental results of Beckermann et al. (1987) and (b) numerical results of Kim et al. (2001)

Table 3.2 Grid Independence study using Nu_{avg} at cold side wall

	Configuration (Number of Nodes)		
Ra	**7802**	**17345**	**30650**
10^6	0.14585 (1.64%)	0.14766 (0.42 %)	0.14829
10^{10}	0.11854 (2.92%)	0.12133 (0.63 %)	0.12210

3.3.5 Results and Discussions

The LTE approach has been used for assessing the impacts of porous bed permeability, heat generated within the bed and thermal conductivity ratio on the fluid flow and heat transfer characteristics within the enclosure. These are evaluated by carrying out parametric studies in terms of *Da*, *Ra* and λ, respectively. In addition to these parameters, the effects of bed configuration as well as bed stratification have also been studied. Working fluid in this analysis is assumed to be liquid water at 293 K (corresponding *Pr* = 6.97).

3.3.5.1 Effect of bed permeability

The effects of bed permeability on fluid flow and heat transfer characteristics have been studied in terms of the dimensionless Darcy number (*Da*) and the analysis has been carried out at a constant heat generation rate ($Ra = 10^8$) and constant thermal conductivity ratio (λ = 1.0). *Da* has been varied in the range of 10^{-1} to 10^{-8} with a lower value of *Da* representing a less permeable media.

Figure 3.3 represents the results pertaining to fluid flow and temperature distribution within the enclosure which are visualised with the help of streamlines and isotherms, respectively. Heat generation within the porous bed induces natural convective fluid motion within the enclosure due to the effects of buoyancy such that the working fluid transfers energy from the porous bed to the cold wall in a counter-clockwise motion. Energy transfer also occurs from the heat-generating porous bed to the adjacent clear fluid region across the fluid-porous interface. The overall energy transfer is, therefore, a balance between these two competing energy transfer mechanisms.

A decrease in *Da* i.e. a lower permeability essentially represents an increase in fluid flow resistance within porous media. This retards fluid circulation within the porous bed which can be corroborated by comparing the axial velocity profiles for various *Da* in Fig. 3.4. Therefore, a decrease in *Da* lowers the energy transfer taking place from the porous bed by convection. This leads to a rise in the maximum bed temperature, as is evident from the magnitudes of θ_{max} in Table 3.3.

Table 3.3 Global Parameters of the enclosure with varying *Ra* & *Da*: $|\psi|_{max}$ (1st row) followed by θ_{max} (2nd row) for H'= 0.5, R' = 0.25, $\phi = 75^{\circ}$

Ra	***Da***							
	$\mathbf{10^{-1}}$	$\mathbf{10^{-2}}$	$\mathbf{10^{-3}}$	$\mathbf{10^{-4}}$	$\mathbf{10^{-5}}$	$\mathbf{10^{-6}}$	$\mathbf{10^{-7}}$	$\mathbf{10^{-8}}$
$\mathbf{10^6}$	8.323	6.66184	4.3576	4.5037	4.7885	4.8205	4.8209	4.8212
	0.03248	0.03535	0.06193	0.106	0.1306	0.1334	0.1337	0.1337
$\mathbf{10^7}$	17.4577	14.7182	9.30597	6.49236	7.3596	7.99261	8.0639	8.071
	0.0174	0.01784	0.02627	0.05821	0.09804	0.1162	0.11789	0.118
$\mathbf{10^8}$	35.8023	31.55	20.7387	11.2945	9.3216	11.5621	12.2772	12.3518
	0.00908	0.00911	0.011	0.02341	0.05619	0.09259	0.10723	0.10845
$\mathbf{10^9}$	69.616	62.6773	46.111	24.9466	14.3742	15.4983	19.2661	20.3105
	0.00467	0.00465	0.0051	0.00873	0.02261	0.05482	0.08925	0.10192
$\mathbf{10^{10}}$	122.803	118.037	98.4412	62.2392	30.2104	23.0086	29.0068	38.0241
	0.00228	0.00231	0.00252	0.00351	0.00795	0.0223	0.0539	0.08758

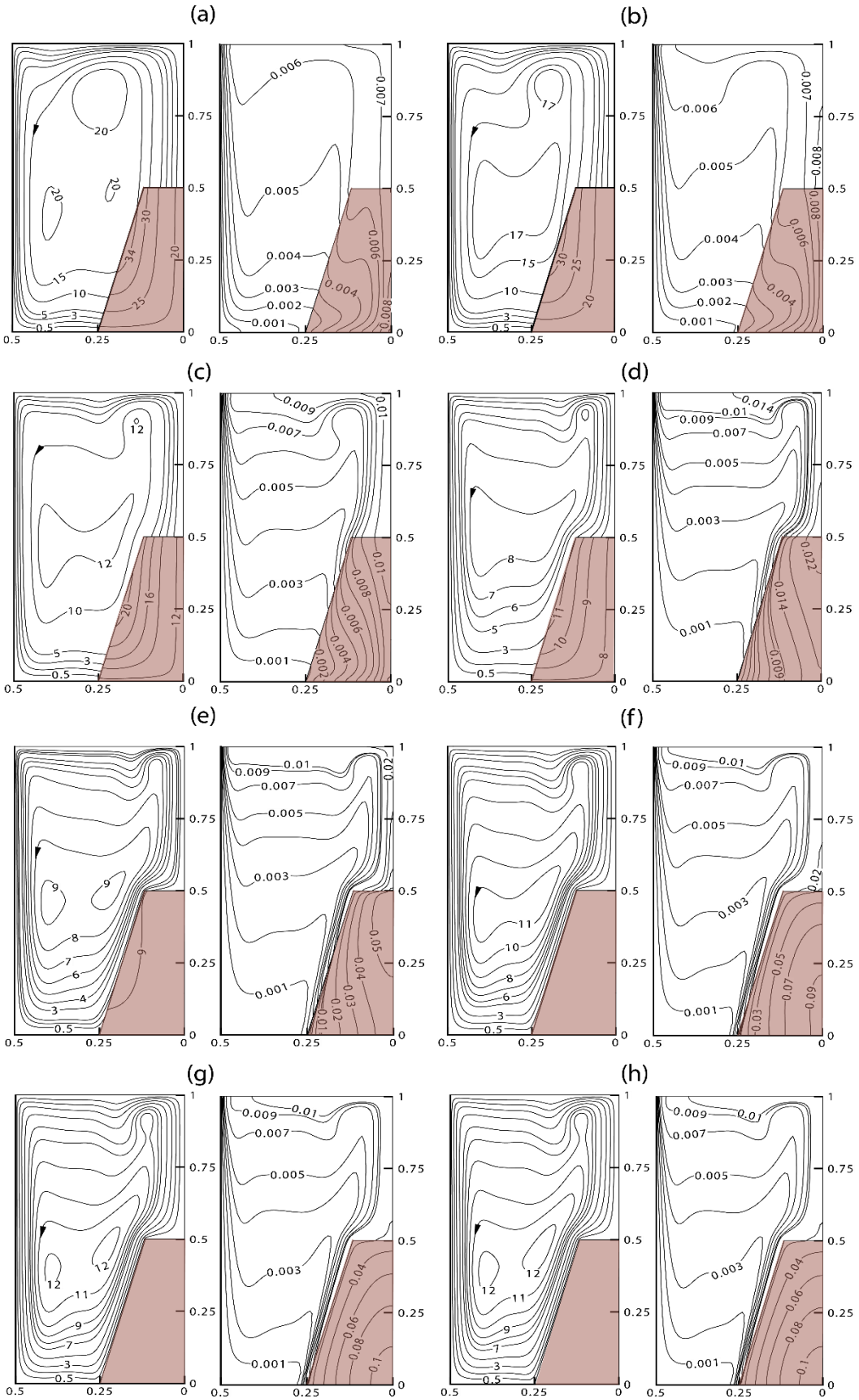

Figure 3.3 Streamline (left) and Isotherm (right) contours at $Ra = 10^8$ for $H' = 0.5$, $R' = 0.25$, $\phi = 75^{\circ}$ with (a) $Da = 10^{-1}$ (b) $Da = 10^{-2}$ (c) $Da = 10^{-3}$ (d) $Da = 10^{-4}$ (e) $Da = 10^{-5}$ (f) $Da = 10^{-6}$ (g) $Da = 10^{-7}$ (h) $Da = 10^{-8}$

The streamline and isotherm distribution for $Da = 10^{-1}$ is almost similar to that of an enclosure filled with a clear fluid. This is due to the negligible flow resistance offered by porous media in this situation. Natural convection is the dominant mode of energy transfer in this situation with an insignificant contribution from energy transfer at the fluid-porous interface. Flow suppression results in progressively lower energy transfer from the inner regions of the bed and consequently, temperature rise is found to be maximum in this region of the bed. Observation shows that the isotherms are slightly distorted within the porous bed when compared to the clear fluid region. This is attributed to heat generation within the porous bed as well as resistance to fluid flow offered by porous media.

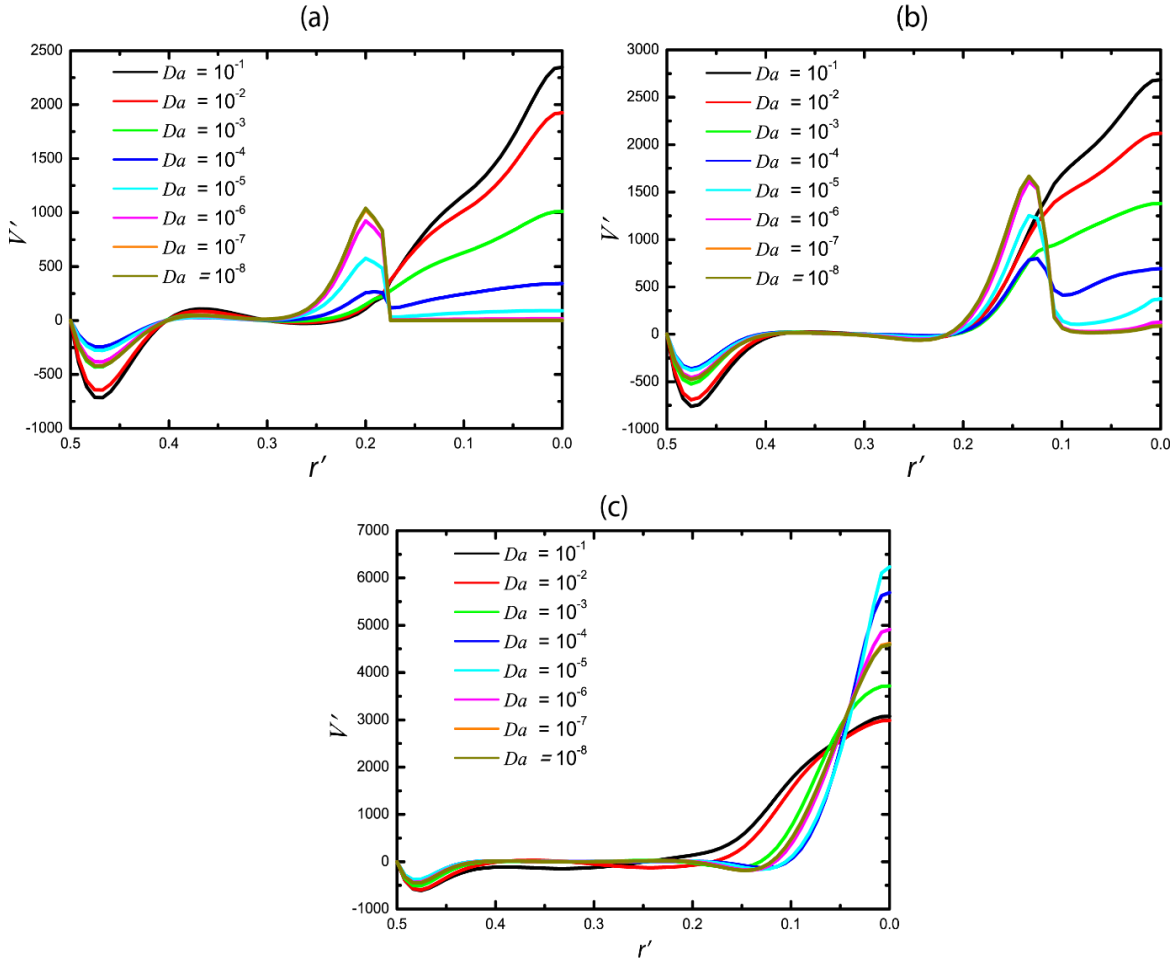

Figure 3.4 Effect of variation in *Da* with $Ra = 10^8$ on axial velocity profile along radial direction at (a) $z' = 0.25$ (b) $z' = 0.5$ (c) $z' = 0.75$

No major change takes place in the mechanism of energy transfer from porous bed to the cold wall as *Da* is gradually reduced to 10^{-3}. This is evident from the corresponding streamline and isotherm contours as well as the energy flux vectors. Weakening of convective strength within the bed, however, gradually intensifies the energy transfer across the fluid-porous interface which ultimately strengthens the overall convection in the clear fluid region. This effect is evident from the increased fluid velocity in the clear fluid region above the bed with reduction of *Da* to 10^{-3}, as can be seen from Fig. 3.4. In line with the above observations, a coarser distribution of isotherms

is observed in the region between the porous bed and the cold wall, while it becomes more concentrated in the region above the bed. This signifies that, in spite of reduction in flow within the bed, the counter-clockwise fluid circulation continues to transfer most of the energy from the bed to the region above it.

3.3.5.2 Effect of bed heat generation

The impact of volumetric heat generation within the porous bed is represented in terms of *Ra*. Parametric variation in Ra is carried out in the range of 10^6 to 10^{10}, at *Da* = 10^{-4} and λ = 1.0. The effects of variation in *Ra* is easily discernible from the magnitudes of the global parameters summarised in Table 3.3. An increase in *Ra*, for a fixed bed configuration, corresponds to greater heat generation within the porous bed. This enhances the energy transfer from the bed to the fluid and strengthens the convection within the enclosure, as is evident from higher value of $|\psi|_{max}$. The strengthening of convection is also clearly indicated by the streamline and isotherm distributions in Fig. 3.5 and can also be corroborated from a comparison of the axial velocity profiles along the radial direction in Fig. 3.6. The result pertaining to the case with *Ra* = 10^8 is not reproduced here since it has already been shown in Fig. 3.3(d).

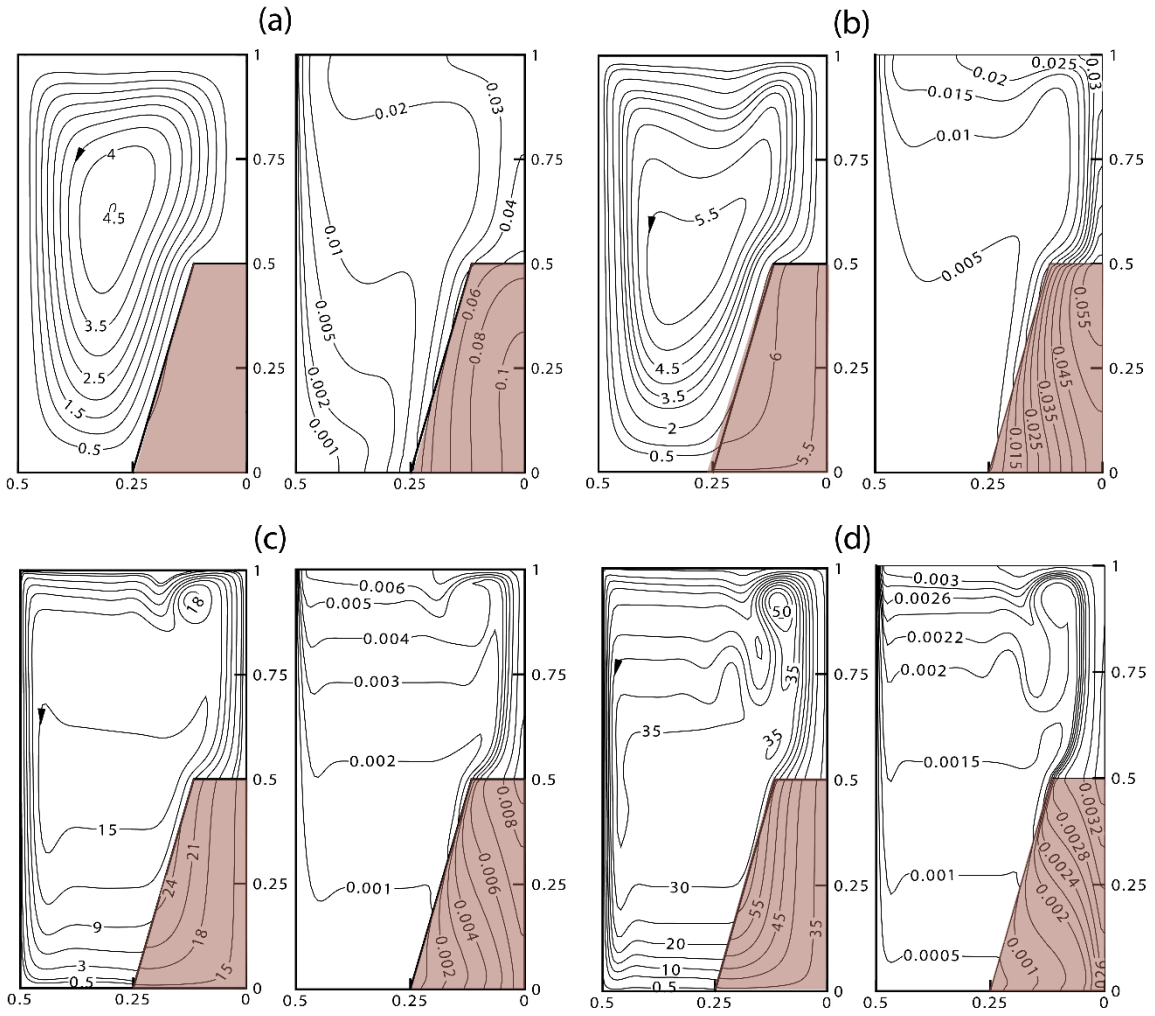

Figure 3.5 Streamline (left) and Isotherm (right) contours at *Da* = 10^{-4} for H'= 0.5, R' = 0.25, ϕ = 75° with (a) *Ra* = 10^6 (b) *Ra* = 10^7 (c) *Ra* = 10^9 (d) *Ra* = 10^{10}

It is expected that increased heat generation will contribute to a larger temperature rise. However, results indicate that θ_{max} has a decreasing trend with increasing *Ra* i.e. increasing heat generation. This happens since an increase in *Ra* also leads to increased ΔT_{ref}, which in turn reduces the value of the scaled temperature (θ). Comparison of dimensionless temperature profiles along the radial direction for different *Ra* and keeping *Da* fixed, as shown in Fig. 3.7(b), corroborates the above observation.

A survey of Table 3.3 further reveals an interesting effect. It is observed that the aforementioned change in mode of energy transfer from the porous bed with a decrease in *Da* is specific to each value of *Ra* (as can be observed from a reversal in the trend of variation of $|\psi|_{max}$). At lower values of *Ra* (<10^8), this reversal takes place at *RaDa* = 10^3 for each case, while at higher values of *Ra* (>10^8) the corresponding value is 10^4. This can be effectively treated as a critical value of *RaDa* – heat transfer becomes conduction-dominated if *RaDa* is lower than this critical value while it remains in the convection-dominated regime for *RaDa* greater than the critical value.

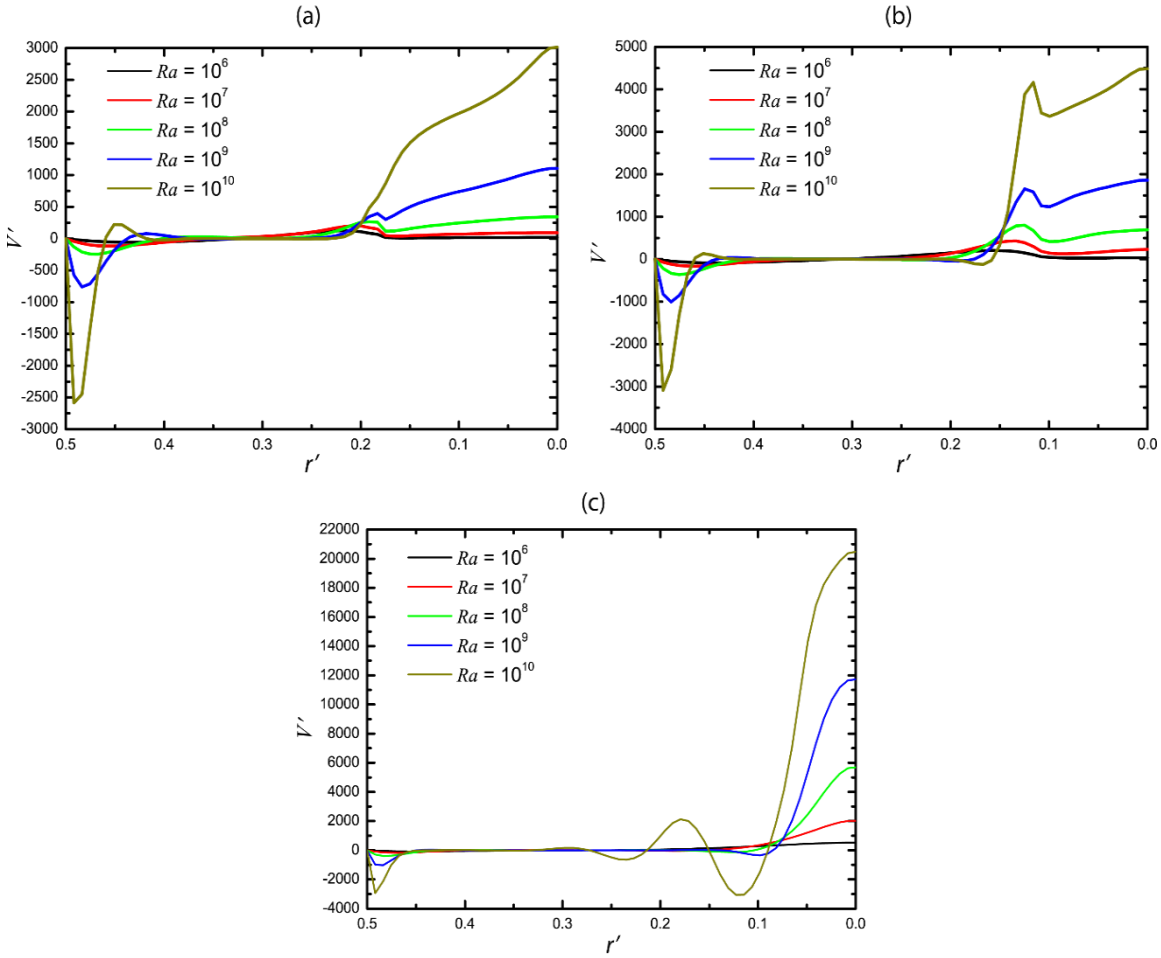

Figure 3.6 Effect of variation in *Ra* with *Da* = 10^{-4} on axial velocity profile along radial direction at (a) z' = 0.25 (b) z' = 0.5 (c) z' = 0.75

Figure 3.8 represents the impact of variation in *Ra* and *Da* on Nu_{avg} for a given bed geometry. Only a marginal variation in Nu_{avg} is observed with *Da* at a fixed *Ra*. A

substantial variation is, however, observed in Nu_{avg} with variation in *Ra* with the effect gaining prominence at higher magnitudes of *Ra*.

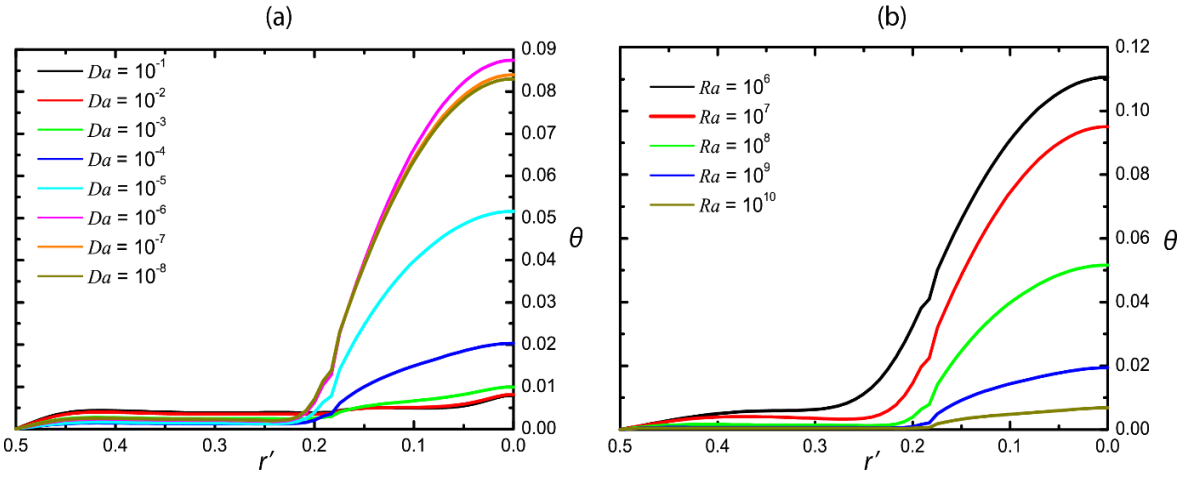

Figure 3.7 Temperature profile along the radial direction at $z' = 0.25$ for (a) various *Da* at $Ra = 10^8$ and (b) various *Ra* at $Da = 10^{-4}$

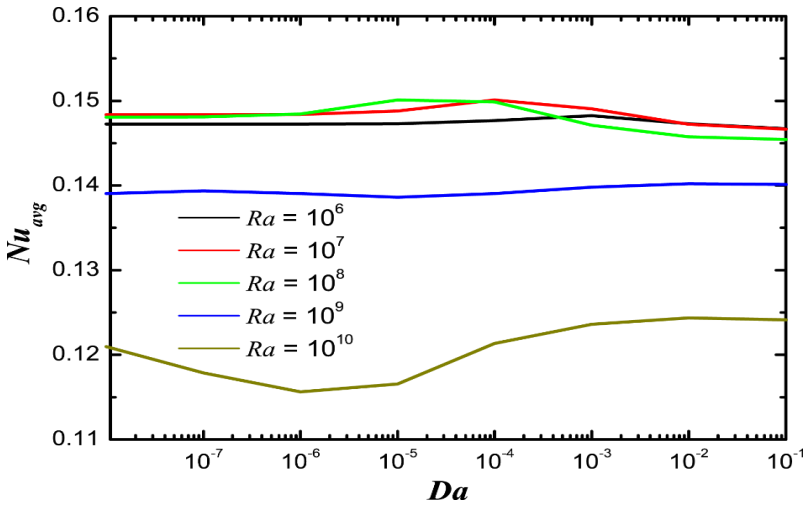

Figure 3.8 Variation of Nu_{avg} with *Da* for different *Ra*

An increase in *Ra*, for a constant bed configuration, necessitates an increase in heat generation and a consequent increase in ΔT_{ref}. The increased bed heat generation rate leads to a higher energy transfer to the cold wall and a consequent increase in Nu_{avg}. At the same time, a higher value of ΔT_{ref} scales down the dimensionless temperature (θ) and results in a lower value of Nu_{avg}. As such, the effective change in Nu_{avg} depends on the relative increase in bed heat generation and ΔT_{ref}. It can be seen that at higher values of *Da*, an increase in *Ra* results in a steady decrease in Nu_{avg} due to the dominating effect of ΔT_{ref}. This trend is, however, not followed as *Da* is progressively decreased. Observation shows that at a certain *Da*, an increase in *Ra* initially results in a marginally higher value of Nu_{avg}. Further increase in *Ra*, however, substantial reduces the magnitude of Nu_{avg}. This suggests that at higher *Ra*, the effect of ΔT_{ref} on Nu_{avg} dominates over that of heat generation, while the latter dominates at lower values

of *Ra*. Similar observations have also been reported by Du and Bilgen (1990) and Kim et al. (2001), albeit for different geometries.

A scale analysis reported by Kim et al. (2001) shows that normalised fluid temperature in thermal boundary layer at the cold wall is a function of *Ra* and the extent of the porous layer. This can be expressed as

$$\theta \approx \frac{t}{(tRa)^{1/5}}$$

where, t is the dimensionless extent of the porous layer. Thus, permeability of the porous medium (i.e. *Da*) do not have any effect on temperature in the thermal boundary layer and hence, on thermal gradient established at the cold wall. This can also be corroborated by the temperature profiles along radial direction obtained in the present analysis for various *Da* as shown in Fig. 3.8(a). A review of Eq. 3.18 shows that Nu is calculated based on the established thermal gradient at the cold wall. As a result, the magnitude of Nu and hence, Nu_{avg} is almost invariant with change in *Da*.

3.3.5.3 Effect of thermal conductivity ratio

Assessing the impact of thermal conductivity becomes necessary since the assumption of λ = 1.0 does not remain valid in most practical situations. This is evaluated by varying the thermal conductivity ratio in the range of 1.0 and 10.0, with *Ra* = 10^8 and *Da* = 10^{-4} and for a fixed bed configuration (H'= 0.5, R' = 0.25 and ϕ = 75°). It can be observed from the streamline and isotherm patterns, as shown in Fig. 3.9, that no significant change takes place with respect to fluid flow and mode of energy transfer from the porous bed.

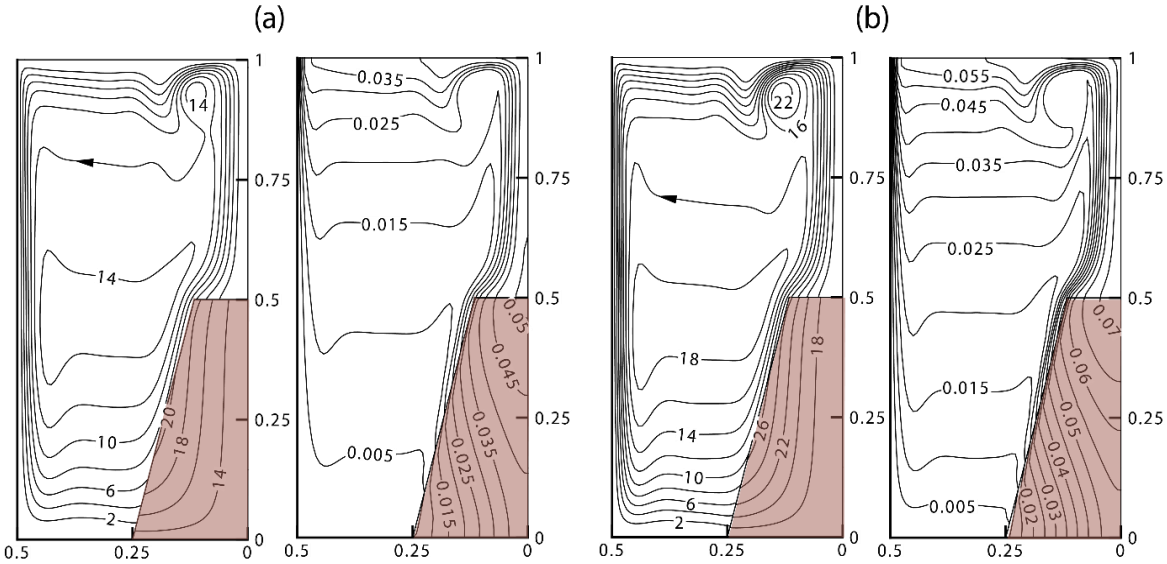

Figure 3.9 Streamline (left) and Isotherm (right) contours at *Ra* = 10^8, *Da* = 10^{-4} for H'= 0.5, R' = 0.25, ϕ = 75° with (a) λ = 5.0 (b) λ = 10.0

An increase in λ essentially refers to a larger magnitude of k_{eff} with respect to k_f. This necessitates an increase in the volumetric heat generation rate (q_s''') since the governing parameter (*Ra*) is kept constant (see Eq. 3.7). The increased magnitude of q_s''' should result in a higher bed temperature since all other parameters are invariant. It is also

expected that greater heat transfer will take place from the solid particles to the fluid phase as the thermal conductivity ratio is increased. Both these factors strengthens convective flow within the bed as well as the clear fluid region (indicated by increasing $|\psi|_{max}$ in Table 3.4) and consequently enhances heat transfer at the cold wall. The increase in wall heat transfer is indicated by the rising magnitudes of Nu_{avg} in Table 3.4. Temperature rise within the bed is also observed to increase with increase in λ as evident from θ_{max} in Table 3.4.

Table 3.4 Global Parameters of the enclosure with varying thermal conductivity ratio at $Ra = 10^8$, $Da = 10^{-4}$ with $H' = 0.5$, $R' = 0.25$, $\phi = 75^{\circ}$

λ	$\|\psi\|_{max}$	θ_{max}	Nu_{avg}
1.0	11.2945	0.02342	0.14988
5.0	20.5360	0.05076	0.69978
10.0	26.8283	0.07219	1.39957

3.3.5.4 Effect of bed geometry

The effect of change in bed geometry is assessed by performing independent parametric variations of bed height, bed width and bed angle, at $Ra = 10^8$, $Da = 10^{-4}$ and $\lambda = 1.0$. Variation of any of these parameters leads to a change in the bed volume and consequently, the bed heat generation. This presents a challenge when comparing the thermal-hydraulic characteristics of differing geometries. Therefore, a supplementary study is also carried out by comparing different bed configurations of equivalent volume.

3.3.5.4.1 Effect of bed height

The effect of change in bed height is assessed by varying H' between 1.0 and 0.25, while keeping $R'$and ϕ constant at 0.25 and 80°, respectively. Figure 3.10 represents the corresponding streamline and isotherm distributions. The respective values of $|\psi|_{max}$ and θ_{max} are listed in Table 3.5. Fluid circulation occurs only in the region between the fluid-porous interface and the cold wall of the enclosure when the height of the porous bed is equal to the enclosure height i.e. $H' = 1.0$. As a result, the entire energy transfer from the bed takes place only across the left fluid-porous interface.

A reduction in bed height, keeping *Ra* fixed, necessitates an increased heat generation rate within the bed and as such, results in a larger value of θ_{max}. This leads to a higher energy transfer from the bed to the working fluid. Reduction in H' below 1.0 allows fluid circulation in the region above the porous bed which enables energy transfer across the top fluid-porous interface as well, in addition to the left fluid-porous interface. The combined effect of all these factors strengthen the flow field within the enclosure, as represented by higher values of $|\psi|_{max}$.

Observations also reveal a relatively greater concentration of streamlines near the fluid-porous interfaces and the cold wall with decrease in bed height. This signifies a gradually thinning velocity boundary layer in these regions with decreasing bed height and a strongly convection dominated energy flow. Consistent with this observation, a

thinner thermal boundary layer is seen with gradual decrease in bed height due to increasing dominance of convection in energy transfer.

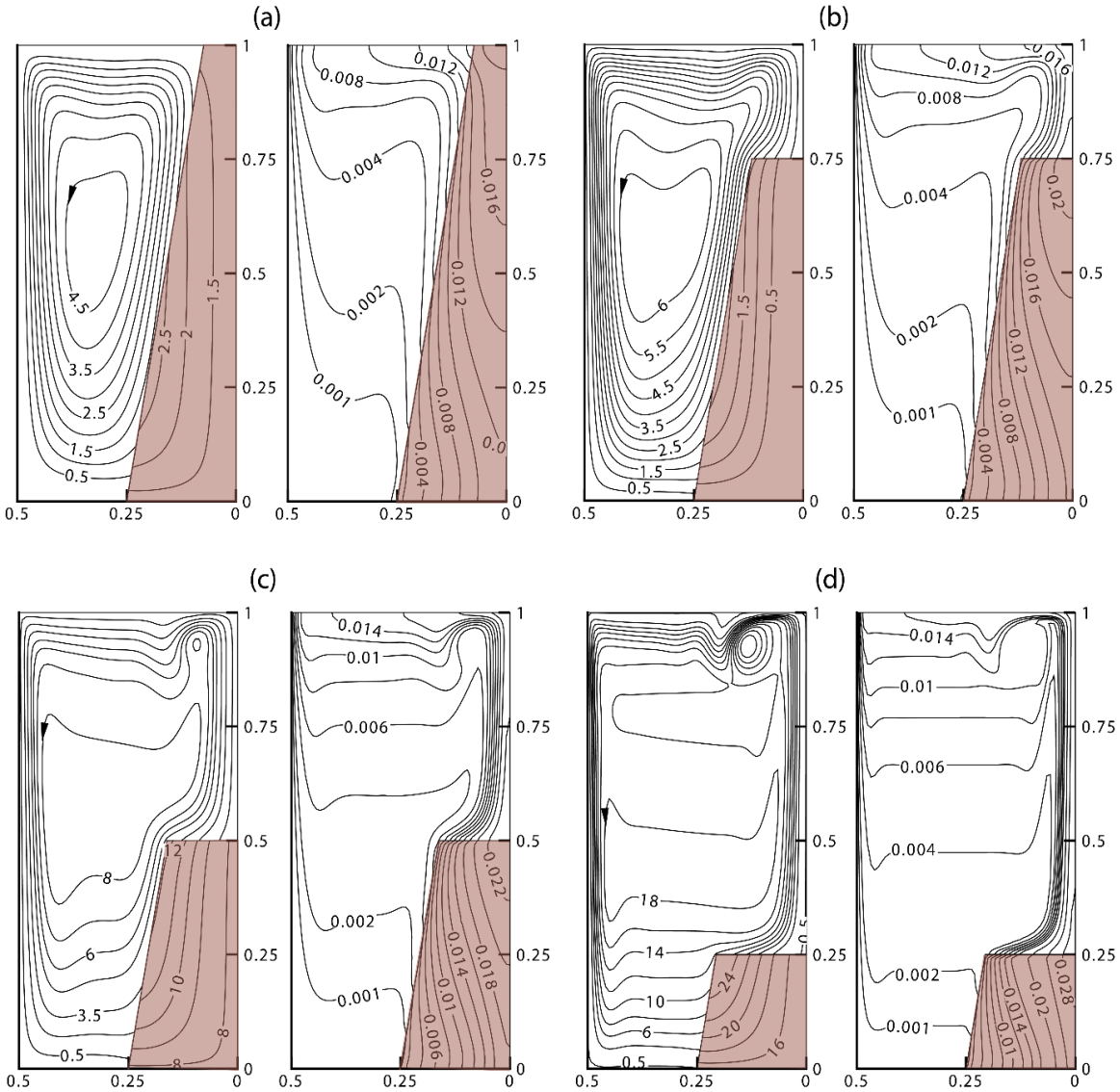

Figure 3.10 Streamline (left) and Isotherm (right) contours at $Ra = 10^8$, $Da = 10^{-4}$ for R' = 0.25, ϕ = 80° with (a) H' = 1.0 (b) H' = 0.75 (c) H' = 0.5 (d) H' = 0.25

3.3.5.4.2 Effect of bed radius

Figure 3.11 represents the effects of bed radius on the corresponding streamline and isotherm distribution. R' is varied in the range of 0.125 to 0.5, while keeping H' and ϕ fixed at 0.5 and 80°, respectively. A constant *Ra* and bed height results in a fixed value of the volumetric heat generation rate. However, the bed volume changes with changing bed radius and consequently, the bed heat generation also varies. An increase in bed radius, as such, results in a larger bed heat generation and leads to a greater value of θ_{max}. As a consequence of the higher heat generation, greater energy transfer from takes place from the bed to the working fluid which induces a corresponding flow enhancement within the enclosure. This is evident from the magnitude of $|\psi|_{max}$ in Table 3.5.

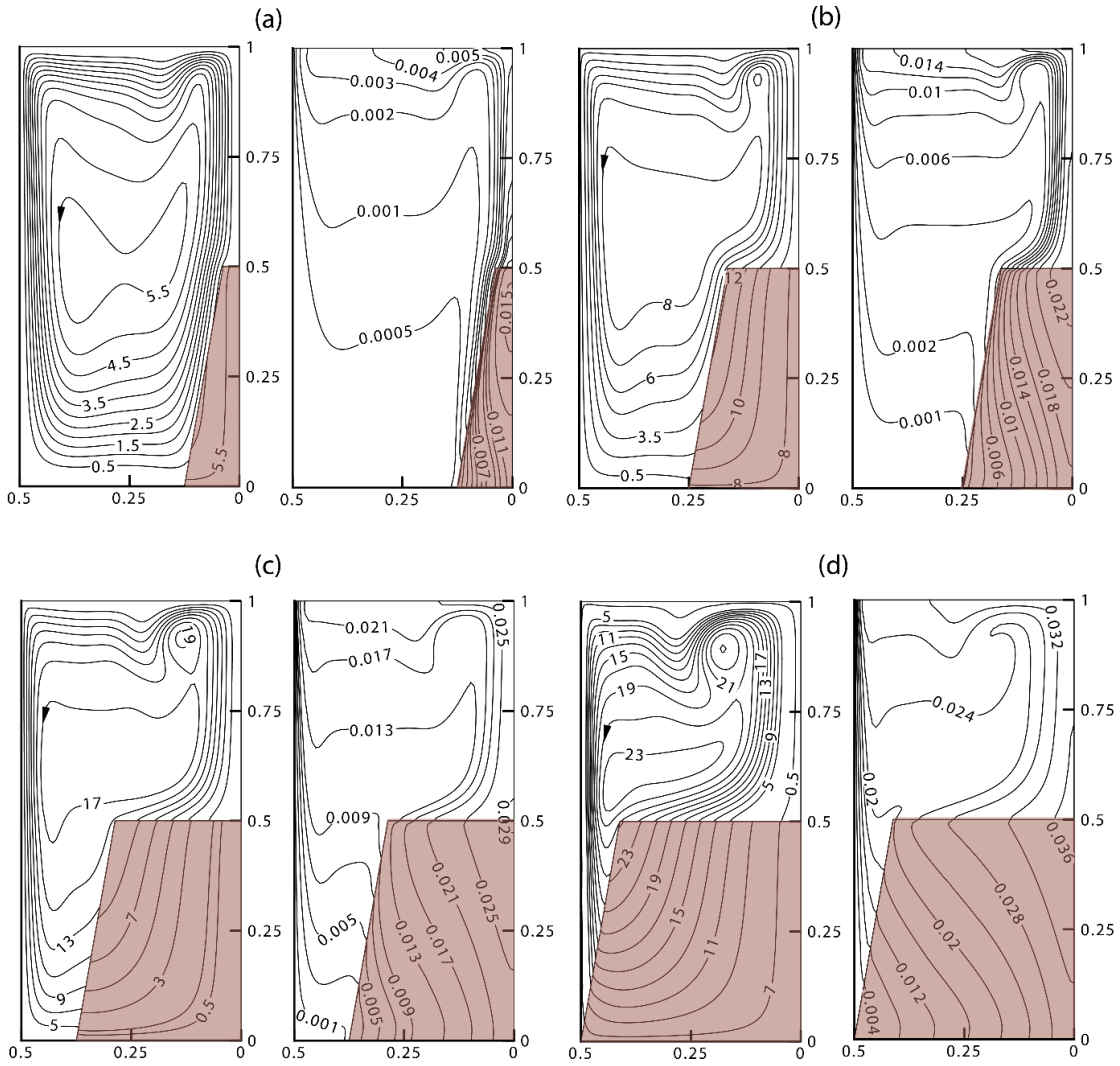

Figure 3.11 Streamline (left) and Isotherm (right) contours at $Ra = 10^8$, $Da = 10^{-4}$ for H' = 0.5, $\phi = 80°$ with (a) R' = 0.125 (b) R' = 0.25 (c) R' = 0.375 (d) R' = 0.5

The increase in bed radius, however, also results in reduced flow passage between the left fluid-porous interface and the cold wall. This retards fluid flow in this region which is conspicuous from a comparison of the velocity profiles for R' of 0.25 and 0.375 in Fig. 3.12. It can be observed that, in spite of increasing heat generation, velocity reduces near the fluid-porous interface as the bed radius is progressively increased. A higher energy transfer to the cold wall at large bed radii, however, results in a substantial increase in flow velocity near the cold wall.

The pattern of isotherm distribution remains similar within the porous bed as well as within the enclosure in all situations. This suggests no major change in mode of energy transfer which remains strongly dominated by convection. The gradually decreasing thickness of thermal boundary layer as well as velocity boundary layer, however, highlights the increasing dominance of convection in energy transfer as a consequence of higher bed heat generation.

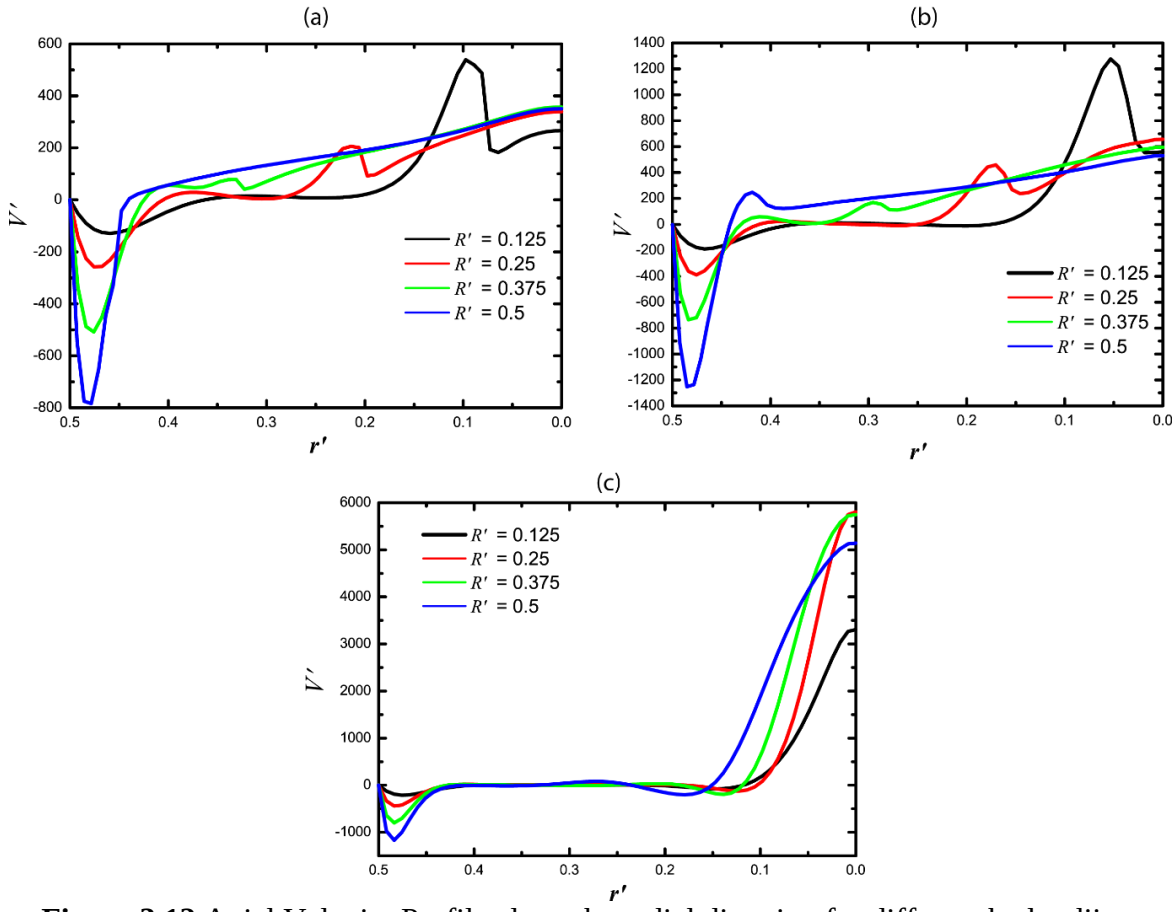

Figure 3.12 Axial Velocity Profile along the radial direction for different bed radii at (a) $z' = 0.25$ (b) $z' = 0.5$ (c) $z' = 0.75$

3.3.5.4.3 Effect of bed angle

The effect of bed angle (ϕ) is assessed by varying the bed angle between the extremities of a cylindrical bed ($\phi = 90^0$) and a conical bed. Bed height (H') and bed radius (R') are considered to be 0.5 and 0.25, respectively while *Ra* and *Da* are kept constant at 10^8 and 10^{-4}, respectively. It can be observed from the corresponding streamline and isotherm distributions in Fig. 3.13 that no substantial change takes place in the mode of energy transfer, which remains strongly convection dominated. The global parameters obtained from this analysis is summarised in Table 3.5.

A reduction in bed angle results in a decrease in bed volume and leads to a consequent decrease in bed heat generation and a marginal reduction in θ_{max}. It is to be noted that θ_{max} progressively decreases with a reduction in bed angle for all bed widths, as can be seen from Table 3.4. The change in $|\psi|_{max}$, however, is more complex. Decrease in bed heat generation results in lesser energy being transferred from the bed to the working fluid and this leads to a retardation in fluid circulation within the enclosure. Simultaneously, a decrease in ϕ increases the fluid flow passage enabling greater fluid circulation. Flow within the enclosure is, therefore, governed by the relative dominance of the above mentioned effects.

In case of the bed geometry with $R' = 0.125$, flow passage within the enclosure is sufficiently large such that a marginal increase in the flow passage does not substantially

contribute to flow enhancement. The dominating factor governing the fluid flow in this case is, therefore, the reduction in heat generation.

Table 3.5 Global Parameters of the enclosure with varying bed height, bed radius and bed angle at $Ra = 10^8$, $Da = 10^{-4}$

H'	R'	ϕ	$\lvert\psi\rvert_{max}$	θ_{max}
1.0	0.25	80	4.84999	0.01498
0.75			6.4674	0.0209
0.5			12.5762	0.02354
0.25			26.4019	0.03005
0.5	0.125	90	6.2232	0.01838
		85	6.1984	0.0175
		80	6.1354	0.01556
		75.96	6.0811	0.01364
0.5	0.25	90	11.2241	0.02393
		85	9.7846	0.0237
		80	12.5762	0.02354
		75	11.2945	0.02341
		70	9.139	0.02328
		65	10.1153	0.02264
		63.435	9.1162	0.02189
0.5	0.375	90	19.9226	0.03036
		85	27.0458	0.02976
		80	19.5645	0.02925
		75	14.0338	0.02885
		70	14.0956	0.02855
		65	13.1109	0.02834
		60	14.2079	0.02821
		55	14.8967	0.02811
		53.16	12.5482	0.02777
0.5	0.5	90	28.387	0.04525
		85	42.5118	0.03939
		80	25.5531	0.03693
		75	35.5696	0.03577
		70	20.7852	0.03492
		65	28.7225	0.03426
		60	16.4316	0.03376
		55	15.3999	0.03337
		50	14.6689	0.03311
		45	18.5335	0.03281

The relative effects of bed heat generation and flow passage modification gains prominence in bed configurations with larger radii i.e. for $R' = 0.25, 0.375$ and 0.5. A decrease in $|\psi|_{max}$with reduction of ϕ indicates the dominating influence of bed heat generation (which weakens the convective flow), while an increase in $|\psi|_{max}$ points to the dominating influence of flow passage modification (which strengthens the flow). A close competition exists between the effects of the two factors which is evident from the

fluctuating behaviour of $|\psi|_{max}$. It should be noted that this fluctuation in flow characteristics occurs at different bed angles for different bed geometries.

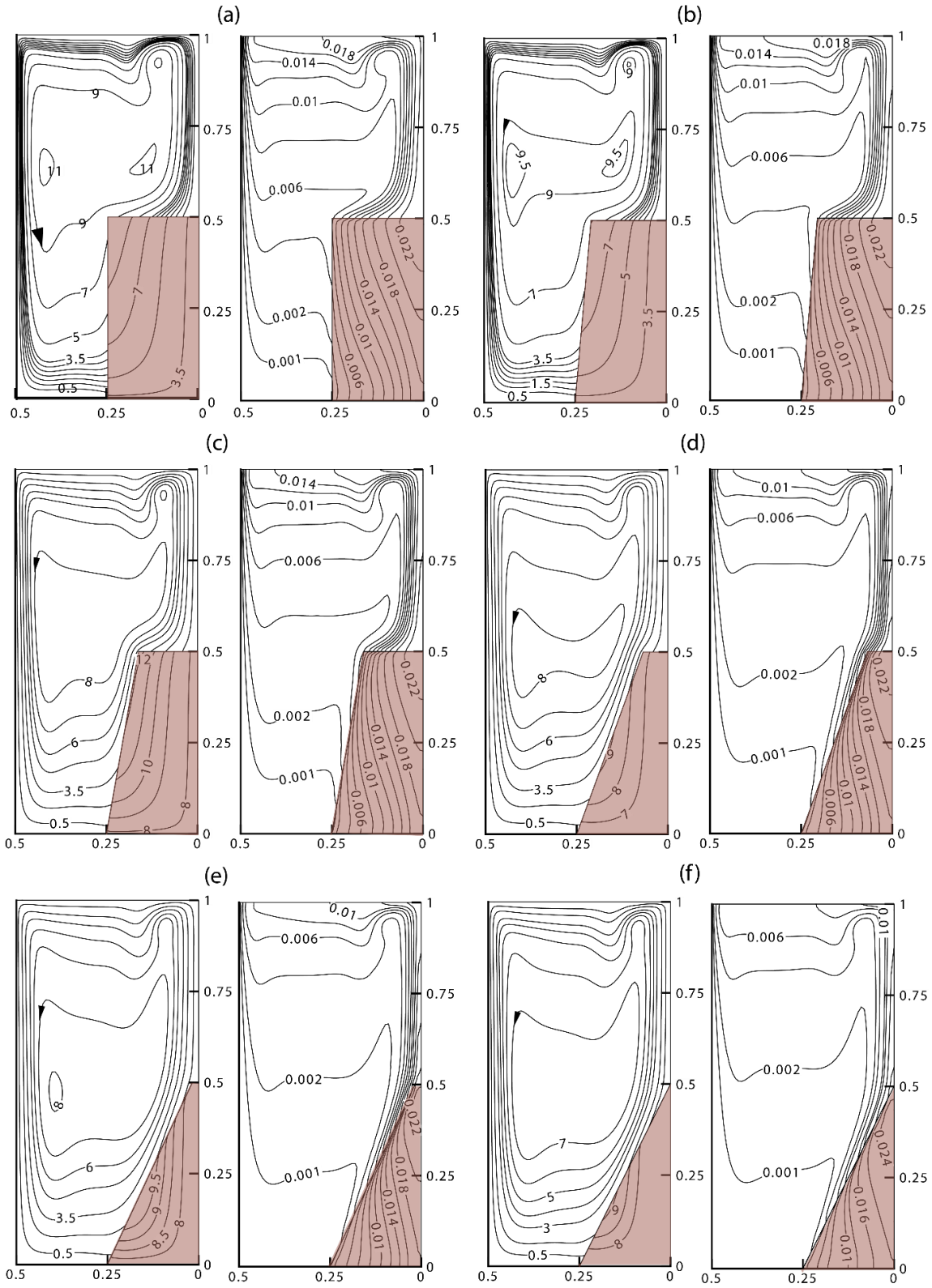

Figure 3.13 Streamline (left) and Isotherm (right) contours at $Ra = 10^8$, $Da = 10^{-4}$ for H' = 0.5, R' = 0.25 with (a) $\phi = 90°$ (b) $\phi = 85°$ (c) $\phi = 80°$ (d) $\phi = 70°$ (e) $\phi = 65°$ (f) $\phi = 63.435°$

It is worthwhile to take note of the change in flow characteristics on reduction of bed angle from 90° to 85° for $R' = 0.375$ and 0.5. In either case, a relative increase in $|\psi|_{max}$ is observed on making the aforesaid change in bed angle. In case of $R' = 0.375$, the existing narrow flow passage between the lateral fluid-porous interface and the side wall increases marginally. This allows greater fluid circulation in this region. In case of $R' = 0.5$ with $\phi = 90^0$, the entire fluid circulation is restricted to the clear fluid region above the porous bed. As such, energy transfer from the bed to the working fluid takes place only across the top fluid-porous interface. With decrease in bed angle to 85°, a small flow passage is created in the region between left interface and the side wall. This enables fluid movement across the lateral fluid-porous interface as well and as such, allows greater fluid penetration into the porous bed. Thus, although bed heat generation is reduced, greater energy transfer takes place from the bed to the working fluid and leads to flow enhancement within the enclosure. Combined effect of the above factors strengthens the overall fluid circulation within the enclosure as indicated by a substantial increase in $|\psi|_{max}$.

3.3.5.4.4 Effect of bed geometry parameters on average Nusselt number

The effects of the bed geometry variations on average Nusselt number at the cold wall is represented in Fig. 3.14. In Fig. 3.14(a), the variation of Nu_{avg} is shown with change in ϕ for $H' = 0.5$ and different bed radii. Since an increase in bed radius, keeping all other parameters constant, results in a greater bed heat generation, larger energy transfer takes place to the cold wall. Hence, Nu_{avg} increases with increase in bed radius. As stated before, any reduction in bed angle for a given bed radius and bed height leads to a decrease in bed heat generation. This results in a consequent reduction in energy transfer to the cold wall. As such, Nu_{avg} has a decreasing trend with decrease in bed angle for all bed radii.

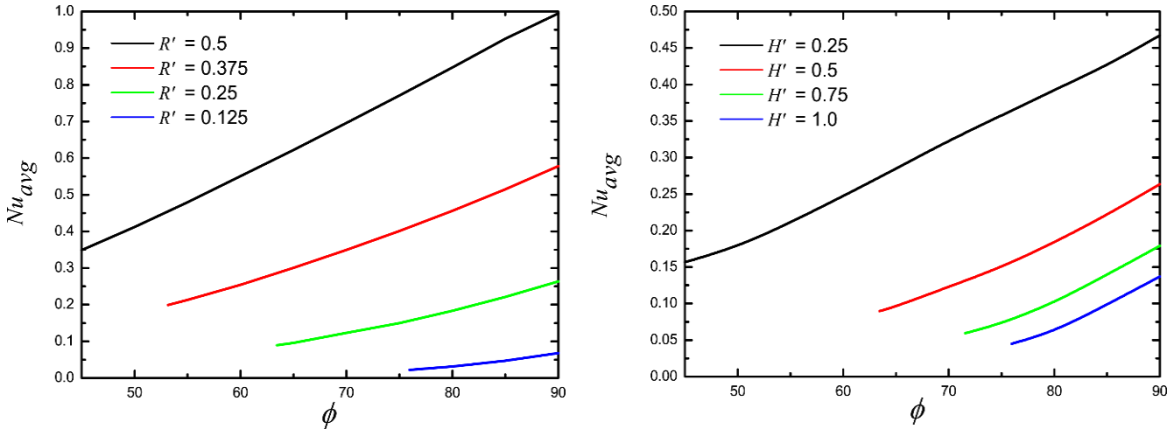

Figure 3.14 Variation of Nu_{avg} with ϕ at $Ra = 10^8$, $Da = 10^{-4}$ for (a) different bed radii at $H' = 0.5$ (b) different bed height at $R' = 0.25$

A similar variation of Nu_{avg} with ϕ is also found for a constant bed radius of 0.25 at all bed heights, as shown in Fig. 3.14(b). It is also observed that the magnitude of

Nu_{avg} is larger at lower bed heights, indicating greater energy transfer to the cold wall. This effect becomes progressively larger as the bed height is gradually decreased. A review of Eq. 3.7 indicates that a decrease in bed height, keeping *Ra* constant, must result in an increase in the heat generation rate within the bed along with an increase in ΔT_{ref}. This leads to a higher energy transfer to the cold wall and a consequent increase in Nu_{avg}. At the same time, a higher value of ΔT_{ref} scales down the magnitude of Nu_{avg}. The effective change in Nu_{avg} is, therefore, governed by the relative increase in bed heat generation rate and ΔT_{ref}. It is clearly evident that, on reduction in bed height, the magnitude of increase in bed heat generation rate is always greater than the increase in ΔT_{ref}. As such, Nu_{avg} steadily increases with a decrease in bed height. Further, the magnitude of relative increase in the above factors becomes higher at lower bed heights and hence, the relative increase in Nu_{avg} is greater at lower bed heights.

3.3.5.4.5 Comparison of different bed configurations

The preceding sections highlight the variations observed in thermal-hydraulic characteristics as a result of change in bed geometry. However, the associated bed volume also undergoes change with any such change in the geometrical parameters. As such, the bed heat generation and hence, ΔT_{ref} does not remain constant even when *Ra* is kept constant. This presents a considerable difficulty when comparing the heat transfer at the walls and the temperature rise within the bed.

In this regard, a comparative study has been carried out between three different bed configurations viz. truncated cone, conical and cylindrical, with equivalent bed volume and hence, equal bed heat generation. Figure 3.15 schematically represents the various bed configurations considered. Dimensions of the beds are selected such that the bed volume becomes equal to that of the truncated conical bed with H'= 0.5, R' = 0.25 and ϕ = 75°. The corresponding *Ra* is modified accordingly to maintain a constant total bed heat generation. The observations from this study are summarised in Table 3.6.

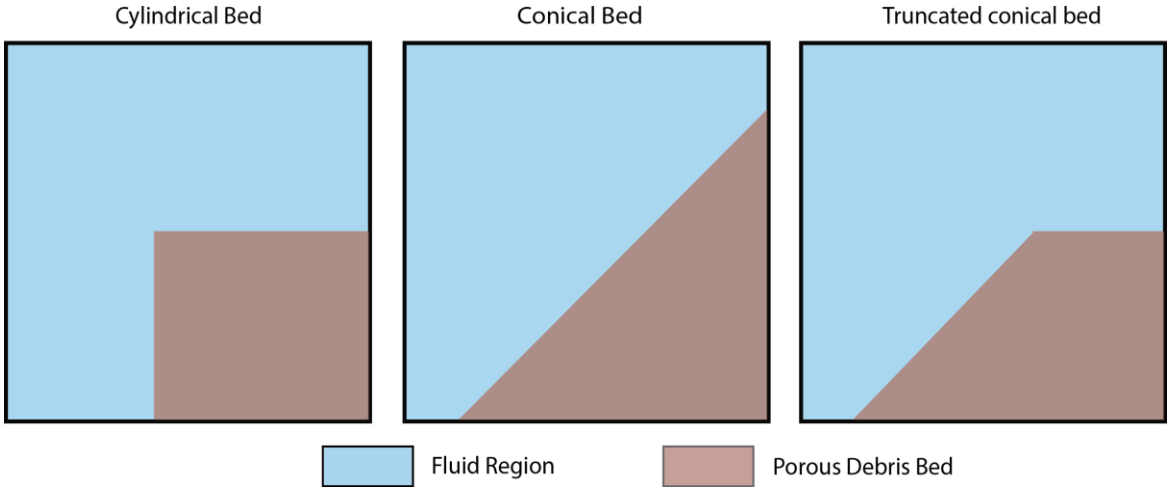

Figure 3.15 Schematic representation of different bed configurations considered

It can be observed that the maximum temperature (θ_{max}) in the conical configuration is much higher than that in the truncated conical configuration. Non-

existence of the top fluid-porous interface in the conical configuration reduces the effective surface area of the structure and hence, heat removal from the conical bed is lower when compared to the truncated conical bed. The temperature rise in the conical bed, therefore, is also much higher.

Configuration of the cylindrical bed is similar to that of the truncated conical bed with respect to the fluid-porous interfaces and as such, the heat removal mechanism from the bed also remains same. However, the surface area of the cylindrical bed considered is slightly larger than the truncated conical bed. As a result, heat removal from the cylindrical bed is larger than that from the truncated conical bed leading to a lower bed temperature in the cylindrical bed.

Table 3.6 Comparison of θ_{max} for various bed configuration with equivalent bed volume

Bed Configuration	**Dimensionless Extents**	$\boldsymbol{\theta_{max}}$	**% change**
Truncated Conical	H'= 0.5, R' = 0.25, ϕ = 75°	0.02341	--
Conical	H'= 0.5, R' = 0.3239	0.0303	29.43
Cylindrical	H'= 0.5, R' = 0.187	0.02128	9.09

3.3.5.5 Effect of bed stratification

The assumption of a homogeneous porous medium does not remain valid in most practical situations. Experimental investigations have found that porosity as well as particle size and hence, bed permeability has a spatially non-uniform distribution within debris beds. It has also been observed that permeability of such beds progressively decrease towards the interior of the bed (Magallon 2006; Karbojian et al. 2006).

Both radial and axial stratification of the bed has been considered in this analysis. The stratification has been implemented by considering two separate zones having differing properties, as shown schematically in Fig. 3.16. The inner layer (in case of radial stratification) and the bottom layer (in case of axial stratification) is assumed to have a lower porosity (ε_f = 0.3) and smaller particle size (D_p = 1 mm) and hence, a lower permeability (ε_f = 0.4, D_p = 3 mm) than the outer layer (in case of radial stratification) and the top layer (in case of axial stratification), respectively. Figure 3.16 schematically represents the composition of the stratified beds. It is to be noted that in this analysis the top wall of the enclosure is assumed to be isothermal. The analysis has been carried out at a constant *Ra* (= 10^{10}).

In this respect, the following two parameters have been defined to characterise the bed stratification –

1. Radial Stratification Ratio (*RSR*): This is defined as the ratio of radius of the inner layer to that of the outer layer. An increase in *RSR*, thus, indicates a larger inner layer and vice-versa.

2. Axial Stratification Ratio (*ASR*): This is defined as the ratio of radius of the bottom layer to that of the top layer. An increase in *ASR*, thus, indicates a larger bottom layer and vice-versa.

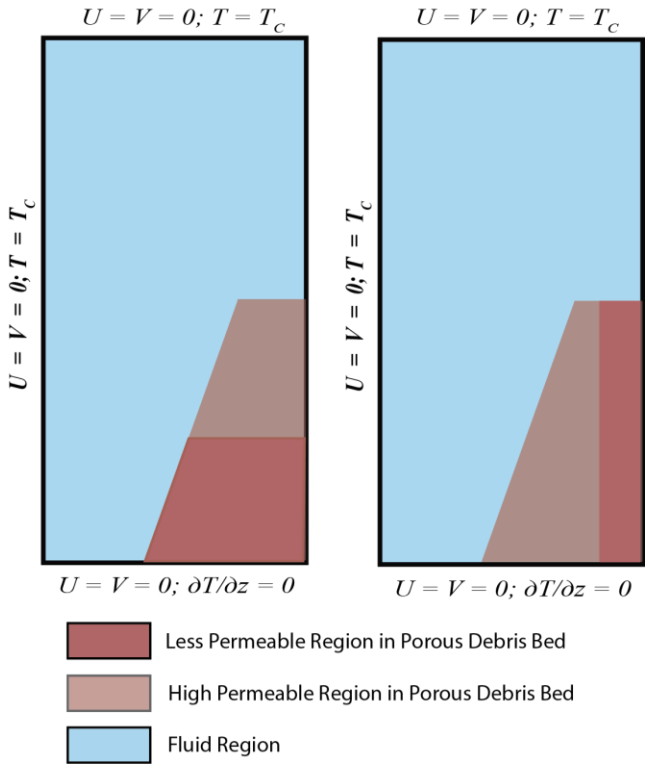

Figure 3.16 Schematic representation of the stratified beds

Figure 3.17 represents the variation in Nu_{avg} with change in stratification conditions. Results indicate that natural convective fluid flow and the associated heat transfer characteristics is governed by the permeability of the dominant porous layer within the bed.

In case of the radially stratified bed, the outer layer plays a dominant role in influencing convection within the enclosure when the inner layer is very thin (corresponding to very low value of *RSR*). Heat transfer characteristic is, thus, almost similar to a homogeneous bed comprising of the outer porous layer. The dominancy of the inner layer increases progressively with increase in the thickness of the inner layer. It can be observed from Fig. 3.17 that Nu_{avg} is highly sensitive to change in *RSR* at very low magnitude of *RSR*. Beyond a certain *RSR* i.e. beyond a certain thickness of the inner layer, however, this change becomes negligible. This represents the inner layer thickness beyond which influence of the outer layer is negligible and the porous bed behaves as a homogeneous bed comprised of the inner porous layer.

The effect of axial stratification within the porous bed is also assessed in a similar manner. Axial stratification ratio (*ASR*) is gradually increased such that thickness of the less permeable bottom layer progressively increases. It is evident from Fig. 3.17 that axial stratification has an almost similar effect on heat transfer characteristics of the enclosure as radial stratification. This suggests that, in case of stratified beds, the properties of the

stratified layers play the dominant role in affecting fluid flow and heat transfer in the enclosure, while the mode of stratification only has a negligible effect.

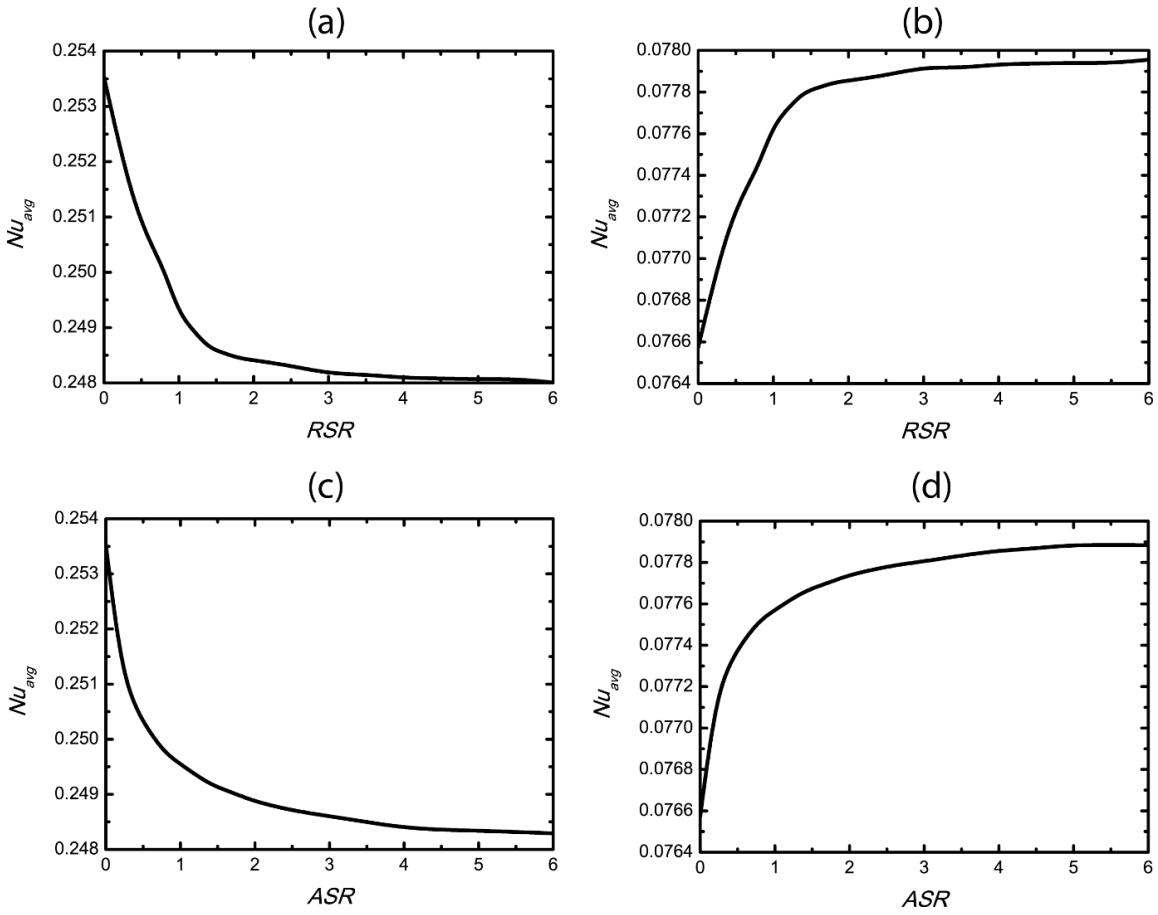

Figure 3.17 Variation in Nu_{avg} at top wall (left column) and side wall (right column) with different stratified conditions

3.4 Local Thermal Non-Equilibrium (LTNE) approach

3.4.1 Governing equations

The transport equations of mass, momentum and energy for the clear fluid region and the heat-generating porous bed are derived, in terms of extrinsic average velocity, from the generalised transport equations formulated in *Chapter 2* taking into account the above stated assumptions and considering thermal non-equilibrium in the porous media. The mass, momentum and energy transport equations for the clear fluid region are derived from Eqs. 2.23, 2.36 and 2.49, respectively, while that for the porous bed are derived from Eqs. 2.54, 2.61, 2.65 and 2.66, respectively. These are stated below –

Clear Fluid Region:

$$\nabla.\left(\rho_f\langle \boldsymbol{V}_f\rangle\right) = 0 \tag{3.20}$$

$$\nabla.\left(\rho_f\langle \boldsymbol{V}_f\rangle\langle \boldsymbol{V}_f\rangle\right) = -\nabla p + \mu_f\nabla^2\langle \boldsymbol{V}_f\rangle + \rho_f \boldsymbol{g}\beta\Delta T_f \tag{3.21}$$

$$\rho_f c_{p,f}\langle \boldsymbol{V}_f\rangle\nabla.T_f = k_f\nabla^2 T_f \tag{3.22}$$

Porous Region:

$$\nabla.\left(\rho_f\langle \boldsymbol{V}_f\rangle\right)=0 \tag{3.23}$$

$$\frac{1}{\varepsilon_f}\nabla.\left(\frac{\rho_f\langle \boldsymbol{V}_f\rangle\langle \boldsymbol{V}_f\rangle}{\varepsilon_f}\right)=-\nabla p+\frac{\mu_f}{\varepsilon_f}\nabla^2\langle \boldsymbol{V}_f\rangle - \left(\frac{\mu_f}{\boldsymbol{K}}\langle \boldsymbol{V}_f\rangle+\frac{\rho_f}{\eta}\left|\langle \boldsymbol{V}_f\rangle\right|\langle \boldsymbol{V}_f\rangle\right)+\rho_f \boldsymbol{g}\beta\Delta T_f \tag{3.24}$$

$$\left(\rho c_p\right)_f\langle \boldsymbol{V}_f\rangle\nabla.T_f=\varepsilon_f k_f\nabla^2T_f+ha_i\left(T_s-T_f\right) \tag{3.25}$$

$$0=\left(1-\varepsilon_f\right)k_s\nabla^2T_s+ha_i\left(T_f-T_s\right)+\ {q_s}''' \tag{3.26}$$

The dimensional equations stated above are converted into a dimensionless form by utilising the following dimensionless parameters –

$$r'=\frac{r}{L}\,,z'=\frac{z}{L}\,,H'=\frac{H}{L}\,,R'=\frac{R}{L}\,,\alpha_f=\frac{k_f}{\rho_f c_{p,f}}\,,U'=\frac{UL}{\alpha_f}\,,V'=\frac{VL}{\alpha_f},$$
$$p'=\frac{pL^2}{\rho_f{\alpha_f}^2},Pr=\frac{\nu_f}{\alpha_f}\,,Da=\frac{K}{L^2}\,,F_c=\frac{1.75}{\sqrt{150}}\,,\theta=\frac{T-T_c}{\Delta T_{ref}}\,,\Delta T_{ref}=\frac{{q_s}'''H^2}{2k_s},$$
$$h'=\frac{ha_iL^2}{\varepsilon_f k_f},\gamma=\frac{\varepsilon_f k_f}{\left(1-\varepsilon_f\right)k_s},Ra=\frac{g\beta\Delta T_{ref}H^3}{\nu_f\alpha_f} \tag{3.27}$$

The dimensionless equations thus obtained are stated below. It should be noted that the symbol for averaged quantities is not used in Eq. 3.7 and subsequent equations for simplification of notations.

Clear Fluid Region:

$$\frac{1}{r'}\frac{\partial(r'U')}{\partial r'}+\frac{\partial V'}{\partial z'}=0 \tag{3.28}$$

$$U'\frac{\partial U'}{\partial r'}+V'\frac{\partial U'}{\partial z'}=-\frac{\partial p'}{\partial r'}+Pr\left[\frac{1}{r'}\frac{\partial}{\partial r'}\left(r'\frac{\partial U'}{\partial r'}\right)-\frac{U'}{{r'}^2}+\frac{\partial^2U'}{\partial {z'}^2}\right] \tag{3.29}$$

$$U'\frac{\partial V'}{\partial r'}+V'\frac{\partial V'}{\partial z'}=-\frac{\partial p'}{\partial z'}+Pr\left[\frac{1}{r'}\frac{\partial}{\partial r'}\left(r'\frac{\partial V'}{\partial r'}\right)+\frac{\partial^2V'}{\partial {z'}^2}\right]+\frac{RaPr}{{H'}^3}\theta_f \tag{3.30}$$

$$U'\frac{\partial \theta_f}{\partial r'}+V'\frac{\partial \theta_f}{\partial z'}=\frac{1}{r'}\frac{\partial}{\partial r'}\left(r'\frac{\partial \theta_f}{\partial r'}\right)+\frac{\partial^2\theta_f}{\partial {z'}^2} \tag{3.31}$$

Porous Region:

$$\frac{1}{r'}\frac{\partial(r'U')}{\partial r'}+\frac{\partial V'}{\partial z'}=0 \tag{3.32}$$

$$\frac{1}{{\varepsilon_f}^2}\left(U'\frac{\partial U'}{\partial r'}+V'\frac{\partial U'}{\partial z'}\right)=-\frac{\partial p'}{\partial r'}+\frac{Pr}{\varepsilon_f}\left[\frac{1}{r'}\frac{\partial}{\partial r'}\left(r'\frac{\partial U'}{\partial r'}\right)-\frac{U'}{{r'}^2}+\frac{\partial^2U'}{\partial {z'}^2}\right] - \frac{Pr}{DaH'^2}U'-\frac{F_c}{\sqrt{Da}H'{\varepsilon_f}^{3/2}}|U'|U' \tag{3.33}$$

$$\frac{1}{{\varepsilon_f}^2}\left(U'\frac{\partial V'}{\partial r'}+V'\frac{\partial V'}{\partial z'}\right)=-\frac{\partial p'}{\partial z'}+\frac{Pr}{\varepsilon_f}\left[\frac{1}{r'}\frac{\partial}{\partial r'}\left(r'\frac{\partial V'}{\partial r'}\right)+\frac{\partial^2 V'}{\partial {z'}^2}\right]-\frac{Pr}{DaH'^2}V' - \frac{F_c}{\sqrt{Da}H'{\varepsilon_f}^{3/2}}|V'|V'+\frac{RaPr}{H'^3}\theta_f \tag{3.34}$$

$$U'\frac{\partial \theta_f}{\partial r'}+V'\frac{\partial \theta_f}{\partial z'}=\left(\frac{1}{r'}\frac{\partial}{\partial r'}\left(r'\frac{\partial \theta_f}{\partial r'}\right)+\frac{\partial^2 \theta_f}{\partial {z'}^2}\right)+h'\left(\theta_s-\theta_f\right) \tag{3.35}$$

$$0=\left(\frac{1}{r'}\frac{\partial}{\partial r'}\left(r'\frac{\partial \theta_s}{\partial r'}\right)+\frac{\partial^2 \theta_s}{\partial {z'}^2}\right)+\gamma h'\left(\theta_f-\theta_s\right)+\frac{2}{H'^2} \tag{3.36}$$

3.4.2 Interfacial heat transfer assessment

Interfacial heat transfer between the heat-generating solid particles and the fluid phase is evaluated using the heat transfer correlation proposed by Ranz and Marshall (1952). This correlation is usually applied in situations involving flow over spherical particles and has been widely used in heat transfer calculations in porous media (Kakaç 1991) well as heat-generating debris (Takasuo 2015). The heat transfer coefficient (h) is evaluated as follows –

$$h=\frac{Nuk_f}{D_p}=\frac{\left(2+0.66Re^{1/2}Pr^{1/3}\right)k_f}{D_p} \tag{3.37}$$

In the above assessment, the Reynolds number (Re) and the interfacial area density (a_i) are calculated using the following expressions –

$$Re=\frac{\rho_f D_p\left|\langle \boldsymbol{V}_f\rangle^f\right|}{\mu_f} \tag{3.38}$$

$$a_i=\frac{6\left(1-\varepsilon_f\right)}{D_p} \tag{3.39}$$

3.4.3 Boundary conditions and Interfacial conditions

The associated boundary conditions in dimensionless form are expressed as –

$$U'=V'=0,\theta_f=0\ at\ r'=0.5,0<z'\leq 1$$
$$U'=V'=0,\theta_f=0\ at\ z'=1.0,0<r'\leq 0.5$$
$$U'=V'=0,\frac{\partial \theta_f}{\partial z'}=\frac{\partial \theta_s}{\partial z'}=0\ at\ z'=0\ and\ 0<r'\leq 0.5 \tag{3.40}$$

In addition to the above stated boundary conditions, it is also necessary to properly model the interface conditions at the porous-fluid interface. This is done by ensuring a continuity of variables and fluxes at the interface. These are stated as follows –

$$U'|_f=U'|_p;\ Pr\left[\frac{1}{r'}\frac{\partial}{\partial r'}\left(r'\frac{\partial U'}{\partial r'}\right)-\frac{U'}{r'^2}+\frac{\partial^2 U'}{\partial {z'}^2}\right]\Bigg|_f=\frac{Pr}{\varepsilon_f}\left[\frac{1}{r'}\frac{\partial}{\partial r'}\left(r'\frac{\partial U'}{\partial r'}\right)-\frac{U'}{r'^2}+\frac{\partial^2 U'}{\partial {z'}^2}\right]\Bigg|_p$$

$$V'|_f=V'|_p;\ Pr\left[\frac{1}{r'}\frac{\partial}{\partial r'}\left(r'\frac{\partial V'}{\partial r'}\right)+\frac{\partial^2 V'}{\partial {z'}^2}\right]\Bigg|_f=\frac{Pr}{\varepsilon_f}\left[\frac{1}{r'}\frac{\partial}{\partial r'}\left(r'\frac{\partial V'}{\partial r'}\right)+\frac{\partial^2 V'}{\partial {z'}^2}\right]\Bigg|_p$$

$$\theta_f\big|_f = \theta_f\big|_p$$

$$\frac{1}{r'}\frac{\partial}{\partial r'}\left(r'\frac{\partial\theta_f}{\partial r'}\right) + \left.\frac{\partial^2\theta_f}{\partial z'^2}\right|_f = \varepsilon_f\left(\frac{1}{r'}\frac{\partial}{\partial r'}\left(r'\frac{\partial\theta_f}{\partial r'}\right) + \frac{\partial^2\theta_f}{\partial z'^2}\right)\Bigg|_p + \varepsilon_s\left(\frac{1}{r'}\frac{\partial}{\partial r'}\left(r'\frac{\partial\theta_s}{\partial r'}\right) + \frac{\partial^2\theta_s}{\partial z'^2}\right)\Bigg|_p \quad (3.41)$$

3.4.4 Wall heat transfer assessment

Heat transfer due to natural convection is assessed at the cold enclosure walls in terms of the dimensionless Nusselt number (Nu). This is calculated as follows –

$$Nu = -\frac{\partial\theta_f}{\partial n} \quad (3.42)$$

$$Nu_{avg} = \int Nu dn \Big/ \int dn \quad (3.43)$$

3.4.5 Energy flux vector

Energy flux vectors, as defined by Hooman (2010), have been used for visualisation of convective energy transfer within the enclosure. Mathematically, the energy flux vector is expressed in cylindrical coordinate system as –

$$\vec{E} = \left(\frac{\partial\Pi}{\partial z'}\right)\vec{\imath} - \left(\frac{1}{r'}\frac{\partial\Pi}{\partial r'}\right)\vec{\jmath} \quad (3.44)$$

The dimensionless form of the energy flux vectors are separately defined for the fluid and porous regions, following the works of Ejlali and Hooman (2011) and Ejlali et al. (2009), as follows –

Clear Fluid region:

$$\frac{\partial\Pi}{\partial z'} = U'\theta_f - r'\frac{\partial\theta_f}{\partial r'} \quad (3.45)$$

$$-\frac{1}{r'}\frac{\partial\Pi}{\partial r'} = V'\theta_f - \frac{\partial\theta_f}{\partial z'} \quad (3.46)$$

Porous region:

$$\frac{\partial\Pi}{\partial z'} = U'\theta_f - r'\frac{\partial\theta_f}{\partial r'} - r'\frac{\partial\theta_s}{\partial r'} - \left[(1-\gamma)\frac{h'}{4}(\theta_s - \theta_f)r'^2\right] - \frac{r'^2}{2H'^2} \quad (3.47)$$

$$-\frac{1}{r'}\frac{\partial\Pi}{\partial r'} = V'\theta_f - \frac{\partial\theta_f}{\partial z'} - \frac{\partial\theta_s}{\partial z'} - \left[(1-\gamma)\frac{h'}{2}(\theta_s - \theta_f)z'\right] - \frac{z'}{H'^2} \quad (3.48)$$

3.4.6 Numerical procedure

The pressure-based solver of ANSYS FLUENT is used for obtaining solution of the aforementioned dimensionless governing equations (Eqs. 3.28 – 3.36). Numerical schemes utilised in solving are listed in Table 3.7. A convergence criterion of all residuals below 10^{-8} is followed in this analysis. The entire analysis is carried out with a mesh comprising 17345 nodes and 16929 elements.

The LTNE approach requires the solution of the energy transport equation for the solid particles in addition to the mass, momentum and energy transport equations for the fluid phase. This is achieved by defining the solid temperature as a user-defined scalar (UDS) in ANSYS FLUENT and solving the associated energy transport equation using the UDS transport equation utility. Various terms of the energy transport equation are solved using appropriate user-defined function (UDF) modules. In addition to this, calculations for determining the interfacial heat transfer and the energy flux vectors are also achieved using various UDFs. Table 3.8 lists all the UDF modules utilised.

Table 3.7 Numerical schemes adopted for simulation

Parameter/Equation	**Numerical Scheme**
Pressure-Velocity Coupling	SIMPLE
Pressure	PRESTO
Momentum	QUICK
Energy	QUICK
UDS	QUICK

Table 3.8 UDF modules used for implementation of different terms in ANSYS FLUENT

Term Implemented	**UDF Module**
Interfacial heat transfer	DEFINE_SOURCE
Diffusive term in Eq. 3.27	DEFINE_DIFFUSIVITY
Energy flux vectors	DEFINE_ON_DEMAND

3.4.6.1 Model Validation

Results obtained using the LTNE model has been validated with the solution reported by Baytaş (2003) for a square enclosure with cold isothermal walls and fully filled with heat generating porous media. Figure 3.18 gives a comparison between the results obtained using the present model and that of Baytaş (2003) in terms of Nu_{avg} for both solid and fluid phases at the top wall for a wide range of h' with γ = 1.0, Ra = 10^7 and Da = 10^{-2}. The results indicate that the numerical solution obtained validates very well with the published results and as such, justifies the use of this numerical model for further study.

3.4.6.2 Grid-independence study

A grid-independence study has been carried out with different configurations of the computational domain in order to ensure that the solutions obtained are not influenced by the structure of computational domain, Table 3.9 lists the Nu_{avg} values for both cold walls of the enclosure with three different configurations. It can be seen that as the grid is refined beyond 17345 nodes, only a minor change takes place in Nu_{avg} for either cold wall of the enclosure. This configuration has, therefore, been utilised for performing further computations.

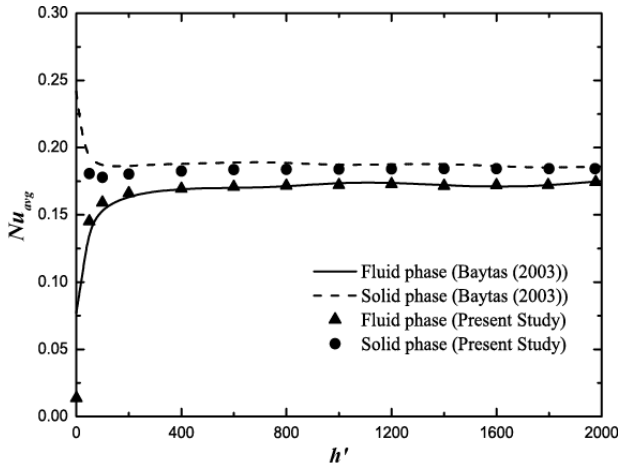

Figure 3.18 Comparison of present numerical model with the solution of Baytaş (2003) in terms of Nu_{avg} at top wall for fluid and solid phases with $Ra = 10^7$, $Da = 10^{-2}$, $\gamma = 1.0$

Table 3.9 Grid Independence study using Nu_{avg} at the side wall (top row) and top wall (bottom row) of the enclosure

Ra	***Da***	**Configuration (Number of Nodes)**		
		7802	**17345**	**30650**
10^7	10^{-7}	0.02289 (1.29%)	0.02314 (0.21%)	0.02319
		0.07807 (1.26%)	0.07895 (0.15%)	0.07907
10^{11}	10^{-7}	0.09671 (1.39%)	0.09789 (0.2%)	0.09808
		0.4341 (0.89%)	0.4376 (0.091%)	0.438

3.4.7 Results and Discussion

The LTNE approach of modelling heat transfer in porous media has been used in analysing the effects of bed heat generation and bed permeability on the associated fluid flow and heat transfer characteristics. The bed configuration ($H' = 0.5$, $R' = 0.25$, $\phi = 75°$) is considered to remain invariant in this analysis. In addition to streamlines and isotherms, energy flux vectors have also been used in this analysis to have a better interpretation of the results. Working fluid in this analysis has been considered to be liquid water at 300 K (corresponding $Pr = 5.83, k_f = 0.610572$ W/m.K). Thermal conductivity of the solid particles is assumed to be of the order of that in debris beds ($k_s = 2.0$ W/m.K).

3.4.7.1 Effect of bed heat generation

As in the analysis with the LTE approach, the effects of bed heat generation have been studied by carrying out parametric variations in terms of *Ra*. The results are

represented in Fig. 3.19. Heat generation within the solid particles leads to heat transfer from the solid particles to the fluid saturating the porous bed. This induces a buoyancy-driven natural convective fluid circulation in a counter-clockwise direction such that the heat generated within the porous bed is transferred to the cold enclosure walls. The energy flux vectors in Fig. 3.19 adequately highlights this heat transfer mechanism. In addition to this, heat transfer also occurs across the fluid-porous interfaces from the porous bed to the adjacent clear fluid region. The effective heat transfer is, thus, a balance between these two competing heat transfer mechanisms.

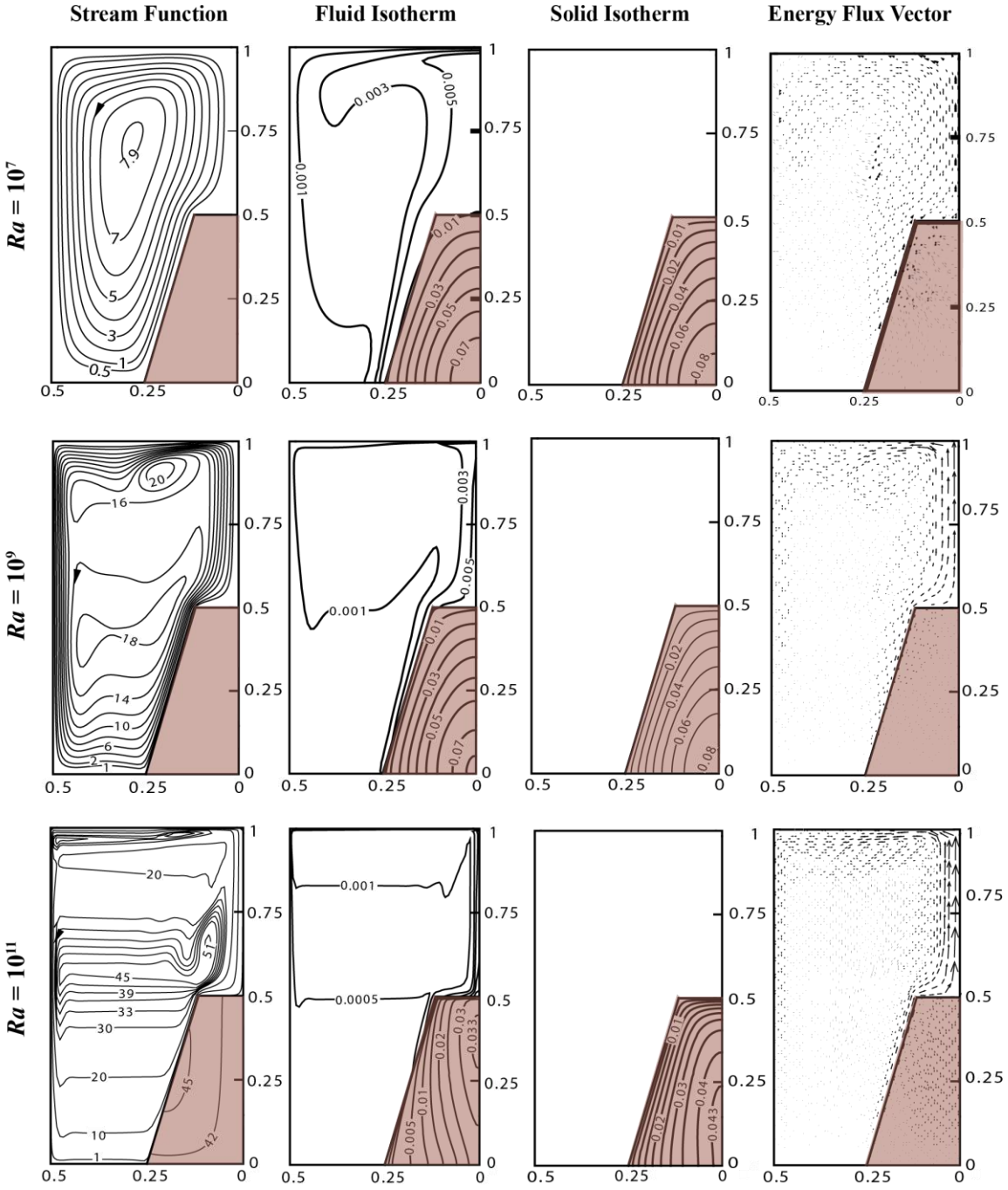

Figure 3.19 Streamline, Isotherm and Energy Flux Vector for various *Ra* at *Da* = 10^{-7}

Table 3.10 Global parameters of the enclosure for the range of study undertaken in terms of *Ra* and *Da*

Ra	***Da***	***RaDa***	$\|\psi\|_{max}$	$\theta_{f,max}$	$\theta_{s,max}$	$Nu_{avg,\ side}$	$Nu_{avg,\ top}$
10^7		1	7.9863	0.07804	0.08411	0.02314	0.07895
10^8		10	12.2602	0.07743	0.08348	0.030749	0.1023
10^9	10^{-7}	10^2	21.6068	0.07597	0.08209	0.03874	0.12258
10^{10}		10^3	34.4527	0.0618	0.06938	0.05239	0.16529
10^{11}		10^4	51.914	0.03359	0.043796	0.097895	0.4376
	10^{-6}	10^4	22.7519	0.02807	0.06069	0.060996	0.3223
	10^{-7}	10^3	34.4527	0.0618	0.06938	0.05239	0.16529
10^{10}	10^{-8}	10^2	40.609	0.07915	0.08107	0.049	0.1426
	10^{-9}	10	41.7287	0.0812	0.0818	0.04904	0.13937
	10^{-10}	1	42.5094	0.08162	0.0818	0.04766	0.1314

A larger magnitude of *Ra* is associated with greater volumetric heat generation rate for a given bed geometry, resulting in a higher ΔT_{ref} and thereby, induces a stronger convective motion within the porous bed as well as the enclosure. This is clearly evident from the progressively increasing magnitude of $|\psi|_{max}$ with *Ra*, as shown in Table 3.10. Strengthening of convection leads to enhancement in energy transfer within the enclosure which in turn, causes a greater heat transfer at the cold walls. Visual observation of the energy flux vectors for various *Ra* corroborates this enhancement of energy transfer with increase in heat generation. The magnitudes of Nu_{avg} at the cold walls reflect the increase in heat transfer.

Similar to that observed with the LTE approach, the dimensionless temperatures ($\theta_{s,max}, \theta_{f,max}$) have a decreasing trend with increase in *Ra* although greater bed heat generation must result in higher temperatures for both solid and fluid phases. Scaling of the dimensional temperature results in the dimensionless temperature (θ) being determined by the relative magnitude of the dimensional temperature with respect to ΔT_{ref}. Thus, although the dimensional temperature of both phases are higher at a higher *Ra*, the simultaneous increase in ΔT_{ref} effectively results in a reduced value of both $\theta_{s,max}$ and $\theta_{f,max}$. However, in contrast to that seen with the LTE approach, the magnitude of Nu_{avg} continues to increase with increase in *Ra*. This signifies that the heat transfer rate is large enough to offset the effect of reduced scaled temperature.

A comparison of the energy flux vectors for different *Ra* further reveals an interesting aspect of the heat transfer mechanism from the porous bed. At a low heat generation rate (corresponding to $Ra = 10^7$), heat transfer from the porous bed mainly takes place across the fluid-porous interface to the adjacent clear fluid region and

subsequently, by convection to the cold walls. Convection within the porous bed is very weak and has a minor contribution to the overall heat transfer. This lack of convection within the bed is also reflected by the overlapping solid and fluid isotherms in Fig. 3.19. A rise in heat generation (corresponding to $Ra = 10^9$) results in a greater contribution from convective heat transfer within the porous bed towards the overall heat transfer and it becomes comparable to heat transfer across the fluid-porous interface at a still higher heat generation (corresponding to $Ra = 10^{11}$). The corresponding fluid and solid isotherms in Fig. 3.19 also reflect this effect. Dimensionless axial velocity profiles along the radial direction in Fig. 3.20 at $z' = 0.25$ (i.e. within the porous bed) further corroborates the above observations.

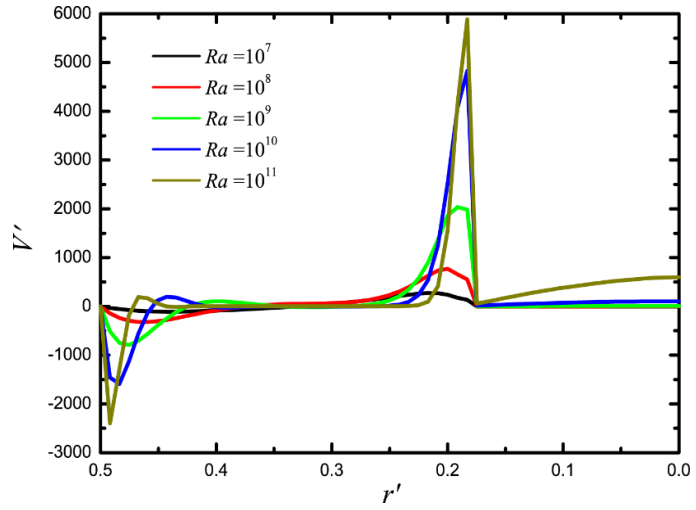

Figure 3.20 Dimensionless axial velocity profile along radial direction at $z' = 0.25$ for various Ra at $Da = 10^{-7}$

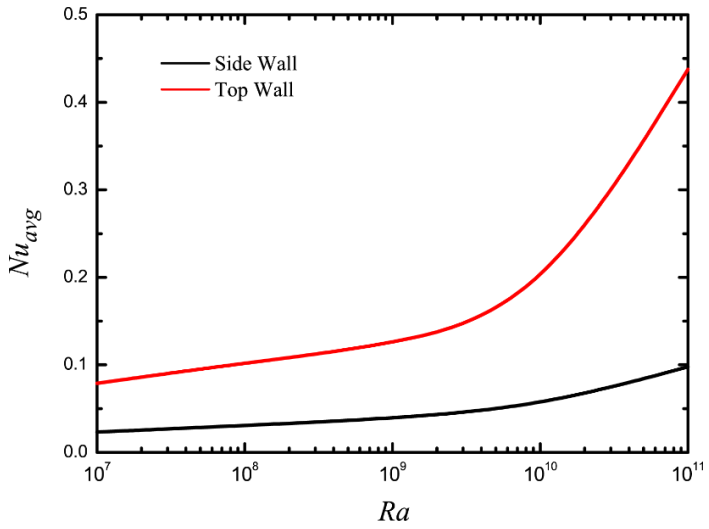

Figure 3.21 Variation of Nu_{avg} for top wall and side wall with Ra at $Da = 10^{-7}$

Although greater heat transfer takes place at the cold walls at higher heat generation rates i.e. at higher Ra, the variation in Nu_{avg} for either wall is not linear as can be seen from Fig. 3.21. The increase in heat transfer is relatively higher at larger magnitudes of

Ra for either wall. It is also observed that the increase in Nu_{avg} for the top wall is comparatively larger than that for the side wall. This is expected since natural convection drives the fluid in a counter-clockwise circulation such that maximum heat transfer takes place at the top wall and only the residual energy is transferred at the side wall. This also accounts for the wide difference evident between the Nu_{avg}values of the top and side walls.

3.4.7.2 Effect of bed permeability

A change in Darcy number (*Da*) essentially represents modification of fluid flow passage i.e. permeability in a porous medium. A reduction in *Da* indicates greater resistance to fluid flow and hence, lower velocity and vice-versa. Similar to that observed in the study using the LTE approach, a smaller value of *Da* for a certain *Ra* reduces convection induced fluid motion within the porous bed and vice-versa. This is corroborated by the axial velocity profiles for various *Da* as shown in Fig. 3.22.

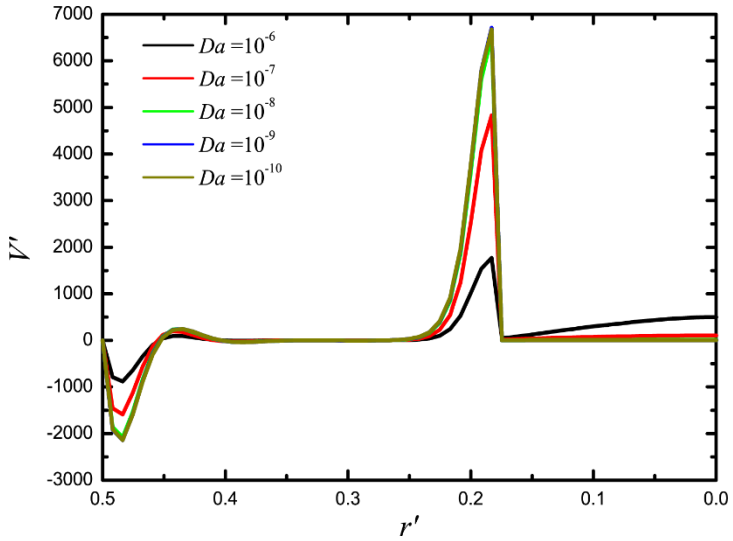

Figure 3.22 Dimensionless axial velocity profile along radial direction at $z' = 0.25$ for various *Da* at $Ra = 10^{10}$

Stream function, isotherm and energy flux vectors for three different *Da* (10^{-6}, 10^{-8}, 10^{-10}) at $Ra = 10^{10}$ are represented in Fig. 3.23. Greater bed permeability at a higher *Da* allows significant convective fluid motion to take place within the porous bed and hence, the dominant heat transfer mechanism from the bed is by convection of the saturating fluid. A decrease in bed permeability i.e. reduction in *Da* retards fluid motion within the bed and thereby, reduces the contribution of convective heat transfer from the bed towards overall heat transfer. The enthalpy content of the porous bed remains high as a result of this and as a consequence, the corresponding heat transfer across the fluid-porous interface increases. A comparison of energy flux vectors in Fig. 3.23 adequately highlights this effect. Greater heat transfer leads to a higher fluid velocity along the interface and thus, successively greater velocity jumps are observed at the fluid-porous interface as *Da* is reduced in Fig. 3.22.

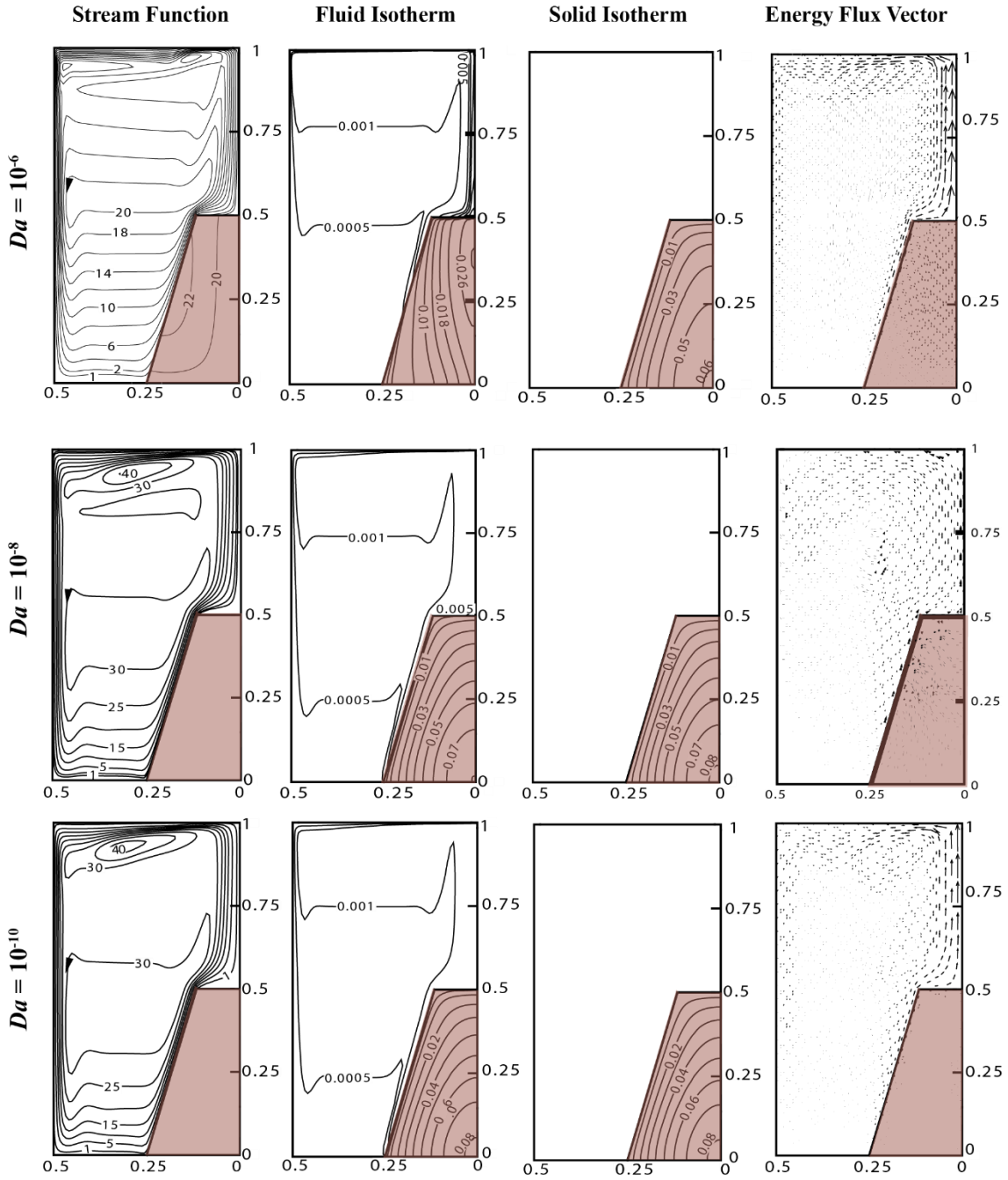

Figure 3.23 Streamline, Isotherm and Energy Flux Vectors for various *Da* at *Ra* = 10^{10}

The net effect of reduced convective heat transfer from the bed is greater enthalpy content and hence, higher temperature within the porous bed. The temperature rise within the bed is significantly higher at low *Da* as can be observed from the magnitude of $\theta_{s,max}$ and $\theta_{f,max}$ in Table 3.10. Heat transfer at the cold walls also reduce as *Da* is progressively reduced. This is represented in terms of Nu_{avg} at the cold walls for a given *Ra* in Fig. 3.24. It can be observed that the variation in Nu_{avg} with *Da* at a fixed *Ra* is similar to the variation of Nu_{avg} with *Ra* for a given *Da* in Fig. 3.21.

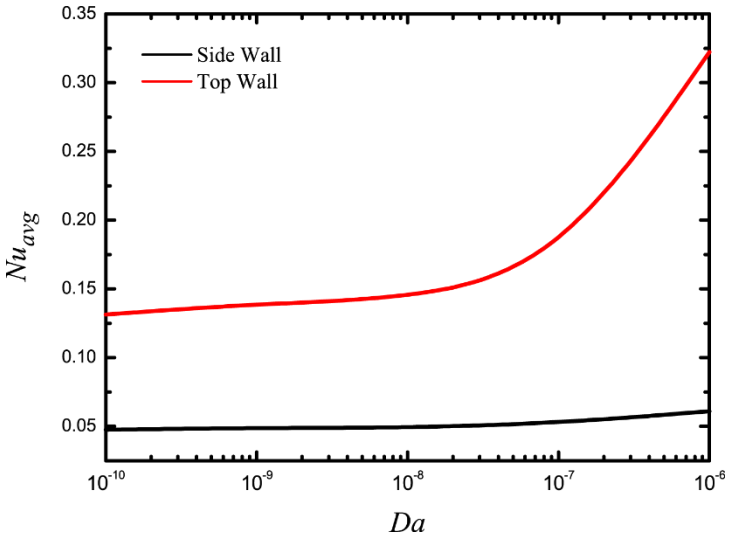

Figure 3.24 Variation of Nu_{avg} for top wall and side wall with Da at $Ra = 10^{10}$

3.5 Conclusions

The problem of natural convective heat removal from a heat-generating porous bed has been analysed in this chapter in a dimensionless manner following the local thermal equilibrium (LTE) as well as the local thermal non-equilibrium (LTNE) approach. Phase change of the working fluid has not been considered in this analysis. The impacts of bed permeability, bed heat generation, thermal conductivity ratio, bed configuration and bed stratification have been investigated in this analysis.

The following major conclusions could be drawn from the aforementioned analyses –

a. A counter-clockwise buoyancy-driven fluid circulation is observed to be established within the enclosure which transfers the heat generated within the bed to the cold enclosure walls.

b. It is observed that the convective fluid flow and heat transfer within the enclosure is mainly governed by bed heat generation and bed permeability. In addition, available fluid flow passage around the bed (as determined by the bed configuration) and the thermal conductivity ratio also have a substantial effect on the natural convective heat transfer mechanism.

c. The reference temperature adopted (ΔT_{ref}) significantly affects the scaled temperature (θ) and the wall heat transfer characterisation (in terms of Nu_{avg}). Hence, proper care must be taken while interpreting the results in a dimensionless form.

d. The dominant mode of heat transfer from the porous bed to the fluid region is dependent on the associated heat generation rate as well as bed permeability. At a constant heat generation, convective heat transfer dominates in a highly permeable bed while conductive heat transfer is observed to have the major contribution when permeability decreases. At a certain bed permeability, increase in heat generation strengthens the convective flow and vice-versa. This change is observed to happen at a specific bed permeability for a given bed heat generation and is characterised in

terms of *RaDa*. In the LTE approach, the critical magnitude of *RaDa* corresponding to this change in dominant mode of heat transfer is observed to be 10^3 for *Ra* <= 10^8 and 10^4 for *Ra* > 10^8. In the LTNE approach, the critical magnitude is observed to be 100. The dominancy of convective heat transfer from the porous bed is also reflected by the rapid increase of Nu_{avg} beyond *RaDa* = 100 in Figs. 3.21 and 3.24.

e. The impact of bed stratification is limited only to the extent that the heat transfer characteristics is determined by the dominant porous zone within the bed.

f. In the LTNE approach, it can be seen that for *RaDa* < 100, the magnitude of $\theta_{s,max}$ tends to that of $\theta_{f,max}$, and the respective isotherms almost overlap each other. A significant difference however, is evident at higher values of *RaDa*. Hence, it can be concluded that the LTE model of energy equation may be applied to problems with *RaDa* < 100 (i.e. conductive regime), while it must definitely not be used for problems involving *RaDa* > 100 (i.e. convective regime).

Chapter 4

SINGLE PHASE MIXED CONVECTION IN AN ENCLOSURE CONTAINING A HEAT-GENERATING, BOTTOM-FLOODED POROUS DEBRIS BED

This chapter reports the findings of the numerical analysis that has been carried out for characterising the mechanism of heat removal from a heat-generating porous debris bed under the influence of forced coolant injection from the bottom of the bed. Phase change of the working fluid has not been considered in this analysis. The local thermal equilibrium (LTE) approach as well as the local thermal non-equilibrium (LTNE) approach has been utilised to analyse the problem in a dimensionless form. In addition, a comparative assessment of the two approaches has also been made.

Section 4.1 briefly reviews the existing studies on heat-generating porous media in such situations. *Section 4.2* gives a description of the problem that has been considered for analysis and the modelling assumptions made. *Section 4.3* and *Section 4.4* details the modelling approaches and the observations made using the local thermal equilibrium (LTE) and the local thermal non-equilibrium (LTNE) approaches, respectively. *Section 4.5* summarises the observations from these analyses.

4.1 Literature review and Objectives

The motivation for this analysis is derived from the application of coolant flooding from the bottom of a debris bed, as a supplementary method to top-flooding, in ensuring debris bed coolability in post-accident situations (see *Chapter 1*). The forced coolant injection, coupled with the effects of buoyancy induced due to heat generation within the solid particles of the porous bed, creates a mixed convective flow situation within the domain. Mixed convective flow involving heat-generating porous media is also encountered in several other natural as well as industrial processes. Significant applications among these include extraction of geothermal energy, convection within the earth's mantle, electronic chip cooling, storage of spent fuel of nuclear power plants etc.

Several studies have been carried out over the years which characterise mixed convection involving porous media for different geometries using the local thermal equilibrium (LTE) approximation. Al-Amiri (2000) highlighted the effect of the quadratic drag term on fluid flow and associated heat transfer characteristics in a non-Darcian porous medium. Khanafer and Vafai (2002) also adopted a non-Darcian porous medium for analysing double diffusive mixed convection. Santosh Kumar et al. (2009) compared the numerical predictions using the Brinkmann-extended Darcy model and Brinkmann-Forchheimer-Darcy model in a double lid-driven cavity, with the vertical walls maintained at different temperatures and moving in opposite directions. The impact of non-uniform heating over uniform heating was assessed by Basak et al. (2010) in a lid-driven square cavity, filled with a Darcian porous medium, having differentially heated vertical walls and a heated bottom wall. Basak et al. (2011) utilised heatlines to analyse

the impact of various thermal boundary conditions on mixed convective flow in a lid-driven porous square cavity. Mixed convection in a vented enclosure filled with porous medium was studied by Mahmud and Pop (2006). They concluded that dimensions of the enclosure have a significant impact on the fluid flow patterns and thereby, heat transfer in the enclosure. Shuja et al. (2009) assessed the effect of the presence of porous blocks in a vented enclosure. Krishna Murthy and Ratish Kumar (2010) reported the effects of non-uniform heating in a vented square enclosure filled with a non-Darcian porous medium. The effect of multiple suction/injection was analysed by Ratish Kumar and Krishna Murthy (2010). Moraga et al. (2010) assessed the effects of the presence of multiple distinct porous layers in their study on mixed convection in a vented square enclosure. Several other researchers have also investigated mixed convection in porous channels (Umavathi et al. 2005; Bera and Khalili 2006; Guerroudj and Kahalerras 2010).

Saeid (2004) performed an analysis on mixed convection in a vertical porous layer using the local thermal non-equilibrium (LTNE) approach considering aiding as well as opposing nature of the externally imposed flow and the buoyancy-driven flow. Khandelwal and Bera (2012) adopted a similar configuration in their analysis albeit with linearly heated channel walls. Only aiding flow was considered in their study. An annular vertical cylinder, filled with porous media, was the subject of study by Salman Ahmed et al. (2011). They reported on the effect of different parameters on the enhancement or retardation of the heat transfer rate at the cold wall. Studies have also been carried out on jet impingement cooling in porous layers using the LTNE approach, as reported by Buonomo et al. (2016) and Wong and Saeid (2009) among several others.

In contrast to the aforementioned works, there is a dearth of substantial research on mixed convection involving heat-generating porous media. Only limited studies have been reported using the LTE approach while studies using the LTNE approach are non-existent. Khanafer and Chamkha (1999) analysed a laminar mixed convective flow situation in a lid-driven square cavity filled with a fluid-saturated Darcian porous medium following the LTE approach. The horizontal and the vertical walls were assumed to be differentially heated and adiabatic, respectively. They concluded that the flow mechanism and as such, the heat transfer characteristics are strongly dependent on the Richardson number (Ri) and the Darcy number (Da). Internal heat generation was observed to significantly affect the isotherm distribution within the domain, although the fluid flow mechanism remained almost unaffected. The analysis of Kumari and Nath (2011) using a similar geometry also highlighted Ri and Da as the pertinent parameters affecting mixed convection. Muthtamilselvan et al. (2010) considered a double lid-driven cavity filled with heat-generating porous media in their analysis. The horizontal walls were assumed to be differentially heated and moving in opposing directions, while the vertical walls were assumed to be stationary as well as adiabatic. They reported that the heat transfer mode switches from conduction to convection for $Da > 10^{-3}$ and also observed the heat transfer rate to decrease at a fixed Da for internal $Ra > 10^{2}$. These observations were found to be valid in case of uniform as well as non-uniform heating of the hot wall. Results from an analysis on mixed convection in a heat-generating porous annulus, by Khanafer and Chamkha (2003), indicate that in addition to Ri and Da, Reynolds number

(Re) and the annulus dimensions also play a significant role in determining the fluid flow mechanism and heat transfer within the annulus. Umavathi and Sultana (2013) reported on the effects of different dimensionless parameters on mixed convective flow in a vertical porous channel with boundary conditions of the third kind. Jha et al. (2016) analytically studied laminar mixed convective flow in a vertical tube filled with isotropic porous material considering heat generation/absorption.

A review of the above cited works will show that the problem of mixed convection in an enclosure with a heat-generating porous bed and cold fluid injection from the bottom of the bed has not been addressed yet, either with LTE or LTNE approaches. Therefore, an analysis is required to characterise the fluid flow and the associated heat transfer mechanism in such a situation. The analysis has been carried out using the LTE as well as the LTNE approaches and a comparative assessment has also been made between the predictions of the two models.

4.2 Problem statement

Figure 4.1 is a schematic representation of the geometric configuration considered for analysing mixed convective heat transfer. The corresponding dimensionless extents of the problem geometry are listed in Table 4.1.

The truncated conical porous bed is assumed to be placed centrally on the base of the cylindrical enclosure. All walls of the enclosure (except the bottom wall) are considered to be at an isothermal condition. Adiabatic condition is imposed on the bottom wall of the enclosure. The walls of the enclosure are assumed to be impermeable to fluid flow except at the inlet and outlet channels which allow complete fluid movement. Inlet channel of the enclosure is considered to be located mid-way on the bottom wall while the outlet channels are located at the top of the side walls.

Other important assumptions made in this study are summarised as follows –

1. The configuration of the porous debris bed within the enclosure is considered to be invariant in this analysis.
2. Steady incompressible fluid flow and heat transfer takes place in a 2D Cartesian co-ordinate system.
3. Fluid flow remains in the laminar regime.
4. Newtonian fluid is considered.
5. Barring density, which is modelled using Boussinesq approximation, all other thermos-physical properties are constant.
6. Porous medium is fluid saturated and is homogeneous as well as isotropic.
7. Heat generation is uniform and does not cause phase change of the working fluid.
8. The solid particles comprising the porous media are perfectly spherical i.e. $\psi = 1$ in the expression for permeability (Eq. 2.64).

Properties of the porous material are considered based on the reported experimental data for debris beds in this regard (see *Chapter 1*). Porosity of the porous material is assumed to be 0.4 (Schmidt 2004) while the dimensionless parameter characterising permeability is assumed such that it is in accordance with the reported permeability for

debris beds (see *Chapter 1*). Liquid water at 300 K (corresponding *Pr* = 5.83) is selected as the working fluid in this study.

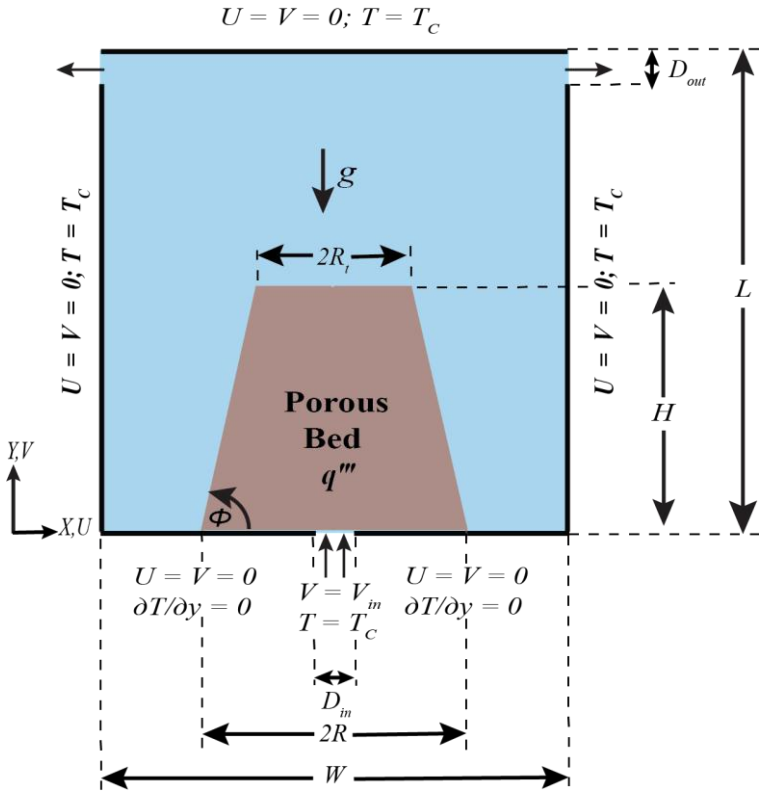

Figure 4.1 Schematic representation of the configuration assumed for analysing mixed convective heat transfer

Table 4.1 Dimensionless extent of the problem geometry

Geometric parameter	Dimensionless extent
L'	1.0
W'	0.5
H'	0.5
R'	0.25
R_t'	0.1339
ϕ	75°
D_{in}'	0.05
D_{out}'	0.1

4.3 Local Thermal Equilibrium (LTE) approach

4.3.1 Governing equations

The governing equations for the clear fluid region and the heat-generating porous bed are derived, in terms of extrinsic average velocity, from the generalised transport equations formulated in *Chapter 2* taking into account the above stated assumptions. It is further assumed that the component phases of the porous medium are in thermal

equilibrium with each other. The mass, momentum and energy transport equations for the clear fluid region are derived from Eqs. 2.23, 2.36 and 2.49, respectively, while that for the porous bed are derived from Eqs. 2.54, 2.61 and 2.69, respectively. These are stated below –

Clear Fluid Region:

$$\nabla.\left(\rho_f\langle \boldsymbol{V}_f\rangle\right) = 0 \tag{4.1}$$

$$\nabla.\left(\rho_f\langle \boldsymbol{V}_f\rangle\langle \boldsymbol{V}_f\rangle\right) = -\nabla p + \mu_f\nabla^2\langle \boldsymbol{V}_f\rangle + \rho_f \boldsymbol{g}\beta\Delta T \tag{4.2}$$

$$\rho_f c_{p,f}\langle \boldsymbol{V}_f\rangle\nabla.T = k_f\nabla^2 T \tag{4.3}$$

Porous Region:

$$\nabla.\left(\rho_f\langle \boldsymbol{V}_f\rangle\right) = 0 \tag{4.4}$$

$$\frac{1}{\varepsilon_f}\nabla.\left(\frac{\rho_f\langle \boldsymbol{V}_f\rangle\langle \boldsymbol{V}_f\rangle}{\varepsilon_f}\right) = -\nabla p + \frac{\mu_f}{\varepsilon_f}\nabla^2\langle \boldsymbol{V}_f\rangle - \left(\frac{\mu_f}{\boldsymbol{K}}\langle \boldsymbol{V}_f\rangle + \frac{\rho_f}{\eta}\left|\langle \boldsymbol{V}_f\rangle\right|\langle \boldsymbol{V}_f\rangle\right) + \rho_f \boldsymbol{g}\beta\Delta T \tag{4.5}$$

$$\left(\rho c_p\right)_{eff}\langle \boldsymbol{V}_f\rangle\nabla.T = k_{eff}\nabla^2 T + {q_{eff}}''' \tag{4.6}$$

The dimensional equations stated above are converted into a dimensionless form by appropriate choice of the following dimensionless parameters –

$$X' = \frac{X}{L}, Y' = \frac{Y}{L}, H' = \frac{H}{L}, R' = \frac{R}{L}, \alpha_f = \frac{k_f}{\rho_f c_{p,f}}, \alpha_{eff} = \frac{k_{eff}}{\left(\rho c_p\right)_{eff}}, U' = \frac{U}{V_{in}}, V' = \frac{V}{V_{in}},$$

$$p' = \frac{p}{\rho_f {V_{in}}^2}, Pr = \frac{\nu_f}{\alpha_f}, Da = \frac{K}{L^2}, F_c = \frac{1.75}{\sqrt{150}}, \theta = \frac{T - T_c}{\Delta T_{ref}}, \Delta T_{ref} = \frac{{q_{eff}}''' H^2}{2k_{eff}},$$

$$\lambda = \frac{\alpha_{eff}}{\alpha_f}, Gr = \frac{g\beta\Delta T_{ref} H^3}{{\nu_f}^2}, Re = \frac{V_{in} L}{\nu_f}, Ri = \frac{Gr}{Re^2} \tag{4.7}$$

The dimensionless equations thus obtained are stated below. It should be noted that the symbol for averaged quantities and vectors are not used in Eq. 4.7 and the subsequent equations for simplification of notations.

Clear Fluid Region:

$$\frac{\partial U'}{\partial X'} + \frac{\partial V'}{\partial Y'} = 0 \tag{4.8}$$

$$U'\frac{\partial U'}{\partial X'} + V'\frac{\partial U'}{\partial Y'} = -\frac{\partial p'}{\partial X'} + \frac{1}{Re}\left[\frac{\partial^2 U'}{\partial {X'}^2} + \frac{\partial^2 U'}{\partial {Y'}^2}\right] \tag{4.9}$$

$$U'\frac{\partial V'}{\partial X'} + V'\frac{\partial V'}{\partial Y'} = -\frac{\partial p'}{\partial Y'} + \frac{1}{Re}\left[\frac{\partial^2 V'}{\partial {X'}^2} + \frac{\partial^2 V'}{\partial {Y'}^2}\right] + \frac{Ri}{H'^3}\theta \tag{4.10}$$

$$U'\frac{\partial \theta}{\partial X'} + V'\frac{\partial \theta}{\partial Y'} = \frac{1}{RePr}\left(\frac{\partial^2 \theta}{\partial {X'}^2} + \frac{\partial^2 \theta}{\partial {Y'}^2}\right) \tag{4.11}$$

Porous Region:

$$\frac{\partial U'}{\partial X'} + \frac{\partial V'}{\partial Y'} = 0 \tag{4.12}$$

$$\frac{1}{{\varepsilon_f}^2}\left(U'\frac{\partial U'}{\partial X'} + V'\frac{\partial U'}{\partial Y'}\right) = -\frac{\partial p'}{\partial X'} + \frac{1}{\varepsilon_f Re}\left[\frac{\partial^2 U'}{\partial {X'}^2} + \frac{\partial^2 U'}{\partial {Y'}^2}\right] - \frac{1}{ReDaH'^2}U' - \frac{F_c}{\sqrt{Da}H'{\varepsilon_f}^{3/2}}|U'|U' \tag{4.13}$$

$$\frac{1}{{\varepsilon_f}^2}\left(U'\frac{\partial V'}{\partial X'} + V'\frac{\partial V'}{\partial Y'}\right) = -\frac{\partial p'}{\partial Y'} + \frac{1}{\varepsilon_f Re}\left[\frac{\partial^2 V'}{\partial {X'}^2} + \frac{\partial^2 V'}{\partial {Y'}^2}\right] - \frac{1}{ReDaH'^2}V' - \frac{F_c}{\sqrt{Da}H'{\varepsilon_f}^{3/2}}|V'|V' + \frac{Ri}{H'^3}\theta \tag{4.14}$$

$$U'\frac{\partial \theta}{\partial X'} + V'\frac{\partial \theta}{\partial Y'} = \frac{\lambda}{RePr}\left(\frac{\partial^2 \theta}{\partial {X'}^2} + \frac{\partial^2 \theta}{\partial {Y'}^2}\right) + \frac{\lambda}{RePrH'^2} \tag{4.15}$$

4.3.2 Boundary conditions and Interfacial conditions

The associated boundary conditions in dimensionless form are expressed as follows –

$$U' = V' = 0, \theta = 0 \; at \; X' = 0{,}1 \; and \; 0 < Y' \leq 0.9\,,$$
$$U' = V' = 0, \theta = 0 \; at \; Y' = 1 \; and \; 0 < X' \leq 1\,,$$
$$U' = V' = 0, \frac{\partial \theta}{\partial Y'} = 0 \; at \; Y' = 0 \; and \; 0 < X' \leq 0.475, 0.525 < X' \leq 1\,,$$
$$U' = 0, V' = 1, \theta = 0 \; at \; Y' = 0 \; and \; 0.475 < X' \leq 0.525\,,$$
$$p' = 0, \frac{\partial \theta}{\partial X'} = 0 \; at \; X' = 0{,}1 \; and \; 0.9 < Y' \leq 1\,. \tag{4.16}$$

In addition to the above stated boundary conditions, it is also necessary to properly model the interface conditions at the porous-fluid interface. This is done by ensuring a continuity of variables and fluxes at the interface. These are stated as follows –

$$U'|_f = U'|_p \; and \; \frac{1}{Re}\left(\frac{\partial^2 U'}{\partial {X'}^2} + \frac{\partial^2 U'}{\partial {Y'}^2}\right)\Bigg|_f = \frac{1}{\varepsilon_f Re}\left(\frac{\partial^2 U'}{\partial {X'}^2} + \frac{\partial^2 U'}{\partial {Y'}^2}\right)\Bigg|_p$$

$$V'|_f = V'|_p \; and \; \frac{1}{Re}\left(\frac{\partial^2 V'}{\partial {X'}^2} + \frac{\partial^2 V'}{\partial {Y'}^2}\right)\Bigg|_f = \frac{1}{\varepsilon_f Re}\left(\frac{\partial^2 V'}{\partial {X'}^2} + \frac{\partial^2 V'}{\partial {Y'}^2}\right)\Bigg|_p$$

$$\theta|_f = \theta|_p and \; \left(\frac{\partial^2 \theta}{\partial {X'}^2} + \frac{\partial^2 \theta}{\partial {Y'}^2}\right)\Bigg|_f = \frac{\lambda}{RePr}\left(\frac{\partial^2 \theta}{\partial {X'}^2} + \frac{\partial^2 \theta}{\partial {Y'}^2}\right)\Bigg|_p \tag{4.17}$$

4.3.3 Wall heat transfer assessment

Heat transfer by means of mixed convection is assessed in terms of the dimensionless Nusselt number (Nu) at the cold enclosure walls. This is estimated as follows –

$$Nu = \begin{cases} -\dfrac{\partial\theta}{\partial X'}, & \text{for side walls} \\ -\dfrac{\partial\theta}{\partial Y'}, & \text{for top wall} \end{cases} \tag{4.18}$$

$$Nu_{avg} = \begin{cases} \displaystyle\int_0^{L-D_{out}} NudY' \Big/ \int_0^{L-D_{out}} dY', & \text{for side walls} \\ \displaystyle\int_0^{W} NudX' \Big/ \int_0^{W} dX', & \text{for top wall} \end{cases} \tag{4.19}$$

4.3.4 Energy flux vectors

Energy transport within the enclosure is visualised with the help energy flux vectors (Hooman 2010) in a similar manner as the natural convective problem using the LTNE approach (*Section 3.4*). The individual components of the energy flux vector $\vec{E}$ are defined separately for the fluid and porous regions as follows –

Fluid Region:

$$\frac{\partial\Pi}{\partial Y'} = U'\theta - \frac{1}{RePr}\left(\frac{\partial\theta}{\partial X'}\right) \tag{4.20}$$

$$-\frac{\partial\Pi}{\partial X'} = V'\theta - \frac{1}{RePr}\left(\frac{\partial\theta}{\partial Y'}\right) \tag{4.21}$$

Porous Region:

$$\frac{\partial\Pi}{\partial Y'} = U'\theta - \frac{\lambda}{RePr}\left(\frac{\partial\theta}{\partial X'}\right) - \frac{\lambda}{RePr}\left(\frac{X'}{2H'^2}\right) \tag{4.22}$$

$$-\frac{\partial\Pi}{\partial X'} = V'\theta - \frac{\lambda}{RePr}\left(\frac{\partial\theta}{\partial Y'}\right) - \frac{\lambda}{RePr}\left(\frac{Y'}{2H'^2}\right) \tag{4.23}$$

The energy flux vector is obtained by combining the individual components as follows –

$$\vec{E} = \left(\frac{\partial\Pi}{\partial Y'}\right)\vec{\imath} - \left(\frac{\partial\Pi}{\partial X'}\right)\vec{\jmath} \tag{4.24}$$

4.3.5 Numerical procedure

The pressure-based solver of ANSYS FLUENT is used for obtaining solution of the aforementioned dimensionless governing equations (Eqs. 4.8 – 4.15). Numerical schemes utilised in solving are listed in Table 4.2. The energy flux vectors, defined in *Section 4.3.4*, are computed by post-processing of the results using user-defined function (UDFs) of ANSYS FLUENT. The DEFINE_ON_DEMAND module is specifically utilised in this

respect. A convergence criterion of all residuals below 10^{-8} is followed in this analysis. The entire analysis is carried out with a mesh comprising 10512 nodes.

Table 4.2 Numerical schemes adopted for simulation

Parameter	Numerical Scheme
Pressure-Velocity Coupling	SIMPLE
Pressure	PRESTO
Momentum	QUICK
Energy	QUICK

4.3.5.1 Model validation

Validation of the porous media LTE model has already been discussed in *Chapter 3* (*Section 3.3.4.1*) and hence, it is not repeated here for the sake of brevity. Nonetheless, it becomes necessary to validate the numerical model for mixed convective flow situations. However, no significant studies could be found on mixed convection involving heat-generating porous media with fluid inlet/outlet configurations. Hence, a comparative study has been carried out with Basak et al. (2010) for a porous lid-driven cavity with a moving adiabatic top wall. The side walls are considered to be linearly heated while the bottom wall is assumed to be hot. The comparison has been made in terms of Nu_{avg} of the heated bottom wall and the results obtained are plotted in Fig. 4.2. It can be concluded from the comparative study that the present model is able to satisfactorily model mixed convection in porous cavities and hence, justifies the use of this model for computation of mixed convective flow involving heat-generating porous media.

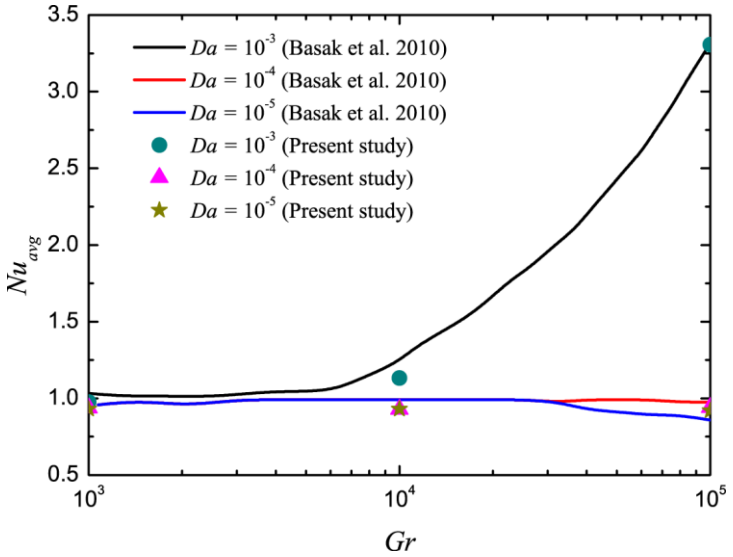

Figure 4.2 Comparison of the present numerical model with the solution of Basak et al. (2010) for different *Gr* and *Da* at *Re* = 10 and *Pr* = 10

4.3.5.2 Grid independence study

An assessment has been made for judging the accuracy of the numerical solution with regard to the effects of the computational domain. Table 4.3 summarises the values of Nu_{avg} at the cold walls of the enclosure for four different configurations of the

domain. As can be observed, the change in Nu_{avg} for each wall is minor as the mesh is refined beyond 10512 nodes. Therefore, this configuration (10512 nodes) has been utilised for performing further computations.

Table 4.3 Grid Independence Study using Nu_{avg} at the top wall (upper row), left wall (middle row) and right wall (lower row)

Ri	***Re***	***Gr***	***Da***	**Configuration (number of nodes)**			
				3874	**6765**	**10512**	**15090**
0.01	50	25	10^{-4}	0.23141 (1.89 %)	0.22967 (1.13 %)	0.22752 (0.18 %)	0.22710
				0.18785 (1.95 %)	0.18671 (1.33 %)	0.18499 (0.4 %)	0.18425
				0.18786 (1.95 %)	0.18671 (1.33 %)	0.18499 (0.4 %)	0.18425
100	500	2.5×10^7		0.15181 (1.95 %)	0.15099 (1.4 %)	0.14925 (0.22 %)	0.14891
				0.07981 (1.84 %)	0.07944 (1.37 %)	0.07894 (0.72 %)	0.07837
				0.07981 (1.84 %)	0.07944 (1.37 %)	0.07887 (0.72 %)	0.07837

4.3.6 Results and Discussions

Heat transfer characterisation for the system considered (see *Fig. 4.1*) requires analysing the effect of the pertinent parameters affecting the fluid flow and heat transfer within the enclosure. In this context, independent parametric studies have been carried out with respect to the two major parameters governing the heat transfer mechanism viz. Richardson number (*Ri*) and Darcy number (*Da*). *Ri* is considered to vary in the range of 0.01 to 100 while *Da* is varied in the range of 10^{-1} to 10^{-4}. The range of Richardson number is selected in order to analyse both the inertial flow as well as buoyancy dominated regimes. The range of *Da* is based on the reported values of bed permeability with coarse particles in porous debris beds (Chikhi et al. 2016). The corresponding ranges of Reynolds number (*Re*) and Grashof number (*Gr*) are 50 – 500 and 10^1 – 10^7, respectively. Consideration of *Gr* is governed by the objective of maintaining laminar flow in the enclosure as well as limiting the heat generation rate and thereby, the temperature rise to levels such that phase change of the working fluid does not occur. The maximum value of *Re* considered is based on the estimated liquid injection velocity (Chikhi et al. 2016) in porous debris beds. In addition, the thermal conductivity ratio is considered to be unity in this analysis.

Analysis of natural convective heat transfer from heat-generating porous beds (*Chapter 3*) have shown us that the fluid flow within the system is governed mainly by the combined effects of porous bed permeability and buoyancy-induced flow due to heat generation within the porous medium. Additional injection of cold fluid through the inlet channel located at the bottom of the porous bed significantly affects the flow

characteristics. These mechanisms, coupled with each other, transfers thermal energy from the heat-generating porous bed to the cold enclosure walls and towards the system outlet. It is observed that irrespective of the flow situation, fluid circulation is symmetric within the enclosure and heat transfer at the top wall significantly exceeds that at the side walls. The symmetric nature of flow is evident from the contours of stream function, isotherm and energy flux vector for various cases (Figs. 4.3, 4.7 and 4.8). This flow pattern also results in similar heat transfer characteristics at the right and the left walls which allows representation of the heat transfer characteristics at the side walls using only a single plot. Heat transfer characteristics at the cold walls can be comprehended by a comparison of Nu_{avg} between the top wall and the side walls for different situations. Another common feature observed is the location of the maximum temperature zone near the top of the bed and the adjoining fluid region. This occurs due to the effect of cold fluid injection from the bottom of the bed and is in stark contrast to that observed in natural convective situations (see *Chapter 3*) where maximum temperature is observed in the inner regions of the bed.

The relative dominancy of the buoyancy-induced flow and the inertia-driven flow mechanisms in the overall fluid flow within the enclosure is represented by the Richardson number (Ri) such that $Ri > 1$ indicates dominancy of buoyancy-induced flow while $Ri < 1$ indicates an inertia-driven flow. The effect of porous media on the flow field is characterised by the Darcy number (Da). An interesting outcome of non-dimensionalisation of the governing equations and the assumptions made is that the reference temperature difference adopted (ΔT_{ref}) scales directly with the Grashof number (Gr). An increase in Gr results in a larger magnitude of ΔT_{ref} and vice-versa. However, a larger Gr also means a greater heat generation which must contribute to a higher temperature rise. The magnitude of the scaled temperature (θ) is, thus, determined by the relative impact of the above mentioned factors.

With respect to the parametric studies, the following effects of the scaling parameters need to be kept in mind –

a. A change in Ri at a fixed Re results in a modification of Gr and hence, the temperature scale is also affected. On the other hand, if Gr is kept constant, then a change in *Ri* will induce a change in *Re* and hence, in the injection strength.
b. A change in Re keeping Ri constant also affects Gr and as such, affects the temperature scale.
c. Darcy number (Da), however, have no influence on the velocity and temperature scales.

4.3.6.1 Effect of Richardson number

The impact of Ri is assessed in the range of 0.01 to 100 such that the assessment spans both the inertia-dominated and buoyancy-dominated regimes. The effect of buoyancy is minimal on the flow field at low Ri (~0.01) and energy transfer in such situation is driven mainly by the inertial movement of the injected fluid. The impact of buoyancy becomes apparent and starts to dominate the flow mechanism when Ri is

progressively to 1 and beyond. This is easily recognisable from the streamline contours due to the formation of two symmetric rolls within the enclosure as Ri is gradually increased as opposed to flows at low Ri.

It is evident from the definition in Eq. 4.7 that Ri is further dependent on two different parameters i.e. Re and Gr. A parametric variation in Ri can, thus, be carried out by either keeping Re constant (with Gr varying) or by keeping Gr constant (with Re varying). Therefore, in order to comprehensively analyse the impact of Ri, the parametric study in Ri has been carried out following both these modes keeping Da constant at 10^{-4}.

4.3.6.1.1 Variation of Ri at fixed Re

Figure 4.3 represents the contour plots of streamline, isotherm and energy flux vectors for different Ri at Re = 50. The corresponding variation of Nu_{avg} with Ri at Da = 10^{-4} and different Re is shown in Fig. 4.4.

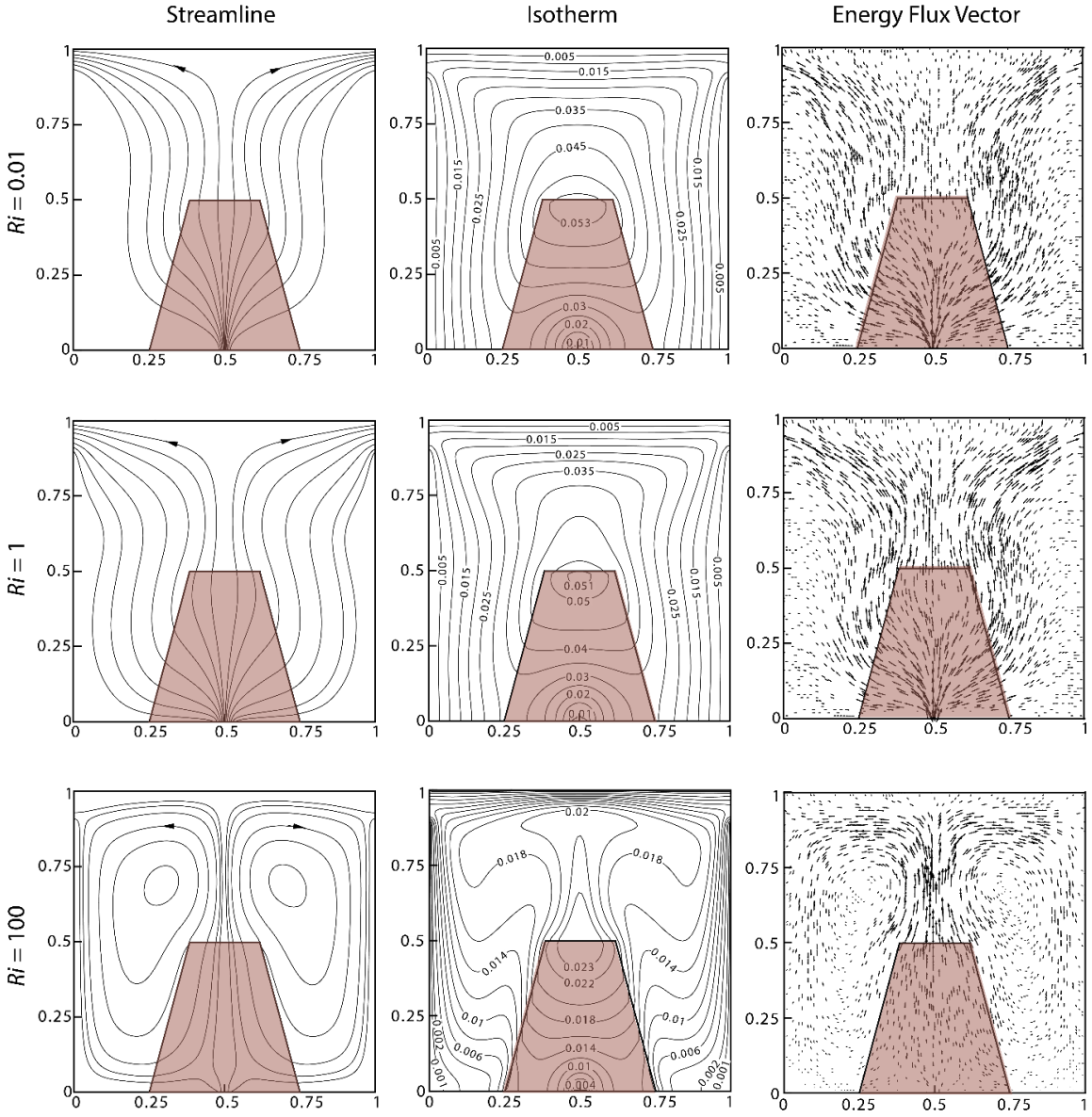

Figure 4.3 Streamline, Isotherms and Energy Flux Vectors for different Ri at Re = 50 and Da = 10^{-4}

Inertia-driven fluid flow at low Ri (~0.01) results in the injected cold fluid transferring the heat generated within the porous bed mainly to the cold top wall and towards the system outlet. The residual energy is transferred to the side walls. As such, Nu_{avg} is relatively larger for the top wall in comparison to the side walls. This characteristics of energy transfer is clearly evident from the corresponding energy flux vector shown in Fig. 4.3. A thinner thermal boundary layer is formed near the top wall as compared to the side walls in this situation (evident from the isotherm contour in Fig. 4.3) also highlights this effect.

A larger impact of buoyancy on the fluid flow mechanism at a higher magnitude of Ri aids the upward movement of the heated fluid from the porous bed such that greater heat transfer takes place at the top wall. This effect can be observed from the variation of Nu_{avg} in Fig. 4.4a. The corresponding heat transfer at the side walls, however, decrease as Ri is increased to 1, as shown in Fig. 4.4b. This is caused by a decrease in the residual energy content of the working fluid as a result of increased heat transfer at the top wall. The thermal boundary layers (as can be seen from the isotherm contours) near the top and side walls of the enclosure becomes thinner and thicker, respectively, with increase in Ri to 1 and thereby, corroborates the above explanation. Interestingly, the corresponding energy flux vectors as well as streamline contours reveal no significant change in the energy transport process.

Table 4.4 Comparison of ψ_{max} and θ_{max} as a function of *Ri* at three different *Re* with $Da = 10^{-4}$

Ri	Re	Gr	ψ_{max}	θ_{max}	$Gr.\theta_{max}$
0.01		2.5×10^1	0.07398	0.05395	1.34875
0.1		2.5×10^2	0.07391	0.05373	13.4325
1	50	2.5×10^3	0.07303	0.05119	127.975
10		2.5×10^4	0.08771	0.03766	941.5
100		2.5×10^5	0.1851	0.02389	5972.5
0.01		6.25×10^2	0.07396	0.01704	10.65
0.1		6.25×10^3	0.07375	0.01678	104.875
1	250	6.25×10^4	0.07163	0.01497	935.625
10		6.25×10^5	0.0699	0.01089	6806.25
100		6.25×10^6	0.10759	0.00773	48312.5
0.01		2.5×10^3	0.07389	0.01002	25.05
0.1		2.5×10^4	0.07365	0.00984	246
1	500	2.5×10^5	0.07148	0.00884	2210
10		2.5×10^6	0.0685	0.00629	15725
100		2.5×10^7	0.09766	0.00445	111250

The aiding effect of buoyancy becomes prominent at very high Ri (~100) such that a much thinner thermal boundary layer is formed near the top wall leading to greater heat

transfer. Simultaneously, convective cells are formed due to buoyancy which forces the relatively colder fluid in the upper region to circulate towards the bottom of the enclosure (as can be observed from the streamlines and the energy flux vectors) and thereby, increases heat transfer at the side walls as well. This can be corroborated by a comparison of the thermal boundary layers near the side walls at high Ri with those at lower Ri in Fig. 4.3.

Table 4.4 lists the global parameters obtained in different cases. It can be seen that as Ri is increased at a constant Re (i.e. corresponding Gr also increases), the maximum dimensionless bed temperature rise becomes lower. A higher Gr (i.e. higher heat generation rate), on the other hand, should lead to a higher bed temperature. This happens due to the effect of ΔT_{ref} on the temperature scale, as discussed previously. It should be noted that the dimensional temperature (which scales directly with $Gr.\theta$) actually rises since the temperature scale increases by a factor larger than that by which the dimensionless temperature falls. At the same time, it can be observed that the maximum temperature rise (indicated by $Gr.\theta_{max}$ in Table 4.4**)** does not increase in the same proportion at which the heat generation (i.e. Gr) increases. This shows the convective heat transfer mechanism to be an effective cooling method.

The characteristics change in Nu_{avg} with change in Ri is similar other Re as well. This can be clearly understood from Fig. 4.4. However, it can be also observed that the magnitude of Nu_{avg} decreases as Re is progressively increased. This is also an outcome of the effects of temperature scaling. As Re is increased at a fixed Ri, Gr also correspondingly increases and hence, the temperature scale is modified accordingly. The scaled temperature, therefore, goes down for the same dimensional temperature. This effect also gets reflected in the magnitude of Nu_{avg}.

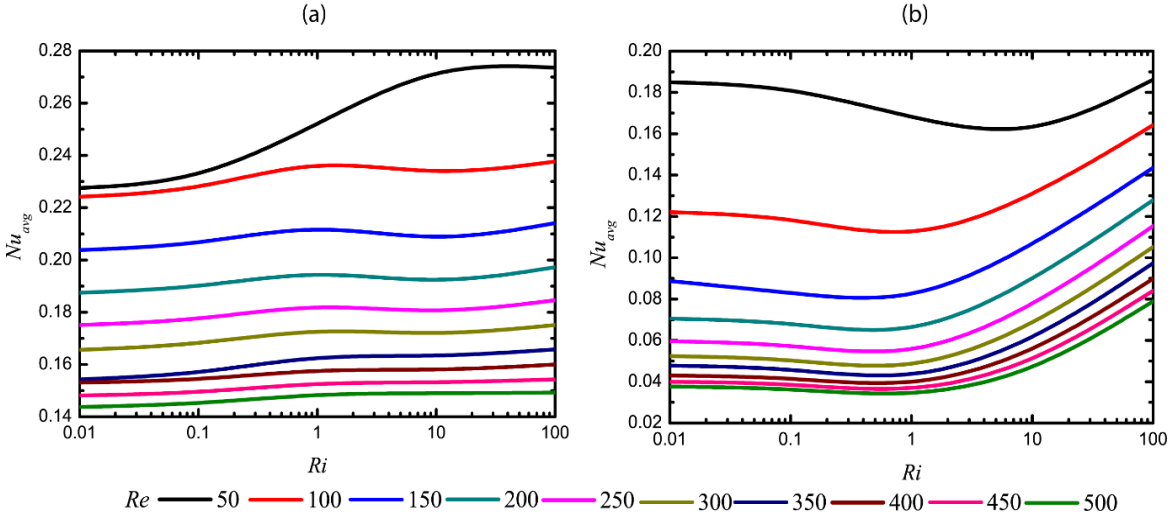

Figure 4.4 Nu_{avg} variation with Ri at different Re and Da = 10^{-4} at (a) top wall and (b) side walls

4.3.6.1.2 Variation of Ri at fixed Gr

In contrast to the parametric variation carried out in terms of Ri with Re at a constant value (*Section 4.3.6.1.1*), if Gr is kept constant while Ri is varied, the

temperature scale remains constant. This allows a more direct comparison of different situations with respect to bed temperature rise. This study is carried out at Gr = 10^5 for different Ri in the range of 0.01 to 100. Re gets modified accordingly.

A rise in Ri at a given Gr necessitates a decrease of *Re* i.e. the injection strength of the cold fluid is reduced. As such, a relatively weaker convection takes place within the heat-generating bed leading to a higher energy content and a consequent higher temperature rise is observed within the bed. This is evident from a comparison of the maximum bed temperature (θ_{max}) for various situations as listed in Table 4.5. This results in the establishment of a larger thermal gradient within the enclosure which, in turn, leads to a higher magnitude of Nu_{avg} as Ri becomes larger.

Table 4.5 Comparison of ψ_{max}, θ_{max} and Nu_{avg} as a function of Ri at a fixed *Gr* with *Da* = 10^{-4}

Ri	***Gr***	***Re***	$\boldsymbol{\psi_{max}}$	$\boldsymbol{\theta_{max}}$	$\boldsymbol{Nu_{avg}}$		
					Top Wall	**Left Wall**	**Right Wall**
0.01	10^5	3162.278	0.07431	0.00205	0.07274	0.01512	0.01513
0.1		1000	0.07415	0.00562	0.11562	0.02593	0.02593
1		316.278	0.07138	0.01251	0.17138	0.04215	0.04214
10		100	0.14101	0.01508	0.23767	0.16432	0.16404
100		31.6278	0.21387	0.03204	0.29038	0.18333	0.18226

4.3.6.2 Effect of Darcy number

The impact of Da has been studied between 10^{-1} and 10^{-4} for the entire range of Ri (0.01 – 100) and Re (50 – 500) considered in this study. Profiles of axial velocity and temperature for the various cases studies are shown at two locations within the enclosure in Figs. 4.5 and 4.6, respectively. The corresponding contours of streamline and isotherm as well as the energy flux vectors are represented in Figs. 4.7 and 4.8. Fig. 4.9 shows the variation of Nu_{avg} at the cold enclosure walls with change in Da.

Table 4.6 Comparison of ψ_{max} and θ_{max} with change in *Da* at different combinations of *Ri* and *Re*

Ri	***Re***	***Da***	$\boldsymbol{\psi_{max}}$	$\boldsymbol{\theta_{max}}$
0.01	50	10^{-1}	0.07491	0.04618
		10^{-4}	0.07398	0.05395
	500	10^{-1}	0.09783	0.00689
		10^{-4}	0.07389	0.01001
100	50	10^{-1}	0.2296	0.01992
		10^{-4}	0.18514	0.02388
	500	10^{-1}	0.11224	0.00414
		10^{-4}	0.09766	0.00445

It has been observed in *Chapter 3* that reduction of Da at a fixed heat generation rate weakens the fluid flow within the porous region. A similar outcome is observed in a mixed convective situation which can be inferred from a comparison of the velocity profiles in Fig. 4.5. At a high magnitude of Da, fluid flow within the bed is primarily confined to the central region due to the effect of fluid injection from the bottom. However, greater flow resistance as Da is reduced disturbs this flow pattern and leads to spreading of the injected fluid towards the peripheral region of the bed. This effect creates a bulge in the velocity profile in the aforementioned region for $Y' = 0.25$ and $Da = 10^{-4}$. A comparison of the corresponding streamline contour and energy flux vectors in Fig. 4.7 also corroborates this effect. Further, reduced fluid flow results in lesser heat removal from the porous bed and consequently, a relatively higher bed temperature is observed as Da is progressively reduced. A comparison of θ_{max} in Table 4.6 adequately highlights this effect.

However, significant differences are observed in the heat transfer characteristics at the walls as Da is varied depending on the magnitudes of Ri and Re. These are explained in the following sections for different combinations of Ri and Re.

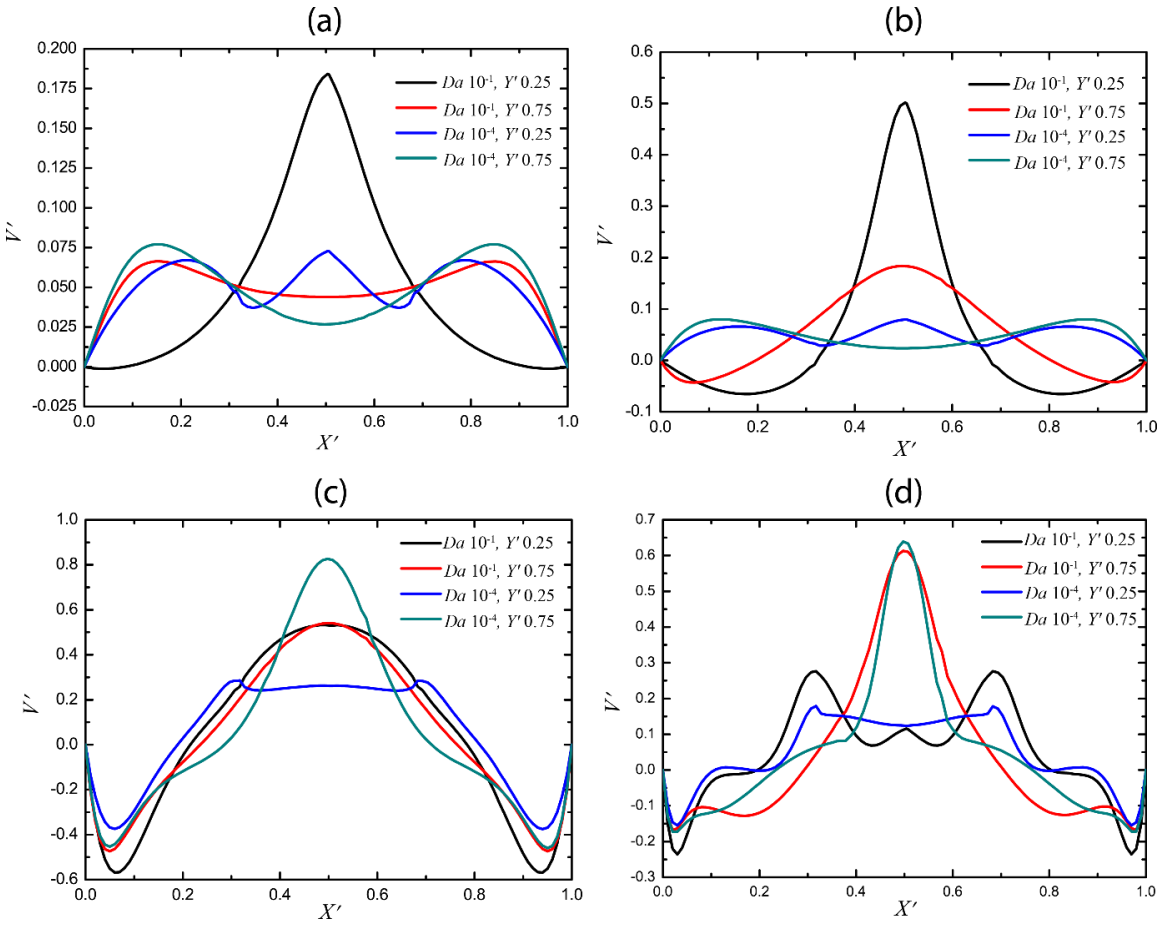

Figure 4.5 Dimensionless axial velocity profiles along the X direction at $Y' = 0.25$ and 0.75 for Da = 10^{-1} and 10^{-4} and (a) $Ri = 0.01$, $Re = 50$ (b) $Ri = 0.01$, $Re = 500$ (c) $Ri = 100$, $Re = 50$ (d) $Ri = 100$, $Re = 500$

4.3.6.2.1 Low Ri- Low Re situation

In a situation with low Ri and low Re, as Da is reduced, the lateral spreading of the injected fluid results in the heated fluid initially coming into contact with the lower region of the cold side walls. A thinner thermal boundary layer is established in the vicinity of the side walls as a result of this spreading and as a result, a larger amount of heat transfer takes place at the side walls. This is evident from Fig. 4.9. The thinning of the thermal boundary layer at the side walls can be observed from the temperature profiles at $Y' = 0.25$ in Fig. 4.6a as well as the corresponding isotherm contours in Fig. 4.7.

This rise in heat transfer at the side walls must be compensated by a reduction in heat transfer at the top wall since the heat generation remains invariant. This can be observed from the characteristics of Nu_{avg} at the top wall in Fig. 4.9. The corresponding thickening of the thermal boundary layer in the vicinity of the top wall is evident from the temperature profiles at $Y' = 0.75$ in Fig. 4.6a and the isotherm contours in Fig. 4.7.

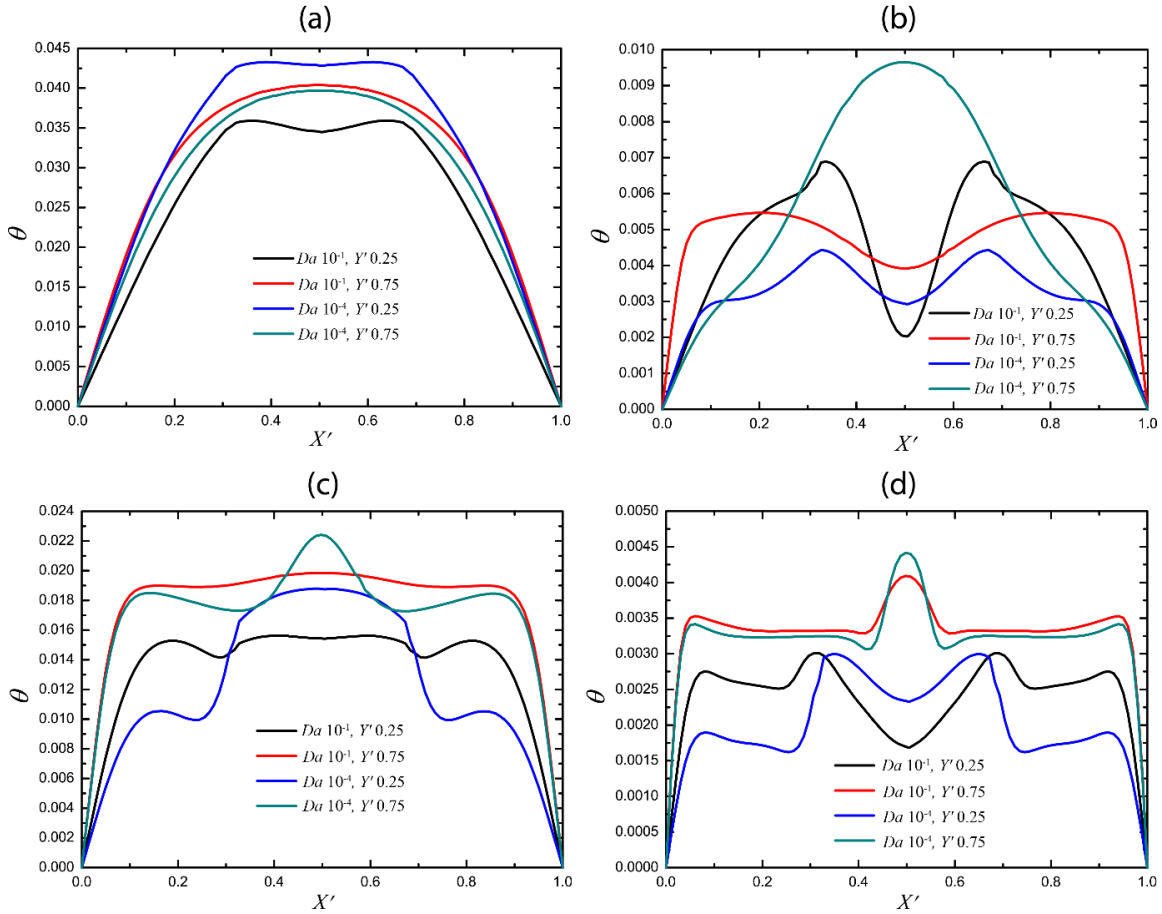

Figure 4.6 Dimensionless temperature profiles along the X direction at $Y' = 0.25$ and 0.75 for Da = 10^{-1} and 10^{-4} and (a) $Ri = 0.01$, $Re = 50$ (b) $Ri = 0.01$, $Re = 500$ (c) $Ri = 100$, $Re = 50$ (d) $Ri = 100$, $Re = 500$

4.3.6.2.2 Low Ri – High Re situation

The aforementioned spreading effect of the injected fluid towards the periphery of the porous bed is observed in low Ri – high Re situations as well. A comparison of

velocity profiles at $Y' = 0.25$ in Fig. 4.5b as well as the energy flux vectors in Fig. 4.7 highlights this effect.

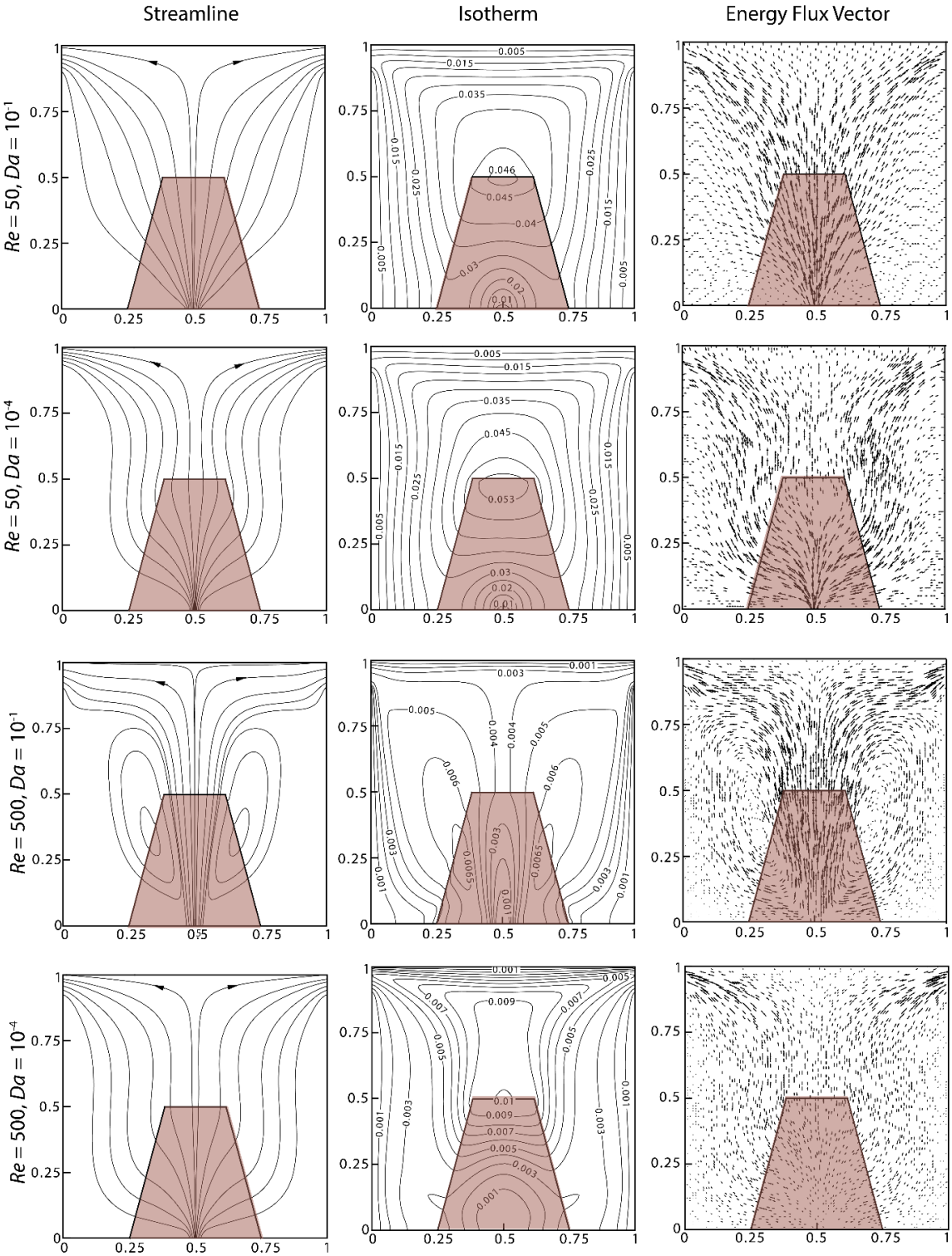

Figure 4.7 Streamline, Isotherms and Energy Flux Vectors for $Ri = 0.01$ and Re = 50, 500 at Da = 10^{-1}, 10^{-4}

However, in contrast to the heat transfer characteristics in low Ri – low Re situations, heat transfer at the top wall increases while that at the side walls decrease as

Da is reduced. This is evident from the variation of Nu_{avg} in Fig. 4.9. The corresponding change in the respective thermal boundary layers, as shown in Fig. 4.6b and Fig. 4.7, further corroborates this observation.

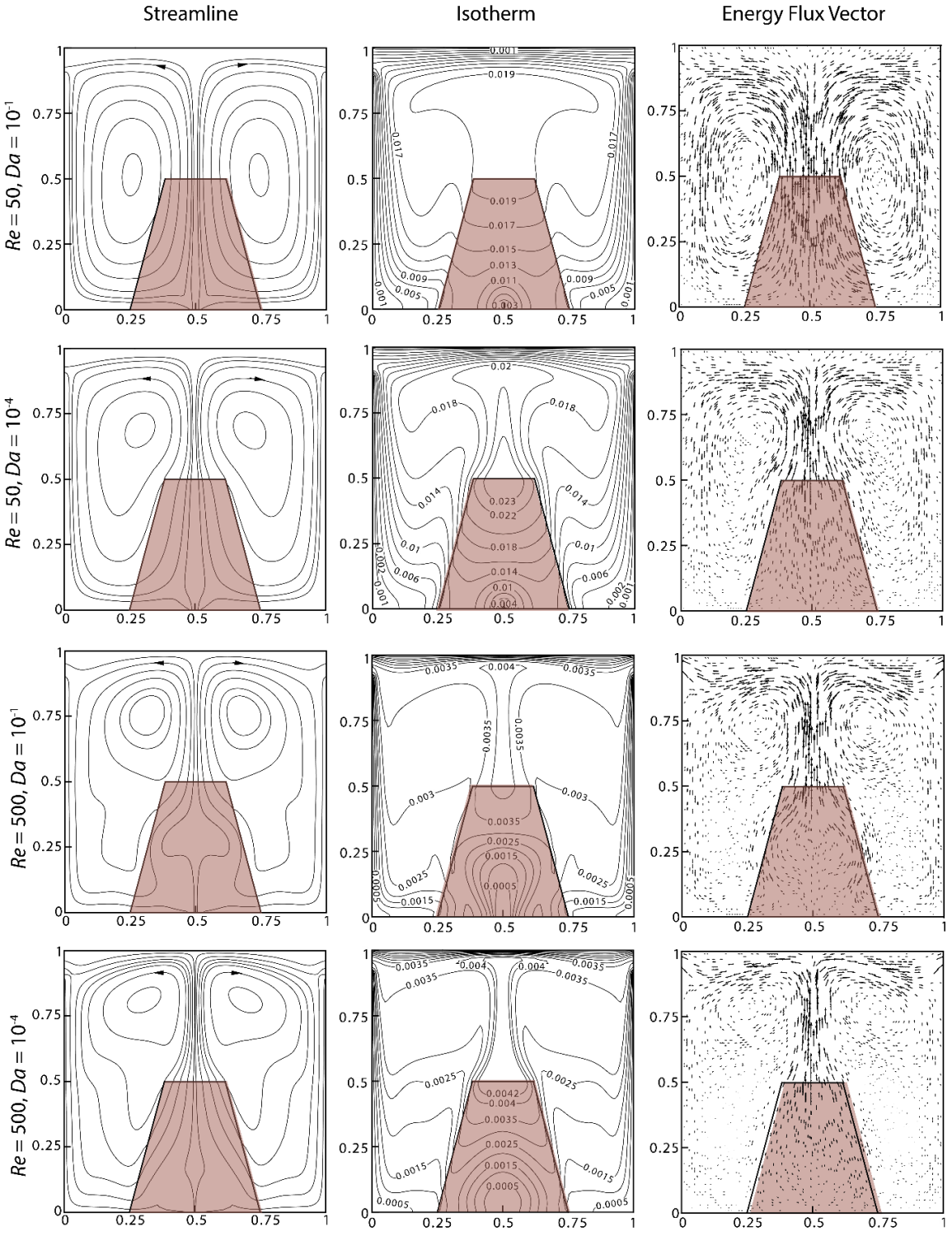

Figure 4.8 Streamline, Isotherms and Energy Flux Vectors for $Ri = 100$ and Re = 50, 500 at Da = 10^{-1}, 10^{-4}

An increased strength of injection velocity, in high Re situations, pushes the circulating fluid towards the top wall in spite of the spreading effect in the lower region of the bed. Also, the energy content of the bed is higher at lower Da due to weaker convection within the bed and contributes to a larger rise in the bed temperature. This is evident from a comparison of θ_{max} in Table 4.6. The working fluid, therefore, transfers a greater amount of thermal energy towards the top wall in low Da situations leading to the establishment of a thinner thermal boundary layer and consequently, increases the heat transfer. The residual energy deposited by the fluid at the side walls, as a result, decrease.

4.3.6.2.3 High Ri situation

A high Ri situation is akin to the natural convective situation where buoyancy effects dominate the fluid circulation within the enclosure. As a result, although the spreading of injected fluid occurs as Da is reduced, the dominating effect of buoyancy establishes two symmetric convective cells about the bed. The fluid circulation, therefore, is able to transfer most of the thermal energy towards the top wall and the residual energy is transferred at the side walls. The energy flux vectors as well as the stream function in Fig. 9 adequately highlights this effect. Heat transfer characteristics in high Ri situations is similar to that observed in a low Ri – high Re situation with relative increase and decrease in heat transfer at the top wall and side walls, respectively.

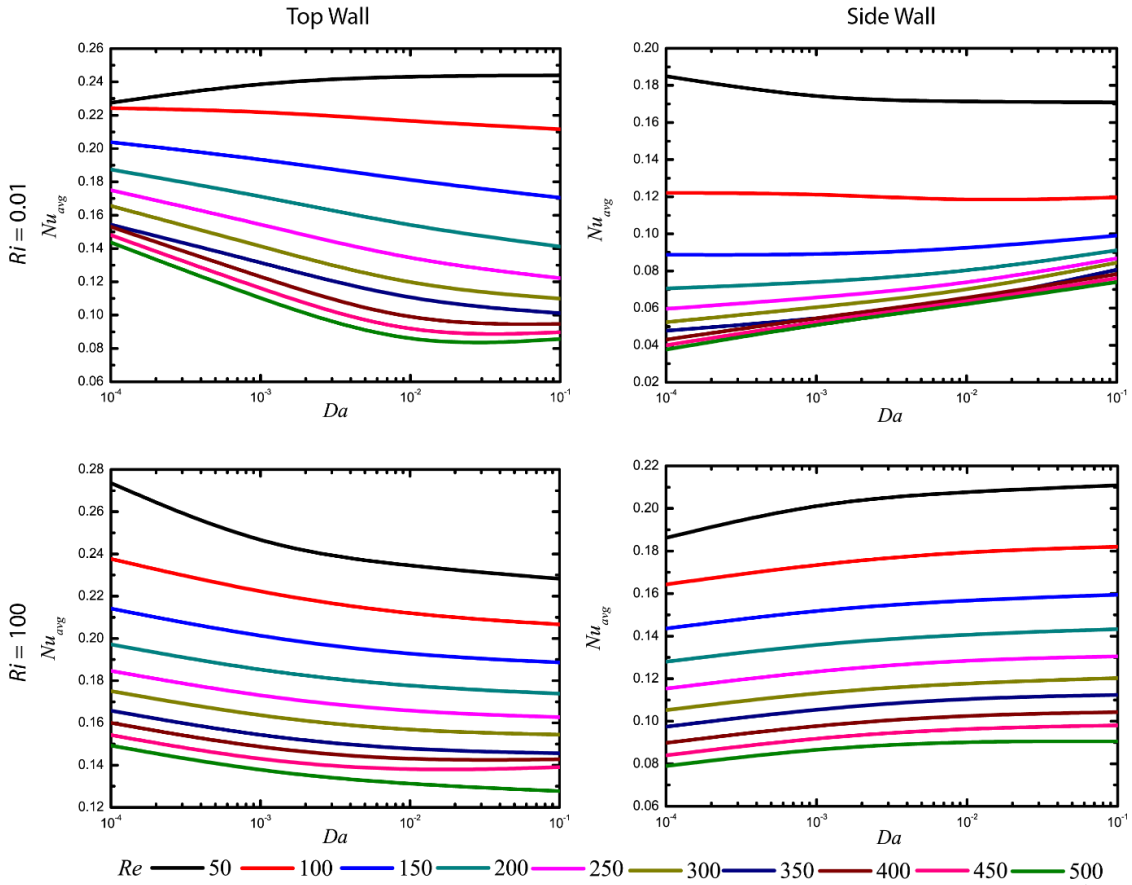

Figure 4.9 Nu_{avg} variation with $Ri = 0.01$ and 100 at different Re and Da = 10^{-4}

4.4 Local Thermal Non-Equilibrium (LTNE) approach

4.4.1 Governing equations

The transport equations of mass, momentum and energy for the clear fluid region and the heat-generating porous bed are derived, in terms of extrinsic average velocity, from the generalised transport equations formulated in *Chapter 2* taking into account the above stated assumptions and considering thermal non-equilibrium in the porous media. The mass, momentum and energy transport equations for the clear fluid region are derived from Eqs. 2.23, 2.36 and 2.49, respectively, while that for the porous bed are derived from Eqs. 2.54, 2.61, 2.65 and 2.66, respectively. These are stated below –

Clear Fluid Region:

$$\nabla.\left(\rho_f\langle \boldsymbol{V}_f\rangle\right) = 0 \tag{4.25}$$

$$\nabla.\left(\rho_f\langle \boldsymbol{V}_f\rangle\langle \boldsymbol{V}_f\rangle\right) = -\nabla p + \mu_f\nabla^2\langle \boldsymbol{V}_f\rangle + \rho_f \boldsymbol{g}\beta\Delta T_f \tag{4.26}$$

$$\rho_f c_{p,f}\langle \boldsymbol{V}_f\rangle\nabla.T_f = k_f\nabla^2 T_f \tag{4.27}$$

Porous Region:

$$\nabla.\left(\rho_f\langle \boldsymbol{V}_f\rangle\right) = 0 \tag{4.28}$$

$$\frac{1}{\varepsilon_f}\nabla.\left(\frac{\rho_f\langle \boldsymbol{V}_f\rangle\langle \boldsymbol{V}_f\rangle}{\varepsilon_f}\right) = -\nabla p + \frac{\mu_f}{\varepsilon_f}\nabla^2\langle \boldsymbol{V}_f\rangle - \left(\frac{\mu_f}{\boldsymbol{K}}\langle \boldsymbol{V}_f\rangle + \frac{\rho_f}{\eta}\left|\langle \boldsymbol{V}_f\rangle\right|\langle \boldsymbol{V}_f\rangle\right) + \rho_f \boldsymbol{g}\beta\Delta T_f \tag{4.29}$$

$$\left(\rho c_p\right)_f\langle \boldsymbol{V}_f\rangle\nabla.T_f = \varepsilon_f k_f\nabla^2 T_f + ha_i\left(T_s - T_f\right) \tag{4.30}$$

$$0 = \left(1-\varepsilon_f\right)k_s\nabla^2 T_s + ha_i\left(T_f - T_s\right) + q_s''' \tag{4.31}$$

The dimensional equations stated above are converted into a dimensionless form by utilising the following dimensionless parameters –

$$X' = \frac{X}{L}, Y' = \frac{Y}{L}, H' = \frac{H}{L}, R' = \frac{R}{L}, \alpha_f = \frac{k_f}{\rho_f c_{p,f}}, U' = \frac{U}{V_{in}}, V' = \frac{V}{V_{in}},$$
$$p' = \frac{p}{\rho_f {V_{in}}^2}, Pr = \frac{\nu_f}{\alpha_f}, Da = \frac{K}{L^2}, F_c = \frac{1.75}{\sqrt{150}}, \theta = \frac{T - T_c}{\Delta T_{ref}}, \Delta T_{ref} = \frac{q_s''' H^2}{k_s},$$
$$\lambda_s = \frac{k_s}{k_f}, h' = \frac{ha_i L^2}{\varepsilon_f k_f}, Gr = \frac{g\beta\Delta T_{ref} H^3}{{\nu_f}^2}, Re = \frac{V_{in} L}{\nu_f}, Ri = \frac{Gr}{Re^2} \tag{4.32}$$

The dimensionless equations thus obtained are stated below. It should be noted that the symbol for averaged quantities is not used in Eq. 3.7 and subsequent equations for simplification of notations.

Clear Fluid Region:

$$\frac{\partial U'}{\partial X'} + \frac{\partial V'}{\partial Y'} = 0 \tag{4.33}$$

$$U'\frac{\partial U'}{\partial X'}+V'\frac{\partial U'}{\partial Y'}=-\frac{\partial p'}{\partial X'}+\frac{1}{Re}\left[\frac{\partial^2 U'}{\partial X'^2}+\frac{\partial^2 U'}{\partial Y'^2}\right] \tag{4.34}$$

$$U'\frac{\partial V'}{\partial X'}+V'\frac{\partial V'}{\partial Y'}=-\frac{\partial p'}{\partial Y'}+\frac{1}{Re}\left[\frac{\partial^2 V'}{\partial X'^2}+\frac{\partial^2 V'}{\partial Y'^2}\right]+\frac{Ri}{H'^3}\theta_f \tag{4.35}$$

$$U'\frac{\partial \theta_f}{\partial X'}+V'\frac{\partial \theta_f}{\partial Y'}=\frac{1}{RePr}\left(\frac{\partial^2 \theta_f}{\partial X'^2}+\frac{\partial^2 \theta_f}{\partial Y'^2}\right) \tag{4.36}$$

Porous Region:

$$\frac{\partial U'}{\partial X'}+\frac{\partial V'}{\partial Y'}=0 \tag{4.37}$$

$$\frac{1}{{\varepsilon_f}^2}\left(U'\frac{\partial U'}{\partial X'}+V'\frac{\partial U'}{\partial Y'}\right)=-\frac{\partial p'}{\partial X'}+\frac{1}{\varepsilon_f Re}\left[\frac{\partial^2 U'}{\partial X'^2}+\frac{\partial^2 U'}{\partial Y'^2}\right]-\frac{1}{ReDaH'^2}U' -\frac{F_c}{\sqrt{Da}H'{\varepsilon_f}^{3/2}}|U'|U' \tag{4.38}$$

$$\frac{1}{{\varepsilon_f}^2}\left(U'\frac{\partial V'}{\partial X'}+V'\frac{\partial V'}{\partial Y'}\right)=-\frac{\partial p'}{\partial Y'}+\frac{1}{\varepsilon_f Re}\left[\frac{\partial^2 V'}{\partial X'^2}+\frac{\partial^2 V'}{\partial Y'^2}\right]-\frac{1}{ReDaH'^2}V' -\frac{F_c}{\sqrt{Da}H'{\varepsilon_f}^{3/2}}|V'|V'+\frac{Ri}{H'^3}\theta_f \tag{4.39}$$

$$U'\frac{\partial \theta_f}{\partial X'}+V'\frac{\partial \theta_f}{\partial Y'}=\frac{\varepsilon_f}{RePr}\left(\frac{\partial^2 \theta_f}{\partial X'^2}+\frac{\partial^2 \theta_f}{\partial Y'^2}\right)+\frac{\varepsilon_f h'}{RePr}\left(\theta_s-\theta_f\right) \tag{4.40}$$

$$0=\frac{\lambda_s\left(1-\varepsilon_f\right)}{RePr}\left(\frac{\partial^2 \theta_s}{\partial X'^2}+\frac{\partial^2 \theta_s}{\partial Y'^2}\right)+\frac{\varepsilon_f h'}{RePr}\left(\theta_f-\theta_s\right)+\frac{\lambda_s}{RePrH'^2} \tag{4.41}$$

4.4.2 Interfacial heat transfer assessment

Interfacial heat transfer between the heat-generating solid particles and the fluid phase is evaluated using the heat transfer correlation proposed by Ranz and Marshall (1952) in a manner similar to that adopted in the analysis of natural convective situation (*Section 3.4*). This is a widely-used correlation and usually finds application in situations involving flow over spherical particles. It has also been extensively used in heat transfer calculations involving porous media (Kakaç 1991) well as heat-generating debris (Takasuo 2015). The heat transfer coefficient (h) is evaluated using this correlation as –

$$h=\frac{Nuk_f}{D_p}=\frac{\left(2+0.66Re^{1/2}Pr^{1/3}\right)k_f}{D_p} \tag{4.42}$$

The Reynolds number (Re) and the interfacial area density (a_i) in the above expression are determined as follows –

$$Re = \frac{\rho_f D_p \left| \langle \boldsymbol{V}_f \rangle^f \right|}{\mu_f} \tag{4.43}$$

$$a_i = \frac{6\left(1-\varepsilon_f\right)}{D_p} \tag{4.44}$$

4.4.3 Boundary conditions and Interfacial conditions

The associated boundary conditions are expressed in a dimensionless form as –

$$U' = V' = 0, \theta_f = 0 \;\; at\; X' = 0{,}1 \; and \; 0 < Y' \leq 0.9 \,,$$

$$U' = V' = 0, \theta_f = 0 \; at\; Y' = 1 \; and \; 0 < X' \leq 1 \,,$$

$$U' = V' = 0, \frac{\partial \theta_f}{\partial Y'} = 0 \; at\; Y' = 0 \; and \; 0 < X' \leq 0.25, 0.75 < X' \leq 1 \,,$$

$$U' = V' = 0, \frac{\partial \theta_f}{\partial Y'} = \frac{\partial \theta_s}{\partial Y'} = 0 \; at\; Y' = 0 \; and \; 0.25 < X' \leq 0.475, 0.525 < X' \leq 0.75 \,,$$

$$U' = 0, V' = 1, \theta_f = 0, \frac{\partial \theta_s}{\partial Y'} = 0 \;\; at\; Y' = 0 \; and \; 0.475 < X' \leq 0.525 \,,$$

$$p' = 0 \; at\; X' = 0{,}1 \; and \; 0.9 < Y' \leq 1 \,. \tag{4.45}$$

In addition to the above stated boundary conditions, it is also necessary to properly model the interface conditions at the porous-fluid interface. This is done by ensuring a continuity of variables and fluxes at the interface. These are stated as follows –

$$U'|_f = U'|_p \; and \; \frac{1}{Re}\left(\frac{\partial^2 U'}{\partial X'^2} + \frac{\partial^2 U'}{\partial Y'^2}\right)\Bigg|_f = \frac{1}{\varepsilon_f Re}\left(\frac{\partial^2 U'}{\partial X'^2} + \frac{\partial^2 U'}{\partial Y'^2}\right)\Bigg|_p$$

$$V'|_f = V'|_p \; and \; \frac{1}{Re}\left(\frac{\partial^2 V'}{\partial X'^2} + \frac{\partial^2 V'}{\partial Y'^2}\right)\Bigg|_f = \frac{1}{\varepsilon_f Re}\left(\frac{\partial^2 V'}{\partial X'^2} + \frac{\partial^2 V'}{\partial Y'^2}\right)\Bigg|_p$$

$$\theta_f\big|_f = \theta_f\big|_p$$

$$\left(\frac{\partial^2 \theta_f}{\partial X'^2} + \frac{\partial^2 \theta_f}{\partial Y'^2}\right)\Bigg|_f = \frac{\varepsilon_f}{RePr}\left(\frac{\partial^2 \theta_f}{\partial X'^2} + \frac{\partial^2 \theta_f}{\partial Y'^2}\right)\Bigg|_p + \frac{\lambda_s\left(1-\varepsilon_f\right)}{RePr}\left(\frac{\partial^2 \theta_s}{\partial X'^2} + \frac{\partial^2 \theta_s}{\partial Y'^2}\right) \tag{4.46}$$

4.4.4 Wall heat transfer assessment

Heat transfer is assessed at the cold enclosure walls in terms of the dimensionless Nusselt number (Nu). This is calculated as follows –

$$Nu = \begin{cases} -\dfrac{\partial \theta_f}{\partial X'}, & \text{for side walls} \\ -\dfrac{\partial \theta_f}{\partial Y'}, & \text{for top wall} \end{cases} \tag{4.47}$$

$$Nu_{avg} = \begin{cases} \int_0^{L-D_{out}} NudY' \Big/ \int_0^{L-D_{out}} dY', & \text{for side walls} \\ \int_0^{W} NudX' \Big/ \int_0^{W} dX', & \text{for top wall} \end{cases} \tag{4.48}$$

4.4.5 Energy flux vector

Energy flux vectors, as defined by Hooman (2010), have been used for visualisation of convective energy transfer within the enclosure. Mathematically, the energy flux vector is expressed in cylindrical coordinate system as –

$$\vec{E} = \left(\frac{\partial \Pi}{\partial Y'}\right)\vec{\imath} - \left(\frac{\partial \Pi}{\partial X'}\right)\vec{\jmath} \tag{4.49}$$

The dimensionless form of the energy flux vectors are separately defined for the fluid and porous regions, following the works of Ejlali and Hooman (2011) and Ejlali et al. (2009), as follows –

Clear Fluid region:

$$\frac{\partial \Pi}{\partial Y'} = U'\theta_f - \frac{1}{RePr}\left(\frac{\partial \theta_f}{\partial X'}\right) \tag{4.50}$$

$$-\frac{\partial \Pi}{\partial X'} = V'\theta_f - \frac{1}{RePr}\left(\frac{\partial \theta_f}{\partial X'}\right) \tag{4.51}$$

Porous region:

$$\frac{\partial \Pi}{\partial Y'} = U'\theta_f - \frac{\varepsilon_f}{RePr}\left(\frac{\partial \theta_f}{\partial X'}\right) - \frac{\lambda_s(1-\varepsilon_f)}{RePr}\left(\frac{\partial \theta_s}{\partial X'}\right) - \frac{\lambda_s}{2RePrH'^2}X' \tag{4.52}$$

$$-\frac{\partial \Pi}{\partial X'} = V'\theta_f - \frac{\varepsilon_f}{RePr}\left(\frac{\partial \theta_f}{\partial Y'}\right) - \frac{\lambda_s(1-\varepsilon_f)}{RePr}\left(\frac{\partial \theta_s}{\partial Y'}\right) - \frac{\lambda_s}{2RePrH'^2}Y' \tag{4.53}$$

4.4.6 Numerical procedure

The pressure-based solver of ANSYS FLUENT is used for obtaining solution of the aforementioned dimensionless governing equations (Eqs. 4.33 – 4.41). Numerical schemes utilised in solving are listed in Table 4.7. A convergence criterion of all residuals below 10^{-8} is followed in this analysis. The entire analysis is carried out with a mesh comprising 10512 nodes.

Table 4.7 Numerical schemes adopted for simulation

Parameter/Equation	Numerical Scheme
Pressure-Velocity Coupling	SIMPLE
Pressure	PRESTO
Momentum	QUICK
Energy	QUICK
UDS	QUICK

The energy transport equation for the solid phase of the porous medium is solved by adopting a similar approach as in the natural convection problem (*Section 3.4*). The solid temperature is defined as a user-defined scalar (UDS) in ANSYS FLUENT and the associated energy transport equation is solved using the UDS transport equation utility. Various terms of the energy transport equation are defined using appropriate user-defined function (UDF) modules. In addition to this, calculations for determining the interfacial heat transfer and the energy flux vectors are also implemented using various UDFs. Table 4.8 lists all the UDF modules utilised.

Table 4.8 UDF modules used for implementation of different terms in ANSYS FLUENT

Term Implemented	UDF Module
Interfacial heat transfer	DEFINE_SOURCE
Diffusive term in Eq. 3.27	DEFINE_DIFFUSIVITY
Energy flux vectors	DEFINE_ON_DEMAND

4.4.6.1 Model validation

Direct validation of the LTNE model in a mixed convective situation involving heat generation within porous media is not possible due to a lack of resources in this regard (see *Section 4.1*). The porous media model used in the analysis is, however, extensively validated with experimental as well as numerical data using the LTE approach (see *Section 3.3.4.1*) and with numerical data for the LTNE approach (see *Section 3.4.6.1*). Validation with regard to a mixed convective flow situation has also been carried out (see *Section 4.3.5.1*). Combining all these validations, it can be safely assumed that the numerical model used to analyse the mixed convective flow using the LTNE approach will give satisfactory results.

Table 4.9 Grid Independence Study using Nu_{avg} at the top wall (upper row) and side wall (lower row)

Ri	***Re***	***Gr***	$\boldsymbol{\lambda_s}$	***Da***	**Configuration (number of nodes)**			
					3874	**6765**	**10512**	**15090**
0.01	100	100	0.1	10^{-4}	0.01433 (1.91 %)	0.01445 (1.09 %)	0.01459 (0.13 %)	0.01461
					0.00677 (2.02 %)	0.00681 (1.44 %)	0.00689 (0.29 %)	0.00691
100	500	2.5×10^7	100		6.1917 (1.95 %)	6.2264 (1.39 %)	6.3058 (0.14 %)	6.3148
					0.5279 (1.85 %)	0.53048 (1.37 %)	0.53589 (0.36 %)	0.53785

4.4.6.2 Grid independence study

The accuracy of the numerical solution with regard to the effects of the computational domain has been assessed by considering different mesh configurations. Table 4.9 summarises the values of Nu_{avg} at the cold walls of the enclosure for four

different configurations of the domain. As can be observed, the change in Nu_{avg} for each wall is minor as the mesh is refined beyond 10512 nodes. Therefore, this configuration (10512 nodes) has been utilised for performing further computations.

Table 4.10 Comparison of dimensionless temperatures obtained using the LTE and LTNE model for $Ri = 0.01$

Ri	Re	λ_s	LTNE		LTE
			$\theta_{s,max}$	$\theta_{f,max}$	θ
0.01	100	0.1	0.003323	0.002833	0.002824
		1	0.030553	0.027053	0.026304
		10	0.241422	0.21548	0.203255
		50	0.971435	0.88473	0.74999
		100	1.84147	1.68529	1.33195
	500	0.1	0.001068	0.000669	0.000669
		1	0.01044	0.006629	0.006575
		10	0.086675	0.060185	0.059804
		50	0.340633	0.251622	0.229877
		100	0.625926	0.469246	0.397178
1	100	0.1	0.003269	0.002785	0.002777
		1	0.027334	0.023997	0.023445
		10	0.184254	0.1573	0.144786
		50	0.68093	0.57144	0.48906
		100	1.20294	1.00451	0.83828
	500	0.1	0.001051	0.00065863	0.00065867
		1	0.009483	0.00594	0.00588
		10	0.06771	0.04162	0.04073
		50	0.26448	0.16155	0.15134
		100	0.4813	0.29249	0.26818
100	100	0.1	0.0020317	0.00165032	0.00165037
		1	0.013449	0.010574	0.0105272
		10	0.090537	0.064	0.06292
		50	0.30479	0.19974	0.19096
		100	0.50965	0.31769	0.30126
	500	0.1	0.00071912	0.00043279	0.00043257
		1	0.004755	0.002783	0.00299
		10	0.03873	0.01968	0.01907
		50	0.13732	0.05927	0.05735
		100	0.24546	0.10046	0.10037

4.4.7 Results and Discussions

Investigation using the LTNE approach is carried out with focus on analysing the effects of the phasic thermal conductivities on the heat transfer characteristics. The thermal conductivity ratio of the solid particles with respect to the fluid phase (λ_s) is

varied in the range of 0.1 to 100 for this purpose while keeping the fluid thermal conductivity constant. The results obtained are also compared with the results obtained for the equivalent problem using the LTE approach in order to highlight the quantitative differences between the predictions of the two approaches. The bed configuration ($H' = 0.5$, $R' = 0.25$, $\phi = 75°$) is considered to remain invariant in this analysis.

An increase in λ_s essentially refers to a larger magnitude of k_s with respect to k_f. This necessitates an increase in the volumetric heat generation rate (q_s''') if the governing parameters i.e. Ri, Re and Gr are constants (see Eq. 4.32). The increased magnitude of q_s''' should result in a higher bed temperature since all other parameters are invariant. A comparison of the magnitudes of dimensionless temperature in Table 4.10 corroborates this deduction.

Observations from the analysis carried out using the LTE model only (see *Section 4.3*) indicates that the injected fluid, coupled with the effects of buoyancy, pushes the heated working fluid towards the top wall where the major amount of heat transfer takes place. Only the residual thermal energy is transferred to the side walls. A similar flow pattern and heat transfer mechanism is observed using the LTNE model as well. This can be visualised from the corresponding contours of streamline and isotherm as well as energy flux vectors (Fig. 4.10). Figure 4.10 compares the streamline, isotherms of the fluid and solid phases as well as the energy flux vectors for different λ_s at $Ri = 100$, $Re = 500$ and $Da = 10^{-4}$. Buoyant flow within the bed strengthens with increase in λ_s due to a relative rise in the heat generation rate.

Fluid circulation, as such, is observed to shift towards the upper region of the cavity with increase in λ_s (as is evident from the streamlines and energy flux vectors). The increased strength of circulation is clearly evident from a comparison of the axial velocity profiles in Fig. 4.11. Invariance in the pattern of fluid isotherms within the porous region indicates that the mechanism of heat transfer to the fluid phase and as such, the resulting fluid flow mechanism within the porous bed does not change qualitatively with change in λ_s. It can also be observed that the isotherms of the solid and fluid phases are aligned with each other at lower values of λ_s ((≤ 10). This alignment is, however, not observed when λ_s becomes large (~ 100).

A rise in the bed temperature with increase in λ_s, due to increased heat generation, results in the establishment of a larger thermal gradient and leads to a rise in the heat transfer at the walls. The increase in heat transfer rate with increasing λ_s is evident from the plots of Nu_{avg} for various Ri and Re in Figs. 4.12 – 4.14. Observations from these figures also indicate that heat transfer at the top wall substantially exceeds that at the side walls in all cases, irrespective of the energy transport model adopted. Also, heat transfer is observed to increase sharply at either wall beyond $\lambda_s = 10$ in all situations.

The qualitative similarity between the predictions of the LTE and LTNE models are self-evident from the above comparisons. Quantitatively, however, significant differences are observed between the predictions of the LTE and LTNE models. A review of Table 4.10 will show that the predicted dimensional temperature using the LTE model (denoted

by θ) differs substantially from that predicted using the LTNE model (denoted by θ_s, θ_f) for the same combination of Ri, Re and Gr. The quantitative differences between the predictions of the two models with respect to heat transfer at the cold walls are evident from the aforementioned plots of Nu_{avg} in Figs. 4.12 – 4.14.

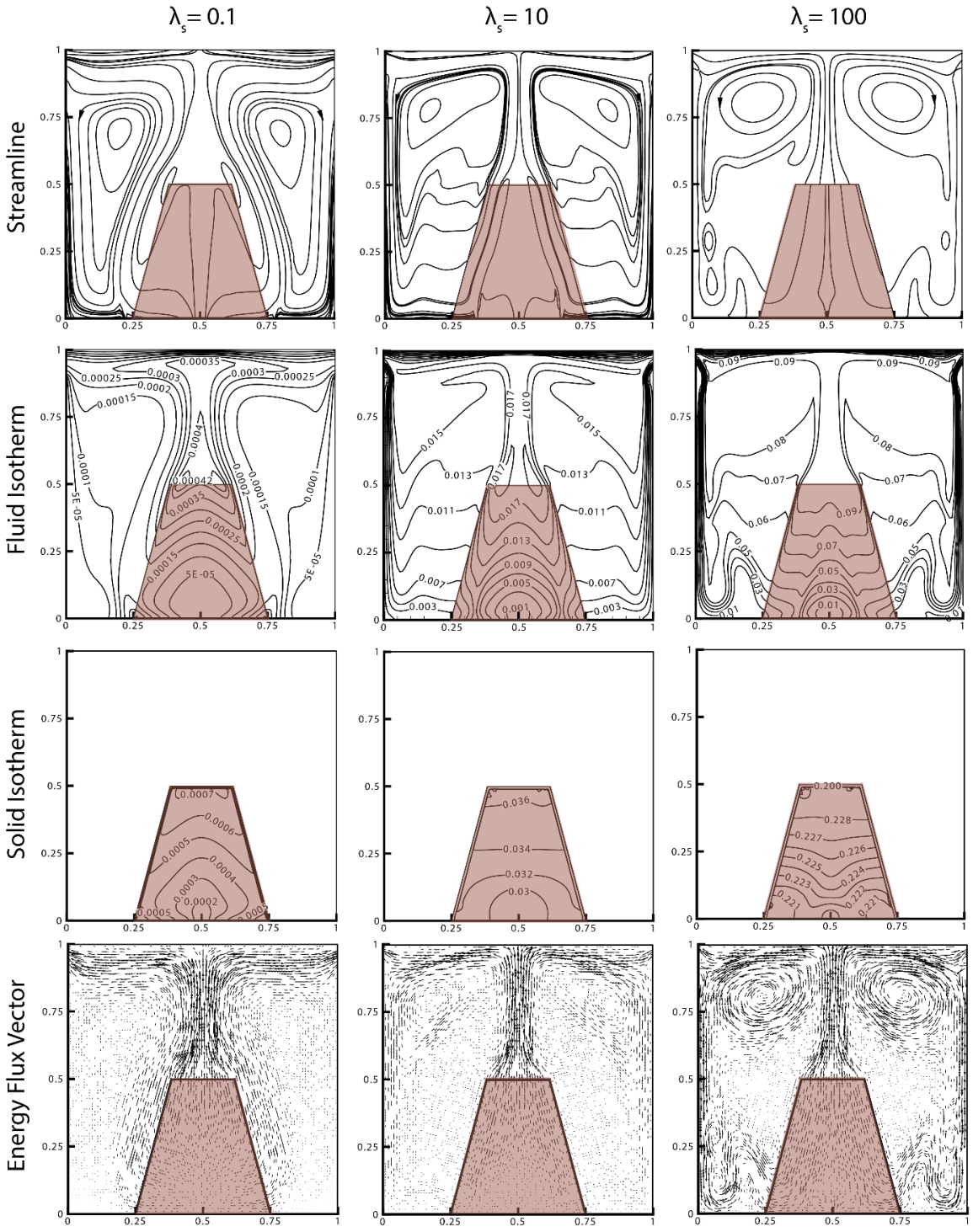

Figure 4.10 Streamline, Isotherms and Energy Flux Vectors for different λ_s at $Ri = 100$, Re = 500, Da = 10^{-4}

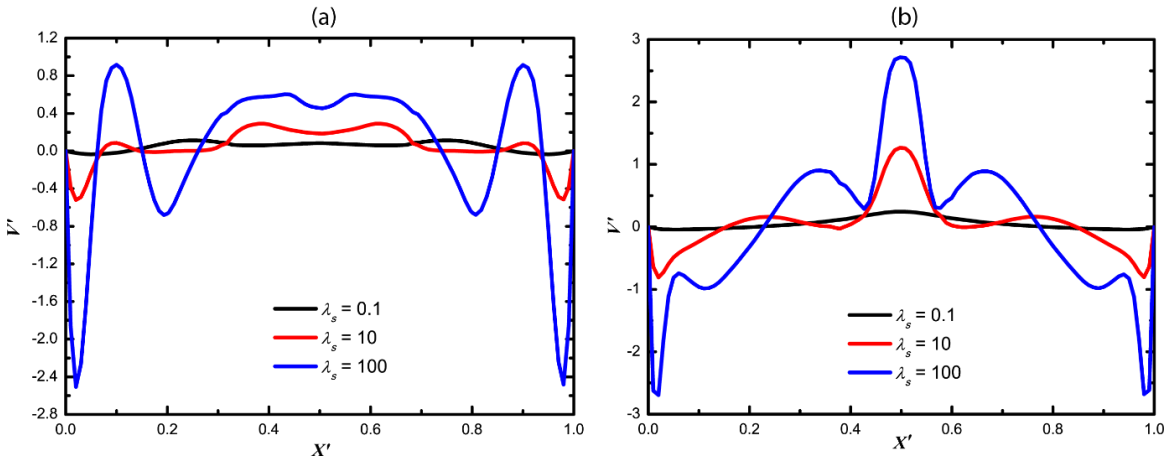

Figure 4.11 Dimensionless axial velocity profiles along the X direction at $Y' = 0.25$ for different λ_s at $Ri = 100$, $Re = 500$, $Da = 10^{-4}$

Figure 4.12 represents the variations of Nu_{avg} for different Re at $Ri = 0.01$. It can be seen that only minor differences exist between the predictions of the two models with respect to Nu_{avg} at the top wall, for all magnitudes of Re when λ_s is small. However, the differences starts increasing as λ_s is gradually increased and becomes substantial when $\lambda_s > 10$. Also, this difference in Nu_{avg} at the top wall is observed to marginally decrease with increase in Re. A similar variation of Nu_{avg} with λ_s is observed at the side walls for $Re = 100$. However, an increase in Re beyond 100 does not results in any substantial increase in the difference between the predictions of the two models. It is interesting to note that the LTE model predicts a higher magnitude of Nu_{avg} at the top wall than that predicted by the LTNE model at $Re = 100$. At higher values of Re, however, the prediction of LTNE model is higher than that of the LTE model.

The variation in Nu_{avg} with λ_s for either wall at $Ri = 1$ is similar to that observed in case of $Ri = 0.01$. This can be observed from Fig. 4.13. However, the LTE model underpredicts the magnitude of Nu_{avg} with respect to the prediction of the LTNE model for both walls and for all Re at $Ri = 1$. Figure 4.14 shows the variation of Nu_{avg} for different Re at $Ri = 100$. The trend of change in Nu_{avg} with λ_s is similar to that observed for $Ri = 0.01$ and 1. However, a smaller difference is evident between the predictions of the LTE and the LTNE models for either wall.

4.5 Conclusions

The problem of heat removal from a heat-generating porous bed, with bottom flooding of cold fluid, creates a mixed convection type situation due to the associated buoyancy effects. This has been analysed in this chapter in a dimensionless manner following the local thermal equilibrium (LTE) as well as the local thermal non-equilibrium (LTNE) approach. Phase change of the working fluid has not been considered in this analysis. Observations from the comparative assessment using the LTE and LTNE approaches reveal that the predictions of the two models are qualitatively similar to each other. However, quantitative differences are observed between these models especially in situations with a high thermal conductivity ratio.

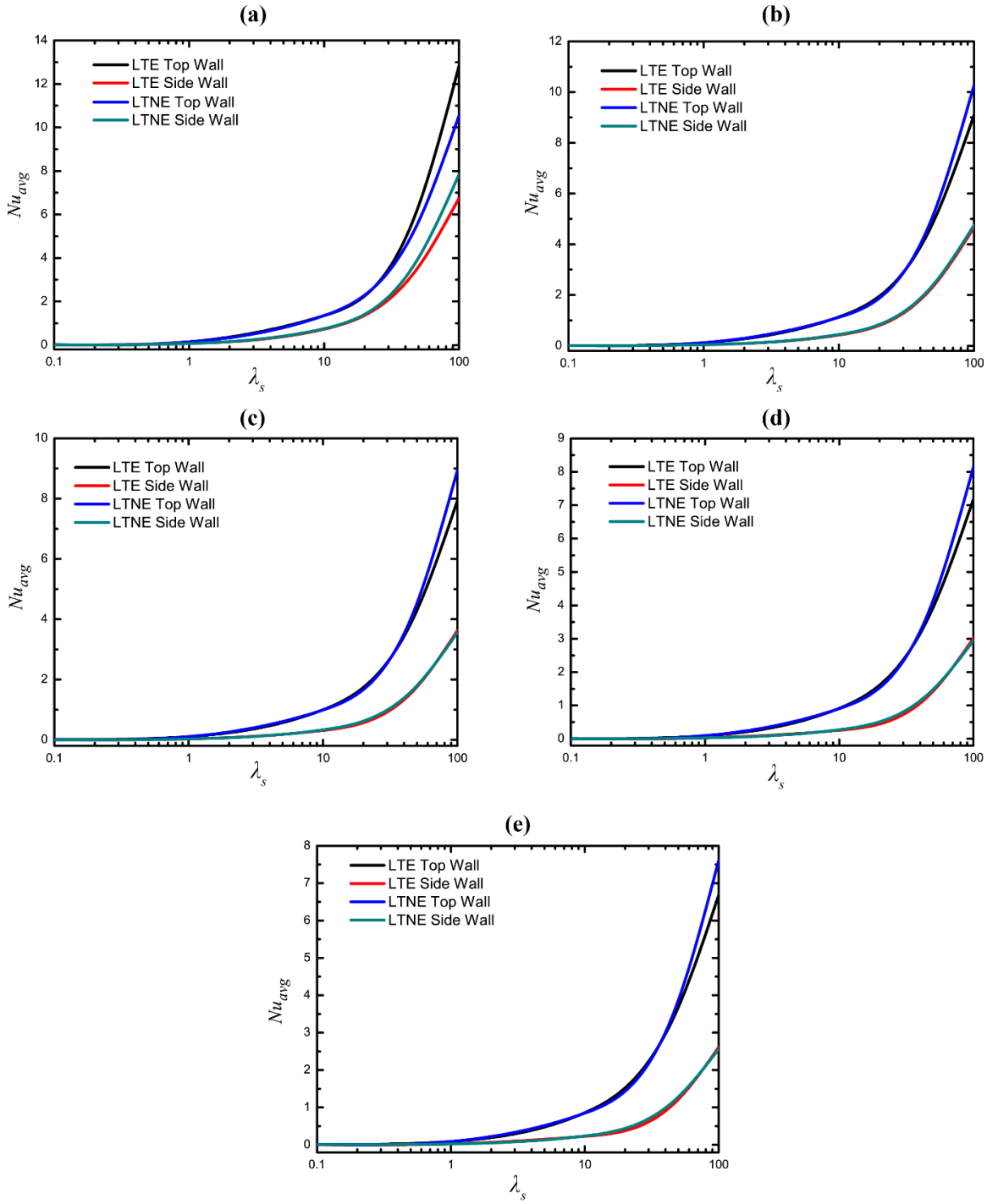

Figure 4.12 Nu_{avg} variation with λ_s at $Ri = 0.01$, $Da = 10^{-4}$ and (a) $Re = 100$ (b) $Re = 200$ (c) $Re = 300$ (d) $Re = 400$ (e) $Re = 500$

Observations indicate that the flow mechanism within the enclosure and the associated heat transfer is governed by the relative dominancy of inertial flow and the buoyancy-driven flow mechanisms, in addition to the effects of bed permeability. The flow mechanism evolves from a strongly inertial flow at very low Ri to a buoyancy-driven flow at very high Ri. Stronger fluid injection at low Ri enables greater heat removal from the heat-generating bed leading to a lower bed temperature rise. Establishment of a weak temperature gradient results in a smaller Nu_{avg} at low Ri. The

strength of fluid injection decreases as Ri is increased and as such, relatively less heat is removed from the bed leading to a very high temperature rise. This also results in a larger temperature gradient within the enclosure and a consequent increase in Nu_{avg}.

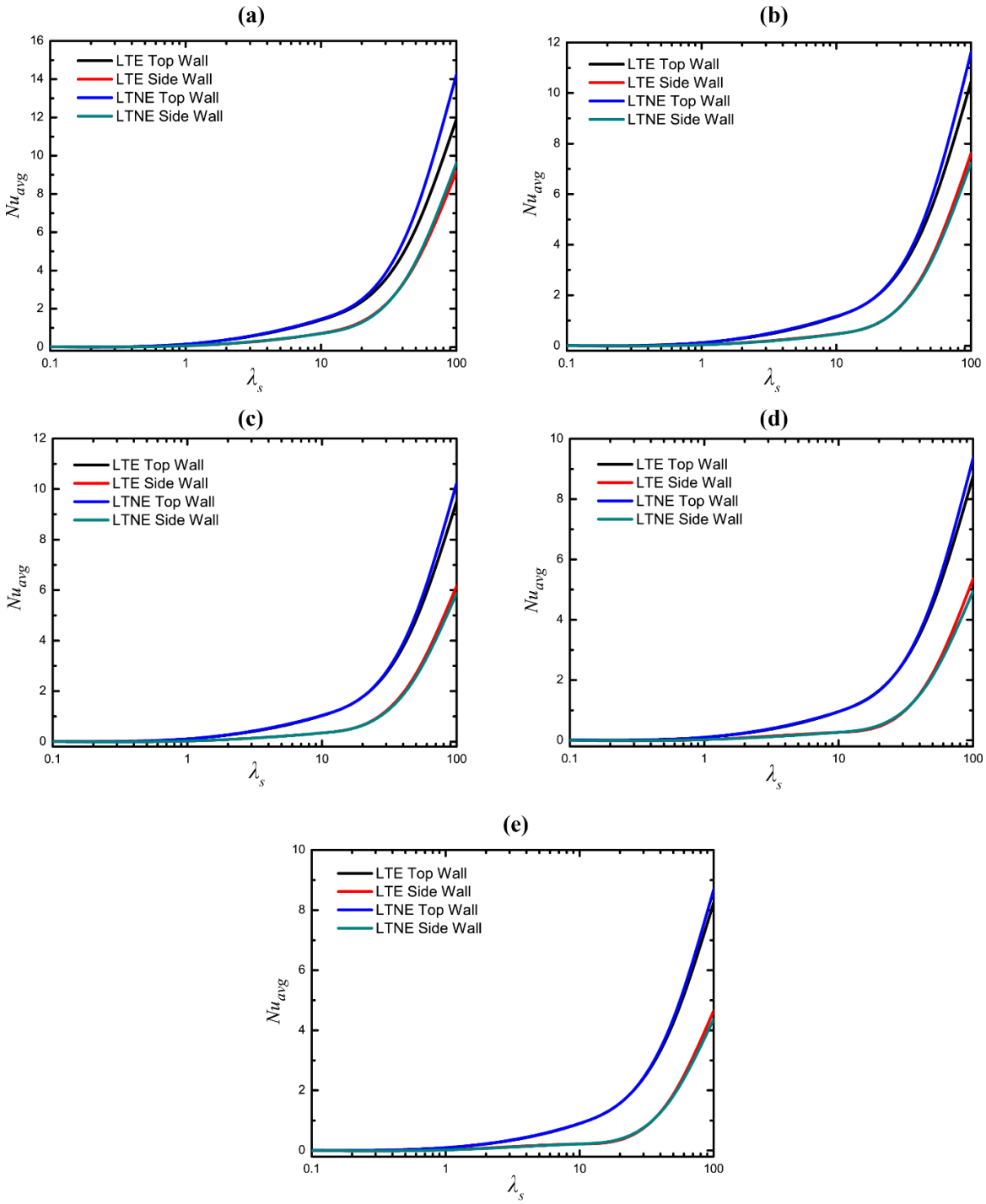

Figure 4.13 Nu_{avg} variation with λ_s at $Ri = 1$, Da = 10^{-4} and (a) $Re = 100$ (b) $Re = 200$ (c) $Re = 300$ (d) $Re = 400$ (e) $Re = 500$

A significant effect of the porous medium is the spreading of flow near the fluid inlet as bed permeability reduces i.e. Da becomes smaller. This effect blocks the cold injected fluid from reaching the upper region of the bed and as such, maximum

temperature is found in this region of the bed and the adjoining fluid region. This is in contrast to the purely buoyancy-driven situation (see *Chapter 3*) where the maximum bed temperature is found in the inner region of the bed. Heat transfer at the top wall increases while that at the side walls decrease as *Da* is reduced. However, the effect of flow spreading increases the heat transfer at the side walls with a corresponding decrease at the top wall in situations with low *Ri* and low *Re*.

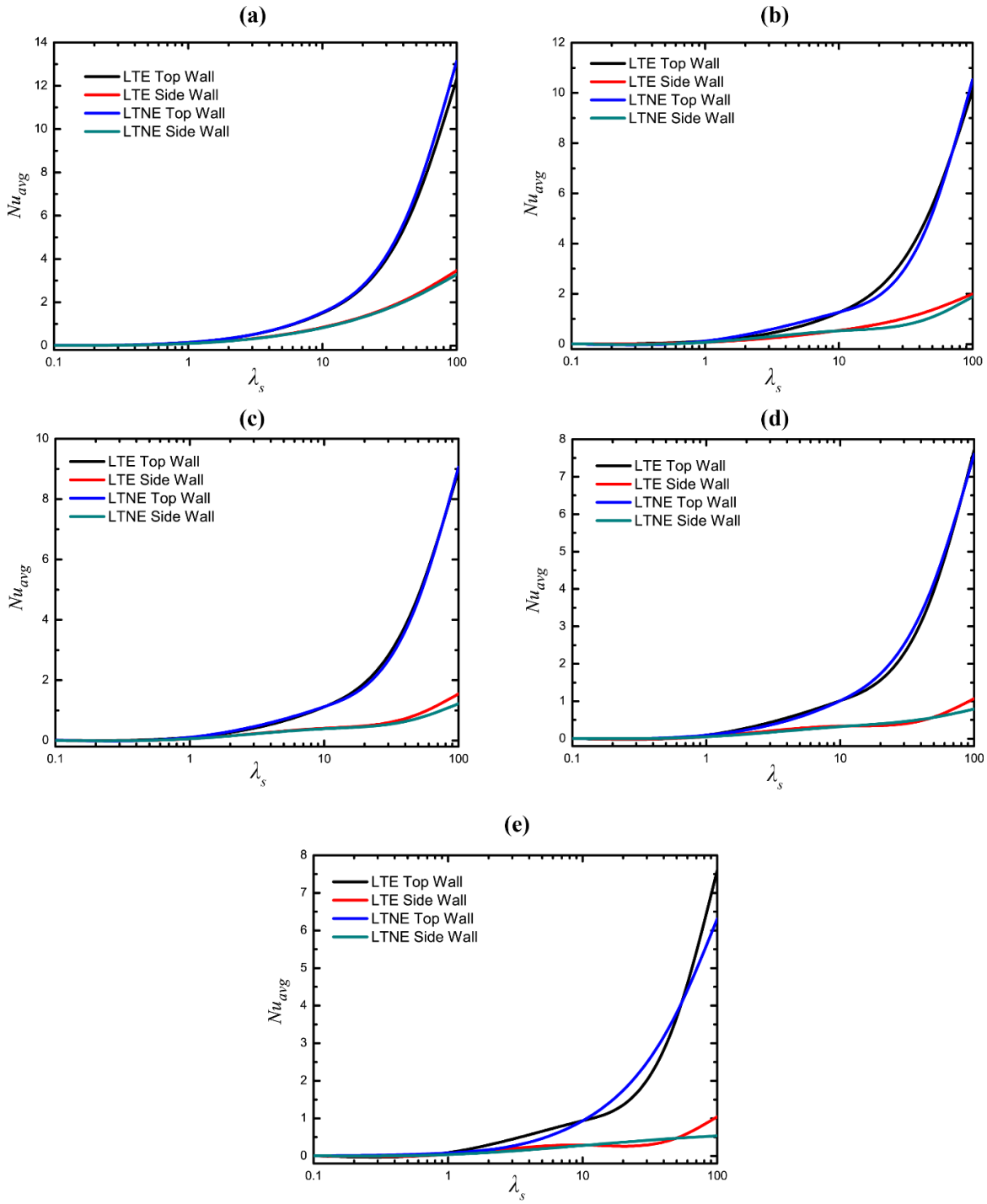

Figure 4.14 Nu_{avg} variation with λ_s at $Ri = 100$, $Da = 10^{-4}$ and (a) $Re = 100$ (b) $Re = 200$ (c) $Re = 300$ (d) $Re = 400$ (e) $Re = 500$

Thermal conductivity ratio between the solid and fluid phases of the porous medium strongly affects the heat transfer. A higher thermal conductivity ratio leads to greater heat generation within the solid particles (since Gr remains invariant) and results in a higher bed temperature. This strengthens the buoyancy-driven flow within the domain and leads to a greater heat transfer at the cold walls. The relative increase in heat transfer progressively becomes larger as the thermal conductivity ratio is increased.

Chapter 5

ANALYSIS OF MULTIPHASE FLOW, HEAT AND MASS TRANSFER, AND PREDICTION OF DRYOUT IN A HEAT-GENERATING POROUS DEBRIS BED

This chapter reports the the findings of the numerical analysis on multiphase flow and prediction of dryout in heat-generating debris beds. An extensive literature review in this regard has already been presented in *Chapter 1* and hence, is not repeated here. *Section 5.1* details the development of the multiphase model while its implementation is discussed in *Section 5.2*. *Section 5.3* gives a description of the problems that has been considered for analysis. *Section 5.4* discusses the numerical procedure adopted in this analysis. The results obtained from the analysis are discussed in *Section 5.5*.

5.1 Model Development

Realistic modelling of multiphase flow and dryout phenomena in debris beds involves solving the mass, momentum and energy transport equations in the porous debris bed as well as the adjoining clear fluid region for the liquid and the vapour phases. The agglomeration of the fragmented particles in the debris bed renders it a porous nature allowing fluid movement through the void between the heat-generating particles. The well-established drag laws of porous media can, thus, be applied for modelling momentum transport in the porous debris bed. The local thermal non-equilibrium (LTNE) model is adopted in modelling energy transport through the porous debris bed in order to account for the large temperature difference existing within the heat-generating solid particles and the fluid phases, especially in dryout conditions. The major assumptions made while developing the numerical model are summarised below –

1. The effect of capillary pressure is not considered in the model. This results in the same static pressure being shared by the constituent fluid phases i.e. $p_l = p_v = p$.
2. The thermo-physical properties of all the phases are constant except the density of the fluid phases. These are modelled using the Boussinesq approximation.
3. Heat generation takes place in the solid particles only.
4. The porous medium constituting the debris bed is homogeneous and isotropic.

The governing equations for the clear fluid region as well as the debris bed are derived from the transport equations detailed in *Chapter 2* taking into account the above-mentioned factors. These are detailed in the following sections.

5.1.1 Governing equations for the clear fluid region

The volume-averaged transport equations for the clear fluid region are derived from Eqs. 2.23, 2.36 and 2.49, and are stated as follows –

Mass transport:

$$\frac{\partial}{\partial t}(\alpha_v \rho_v) + \nabla.(\alpha_v \rho_v \langle \boldsymbol{V}_v \rangle) = {m_{lv}}''' \tag{5.1}$$

$$\frac{\partial}{\partial t}(\alpha_l \rho_l) + \nabla.(\alpha_l \rho_l \langle \boldsymbol{V}_l \rangle) = {m_{vl}}''' \tag{5.2}$$

such that $m_{lv}''' = -{m_{vl}}'''$.

Momentum transport:

$$\frac{\partial}{\partial t}(\alpha_v \rho_v \langle \boldsymbol{V}_v \rangle) + \nabla.(\alpha_v \rho_v \langle \boldsymbol{V}_v \rangle \langle \boldsymbol{V}_v \rangle) = -\nabla(\alpha_v p) + \mu_v \nabla^2 \langle \boldsymbol{V}_v \rangle + m_{lv}''' \langle \boldsymbol{V}_{lv} \rangle + R_{lv}(\langle \boldsymbol{V}_l \rangle - \langle \boldsymbol{V}_v \rangle) + \alpha_v \rho_v \boldsymbol{g} - \nabla.(\rho_v \langle {\boldsymbol{V}_v}' {\boldsymbol{V}_v}' \rangle) \tag{5.3}$$

$$\frac{\partial}{\partial t}(\alpha_l \rho_l \langle \boldsymbol{V}_l \rangle) + \nabla.(\alpha_l \rho_l \langle \boldsymbol{V}_l \rangle \langle \boldsymbol{V}_l \rangle) = -\nabla(\alpha_l p) + \mu_l \nabla^2 \langle \boldsymbol{V}_l \rangle + {m_{vl}}''' \langle \boldsymbol{V}_{vl} \rangle + R_{vl}(\langle \boldsymbol{V}_v \rangle - \langle \boldsymbol{V}_l \rangle) + \alpha_l \rho_l \boldsymbol{g} - \nabla.(\rho_v \langle {\boldsymbol{V}_l}' {\boldsymbol{V}_l}' \rangle) \tag{5.4}$$

Energy transport:

$$\frac{\partial}{\partial t}(\alpha_v \rho_v \langle h_v \rangle^v) + \nabla.(\alpha_v \rho_v \langle \boldsymbol{V}_v \rangle \langle h_v \rangle^v) = \alpha_v \lambda_v \nabla^2 \langle T_v \rangle - \langle {q_{vi}}''' \rangle + {m_{lv}}''' \langle h_{vi} \rangle^v - \nabla.(\rho_v \langle {h_v}' {\boldsymbol{V}_v}' \rangle) \tag{5.5}$$

$$\frac{\partial}{\partial t}(\alpha_l \rho_l \langle h_l \rangle^l) + \nabla.(\alpha_l \rho_l \langle \boldsymbol{V}_l \rangle \langle h_l \rangle^l) = \alpha_l \lambda_l \nabla^2 \langle T_l \rangle - \langle {q_{li}}''' \rangle + {m_{vl}}''' \langle h_{li} \rangle^l - \nabla.(\rho_l \langle {h_l}' {\boldsymbol{V}_l}' \rangle) \tag{5.6}$$

The last terms on the R.H.S of Eq. 5.3 and 5.4 represents the Reynolds stress terms while that in Eq. 5.5 and 5.6 represent the Reynolds scalar flux. These take into account the turbulence effects on the momentum transport and energy transport, respectively.

5.1.2 Governing equations for the debris bed

Equations 2.75, 2.76, 2.79, 2.80, 2.83-85 are utilised in obtaining the governing equations for the heat-generating porous debris bed. These are stated below.

Mass transport:

$$\frac{\partial}{\partial t}\left(\varepsilon_f \alpha_v \rho_v\right) + \nabla.(\alpha_v \rho_v \langle \boldsymbol{V}_v \rangle) = m_{lv}''' \tag{5.7}$$

$$\frac{\partial}{\partial t}\left(\varepsilon_f \alpha_l \rho_l\right) + \nabla.(\alpha_l \rho_l \langle \boldsymbol{V}_l \rangle) = {m_{vl}}''' \tag{5.8}$$

such that $m_{lv}''' = -{m_{vl}}'''$.

Momentum transport:

$$\frac{\partial}{\partial t}(\alpha_v \rho_v \langle \boldsymbol{V}_v \rangle) + \nabla.\left(\frac{\alpha_v \rho_v \langle \boldsymbol{V}_v \rangle \langle \boldsymbol{V}_v \rangle}{\varepsilon_f}\right) = -\nabla\left(\varepsilon_f \alpha_v p\right) + \mu_v \nabla^2 \langle \boldsymbol{V}_v \rangle + \frac{1}{\varepsilon_f}\left(m_{lv}''' \langle \boldsymbol{V}_{lv} \rangle + R_{lv}(\langle \boldsymbol{V}_l \rangle - \langle \boldsymbol{V}_v \rangle)\right) + \varepsilon_f \alpha_v \rho_v \boldsymbol{g} + \langle \boldsymbol{F}_{sv} \rangle \tag{5.9}$$

$$\frac{\partial}{\partial t}(\alpha_l \rho_l \langle \boldsymbol{V}_l \rangle) + \nabla . \left(\frac{\alpha_l \rho_l \langle \boldsymbol{V}_l \rangle \langle \boldsymbol{V}_l \rangle}{\varepsilon_f} \right) = -\nabla \left(\varepsilon_f \alpha_l p \right) + \mu_l \nabla^2 \langle \boldsymbol{V}_l \rangle + \frac{1}{\varepsilon_f} \left({m_{vl}}''' \langle \boldsymbol{V}_{vl} \rangle + R_{vl} (\langle \boldsymbol{V}_v \rangle - \langle \boldsymbol{V}_l \rangle) \right) + \varepsilon_f \alpha_l \rho_l \boldsymbol{g} + \langle \boldsymbol{F}_{sl} \rangle \quad (5.10)$$

Energy transport:

$$\frac{\partial}{\partial t} \left(\varepsilon_f \alpha_v \rho_v \langle h_v \rangle^v \right) + \nabla . \left(\alpha_v \rho_v \langle \boldsymbol{V}_v \rangle \langle h_v \rangle^v \right) = \alpha_v \varepsilon_f \lambda_v \nabla^2 \langle T_v \rangle + \langle {q_{sv}}''' \rangle - \langle {q_{vi}}''' \rangle + {m_{lv}}''' \langle h_{vi} \rangle^v \quad (5.11)$$

$$\frac{\partial}{\partial t} \left(\varepsilon_f \alpha_l \rho_l \langle h_l \rangle^l \right) + \nabla . \left(\alpha_l \rho_l \langle \boldsymbol{V}_l \rangle \langle h_l \rangle^l \right) = \alpha_l \varepsilon_f \lambda_l \nabla^2 \langle T_l \rangle + \langle {q_{sl}}''' \rangle - \langle {q_{li}}''' \rangle + {m_{vl}}''' \langle h_{li} \rangle^l \quad (5.12)$$

Energy transport for solid particles:

$$\frac{\partial}{\partial t} \left(\left(1 - \varepsilon_f \right) \rho_s c_{p,s} \langle T_s \rangle \right) = (1 - \varepsilon_f) \lambda_s \nabla^2 \langle T_s \rangle + \langle {q_s}''' \rangle - \langle {q_{sl}}''' \rangle - \langle {q_{sv}}''' \rangle - \langle {q_{si}}''' \rangle \quad (5.13)$$

In Eq. 5.13, $\langle {q_s}''' \rangle$ represents the volumetric heat generation rate in the solid particles. The term $\langle {q_{si}}''' \rangle$ represents the boiling heat transfer due to heat generation in the solid particles. The terms $\langle {q_{vi}}''' \rangle$ and $\langle {q_{li}}''' \rangle$ represent the interfacial heat transfer that occurs between the respective fluid phases (i.e. liquid or vapour) and the liquid-vapour interface. Heat transfer between the solid particles and the liquid phase is accounted for in the term $\langle {q_{sl}}''' \rangle$ while that between the solid particles and the vapour phase is accounted in $\langle {q_{sv}}''' \rangle$. The last terms on the right hand side of the fluid energy transport equations i.e. Eqs. 5.5, 5.6, 5.11 and 5.12 takes into account the exchange of enthalpy between the phases as a result of phase change. The quantities $\langle h_{vi} \rangle^v$ and $\langle h_{li} \rangle^l$ in these terms represent the intrinsic phase-averaged enthalpy at the phasic interface. The liquid-vapour interface remains at the saturation temperature and as such, the quantities $\langle h_{vi} \rangle^v$ and $\langle h_{li} \rangle^l$ become equivalent to $h_{v,sat}$ and $h_{l,sat}$, respectively.

The phasic temperatures of the fluid phases i.e. T_l and T_v are evaluated from the corresponding phasic enthalpies ($\langle h_l \rangle^l$ and $\langle h_v \rangle^v$). This is achieved considering the saturation condition as the reference state using the relation

$$\langle h_j \rangle^j = h_{j,sat} + \left(c_{p,j,sat} \int_{T_{sat}}^{T_j} dT_j \right) \quad (5.14)$$

where, the suffix *j* denotes the relevant fluid phase. In the momentum transport equations (Eqs. 5.3, 5.4, 5.9 and 5.10), $\boldsymbol{V}_{vl}$ and $\boldsymbol{V}_{lv}$ represent the interphase velocities. These are determined as follows –

$$\boldsymbol{V}_{lv} = \begin{cases} \boldsymbol{V}_l, & if\ {m_{lv}}''' > 0 \\ \boldsymbol{V}_v, & if\ {m_{lv}}''' < 0 \end{cases} \quad (5.15)$$

$$\boldsymbol{V}_{vl} = \begin{cases} \boldsymbol{V}_v, & if\ {m_{vl}}''' > 0 \\ \boldsymbol{V}_l, & if\ {m_{vl}}''' < 0 \end{cases} \quad (5.16)$$

5.1.3 Closure relations

5.1.3.1 Flow regime demarcation

Fluid flow within the domain is assumed to be demarcated into three different regimes depending on the volume fraction of the fluid phases. These are schematically represented in Fig. 5.1. The criteria considered for this regime demarcation is summarised in Table 5.1 in terms of the phasic volume fractions.

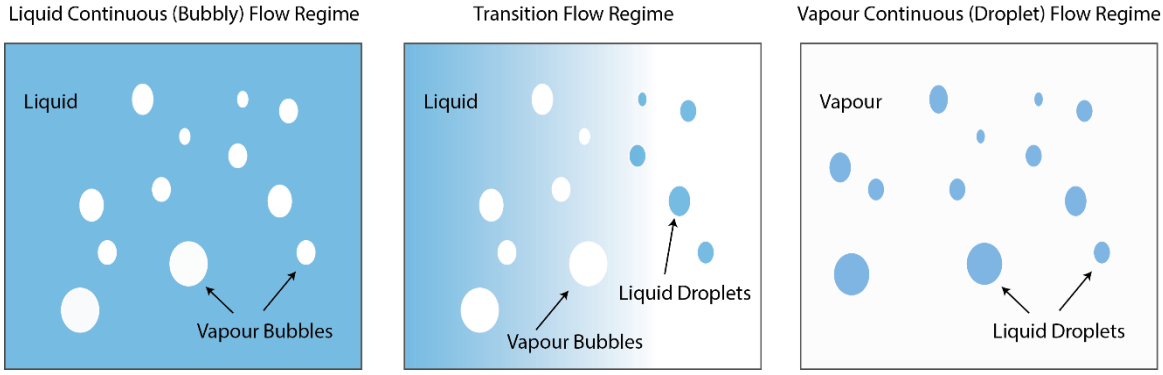

Figure 5.1 Schematic representation of the various fluid flow regimes

A liquid continuous or bubbly flow regime is assumed to exist within the debris bed and the clear fluid region if $\alpha_l \geq 0.7 (\alpha_v \leq 0.3)$ following standard practice (Rahman 2013; Mahapatra et al. 2015). The vapour bubbles are considered to be dispersed in the continuous liquid phase in this flow regime. The vapour continuous or droplet flow regime is considered when $\alpha_l \leq 0.01 (\alpha_v \geq 0.99)$ following the work of Bachrata (2012). In this flow regime, the liquid droplets are assumed to be dispersed in the continuous vapour phase.

Table 5.1 Criterion adopted for demarcating the flow regimes

Flow Regime	α_l	α_v
Liquid Continuous (LC)	$\alpha_l \geq 0.7$	$\alpha_v \leq 0.3$
Transition	$0.01 < \alpha_l < 0.7$	$0.99 > \alpha_v > 0.3$
Vapour Continuous (VC)	$\alpha_l \leq 0.01$	$\alpha_v \geq 0.99$

A transition flow regime is considered between the liquid continuous and vapour continuous regimes when $0.01 < \alpha_l < 0.7 (0.99 > \alpha_v > 0.3)$. A regime weighing parameter (W) is defined in this respect for the transition regime as

$$W = \frac{\left(\alpha_l - \alpha_{l,VC}\right)}{\left(\alpha_{l,LC} - \alpha_{l,VC}\right)} \tag{5.17}$$

where, $\alpha_{l,LC}$ and $\alpha_{l,VC}$ refers to the liquid volume fraction limits for the liquid continuous and vapour continuous regimes, respectively. The diameter of vapour bubbles (D_v) in the liquid continuous regime and of liquid droplets (D_l) in the vapour continuous regime is assumed to be 0.1 mm throughout this analysis (Raverdy et al. 2017). The interfacial area

density (a_i) in the respective flow regimes are defined based on the volume fraction and diameter of the corresponding dispersed phase (denoted by suffix k) as follows –

$$a_i = \frac{6\alpha_k}{D_k} \tag{5.18}$$

The Reynolds number is defined for the liquid continuous and vapour continuous flow regimes as follows –

$$Re_k = \frac{\rho_j \left| \langle \boldsymbol{V}_j \rangle^j - \langle \boldsymbol{V}_k \rangle^k \right| D_k}{\mu_j} \tag{5.19}$$

where, the suffix j and k refers to the continuous and dispersed phases, respectively.

5.1.3.2 Interfacial drag in the clear fluid region

The correlation proposed by Schiller and Naumann (1935) is used to model the liquid-vapour interfacial drag in the clear fluid region. The interfacial momentum exchange coefficient in the momentum transport equations (Eqs. 5.3 and 5.4) is evaluated for the liquid continuous and vapour continuous flow regimes as

$$R_{jk} = R_{kj} = \frac{\rho_k f}{6\tau_k} D_k a_i \tag{5.20}$$

The suffixes j and k in Eq. 5.20 refer to the primary (or continuous) phase and secondary (or dispersed) phase, respectively, which are determined based on the existing fluid flow regime. The parameter f represents the drag function, D_k denotes the diameter of the discrete phase and a_i represents the interfacial area density. The relaxation time (τ_k) is defined as

$$\tau_k = \frac{\rho_k {D_k}^2}{18\mu_j} \tag{5.21}$$

The drag function (f) is expressed as

$$f = \frac{C_D Re_k}{24} \tag{5.22}$$

where,

$$C_D = \begin{cases} \dfrac{24\left(1 + 0.15{Re_k}^{0.687}\right)}{Re_k}, & Re_k \leq 1000 \\ 0.44 \quad , & Re_k > 1000 \end{cases} \tag{5.23}$$

In the above relations, Reynolds number (Re_k) and interfacial area density (a_i) are defined using Eqs. 5.19 and Eq. 5.18, respectively.

The interfacial momentum exchange coefficient in the transition flow regime is determined using a linear interpolation between the liquid continuous and vapour continuous regimes as

$$R_{jk} = R_{kj} = WR_{kj,LC} + (1 - W)R_{kj,VC} \tag{5.24}$$

where, the regime weighing parameter (W) is defined using Eq. 5.17.

5.1.3.3 Interfacial drag in the debris bed

The drag force models used for the debris bed are a combination of the two-phase drag model for porous media and the interfacial liquid-vapour drag. The two-phase drag models for porous media are extensions of the single phase pressure drop model (Ergun 1952) to include the impact of multiple phases. This is achieved by considering relative permeability and relative passability as functions of the phasic volume fractions. The general form of the two-phase drag model in porous media can be written for the vapour and liquid phases as (Schmidt 2007)

$$\langle \boldsymbol{F}_{sj} \rangle = -\varepsilon_f \alpha_j \left(\frac{\mu_i}{K K_{r,j}} \langle \boldsymbol{V}_j \rangle + \frac{\rho_i}{\eta \eta_{r,j}} \left| \langle \boldsymbol{V}_j \rangle \right| \langle \boldsymbol{V}_j \rangle \right) \tag{5.25}$$

In Eq. 5.25, K and η represents the permeability and passability of the porous medium constituting the debris bed and are defined by Eqs. 2.63 and 2.64, respectively. The terms $K_{r,j}$ and $\eta_{r,j}$ represent the relative permeability and relative passability for the phase index j, which may be liquid or vapour. Several models of $K_{r,j}$ and $\eta_{r,j}$ have been proposed over the years which can be broadly classified into two categories – models without and with consideration of liquid-vapour interfacial drag.

5.1.3.3.1 Models not considering interfacial drag between the fluid phases

The models proposed by Lipinski (1981), Reed (1982) and Hu & Theofanous (1991) do not explicitly consider liquid-vapour interfacial drag i.e. $R_{vl} = R_{lv} = 0$. The general form of the relative permeability and passability for these models can be expressed as

$$K_{r,j} = {\alpha_j}^m \tag{5.26}$$

$$\eta_{r,j} = {\alpha_j}^n \tag{5.27}$$

Table 5.2 lists the value of the indices for these models. Among these, the model of Reed (1982) is implemented in the numerical model.

Table 5.2 Model indices for various drag models not considering interfacial drag

Drag Model	Liquid		Vapour	
	m	**n**	**m**	**n**
Lipinski	3	3	3	3
Reed	3	5	3	5
Hu and Theofanous	3	6	3	6

5.1.3.3.2 Models considering interfacial drag between the fluid phases

The models proposed by Schulenberg & Müller (1987) and Tung & Dhir (1988) fall in this category. Refinements to the Tung & Dhir (1988) model have been later introduced by Schmidt (2007), Rahman (2013) and Li et al. (2018). Among these, the

models of Schulenberg & Müller (1987) and Rahman (2007) are implemented in the developed numerical model and are further detailed here.

Model proposed by Schulenberg & Müller

The relative permeabilities and passabilities for the vapour and liquid phases are given by the following relations –

$$K_{r,v} = {\alpha_v}^3 \tag{5.28}$$

$$\eta_{r,v} = \begin{cases} 0.09{\alpha_v}^4, \alpha_v < 0.3 \\ {\alpha_v}^6 \quad , \alpha_v \geq 0.3 \end{cases} \tag{5.29}$$

$$K_{r,l} = {\alpha_l}^3 \tag{5.30}$$

$$\eta_{r,l} = {\alpha_l}^5 \tag{5.31}$$

The interfacial liquid-vapour drag is expressed as

$$R_{vl} = R_{lv} = 350{\alpha_l}^7 \alpha_v \rho_l (\rho_l - \rho_v) \frac{Kg}{\eta\sigma} \left| \frac{\langle \boldsymbol{V}_v \rangle}{\alpha_v} - \frac{\langle \boldsymbol{V}_l \rangle}{\alpha_l} \right| \tag{5.32}$$

Model proposed by Rahman

The relative permeability and passability for the liquid phase is given as –

$$K_{r,l} = {\alpha_l}^2 \tag{5.33}$$

$$\eta_{r,l} = {\alpha_l}^5 \tag{5.34}$$

In case of the vapour phase, the relative permeability and passability are specified depending on the flow regime. These are expressed as –

$$K_{r,v} = \begin{cases} {\alpha_v}^3 & , Liquid\ Continuous\ (LC)\ Regime \\ {\alpha_v}^2 & , Vapour\ Continuous\ (VC)\ Regime \\ [1 - W] \cdot K_{r,v,LC} + W \cdot K_{r,v,VC} & , Transition\ Regime \end{cases} \tag{5.35}$$

$$\eta_{r,v} = \begin{cases} {\alpha_v}^3 & , Liquid\ Continuous\ (LC)\ Regime \\ {\alpha_v}^2 & , Vapour\ Continuous\ (VC)\ Regime \\ [1 - W] \cdot \eta_{r,v,LC} + W \cdot \eta_{r,v,VC} & , Transition\ Regime \end{cases} \tag{5.36}$$

The liquid continuous regime is assumed to exist if $\alpha_v < \alpha_{v,LC}$ while the vapour continuous regime is assumed if $\alpha_v > \alpha_{v,VC}$. The expressions of $\alpha_{v,LC}$ and $\alpha_{v,VC}$ are given in Table 5.3.

The liquid-vapour interfacial drag is determined based on the flow regime classification as mentioned in Table 3. It is to be noted here that $R_{lv} = R_{vl}$ for all flow regimes. These are detailed by the following equations (Eqs. 5.37 – 5.40).

$$R_{lv,LVB} = \left\{ 18\alpha_v \alpha_l \frac{(1+\gamma)}{2} \ln\left(1 + \frac{2}{\gamma}\right) \frac{\mu_l}{{D_v}^2} \right\} + \left\{ 0.34\alpha_v {\alpha_l}^5 \cdot \left[\frac{(1+\gamma)}{2} \ln\left(1 + \frac{2}{\gamma}\right) \right]^2 \cdot \frac{(\rho_l \alpha_l + \rho_l \alpha_l)}{D_v} \cdot \frac{1}{\varepsilon_f} \cdot \left| \frac{\langle \boldsymbol{V}_v \rangle}{\alpha_v} - \frac{\langle \boldsymbol{V}_l \rangle}{\alpha_l} \right| \right\} \tag{5.37}$$

Table 5.3 Flow regime demarcation in the model proposed by Rahman (2013)

Flow Regime		Parameter
Liquid Continuous (LC)	Low void Bubbly (LVB) Flow	$\alpha_v \leq \alpha_{v,LVB}$ $\alpha_{v,LVB} = max\left\{0, \frac{\pi}{3} \cdot \frac{(1-\varepsilon_f)}{\varepsilon_f} \cdot \gamma \cdot (1+\gamma) \cdot [6\beta - 5(1+\gamma)]\right\}$
	High void Bubbly (HVB) Flow	$\alpha_{v,LVB} < \alpha_v \leq \alpha_{v,HVB}$ $\alpha_{v,HVB} = min\left\{\alpha_{v,HVB,TD}, 4 \cdot 10^5 \cdot (D_p - D_{p0})^3 + \alpha_{v,HVB,TD}\right\}$ $\alpha_{v,HVB,TD} = \min(0.3, 0.6 \cdot (1-\gamma)^2)$
	Bubbly-Slug Transition (BST) Flow	$\alpha_{v,HVB} < \alpha_v \leq \alpha_{v,BST}$ $\alpha_{v,BST} = min\left\{\frac{\pi}{6}, 4 \cdot 10^5 \cdot (D_p - D_{p0})^3 + \frac{\pi}{6}\right\}$
	Slug (S) Flow	$\alpha_{v,BST} < \alpha_v \leq \alpha_{v,S}$ $\alpha_{v,LC} = \alpha_{v,S} = min\left\{0.6, 4 \cdot 10^5 \cdot (D_p - D_{p0})^3 + 0.6\right\}$
Transition	Slug-Annular Transition Flow	$\alpha_{v,LC} < \alpha_v \leq \alpha_{v,VC}$
Vapour Continuous (VC)	Annular (A) Flow	$\alpha_{v,VC} = \alpha_{v,A} = min\left\{\frac{\pi\sqrt{2}}{6}, 4 \cdot 10^5 \cdot (D_p - D_{p0})^3 + \frac{\pi\sqrt{2}}{6}\right\}$

$$R_{lv,HVB} = \left\{18\frac{\alpha_l \mu_l}{{D_v}^2}\left[\alpha_{v,LVB}\frac{(1+\gamma)}{2}\ln\left(1+\frac{2}{\gamma}\right) + \alpha_v - \alpha_{v,LVB}\right]\right\}$$
$$+0.34{\alpha_l}^5\frac{(\rho_l\alpha_l + \rho_l\alpha_l)}{D_v} \cdot \left\{\alpha_v\left[\frac{(1+\gamma)}{2}\ln\left(1+\frac{2}{\gamma}\right)\right]^2 + \alpha_v - \alpha_{v,LVB}\right\} \cdot \frac{1}{\varepsilon_f} \cdot \left|\frac{\langle \boldsymbol{V}_v \rangle}{\alpha_v} - \frac{\langle \boldsymbol{V}_l \rangle}{\alpha_l}\right| \quad (5.38)$$

$$R_{lv,S} = \left[\left\{5.21\alpha_l\alpha_v\frac{\mu_l}{{D_v}^2}\right\} + 0.92\alpha_v{\alpha_l}^5\frac{(\rho_l\alpha_l + \rho_l\alpha_l)}{D_v} \cdot \frac{1}{\varepsilon_f} \cdot \left|\frac{\langle \boldsymbol{V}_v \rangle}{\alpha_v} - \frac{\langle \boldsymbol{V}_l \rangle}{\alpha_l}\right|\right] min\left(1, \frac{D_p}{D_{p,0}}\right) \quad (5.39)$$

$$R_{lv,A} = 0.25min\left(1, \frac{D_p}{D_{p,1}}\right)\left[\frac{\varepsilon_f \alpha_l \mu_v}{K{\alpha_v}^2}\left(\frac{1-\varepsilon_f}{1-\varepsilon_f \alpha_v}\right)^{-4/3} + \frac{{\varepsilon_f}^2 \alpha_l \alpha_v}{\eta \alpha_v}\left(\frac{1-\varepsilon_f}{1-\varepsilon_f \alpha_v}\right)^{-2/3} \cdot \frac{1}{\varepsilon_f} \cdot \left|\frac{\langle \boldsymbol{V}_v \rangle}{\alpha_v} - \frac{\langle \boldsymbol{V}_l \rangle}{\alpha_l}\right|\right] \quad (5.40)$$

In the bubbly-slug transition regime as well as the slug-annular transition regime, the interfacial drag is calculated as follows –

$$R_{lv,BST} = [1 - W] \cdot R_{lv,HVB} + W \cdot R_{lv,S} \quad (5.41)$$

$$R_{lv,SAT} = [1 - W] \cdot R_{lv,S} + W \cdot R_{lv,A} \quad (5.42)$$

The weighing parameter (W) utilised in Eqs. 5.35, 5.36, 5.41 and 5.42 is defined in the following manner –

$$W = 3\left(\frac{\alpha_v - \alpha_{v,ll}}{\alpha_{v,ul} - \alpha_{v,ll}}\right)^2 - 2\left(\frac{\alpha_v - \alpha_{v,ll}}{\alpha_{v,ul} - \alpha_{v,ll}}\right)^3 \quad (5.43)$$

Here, $\alpha_{v,ll}$ and $\alpha_{v,ul}$ represent the vapour volume fraction at the lower limit and the upper limit of the transition regime, respectively. Other pertinent parameters used in the above expressions are defined in Table 5.4.

Table 5.4 Pertinent parameters used in the model proposed by Rahman (2013)

Parameter	Definition
γ	$\frac{D_b}{D_p}$
D_b	$1.35\sqrt{\frac{\sigma}{g(\rho_l - \rho_v)}}$
β	$\left(\frac{\pi\sqrt{2}}{6(1-\varepsilon_f)}\right)^{1/3}$
$D_{p,0}$	$1.2 \cdot 10^{-2}$m
$D_{p,1}$	$0.3 \cdot 10^{-2}$m

5.1.3.4 Heat transfer assessment

Along with the porous media drag models, realistic assessment of debris bed coolability also requires proper modelling of the governing heat transfer mechanisms within the porous debris bed and in the surrounding clear fluid region. The major heat transfer mechanisms encountered and the models considered presently are represented in Fig. 5.2 and summarised below.

5.1.3.4.1 Convection to liquid

Convective heat transfer from the solid particles to the liquid phase takes place during the initial stages of heat removal from the bed when the bed remains saturated with liquid water i.e. liquid is the continuous phase ($\alpha_l \geq 0.7$). This is estimated as

$$\langle q_{sl}''' \rangle = a_i h_{sl} (\langle T_s \rangle - \langle T_l \rangle) \tag{5.44}$$

The interfacial area density (a_i) is determined as

$$a_i = \frac{6(1-\varepsilon_f)}{D_p} F(\alpha_l) \tag{5.45}$$

where,

$$F(\alpha_l) = \begin{cases} \dfrac{\alpha_l - 0.7}{0.3}, & \alpha_l \geq 0.7 \\ 0, & \alpha_l < 0.7 \end{cases}$$

The heat transfer coefficient (h_{sl}) in Eq. 5.44 is determined using the correlation of Ranz and Marshall (1952) as –

$$h_{sl} = \left(2 + 0.6 {Re_p}^{0.5} {Pr_l}^{0.33}\right) \frac{\lambda_l}{D_p} \tag{5.46}$$

The Reynolds number (Re_p) in Eq. 5.48 is calculated using Eq. 5.19 considering the solid particles to be dispersed in the continuous liquid phase.

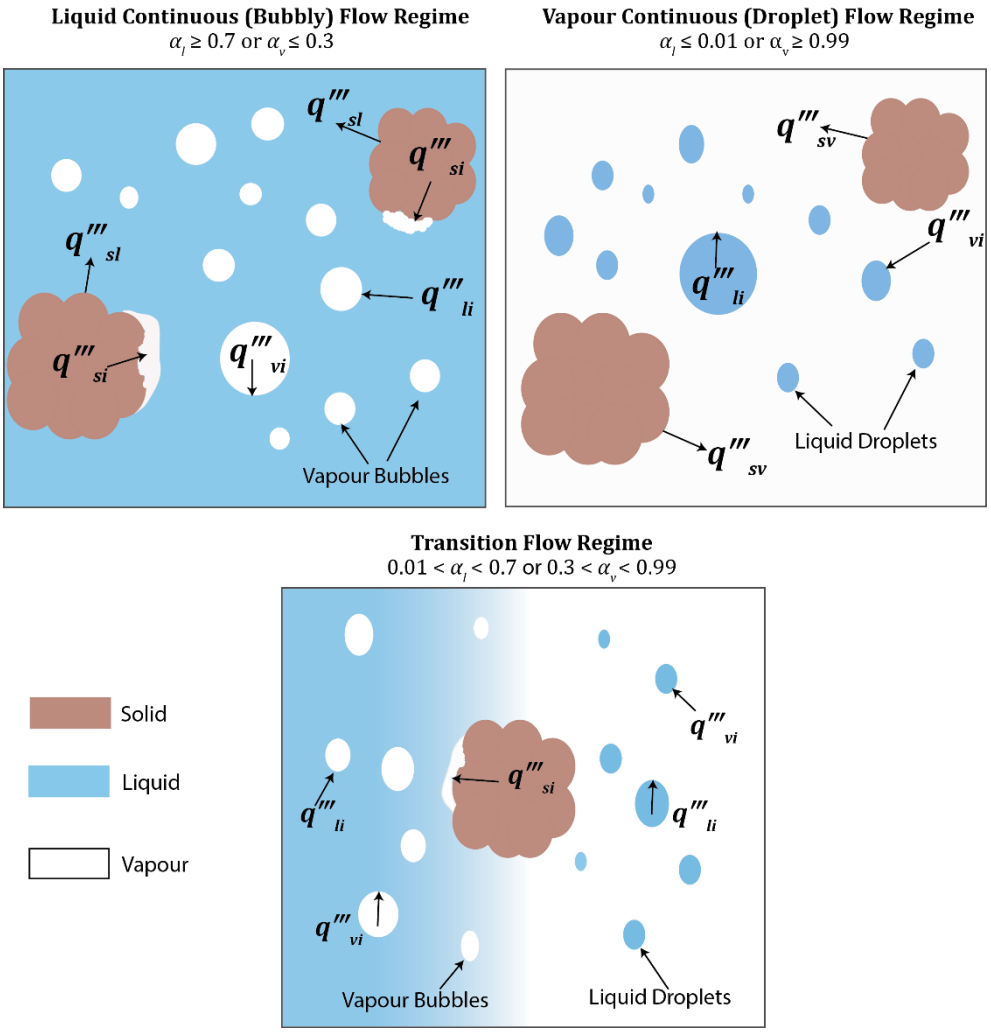

Figure 5.2 Heat transfer mechanisms considered between the heat-generating solid phase, liquid phase and vapour phase for different fluid flow regimes

5.1.3.4.2 Boiling heat transfer

Temperature of the solid particles starts rising if convective heat transfer to the liquid phase is insufficient to remove the decay heat from the bed. In such a situation, if $\langle T_s \rangle$ increases beyond the saturation temperature i.e. $\langle T_s \rangle > T_{sat}$, boiling of the liquid is initiated at the surface of the solid particles and will contribute towards phase change of the liquid. This is estimated as

$$\langle q_{si}''' \rangle = a_i h_{sat} (\langle T_s \rangle - T_{sat}) \tag{5.47}$$

In Eq. 5.47, the interfacial area density (a_i) is determined by

$$a_i = \frac{6(1-\varepsilon_f)}{D_p} F(\alpha_l) \tag{5.48}$$

where,

$$F(\alpha_l) = \begin{cases} 1, & \alpha_l \geq 0.3 \\ \dfrac{\alpha_l}{0.3}, & \alpha_l < 0.3 \end{cases}$$

The heat transfer coefficient (h_{sat}) is determined depending on the prevailing boiling regime. Boiling regimes are demarcated into a nucleate boiling regime and a film boiling regime, with an intervening transition regime, based on the temperature of the solid particles by defining a minimum film boiling temperature ($T_{fb,min}$) and a maximum nucleate boiling temperature ($T_{nb,max}$) (Rahman 2013). These are defined as –

$$T_{fb,min} = T_{sat} + 17 \tag{5.49}$$

$$T_{nb,max} = T_{fb,min} + \Delta\, T_{trans} \tag{5.50}$$

where, $\Delta\, T_{trans} = 100\ K$

Pure nucleate boiling is considered when $\langle T_s \rangle < T_{fb,min}$ and the heat transfer coefficient in this regime is determined using the Rohsenow correlation (1952). It is expressed as –

$$h_{nb,sat} = \frac{{c_{p,l}}^3 \mu_l (\langle T_s \rangle - T_{sat})^2}{\left(h_{v,sat} - h_{l,sat}\right)^2 (0.012 Pr_l)^3 \sqrt{\frac{\sigma}{g(\rho_l - \rho_v)}}} \tag{5.51}$$

Pure film boiling is assumed to occur when $\langle T_s \rangle > T_{nb,max}$. In this regime, the heat transfer coefficient is determined using the Bromley correlation (1950) and is expressed as –

$$h_{fb,sat} = 0.62 \left[\frac{{\lambda_v}^3 g \rho_v (\rho_l - \rho_v)}{D_p \mu_v (\langle T_s \rangle - T_{sat})} {\Delta h_{sat}}^* \right]^{\frac{1}{4}} \tag{5.52}$$

where,

$${\Delta h_{sat}}^* = \left(h_{v,sat} - h_{l,sat}\right)\left(1 + \left(0.968 - \frac{0.163}{Pr_v}\right) Ja\right)$$

$$Ja = \frac{c_{p,v}(\langle T_s \rangle - T_{sat})}{\left(h_{v,sat} - h_{l,sat}\right)}$$

The transition region is assumed to exist when the solid temperature remains between $T_{fb,min}$ and $T_{nb,max}$ i.e. $T_{fb,min} < \langle T_s \rangle < T_{nb,max}$. In this regime, the heat transfer coefficient is determined by linear interpolation between the nucleate and film boiling regimes utilising a weighing parameter (W) as –

$$h_{trans,sat} = [1 - W]h_{nb,sat}(T_{fb,min}) + Wh_{nb,sat}(T_{nb,max}) \tag{5.53}$$

where,

$$W = \frac{(\langle T_s \rangle - T_{fb,min})}{(T_{nb,max} - T_{fb,min})}$$

5.1.3.4.3 Interfacial heat transfer between liquid and vapour

It becomes necessary to consider the interfacial heat transfer between liquid and vapour when the two phases co-exist i.e. $0 < \alpha_v < 1$. This also contributes to phase change of the liquid into vapour and vice-versa. It is to be noted here that this mode of heat transfer needs to be considered in the clear fluid region as well. Heat transfer from liquid to the liquid-vapour interface ($\langle {q_{li}}''' \rangle$) is evaluated for the different flow regimes using the Ranz and Marshall (1952) correlation as follows –

Liquid Continuous Regime:

$$\langle {q_{li}}''' \rangle = \langle {q_{li}}''' \rangle_{LC} = a_i h_{li,LC}(\langle T_l \rangle - T_i) \tag{5.54}$$

$$h_{li,LC} = \left(2 + 0.6 {Re_v}^{0.5} {Pr_l}^{0.33}\right)\frac{\lambda_l}{D_v} \tag{5.55}$$

Vapour Continuous Regime:

$$\langle {q_{li}}''' \rangle = \langle {q_{li}}''' \rangle_{VC} = a_i h_{li,VC}(\langle T_l \rangle - T_i) \tag{5.56}$$

$$h_{li,VC} = \left(2 + 0.6 {Re_l}^{0.5} {Pr_l}^{0.33}\right)\frac{\lambda_l}{D_l} \tag{5.57}$$

Transition Regime:

$$\langle {q_{li}}''' \rangle = W\langle {q_{li}}''' \rangle_{LC} + (1 - W)\langle {q_{li}}''' \rangle_{VC} \tag{5.58}$$

Heat flux from vapour to the liquid-vapour interface ($\langle {q_{vi}}''' \rangle$) is evaluated in a similar manner for the different flow regimes as –

Liquid Continuous Regime:

$$\langle {q_{vi}}''' \rangle = \langle {q_{vi}}''' \rangle_{LC} = a_i h_{vi,LC}(\langle T_v \rangle - T_i) \tag{5.59}$$

$$h_{vi,LC} = \left(2 + 0.6 {Re_v}^{0.5} {Pr_v}^{0.33}\right)\frac{\lambda_v}{D_v} \tag{5.60}$$

Vapour Continuous Regime:

$$\langle {q_{vi}}''' \rangle = \langle {q_{vi}}''' \rangle_{VC} = a_i h_{vi,VC}(\langle T_v \rangle - T_i) \tag{5.61}$$

$$h_{vi,VC} = \left(2 + 0.6 {Re_l}^{0.5} {Pr_v}^{0.33}\right)\frac{\lambda_v}{D_l} \tag{5.62}$$

Transition Regime:

$$\langle q_{vi}{}''' \rangle = W\langle q_{vi}{}''' \rangle_{LC} + (1-W)\langle q_{vi}{}''' \rangle_{VC} \tag{5.63}$$

The temperature at the liquid-vapour interface (T_i) in Eqs. 5.54, 5.56, 5.59 and 5.61 is assumed to be the saturation temperature (T_{sat}) corresponding to the system pressure (i.e. $T_i = T_{sat}$). The interfacial area density (a_i) and Reynolds number in the above equations are evaluated based on the existing flow regime using Eqs. 5.18 and 5.19, respectively.

5.1.3.4.4 Convection to vapour

Heat transfer occurs from the solid particles to the vapour phase if vapour becomes the continuous phase within the debris bed i.e. $\alpha_v \geq 0.99$. This is especially important in dryout conditions and is determined as

$$\langle q_{sv}{}''' \rangle = a_i h_{sv}(\langle T_s \rangle - \langle T_v \rangle) \tag{5.64}$$

The interfacial area density is determined as

$$a_i = \frac{6\left(1-\varepsilon_f\right)}{D_p} F(\alpha_v) \tag{5.65}$$

where,

$$F(\alpha_v) = \begin{cases} \dfrac{\alpha_v - 0.99}{0.01}, & \alpha_v \geq 0.99 \\ 0, & \alpha_v < 0.99 \end{cases}$$

The heat transfer coefficient is determined using the correlation of Ranz and Marshall (1952) as –

$$h_{sv} = \left(2 + 0.6 {Re_p}^{0.5} {Pr_v}^{0.33}\right)\frac{\lambda_v}{D_p} \tag{5.66}$$

The Reynolds number (Re_p) in Eq. 5.66 is calculated using Eq. 5.19 considering the solid particles to be dispersed in the continuous vapour phase.

5.1.3.5 Mass transfer assessment

Interfacial mass transfer between the liquid and vapour phases is assessed using the boiling heat flux and interfacial heat fluxes as follows –

$${m_{lv}}''' = \frac{\langle q_{s,i}{}''' \rangle + \langle q_{v,i}{}''' \rangle + \langle q_{l,i}{}''' \rangle}{h_{v,sat} - h_{l,sat}} \tag{5.67}$$

5.1.3.6 Turbulence modelling

Flow within the porous debris bed remains largely laminar as a result of large resistance against fluid flow. Velocity magnitudes obtained from simulation (see Fig. 5.8) indicate that the maximum magnitude of Reynolds number obtained within the porous debris bed is of the order of 500 for the liquid phase and of the order of 10 for the vapour phase considering the length scale to be the particle size. In the clear fluid region,

however, these magnitudes are approximately 30,00,000 and 55,000 for the liquid and vapour phases, respectively, considering the domain radius as the length scale. This indicates that the fluid flow becomes fully turbulent in the clear fluid region.

Appropriate modelling of turbulence is, therefore, necessary only in the clear fluid region for obtaining realistic results. The $k-\varepsilon$ mixture turbulence model in ANSYS FLUENT (2012a) is utilised for taking into account the effects of turbulence in the present study. The transport equations can be expressed as –

$$\frac{\partial}{\partial t}(\rho_m k) + \nabla.(\rho_m \langle \boldsymbol{V}_m \rangle k) = \nabla.\left[\left(\mu + \frac{\mu_t}{\sigma_k}\right)\nabla k\right] + G_k + G_b - \rho_m \varepsilon \tag{5.68}$$

$$\frac{\partial}{\partial t}(\rho_m \varepsilon) + \nabla.(\rho_m \langle \boldsymbol{V}_m \rangle \varepsilon) = \nabla.\left[\left(\mu + \frac{\mu_t}{\sigma_\varepsilon}\right)\nabla \varepsilon\right] + C_1 \frac{\varepsilon}{k}(G_k + C_3 G_b) - C_2 \rho_m \frac{\varepsilon^2}{k} \tag{5.69}$$

In the above equations, k and ε represents the turbulence kinetic energy and the dissipation rate of the kinetic energy, respectively. The turbulent viscosity (μ_t) is determined using the following relation –

$$\mu_t = C_\mu \rho_m \frac{k^2}{\varepsilon} \tag{5.70}$$

G_k and G_b represents the turbulent kinetic energy generation rate due to mean velocity gradients and buoyancy, respectively. The terms C_1, C_2 and C_μ are constants while σ_k and σ_ε are the turbulent Prandtl numbers for k and ε, respectively. C_3 is determined as a function of the fluid velocity. Magnitude of these parameters adopted in the present model are listed in Table 5.5. The mixture density and mixture velocity is obtained using the following expressions –

$$\rho_m = \alpha_l \rho_l + \alpha_v \rho_v \tag{5.71}$$

$$\boldsymbol{V}_m = \frac{\alpha_l \rho_l \boldsymbol{V}_l + \alpha_v \rho_v \boldsymbol{V}_v}{\rho_m} \tag{5.72}$$

Table 5.5 $k-\varepsilon$ turbulence model parameters

Parameter	Magnitude
C_μ	0.09
C_1	1.44
C_2	1.92
C_3	$\tanh^{-1}\left\lvert\frac{\boldsymbol{V}_{m,r}}{\boldsymbol{V}_{m,z}}\right\rvert$
σ_k	1.0
σ_ε	1.3

5.2 Implementation of the model

The numerical model developed in *Section 5.3* is implemented in the framework of the computational fluid dynamics platform ANSYS FLUENT 14.5. The Eulerian multiphase model of ANSYS FLUENT is utilised in handling the transport equations for

the fluid phases while the porous media model is adopted to take into account the effects of the porous debris bed. Solution of the energy transport equation for the solid particles (Eq. 5.13) is achieved by defining the solid temperature as a user-defined scalar (UDS) and solving a transport equation for the UDS. Various terms of the UDS transport equation are implemented by means of user-defined functions.

Solution of the governing equations, however, requires proper implementation of the various closure relations. These include the interfacial momentum exchange coefficients in the clear fluid region as well as the debris bed, relative permeability and relative passability models for the debris bed, and the various heat transfer mechanisms. The implementation of these terms and coupling of the terms with the respective transport equations are achieved with extensive utilisation of user-defined functions (UDF) utility of ANSYS FLUENT (2012b). Table 5.6 lists all the UDF modules utilised in the implementation.

Table 5.6 UDF modules utilised in implementation of the model

Quantities	UDF Module
Interfacial momentum exchange coefficient	DEFINE_EXCHANGE_PROPERTY
Relative permeability and relative passability	DEFINE_PROFILE
Heat transfer terms	DEFINE_SOURCE
Mass transfer	DEFINE_MASS_TRANSFER
Transient term in Eq. 5.13	DEFINE_UDS_UNSTEADY
Diffusive term in Eq. 5.13	DEFINE_DIFFUSIVITY

5.3 Problem statement

Figure 5.3 illustrates the different configurations of the debris bed analysed in this study. Bed configurations A, B, C and D are cylindrical in structure. Bed configuration E and F are conical and truncated conical in structure, respectively. The debris bed is assumed to be centrally located at the bottom of a fluid-filled cylindrical cavity. In addition, it is assumed that the structure of the debris bed in all the configurations are invariant with time. Dimensions of the debris bed for the different configurations are selected such that the bed volume remains same in all cases. The relevant dimensions are summarised in Table 5.7.

The impact of bed composition and liquid subcooling on the heat transfer characteristics and occurrence of dryout is studied by considering the truncated conical bed configuration (Bed F) only. The effects of debris bed configuration and system pressure are analysed by considering cylindrical (Beds C and D), conical (Bed E) and the truncated conical (Bed F) configurations.

Bed configurations A, B and C are considered in analysing the effect of different flooding modes on the heat transfer characteristics and occurrence of dryout in the debris

bed. Only top-flooding is considered in case of Bed A. Bottom flooding is considered, in addition to top-flooding, in case of bed B by allowing coolant injection through a channel at a specified velocity. In bed configuration C, lateral flooding is considered in addition to top flooding only.

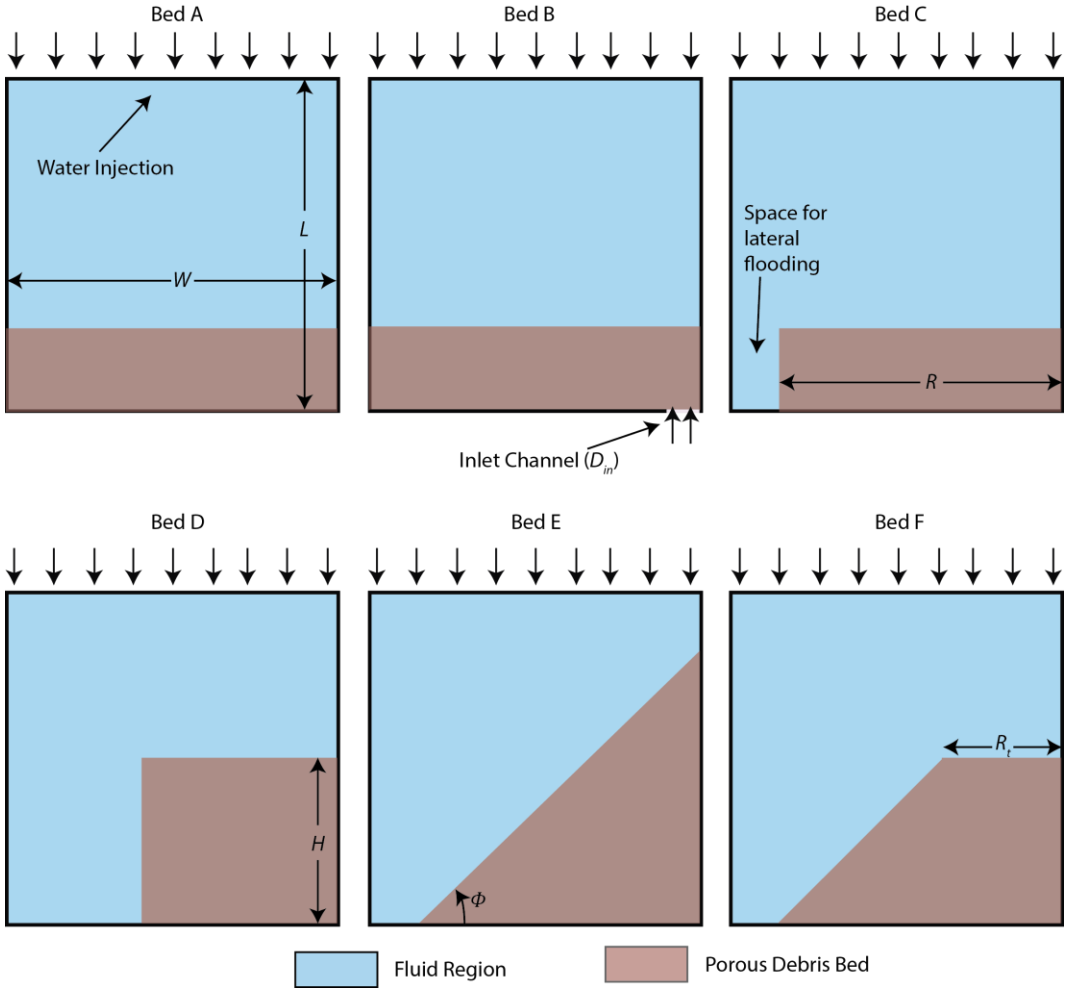

Figure 5.3 Schematic of different configurations analysed (A) Cylindrical bed with top flooding (B) Cylindrical bed with top flooding and bottom flooding (C-D) Cylindrical bed with top flooding and lateral flooding (E) Conical bed (F) Truncated conical bed

Table 5.7 Relevant dimensions for different bed configurations

Bed Configuration	**Bed Volume (m^3)**	***L*** **(m)**	***W*** **(m)**	***H*** **(m)**	***R*** **(m)**	R_t **(m)**	ϕ **(°)**	D_{in} **(m)**
A	0.01532	0.3	0.3	0.054	0.3	0.3	90	0
B				0.054	0.3	0.3		
C				0.078	0.25	0.25		
D				0.15	0.18	0.18		
E				0.234	0.25	0	43.106	
F				0.15	0.25	0.1	45	0.025

The top boundary of the domain is considered to be maintained at a constant pressure allowing fluid movement across the boundary, with the constraint that only the liquid phase can enter the domain while both fluid phases can exit. The bottom and side walls of the cavity are assumed to be impermeable and adiabatic. The entire system is symmetric about the z-axis. Figure 5.4 schematically shows the boundary conditions adopted considering the truncated conical bed as a representative case.

The porous debris bed is assumed to be homogeneous and isotropic in nature. It is also assumed that the constituent solid particles are perfectly spherical (i.e. $\psi = 1$ in Eqs. 2.63 and 2.64) and uniform heat generation takes place in the solid particles only. The thermo-physical properties of all the phases (except density of the fluid phases) are assumed to be constant. Density of the fluid phases are modelled using the Boussinesq approximation. It is further assumed that the entire enclosure is initially saturated with liquid water. The solid particles of the debris bed are assumed to be initially at the saturation temperature corresponding to the prevailing system pressure. The relevant properties of the solid particles are listed in Table 5.8.

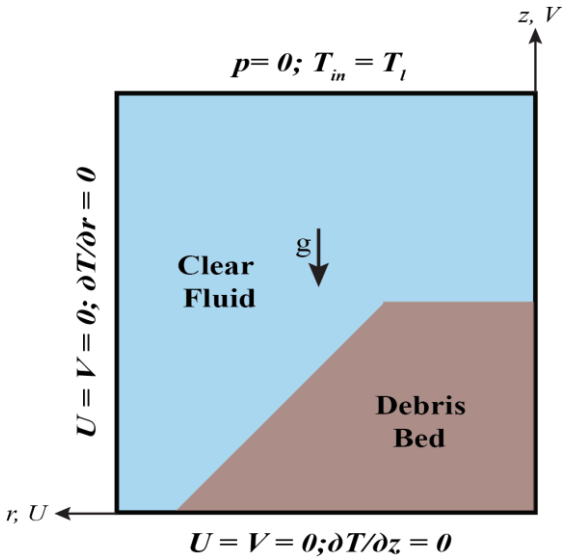

Figure 5.4 Boundary conditions and co-ordinate system considered in the problem

Table 5.8 Material properties assumed for the solid particles (Takasuo et al. 2014)

Property	Magnitude
ρ_s	4200 kg.m^{-3}
λ_s	2 W.m^{-1}.K^{-1}
c_{ps}	775 J.kg^{-1}.K^{-1}

5.4 Numerical procedure

An unstructured computational grid of 3 mm nominal cell size (9560 cells in the entire domain) and a time-step size of 10^{-3}s is used for computations in the present study. The numerical schemes followed for solving the implemented governing equations are listed in Table 5.9. A criterion of all residuals below 10^{-4} is followed for determining convergence of the numerical solution.

Table 5.9 Numerical schemes adopted for simulation

Parameter	Scheme
Pressure-Velocity Coupling	Phase-Coupled SIMPLE
Gradient	Least Squares Cell Based
Momentum, Turbulent Kinetic Energy, Turbulent Dissipation Rate, Energy, UDS	Second Order Upwind
Volume Fraction	QUICK
Transient Formulation	Bounded Second Order Implicit

5.4.1.1 Assessment of bed coolability

A critical issue faced in numerical assessment of coolability of heat-generating porous beds is accurate identification of dryout occurrence within the beds. Previous numerical studies in this domain, however, do not explicitly specify the approach adopted for dryout identification in these studies. Dryout occurrence in the present study is identified from the temporal change of two parameters – minimum liquid saturation ($\alpha_{l,min}$) and maximum solid temperature ($T_{s,max}$) within the heat-generating porous bed. The bed is concluded to be in a dryout condition if the following two conditions are satisfied –

(a) $\alpha_{l,min}$ within the bed attains a zero magnitude and this condition is sustained for the rest of the time period.
(b) The corresponding magnitude of $T_{s,max}$ indicates a sustained rise (of at least 5 K) above the steady state magnitude obtained using the immediately lower power level.

The corresponding dryout location is identified with the help of α_l and T_s distributions within the domain at different time instances. The volumetric heat generation rate at which dryout is observed is identified by initially carrying out simulations at low heat generation rates and then gradually increasing it until dryout is obtained. This is referred to as the *dryout power density* and the corresponding total heat generation rate as the *dryout power*.

5.4.1.2 Model validations

In order to test the validity of the developed numerical model, the numerical predictions are compared with available experimental data for the two most challenging aspects encountered in numerical modelling of heat transfer from the debris bed viz. pressure drop across the porous matrix saturated with a two-phase mixture and heat transfer from the bed.

5.4.1.2.1 Pressure drop in two-phase flow through porous medium

Pressure drop in a two-phase flow situation through porous media is compared with experimental data reported by Li et al. (2015) for experiments carried out in the DEBECO test facility with air and water at isothermal conditions. A specific composition of the porous bed, with $\varepsilon_f = 0.4$ and $D_p = 1.44$ mm (Bed 3 in Li et al. (2015)), is simulated for a specified range of superficial air velocity. It is clearly indicated from the results shown

in Fig. 5.5 that all the drag models considered are able to predict the pressure drop with a reasonable accuracy.

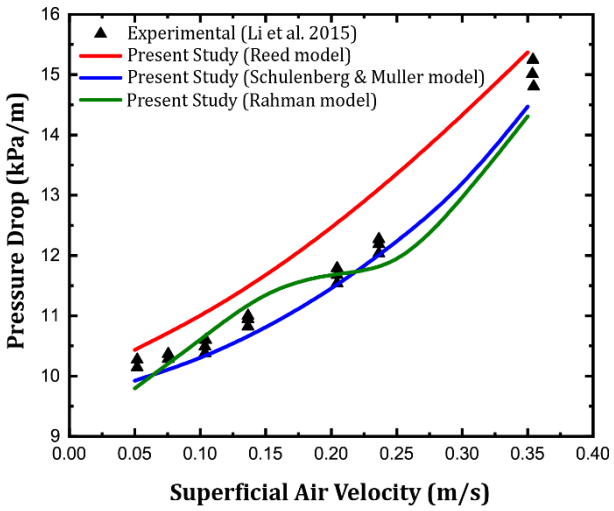

Figure 5.5 Comparison of pressure drop predicted by different drag models with experimental data of Li et al. (2015)

5.4.1.2.2 Heat transfer

Adequacy of the implemented heat transfer correlations has been tested by comparing experimentally determined dryout power with numerical predictions for all bed configurations considered in the present study. The results of this comparative study are summarised in Table 5.10. Dryout in the truncated conical bed configuration is initially assessed using all the implemented porous drag models. It is evident from this comparison that the most accurate prediction is achieved by using the Schulenberg and Müller drag model. Dryout in other bed configurations is, therefore, assessed using the Schulenberg and Müller drag model only. These comparisons clearly show that the present computational model is able to appreciably predict the dryout occurrence in all types of bed configurations considered in this analysis. Further analysis using this computational model is, therefore, justified.

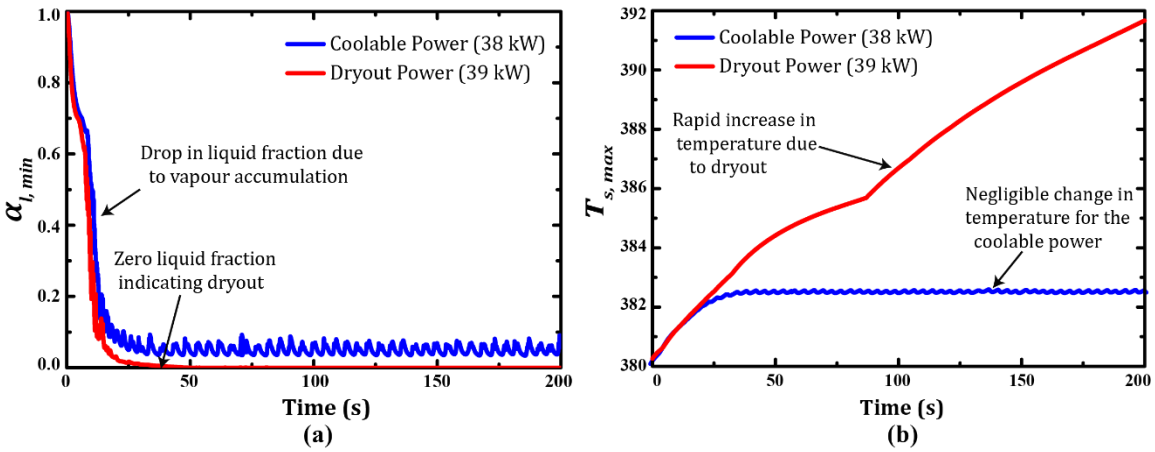

Figure 5.6 Temporal change of (a) $\alpha_{l,min}$ and (b) $T_{s,max}$ with Schulenberg and Müller drag model at two different heating power

Table 5.10 Comparison of experimental and numerical prediction of dryout

Bed Configuration	Dryout Assessment Study	Dryout Power (kW)	Dryout Power Density (kW/m^3)
Truncated Conical	COOLOCE Experiment (Takasuo 2016)	39.2	2602.0
	Present Study with Reed model	40.0	2655.16
	Present Study with Schulenberg & Müller model	39.0	2588.78
	Present Study with Rahman model	45.0	2987.05
Conical	COOLOCE Experiment (Takasuo 2016)	36	2349.87
	Present Study with Schulenberg & Müller model	37	2415.14
Fully-flooded Cylindrical	COOLOCE Experiment (Takasuo 2016)	40.1	2617.49
	Present Study with Schulenberg & Müller model	40	2610.96
Top-flooded Cylindrical	COOLOCE Experiment (Takasuo 2016)	20.4	1331.59
	Present Study with Schulenberg & Müller model	21	1370.75
	POMECO-HT Experiment (Li et al. 2012)	18	750
	Present Study with Schulenberg & Müller model	18	750

Figure 5.6 represents the temporal change of $\alpha_{l,min}$ and $T_{s,max}$ for two different heating power using the Schulenberg and Müller drag model. It can be observed that $\alpha_{l,min}$ drops to a very low value and oscillates about a mean value close to 0.05 in case of 38 kW power. The corresponding magnitude of $T_{s,max}$ remains near the saturation value at the prevalent system pressure of 1.3 bar ($T_{sat} = 380.259$ K). An increase of the heating power to 39 kW, however, results in a further decrease of $\alpha_{l,min}$ which ultimately becomes zero. The corresponding history of $T_{s,max}$ reveals that the solid temperature continues to rise unhindered in this situation. Thus, it can be concluded that dryout has

occurred within the debris bed. The maximum coolable power and the minimum dryout power predicted using the Schulenberg and Müller drag model is, thus, 38 kW and 39 kW, respectively. The minimum dryout powers for the other physical configurations tabulated in Table 5.10 are determined in a similar manner.

5.4.1.3 Grid independence study

The validated model is subjected to a comprehensive grid independence study in order to assess the influence of the computational grids. It is found that a nominal cell size of 3 mm (9560 cells in the entire domain) with a time step of 10^{-3} s is sufficient to appreciably predict the dryout occurrence as well as its location. The entire study is, therefore, carried out with the aforementioned time step size and grid size. Table 5.11 lists the minimum dryout power density obtained with the different grid sizes considered.

Table 5.11 Grid-independence study in terms of minimum dryout power density using the Schulenberg & Müller model

Nominal cell size (mm)	Number of cells	Dryout Power (kW)	Dryout Power Density (kW/m^3)
5	3658	32.0	2088.772 (12.5 %)
4	5771	36.0	2349.869 (7.69 %)
3	9560	39.0	2545.692 (0.0 %)
2	22723	39.0	2545.692

5.5 Results and Discussions

Investigations using the developed model is focused on assessing the impact of some of the pertinent parameters on multiphase flow and heat transfer and hence, on dryout in typical debris beds. The parameters investigated in the present work include bed composition, liquid subcooling, system pressure, bed configuration and flooding modes. In addition, an analysis on natural convective heat transfer considering phase change is also reported. The basic mechanism of multiphase fluid flow and heat transfer leading to dryout of the heat-generating porous bed is discussed briefly at the beginning before analysing the results from the parametric studies.

5.5.1 Basic mechanism of multiphase flow and heat transfer leading to dryout

The basic mechanism of multiphase fluid flow and heat transfer causing dryout in heap-like debris beds is discussed in this section considering a truncated conical bed (see Figs. 5.3 and 5.4). Porosity and particle size in the porous bed is assumed to be 0.4 and 0.95 mm, respectively. In addition, it is also assumed that the cavity is initially filled with saturated liquid water at 1.3 bar (T_{sat} = 380.259 K). The solid phase temperature is also assumed to be initially at the corresponding saturation value.

Heat generation within solid phase of the debris results in a rise in solid phase temperature and a consequent convective heat transfer from solid to the liquid phase. This causes the liquid phase temperature to increase as well. Boiling and interfacial liquid to vapour heat transfer becomes active as soon as the solid and the liquid temperature

exceeds the saturation value, respectively, and triggers vapour generation from the liquid phase. Thereafter, convective heat transfer from solid to vapour and interfacial heat transfer from vapour to liquid also starts contributing to the overall heat transfer. Liquid saturation distribution at 10s, shown in Fig. 5.7, highlights the vapour generation taking place within the debris bed. It must be noticed from the corresponding solid temperature distribution that although vapour generation has started, temperature of the solid phase remains near the saturation temperature suggesting adequate heat transfer from the porous bed.

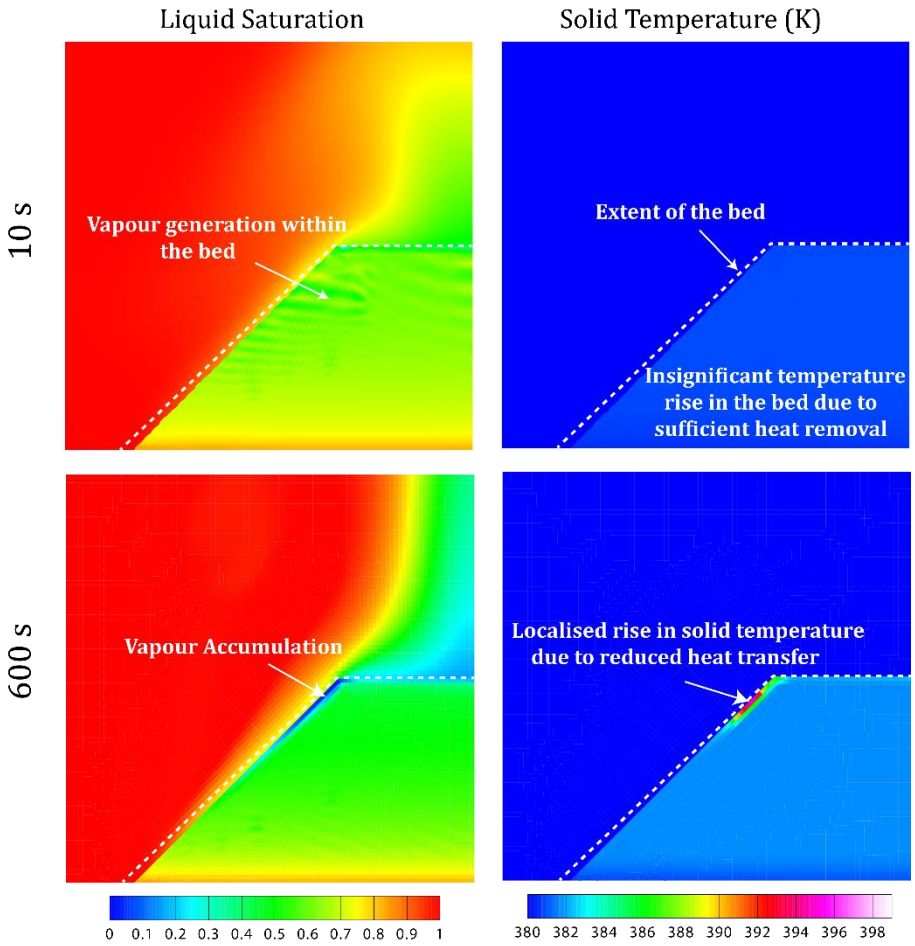

Fig. 5.7 Development of dryout in the debris bed in terms of liquid saturation and solid phase temperature distributions

The rise in temperature of the fluid phases within the debris bed creates a temperature gradient within the domain. This initiates a buoyancy-driven motion of the fluid phases out of the bed. Transport of the heated fluid phases out of the bed draws in the cooler liquid phase from the adjoining clear fluid region and ultimately results in the establishment of a counter-clockwise fluid circulation within the domain. The liquid and vapour velocity vectors within the cavity, represented in Figs. 5.8a and 5.8b, respectively, highlight the counter-clockwise fluid flow mechanism. Downward motion of the cooler liquid phase brings it in contact with the upward moving heated liquid as well as the vapour generated due to phase change. In a heap-like geometry, this interaction typically takes place near the top surface and the upper slant surface of the porous bed. A counter-

current type of flow situation is established in these regions of the bed (see Figs. 5.8c and 5.8d) retarding transport of the heated fluid phases out of the bed. As such, vapour starts to accumulate in such regions of the bed leading to localised dryout. This can be observed from the liquid saturation distribution at 600s in Fig. 5.7. Vapour accumulation reduces heat transfer from the heat-generating solid causing further rise in solid phase temperature (see Fig. 5.7). It is worthwhile to note that increase in solid phase temperature is localised to the dryout region only. Solid phase temperature in the rest of the bed remains close to the saturation temperature indicating sufficient cooling in these regions.

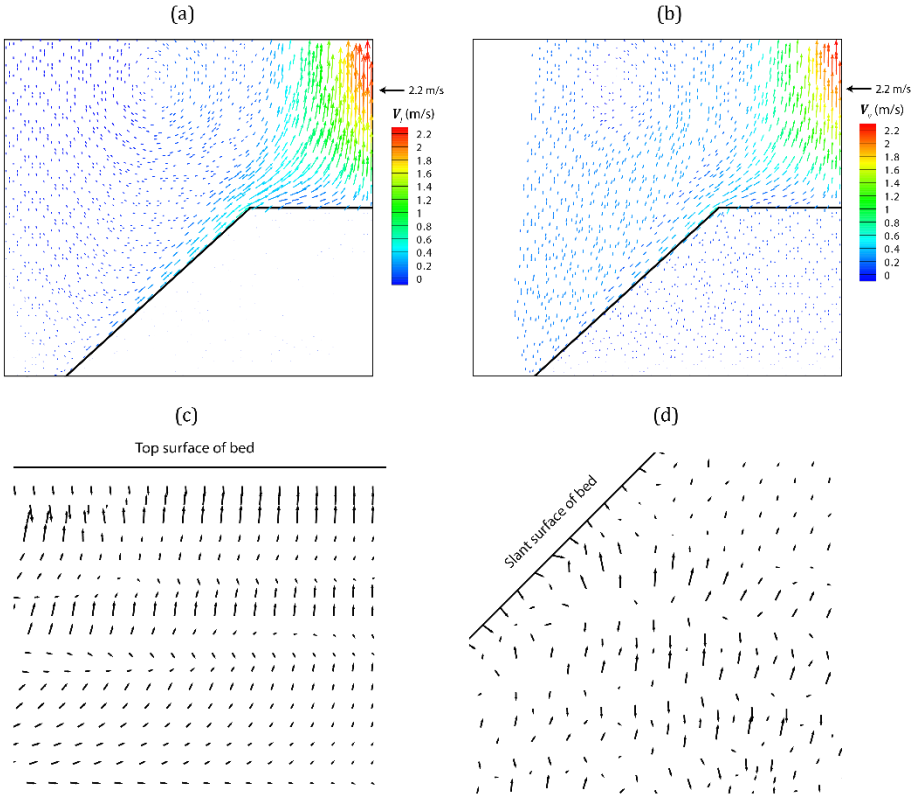

Fig. 5.8 Velocity vectors of (a) Liquid and (b) Vapour and zoomed-in view of liquid velocity vector in the porous bed near (c) top surface and (d) slant surface of the bed

5.5.2 Effect of bed composition

It is a well-established fact that the composition of porous media significantly influences the fluid flow as well as the heat transfer mechanism (see *Chapter 3* and *4*). It is expected that composition of the porous debris bed will have a similar impact in multiphase situations as well and hence, will substantially affect the dryout phenomena in the debris bed. This is analysed by performing independent variations with respect to the two parameters determining the bed composition viz. porosity (ε_f) and particle diameter (D_p). The range of the parameters are selected in accordance with reported experimental data in severe accident situations (see Table 1.1). The entire analysis is carried out at an ambient pressure of 1.3 bar (corresponding $T_{sat} = 380.259\ K$). Saturated liquid inflow is assumed from the top boundary (i.e. $T_{in} = T_{sat}$) and the entire system is initially assumed to be at the corresponding saturation temperature.

5.5.2.1 Bed porosity

The effect of bed porosity is assessed by varying ε_f in the range of 0.25 to 0.7 at a fixed particle size ($D_p = 0.95$ mm). An increase in ε_f at a particular D_p results in a larger bed permeability and vice-versa (see Eq. 2.63). A stronger fluid flow is, therefore, expected to take place through the bed if porosity is increased at a fixed D_p and constant heat generation. This is evident from the axial velocity profiles of the liquid and vapour phase at two different ε_f as represented in Fig. 5.9. The strengthening of fluid flow enables greater heat removal from the debris bed. A review of *Section 5.3* will reveal that porosity also influences heat transfer from the heat-generating solid particles with impact on the effective thermal conductivity of the constituent phases ($(1-\varepsilon_f)\lambda_s$ and $\alpha_j \varepsilon_f \lambda_j;\ j = l, v$) as well as interfacial area density (a_i). An increase in porosity, therefore, reduces the effective thermal conductivity of the solid particles but increases that for the fluid phases. The interfacial area density also decrease as porosity is increased. As a result, reduced heat transfer occurs from the solid particles to the fluid phases and consequently, the vapour generation also reduces.

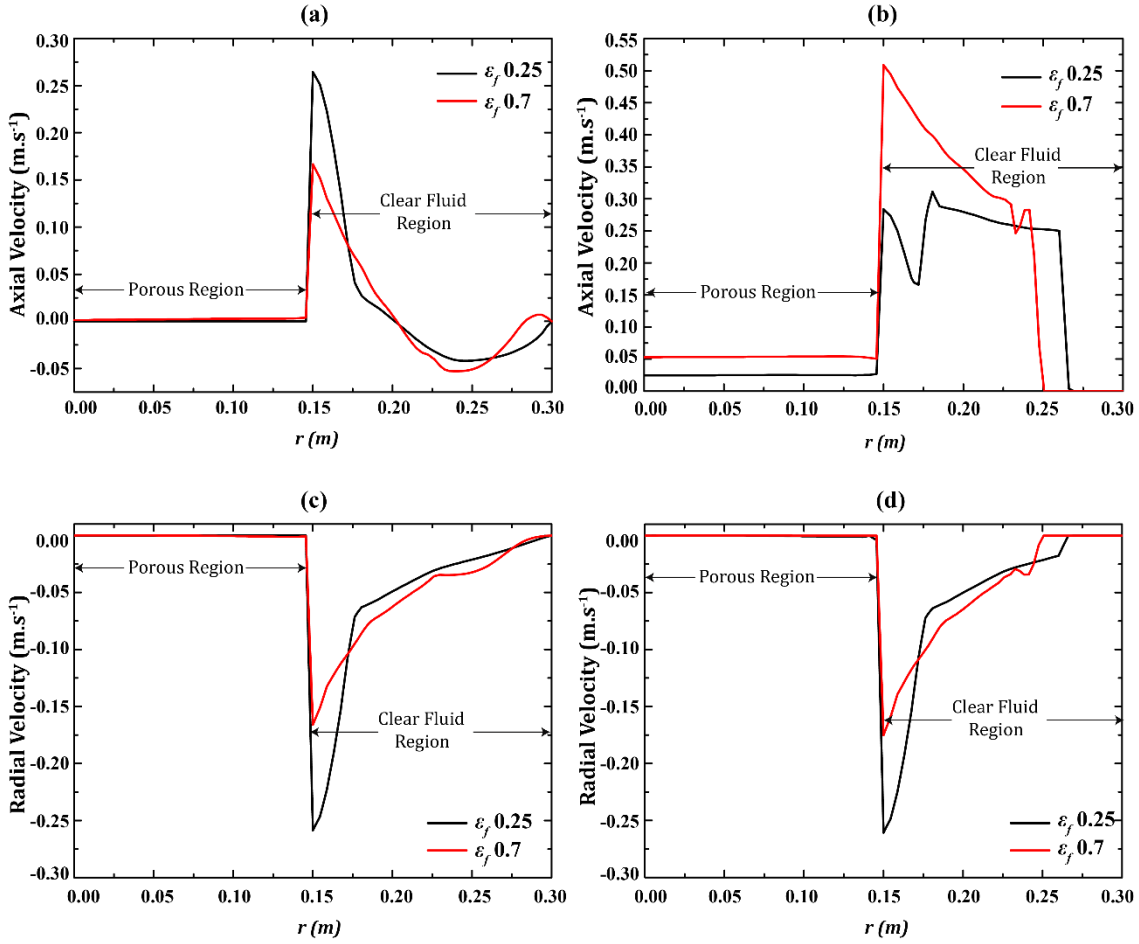

Figure 5.9 Profiles of axial velocity of (a) liquid (b) vapour and of radial velocity of (c) liquid (d) vapour at 300s for two different porosity at a heating power of 15 kW along the radial direction at z = 0.1m

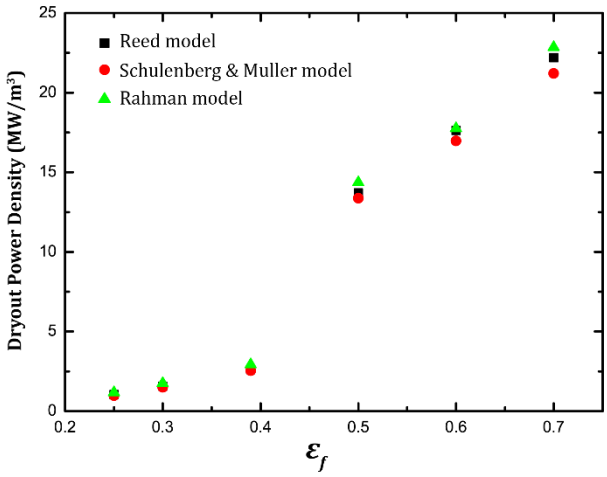

Figure 5.10 Variation in dryout power density with bed porosity at D_p = 0.95 mm

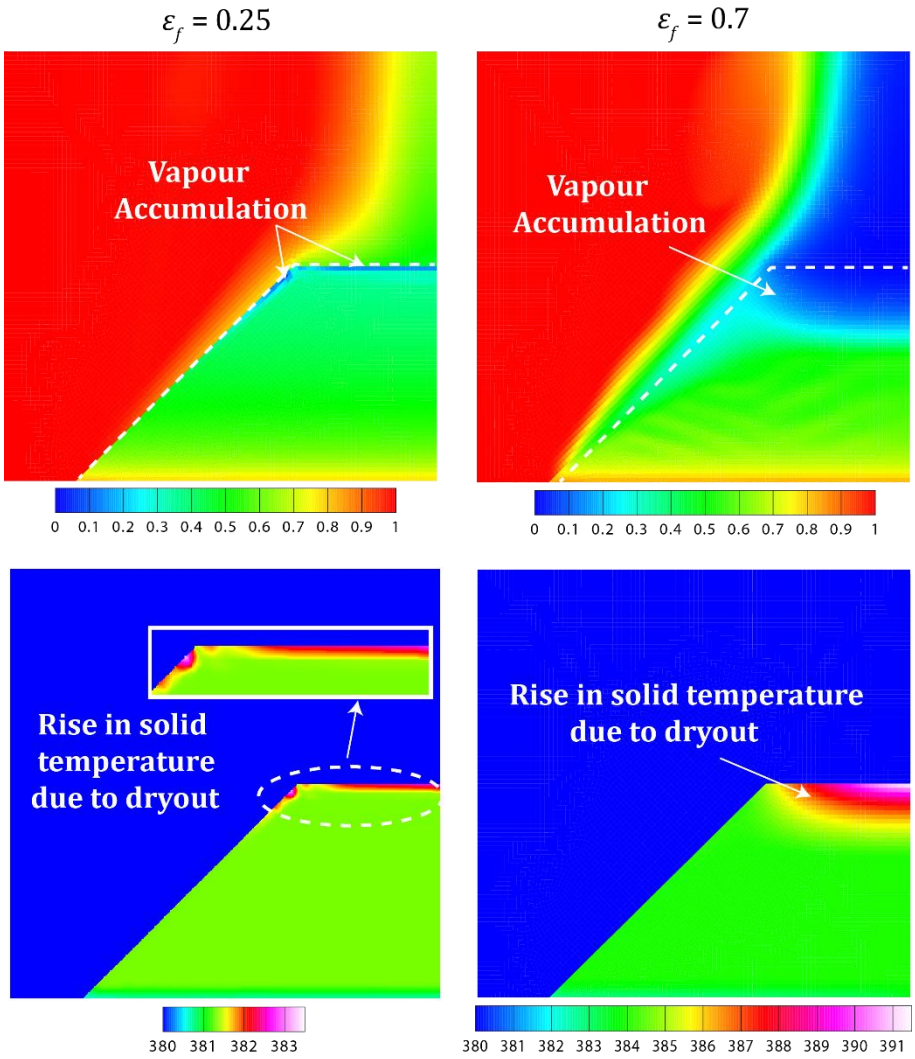

Figure 5.11 Liquid Saturation (upper row) and solid temperature (bottom row) distributions at dryout conditions (300 s) for ε_f = 0.25 and 0.7

Greater heat removal from the debris bed and a simultaneous reduction in vapour generation, leads to the requirement of a higher heat generation rate for substantial vapour accumulation to take place and cause dryout. The increase in dryout power density with

bed porosity is, however, not linear and is determined by the relative impacts of porosity on fluid flow and heat transfer. This is clearly evident from the variation of dryout power density with bed porosity in Figure 5.10. Interestingly, all the drag force correlations of porous media studied implemented in the numerical model predict a qualitatively similar change in dryout power density with bed porosity. However, quantitative differences exist between the predictions of the different correlations. These remain small at lower bed porosities but becomes significant as the porosity is increased.

Figure 5.11 represents the liquid saturation and solid temperature distribution at dryout conditions for bed porosity 0.25 and 0.7. Observation reveals that the dryout zone is formed near the slant face of the bed at low porosity while it shifts towards the top surface of the bed at high porosity.

5.5.2.2 Particle size

The impact of particle size on dryout power density is analysed by considering D_p in the range of 0.25 mm to 10 mm at a constant porosity ($\varepsilon_f = 0.39$) and the results are illustrated in Figs. 5.12 – 5.14. The distributions of liquid saturation and solid temperature at dryout conditions for two different particle diameters are shown in Fig. 5.12. Change in dryout power density with particle size variation is represented in Fig. 5.14.

Observation from Fig. 5.13 shows that an increase in particle size substantially increases the dryout power density. Previous experimental as well as numerical studies have also reported a similar effect of particle diameter on dryout (Bürger et al. 2006). A review of the modelling (*Section 5.3*) will show that D_p is inversely proportional to a_i and heat transfer coefficients. As a result, for a particular heat generation rate, heat transfer from the heat-generating solid particles to the fluid phases and the consequent vapour generation reduces as D_p is increased. A larger particle size also increases the bed permeability (see Eq. 2.63) allowing stronger fluid flow through the bed (see Fig. 5.13) and thereby, enables greater heat removal from the bed. As a consequence of these effects, a larger heat generation is required for substantial vapour accumulation to take place within the bed and cause dryout.

It is evident from Fig. 5.14 that the increase in dryout power density with particle diameter is not linear and is determined by the relative impact of D_p on the various fluid flow and heat transfer parameters. Qualitatively similar characteristics can be observed in the variation of dryout power density with the drag models although distinctive quantitative differences exist, especially at large values of D_p.

5.5.2.3 Overall effect

The discussions on the effects of porosity and particle size establish that both these parameters significantly affect the heat transfer and hence, dryout occurrence in a heat-generating porous debris bed. A considerable difference, however, exists with respect to the extent of these effects. This is represented in terms of the bed permeability in Fig. 5.15 by comparing the change in dryout power densities with porosity as well as particle diameter.

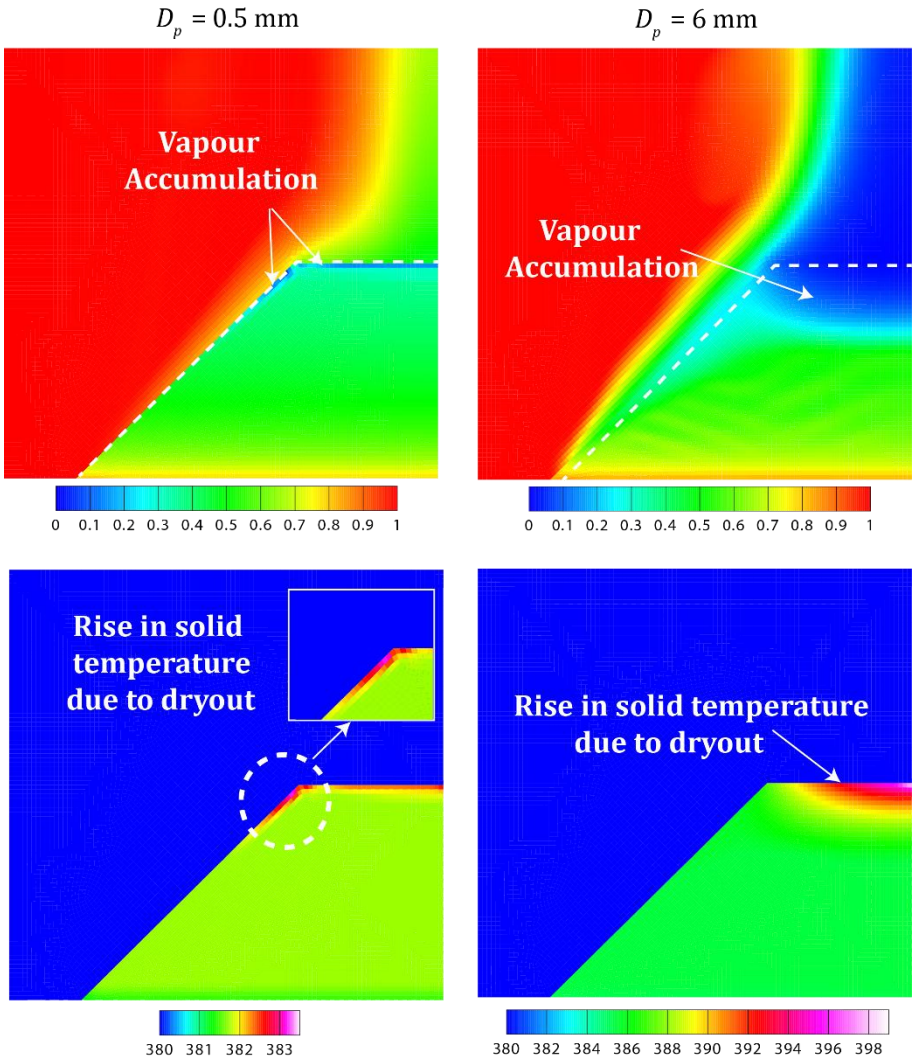

Figure 5.12 Liquid Saturation (upper row) and solid temperature (bottom row) distributions at dryout conditions (200 s) for $D_p = 0.5$ mm and 6 mm

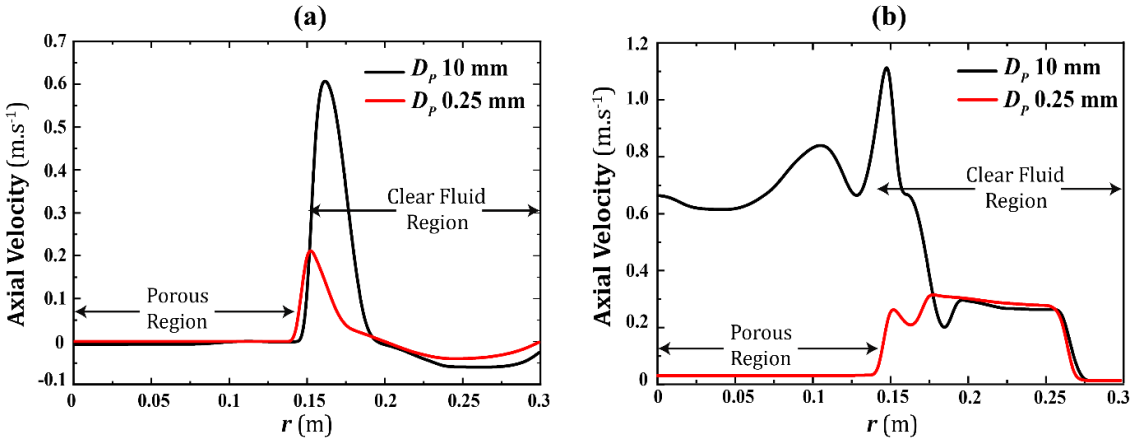

Figure 5.13 Axial velocity profiles of (a) liquid (b) vapour along the radial direction ($z = 0.1$ m) at 300s for two different particle sizes at a heating power of 12 kW

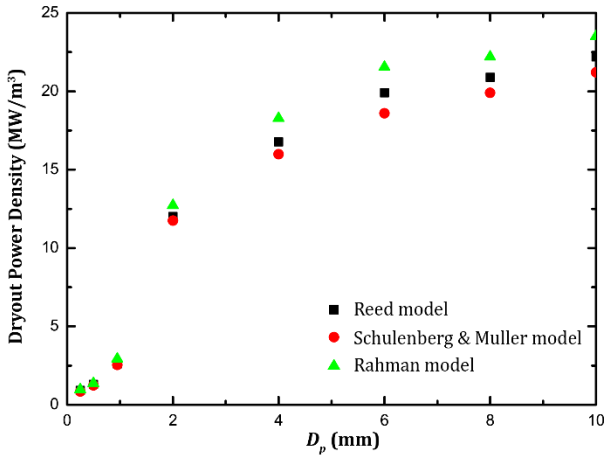

Figure 5.14 Variation in dryout power density with particle diameter at $\varepsilon_f = 0.39$

Although the difference is negligible at very low permeability, it becomes significant as the permeability increases and is indicated by the diverging nature of the two curves. At a particular bed permeability, the dryout power density is observed to be much higher in case of the porosity change than that in case of the particle diameter change. This indicates a much greater impact of porosity on the heat transfer mechanism. It can, thus, be seen that analysing the effect of bed composition on debris bed dryout in terms of bed permeability only is not a sufficient criteria and the analysis must take into account the effects of porosity as well as particle size independently. Interestingly, the location of the dryout zone is observed to be very similar (see Figs. 5.11 and 5.12) at low porosity and small particle size. A similar observation is made at high porosity and large particle size as well. This indicates that the dryout zone is ultimately determined by the bed permeability.

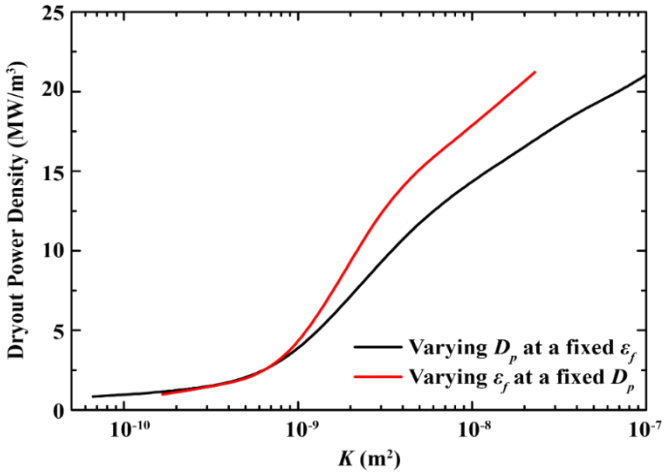

Figure 5.15 Dryout power density variation with bed permeability using the Schulenberg and Müller model

5.5.3 Effect of liquid subcooling

The effect of liquid subcooling on the heat transfer dynamics and occurrence of dryout in the debris bed is estimated by varying the temperature of the inflowing liquid up to 20K below the saturation temperature. The system pressure in this analysis is maintained at 1.3 bar while initial temperature of the debris bed and the saturating liquid

is assumed to be the saturation temperature and the corresponding subcooled temperature, respectively. The porosity and particle diameter of the debris bed are assumed to be constants at 0.39 and 0.95 mm, respectively. The dryout power obtained in case of saturated liquid (see *Section 5.4.1.2.2* and Table 5.10) is used as the reference power density in order to highlight the impact of subcooling on the heat and mass transfer dynamics.

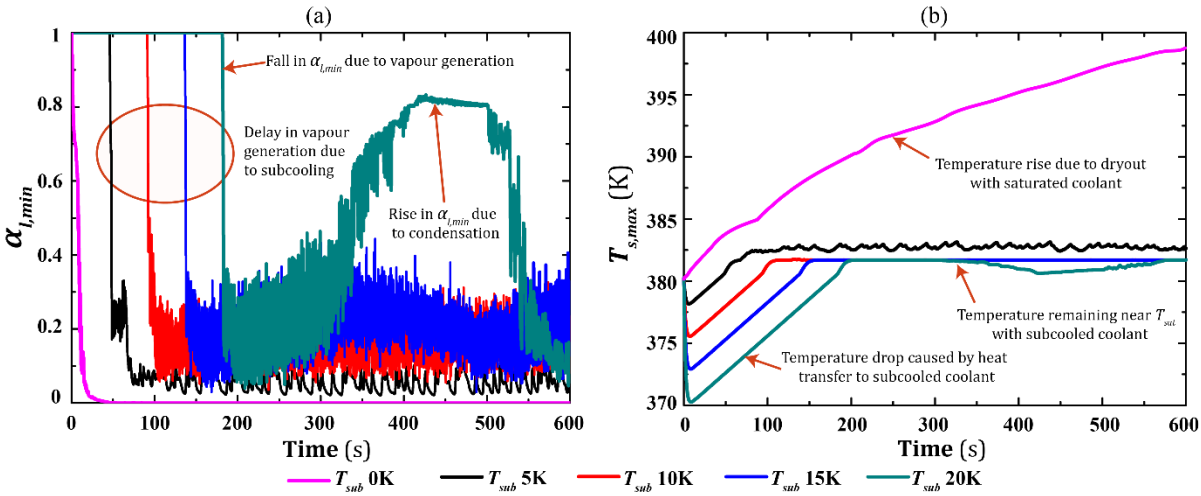

Figure 5.16 Temporal change of (a) minimum liquid saturation and (b) maximum solid temperature for different liquid subcooling using Schulenberg and Müller drag model

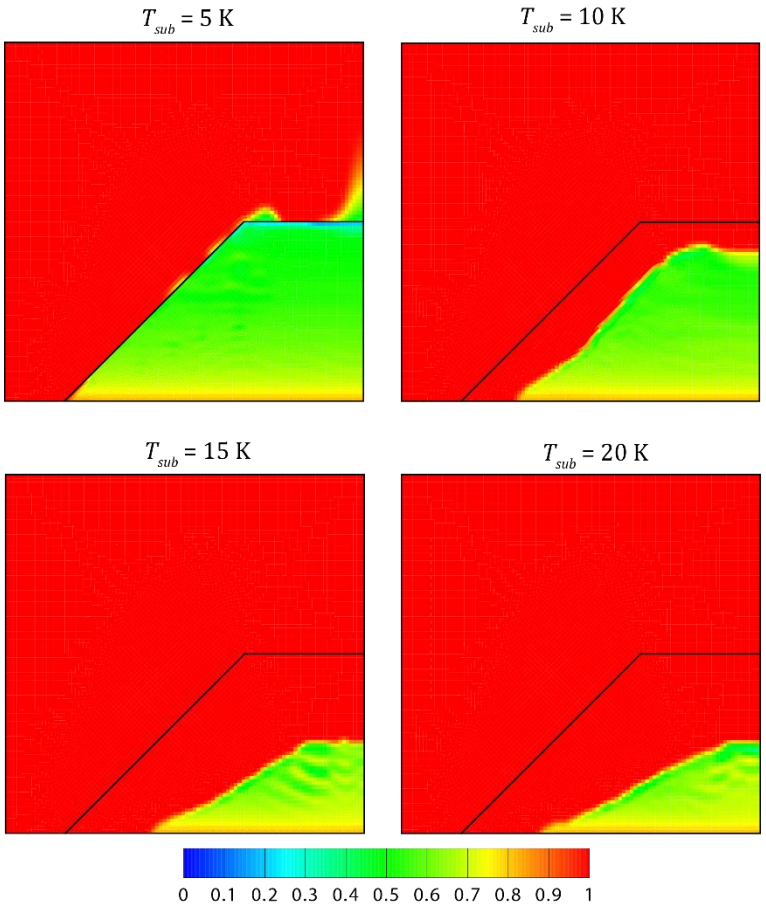

Figure 5.17 Liquid saturation distributions for different liquid subcooling at 250s using the Schulenberg & Müller model

Figure 5.16 shows the temporal change of $\alpha_{l,min}$ and $T_{s,max}$ for different liquid subcooling using the Schulenberg and Müller drag model. Qualitatively similar characteristics are also observed using the models of Reed and Schmidt. In case of saturated liquid inflow i.e. $T_{sub} = 0$K, vapour generation in the heat-generating bed starts almost instantly due to nucleate boiling of the saturated liquid and is reflected by the fall of $\alpha_{l,min}$ below 1.0 in a short time. The magnitude of $\alpha_{l,min}$ continues to decrease and becomes zero after a certain time interval indicating dryout of the debris bed. This is also evident from the sustained rise in $T_{s,max}$ for $T_{sub} = 0$K.

Heat transfer dynamics is observed to change significantly in presence of liquid subcooling. Heat transfer takes place from the heat-generating solid particles to the subcooled liquid leading to a decrease in T_s and a consequent rise in T_l. This continues until the solid particles come to a thermal equilibrium with the liquid phase. It is to be noted here that the temperature at which thermal equilibrium is reached reduces as the subcooling is increased. Thereafter, T_s starts to rise due to negligible heat transfer to the liquid phase and after a certain time interval exceeds the saturation temperature. Nucleate boiling of the saturating liquid starts in this situation resulting in vapour generation and a subsequent drop in the magnitude of $\alpha_{l,min}$. It is also to be noted that the time interval till the onset of boiling gradually becomes longer as liquid subcooling is increased.

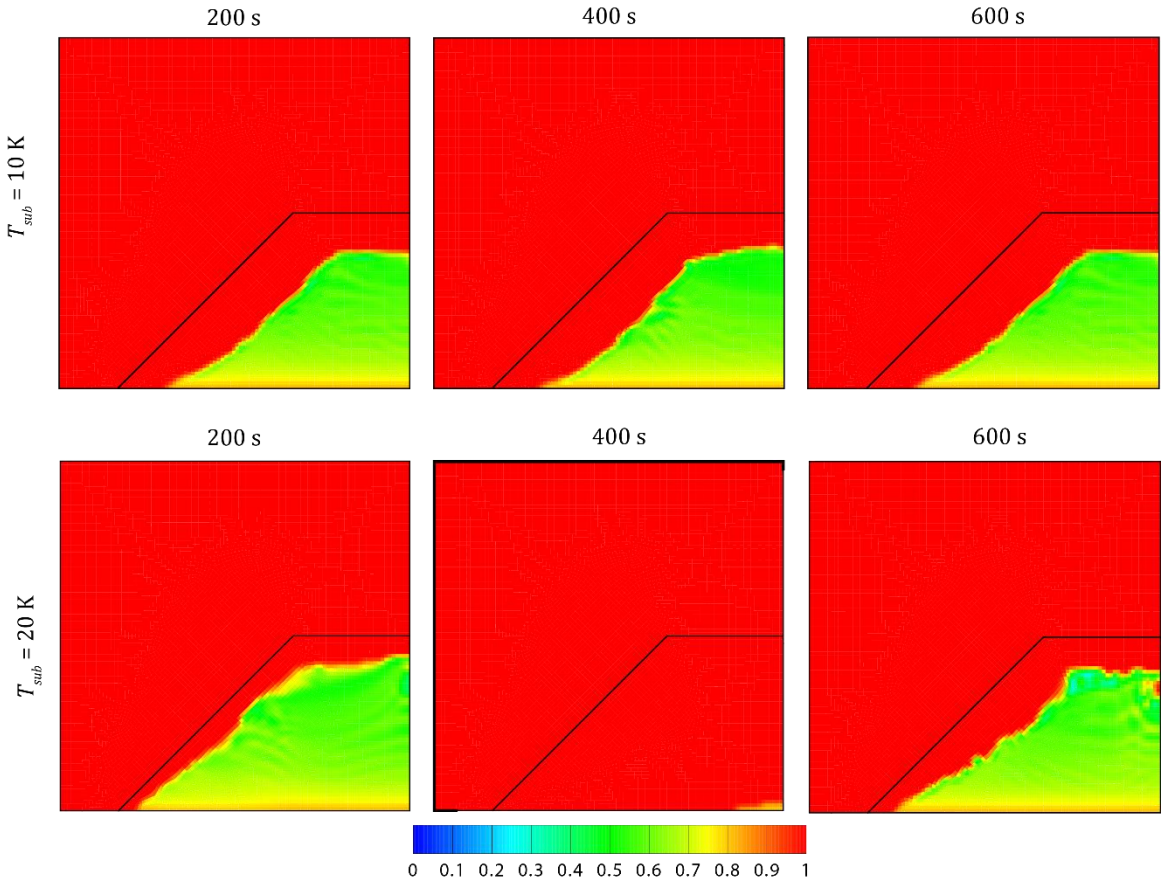

Figure 5.18 Liquid saturation distribution at different time instances for liquid subcooling of 10 K and 20 K

Continuous influx of subcooled liquid into the domain results in the vapour generated coming into contact with the subcooled liquid. This leads to simultaneous condensation of the vapour generated. The total mass of vapour present within the domain at a particular instant of time is, thus, determined by the relative dominancy of the vapour generation and condensation phenomena. Less amount of vapour is expected to be present in case of the highest subcooling due to a higher condensation rate and vice-versa. This can be visualised by a comparison of liquid saturation distribution at a particular time instant between different liquid subcooling in Fig. 5.17. Interestingly, it is observed that greater liquid penetration takes place into the debris bed as the subcooling becomes larger. This enables sufficient heat removal from the peripheral regions of the bed and confines the generated vapour to the inner region of the bed. It is also observed that the volume of the vapour accumulated region shrinks with increase in subcooling.

The competing phenomena of vapour generation and condensation leads to strong oscillations in the magnitude of $\alpha_{l,min}$ for different liquid subcooling as can be observed from Figure 5.16(a). The magnitude of $\alpha_{l,min}$ drops to a very low value and oscillates for liquid subcooling up to 15K. The transient history, however, indicates a significantly different characteristic in case of $T_{sub} = 20$K. A comparison of liquid saturation distributions for $T_{sub} = 20$K at different time instances (Fig. 5.18) reveal that the vapour present within the bed at 200 s condenses almost fully within 400 s leading to an increase in $\alpha_{l,min}$. The vapour generation rate exceeds the condensation rate after a certain time period leading to re-accumulation of vapour within the bed. This is evident from the liquid saturation distribution at 600s. The magnitude of $\alpha_{l,min}$, as such, falls again to a lower value and this phenomena continues with time. Dryout, therefore, does not occur with subcooled liquid at the power density at which dryout is observed with saturated liquid. This is also corroborated by the transient history of $T_{s,max}$ in Fig. 5.16(b).

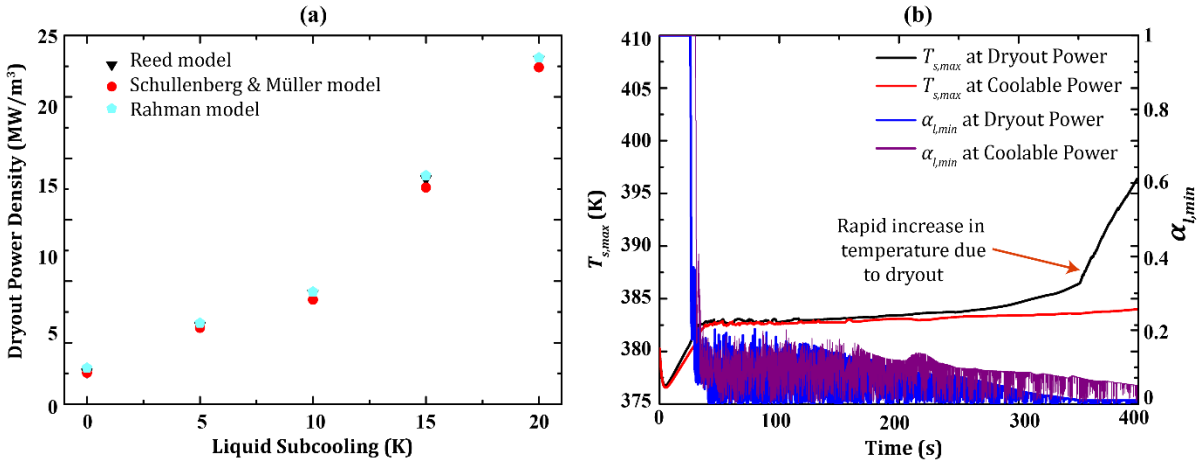

Figure 5.19 (a) Variation of dryout power density with liquid subcooling (b) Transient history of $\alpha_{l,min}$ and $T_{s,max}$ at 10K subcooling using the Schulenberg and Müller model

It is expected, therefore, that a very high power density will be required for substantial vapour accumulation to take place in presence of subcooled liquid and cause dryout of the debris bed. The minimum power density at which dryout occurs becomes

progressively higher as the liquid subcooling increases. This is evident from Fig. 5.19a. Figure 5.19b shows the transient history of $T_{s,max}$ and $\alpha_{l,min}$ with $T_{sub} = 10$ K at two different power densities – a coolable state and a dryout state using the Schulenberg and Müller model. A rapid rise in $T_{s,max}$ indicates the dryout of the bed.

The generated vapour remains confined to the interior of the bed in case of liquid subcooling and hence, the dryout zone is also formed in these regions. This can be visualised from Fig. 5.20 wherein the dryout zone is identified by localised rise in solid temperature.

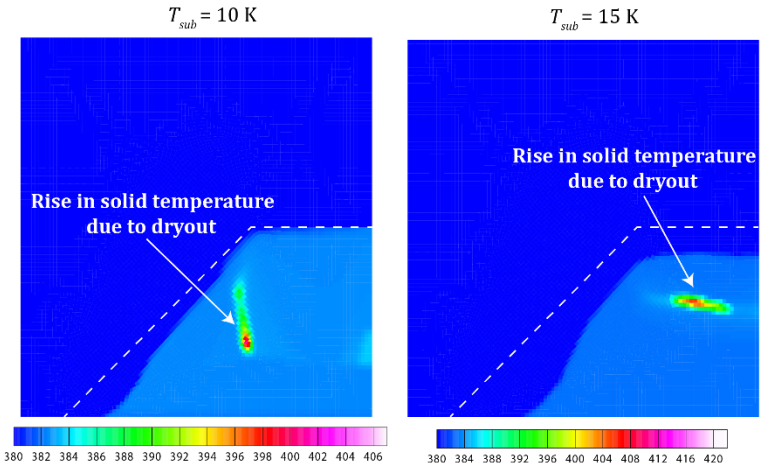

Figure 5.20 Solid temperature distribution at dryout condition (480 s) using the Schulenberg and Müller model for $T_{sub} = 10$ K and 15 K

5.5.4 Effect of system pressure

The effect of system pressure on dryout characteristics of the debris bed is studied by varying the system pressure in the range of 1 – 10 bar, which is relevant to severe accident situations. It can be observed from Fig. 5.21 that the dryout power density increases substantially as the system pressure is progressively raised.

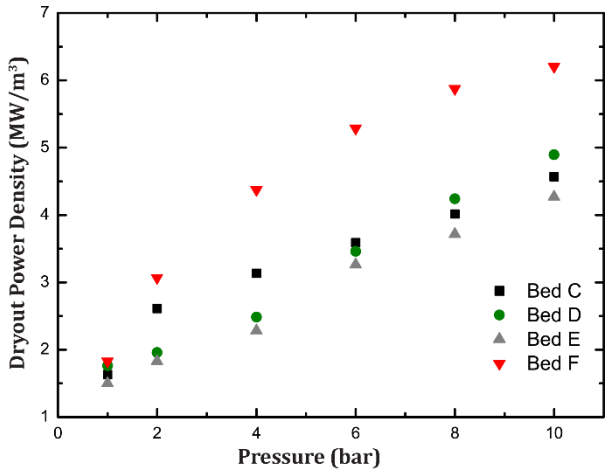

Figure 5.21 Dryout power density obtained with different bed configurations over the entire range of system pressure

A higher operating pressure results in a significant increase in vapour density. The volume occupied by the vapour generated is, therefore, much lower for the same mass transfer rate. Hence, a higher mass transfer rate is required for vapour accumulation necessary for dryout occurrence. At the same time, a reduced volume of vapour formed allows a larger flow area for the liquid water which enhances the heat removal from the debris bed. The above two factors contribute to the necessity of a higher heating power for dryout occurrence.

5.5.5 Effect of bed configuration

The effect of debris bed configuration on dryout occurrence has been studied by considering bed configurations C, D, E and F (see Fig. 5.3) over the entire range of system pressure (1 bar – 10 bar) considered in *Section 5.5.3*. Bed configurations C and D are cylindrical beds while beds E and F are conical and truncated conical in structure, respectively (see Fig. 5.3). As is evident from the schematic layout, heat removal from the debris bed takes place through top flooding and lateral flooding of the coolant in all these configurations. The porosity and particle diameter of the debris bed are assumed to be constants at 0.39 and 0.95 mm, respectively. Figures 5.23 and 5.24 represent the liquid saturation distribution and solid temperature distribution at dryout conditions for different bed configurations at 4 bar system pressure.

It is clearly evident from Fig. 5.21 that the maximum and the minimum dryout power density is achieved for the truncated conical bed (Bed F) and the conical bed (Bed E), respectively, over the entire range of operating pressure considered. An intermediate dryout power density is predicted for the cylindrical beds. A closer observation will reveal that the shallower bed (Bed C) has a relatively higher dryout power density up to an operating pressure of 6 bar beyond which the taller bed (Bed D) is predicted to have a marginally higher dryout power density. This is determined by the impact of increasing pressure on the strength of fluid circulation within the domain and the resistance provided by the lateral flow passage of Beds C and D against fluid circulation.

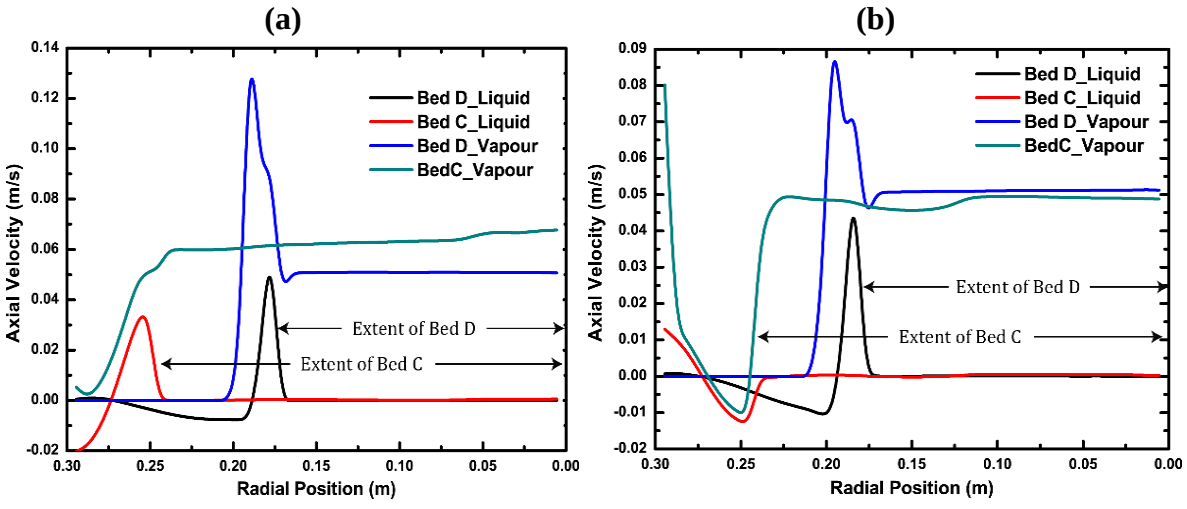

Figure 5.22. Axial velocity profiles along the radial direction at z = 0.05 for Bed C and Bed D at (a) 4 bar and (b) 8 bar

The fluid flow passage in the radial direction reduces drastically for Bed C when compared to Bed D (see Fig. 5.3). In case of Bed D, the fluid flow passage is large enough such that the small flow resistance offered does not significantly influence the flow pattern although the circulation strengths undergo substantial change due to increasing pressure. This is evident from a comparison of the velocity profiles for two different pressures in Fig. 5.22. In contrast, a relatively larger resistance is faced by the fluids while flowing through the narrow passage in case of Bed C. This weakens the fluid circulation in the narrow passage as evident from the velocity profiles in Figs. 5.22a and 5.22b. It can also be observed from Fig. 5.22a that vapour velocity within Bed C is substantially higher than that in Bed D at 4 bar pressure. This enables larger heat transfer from the bed leading to a higher dryout power density for Bed C. Vapour velocity within Bed C, however, reduces to become marginally less than that in Bed D as the pressure is increased to 8 bar (see Fig. 5.22b). As such, heat transfer from the bed decreases and consequently, the dryout power density for Bed C becomes marginally lower than that of Bed D at 8 bar pressure.

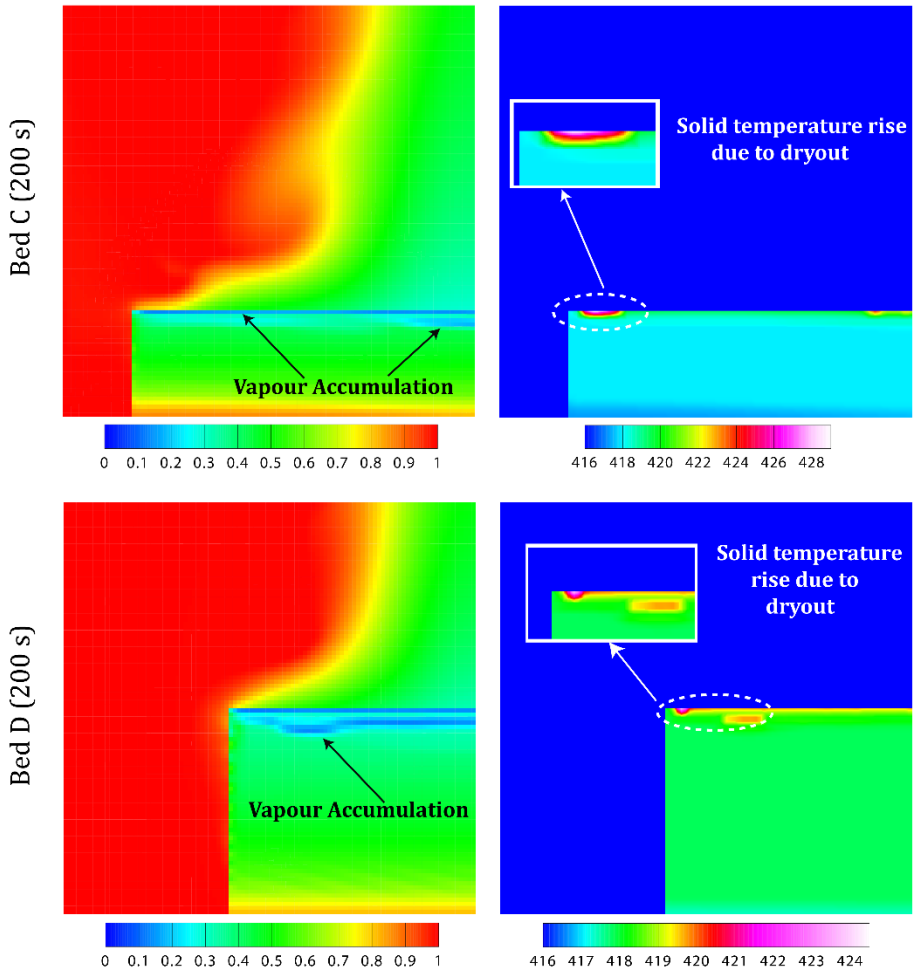

Figure 5.23 Dryout in the cylindrical beds (Bed C and Bed D) at 4 bar operating pressure in terms of liquid saturation (left) and solid temperature (right) distributions. An enlarged view of dryout zone is shown as inset in solid temperature distributions.

This variation in dryout power density with change in bed geometry is determined by the combined effect of two factors, namely - height of the porous bed and surface area of the bed in contact with the clear fluid region. It has been observed experimentally that a shallow bed has a larger dryout power density than a taller bed of equivalent volume. The vapour mass flux necessary for dryout occurrence remains almost same for different bed geometries having equivalent volume. As such, a larger power is required for achieving the vapour mass flux in case of the shallow bed and hence, the higher dryout power density. Surface area of the porous bed in contact with the clear fluid region also has a significant effect on the dryout power density. The top surface of the bed facilitates upward motion of the vapour generated within the bed while the lateral surface is favourable for coolant infiltration into the bed. An increase in the lateral surface area, therefore, favours enhanced heat removal from the bed and contributes to an increase in the dryout power density of the bed.

It is evident from Table 5.12 that the conical bed (Bed E) has the maximum height and largest lateral surface area among all the bed configurations. However, a non-existent top surface forces the water vapour to exit and the cooling water to infiltrate the bed across its lateral surface only (in contrast to cylindrical and truncated conical configurations). This hinders fluid motion across the lateral surface and hence, reduces heat transfer from the bed. As such, the increase in dryout power density due to the large lateral surface area remains relatively low. The overall effect is such that the conical bed has the lowest dryout power density among all the bed configurations considered in the present study.

Table 5.12 Height and surface area for different bed configurations

Bed Configuration	Height (m)	Lateral Surface Area (m^2)	Top Surface Area (m^2)
C	0.078	0.122538	0.196375
D	0.15	0.169668	0.1018008
E	0.234	0.26894	0
F	0.15	0.23325	0.03142

The increase in dryout power density for the other bed configurations (see Fig. 5.21) clearly indicate the effect of reduced bed height on dryout. A closer observation reveals the associated non-linearity. The maximum dryout power density is obtained not for the shallowest bed (Bed C) but for a bed with an intermediate height (Bed F). A substantial difference is also observed between the predicted dryout densities for Bed D and Bed F, which have the same height. These can attributed to the effects of lateral surface area of the porous bed in contact with the fluid region.

The effects of bed height and surface area aid each other for bed configurations D (cylindrical) and F (truncated conical) such that the dryout power density increases for both configurations. Although these bed configurations have the same height, there is a significant difference in the lateral surface area of the beds (see Table 5.12). The configuration with the larger lateral surface area (Bed F) has a larger dryout power

density. In case of Bed C, however, the effects of bed height and surface area are in opposition to each other. The bed height reduces (with respect to Bed D) necessitating an increase in dryout power density. The lateral surface area also reduces (with respect to Bed D) resulting in decreased cooling of the bed and a consequent lower power requirement for dryout. The combined effect of these two factors result in a dryout power density which is substantially higher than that of the conical bed but much lower than that of the truncated conical bed. Further, it can be seen that the increase in dryout power density for Bed C with respect to the Bed D actually reduces with the increase in operating pressure such that it becomes lower than that of Bed D for operating pressure beyond 6 bar.

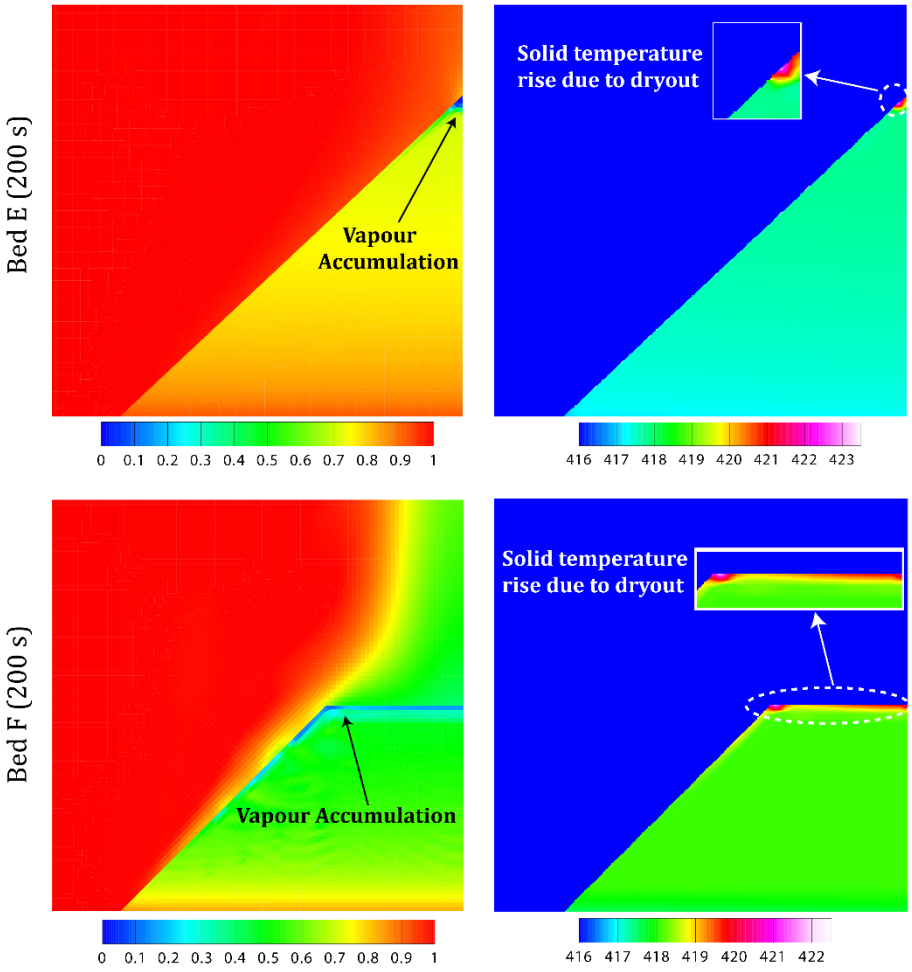

Figure 5.24 Dryout in the conical and truncated conical beds (Bed E and Bed F) at 4 bar operating pressure in terms of liquid saturation (left) and solid temperature (right) distributions. An enlarged view of dryout zone is shown as inset in solid temperature distributions.

Figures 23 and 24 represent the liquid saturation, liquid velocity vectors, solid temperature distribution and vapour velocity vectors at dryout condition for the conical bed (Bed E), cylindrical beds (Bed C and D) and truncated conical bed (Bed F), respectively, at 4 bar operating pressure. The dryout zone in all these bed configurations

is formed in the upper region of the bed indicating that bed configuration does not significantly influence the location of the dryout zone.

5.5.6 Effect of coolant flooding modes

Bed configurations A, B and C (all cylindrical beds) have been taken into consideration while studying the effect of coolant flooding modes on the occurrence of dryout. The operating pressure for this analysis is considered to be 1 bar. Porosity and particle diameter are assumed to be constants in this analysis at 0.39 and 0.95 mm, respectively. The results obtained are represented in Fig. 5.25. It can be observed that the minimum dryout power density is obtained in case of the purely top-flooded bed (Bed A). Substantially higher dryout power densities are obtained in case of the laterally-flooded (Bed C) as well as the bottom-flooded (Bed B) bed configurations.

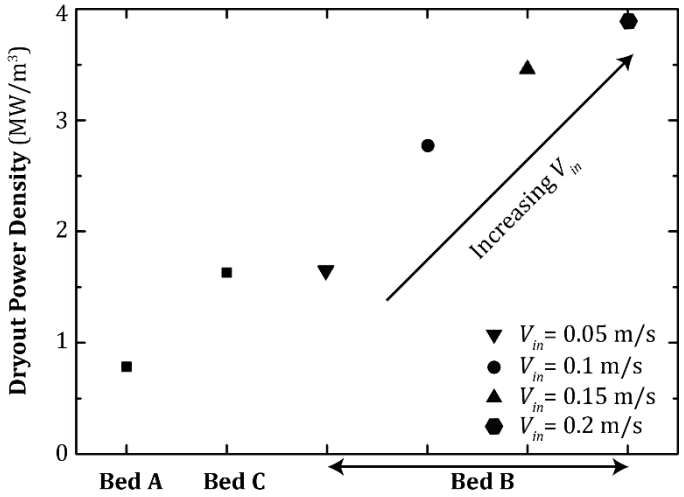

Figure 5.25 Dryout power density obtained with different coolant flooding modes

In the purely top-flooded configuration, the two fluid phases i.e. liquid and vapour have opposing flow paths across the debris bed. Cold water moves downwards and tries to infiltrate the debris bed across the top surface of the bed. Simultaneously, heated water as well as water vapour generated within the bed moves upward due to buoyancy. This establishes a counter-current flow of liquid and vapour across the debris bed as shown in Fig. 5.26a. The upward moving vapour, as such, faces resistance from the downward moving liquid water such that vapour accumulation initially takes place typically in the upper region of the debris bed (Fig. 5.28). The cold liquid phase, therefore, becomes unable to further penetrate into the bed. This is evident from the negligible axial velocity of liquid phase in Fig. 5.27. As a consequence, heat removal from the inner region of the bed reduces substantially and leads to expansion of the vapour accumulated zone with time due to continuing vapour generation (Fig. 5.28). The corresponding solid temperature distribution in Fig. 5.28 shows that the temperature of the solid phase increase and forms a localised hot spot within the vapour accumulated zone, typical to a dryout situation.

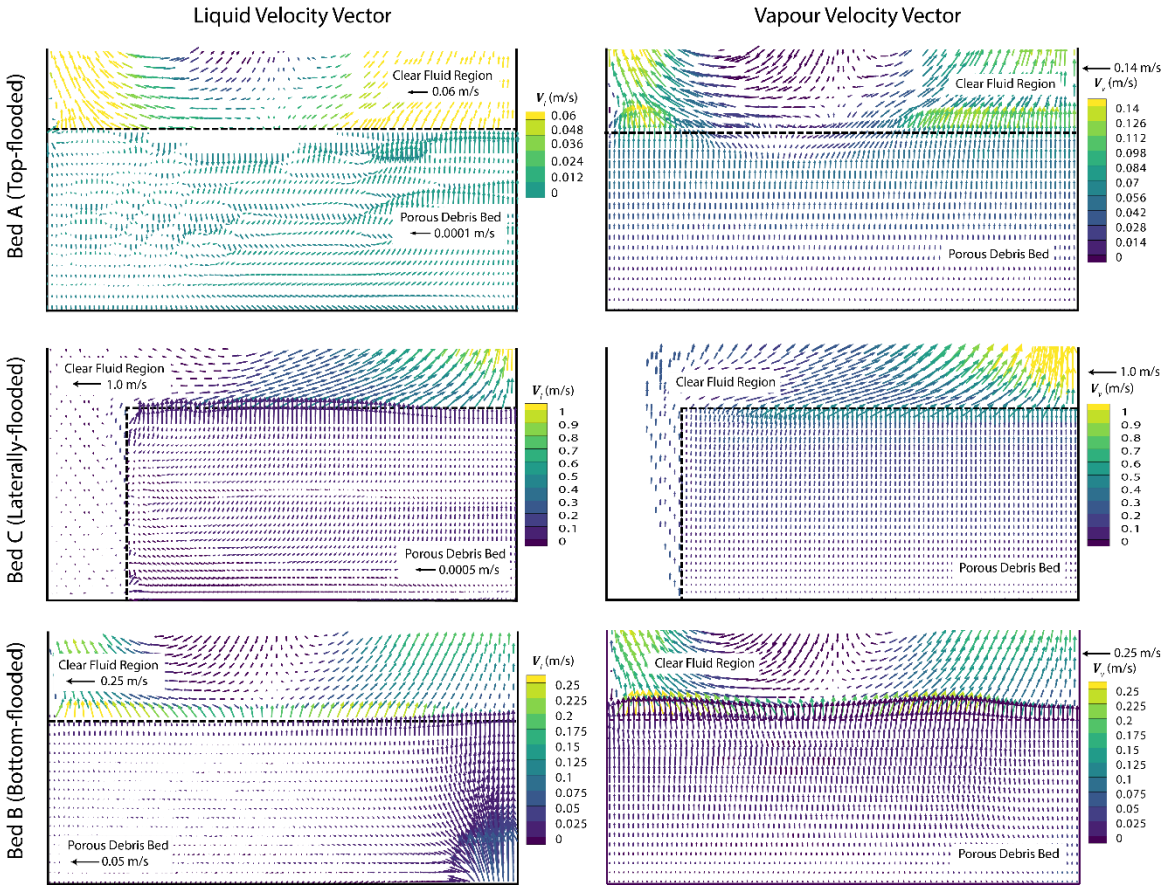

Figure 5.26 Liquid and vapour velocity vectors within the debris bed and the adjacent clear fluid region for top-flooded, laterally-flooded and bottom-flooded bed configurations

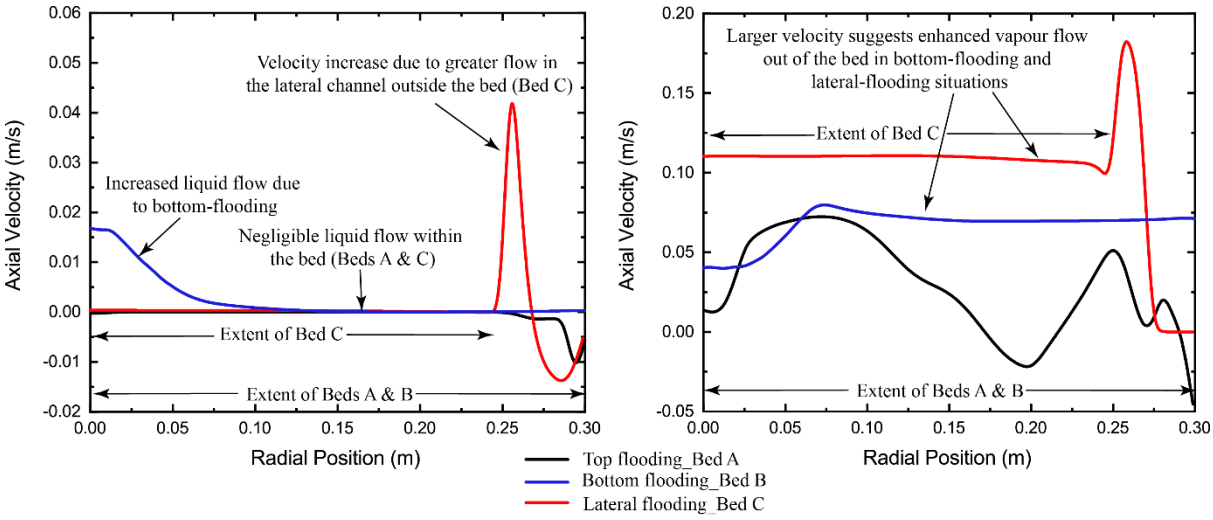

Figure 5.27 Axial velocity profiles of liquid (left) and vapour (right) along the radial direction for Beds A, B and C at $z = 0.03$ m

A provision of fluid flow across the lateral surface of the debris bed allows the cold liquid water to bypass the vapour accumulated region in the upper region of the bed and

effectively remove heat from the lower regions of the bed. The fluid flow pattern in such laterally flooded situations is shown in Fig. 5.26b. A counter-clockwise fluid motion is established such that cold liquid water enters the domain from the top left corner, removes heat from the debris bed and a heated liquid water-water vapour mixture leaves the domain across the top right corner. As a consequence of this flow mechanism, a much higher heating power is required for the requisite vapour accumulation to take place within the bed which can lead to dryout. The dryout power density in laterally flooded beds, therefore, becomes significantly higher. The corresponding liquid saturation distribution and the solid temperature distribution in dryout condition is shown in Fig. 5.29. It can be observed that the hotspot formed is much more localised than that in the top-flooding configuration. This happens since the flow mechanism is such that the vapour generated is pushed out of the bed (as evident from Fig. 5.29) and the vapour accumulation takes place only in a very small region of the bed.

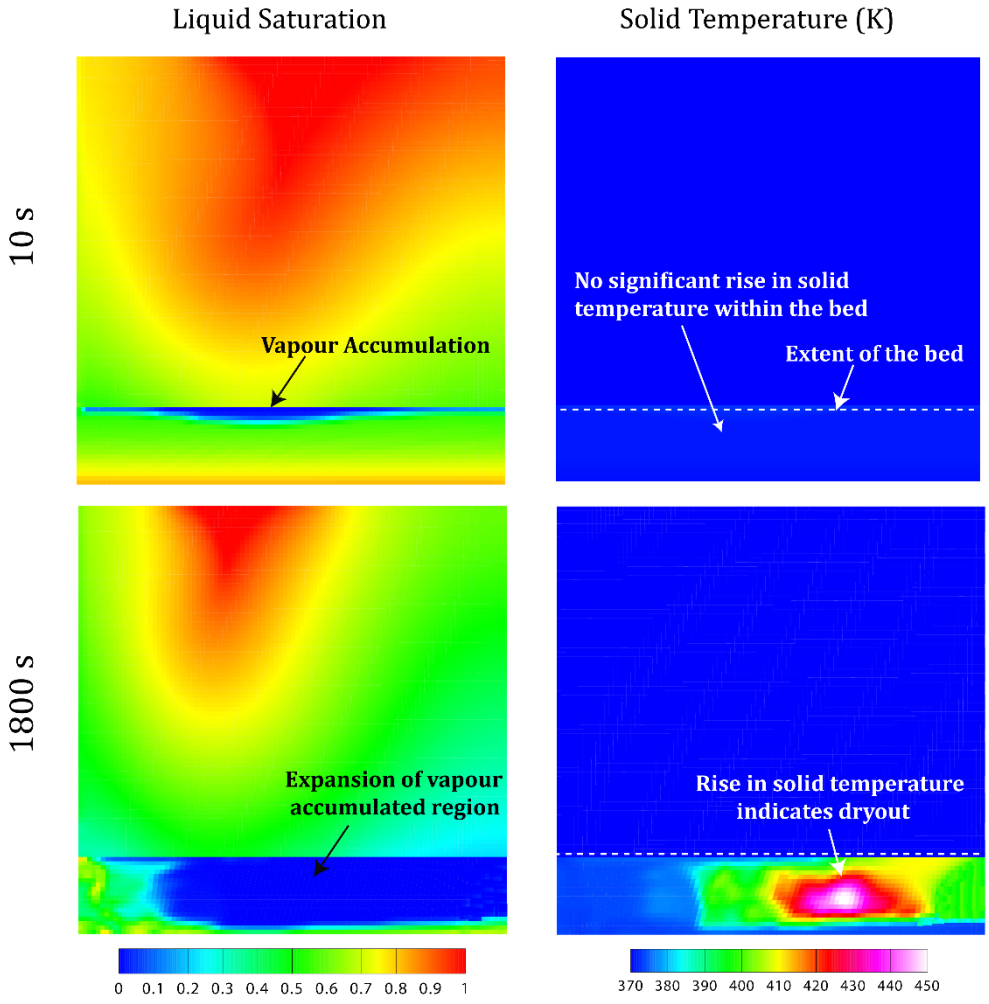

Figure 5.28 Liquid saturation and solid temperature distribution at two different time instances for the top-flooding bed configuration (Bed A)

It is clearly evident from Fig. 5.25 that a much more effective way of augmenting the dryout power density is by injection of cold water through channels placed at the

bottom of the bed. The dryout power density is observed to be enhanced significantly even for a small injection velocity (0.05 m/s) and it continues to increase as the injection velocity is progressively increased. A co-current flow pattern is established within the bed (as shown in Fig. 5.26c) which enables efficient heat removal from the inner regions of the bed. A higher flow velocity further enhances heat transfer from the solid particles to the fluid phases. As a result, a substantially higher heating power is required for the required vapour accumulation within the debris bed which can cause dryout. Figure 5.30 shows the liquid saturation and solid temperature distributions, respectively, at dryout condition for V_{in} = 0.05 m/s.

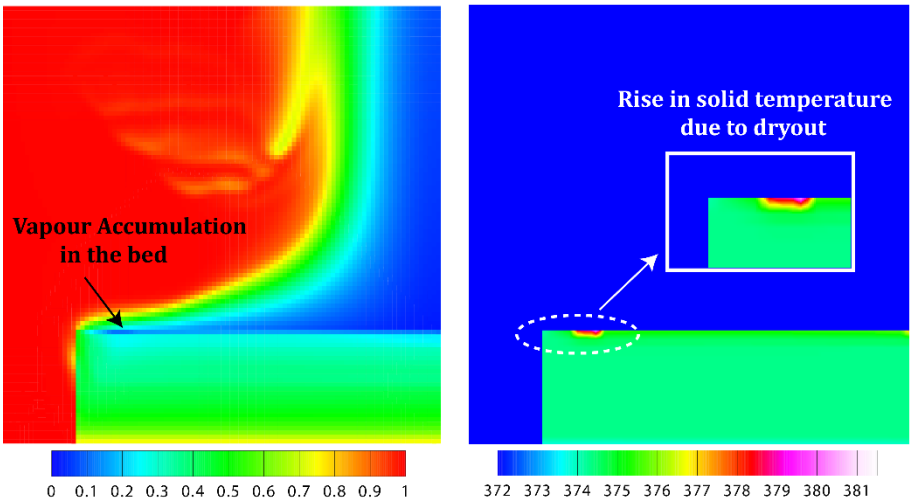

Figure 5.29 Liquid saturation (left) and solid temperature (right; in K) distributions at 600 s for the lateral-flooding bed configuration (Bed C). An enlarged view of dryout zone is shown as inset in the solid temperature distribution.

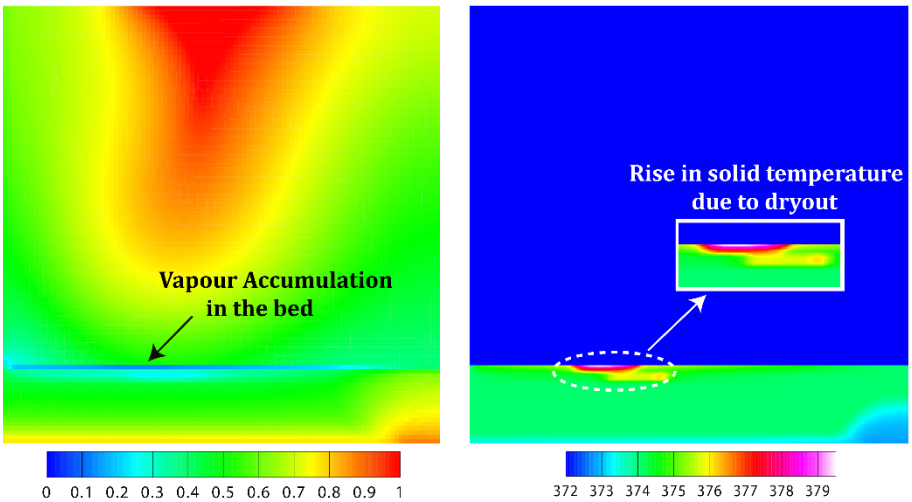

Figure 5.30 Liquid saturation (left) and solid temperature (right; in K) distributions at 260 s for the bottom-flooding bed configuration (Bed B). An enlarged view of dryout zone is shown as inset in the solid temperature distribution.

5.5.7 Natural convection

The analysis of debris coolability under natural convective situation is important in view of ensuring long-term coolability of the debris bed. A heap-like debris bed, approximated by a truncated conical structure, is adopted for this analysis. The boundary conditions utilised in the preceding analyses are modified such that in this analysis the top and side boundaries of the domain are assumed to be impermeable and are maintained at a constant temperature. The modified geometry adopted for this analysis is represented in Fig. 5.31. The porosity and particle diameter of the debris bed are assumed to be constants at 0.39 and 0.95 mm, respectively. The entire analysis has been performed for a total heating power of 20 kW (corresponding power density of 1305.45 kW/m3) at a system pressure of 1.3 bar for different wall temperatures.

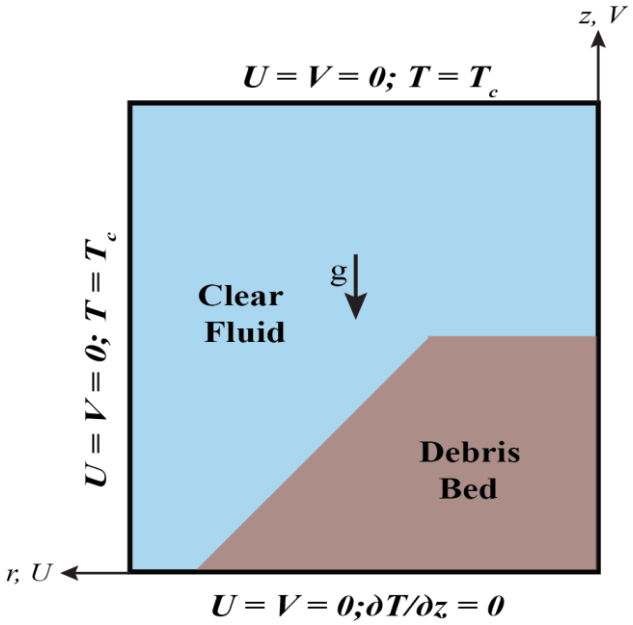

Figure 5.31 Schematic configuration of the problem considered under natural convective situation

Internal heat generation within the porous debris bed induces a buoyancy-driven fluid motion within the enclosure with energy transfer taking place from the heat-generating debris bed to the cold enclosure walls. This establishes a counter-clockwise fluid motion within the enclosure as is evident from the velocity vectors in Figure 5.32. In addition to heat transfer due to the convective fluid motion, heat transfer also occurs across the porous-fluid interfaces mainly due to conduction. The effective heat transfer from the debris bed is, thus, a combination of these two mechanisms. The vapour generated, due to heat transfer from the solid particles and phase change of liquid water, and the heated water rises upwards due to buoyancy and transfers energy at the cold top wall. At this point, the orientation of the enclosure forces the fluids towards the side wall and the residual energy of the fluids are transferred to it. Having transferred most of its energy to the enclosure walls, the cooler fluids sink towards the lower portions of the enclosure thereby establishing the counter-clockwise circulation within the enclosure. This is similar to that observed under single phase situation (see *Chapter 3*).

Figure 5.33 gives a transient history of the pertinent parameters of interest. Figure 5.34 shows the liquid saturation distribution (α_l) within the enclosure at different time instances and for different wall temperatures. It can be observed from Figure 5.33(a) that the minimum liquid saturation within the debris bed falls to zero within a short span of time for all wall temperatures. This is an indication of local dryout occurring within the bed. Interestingly, $\alpha_{l,min}$ starts to increases after a certain time period in case of the walls maintained at subcooled temperatures and reaches a steady value after a considerable time. In case of the walls maintained at saturation temperature, however, the $\alpha_{l,min}$ remains at zero throughout the time period.

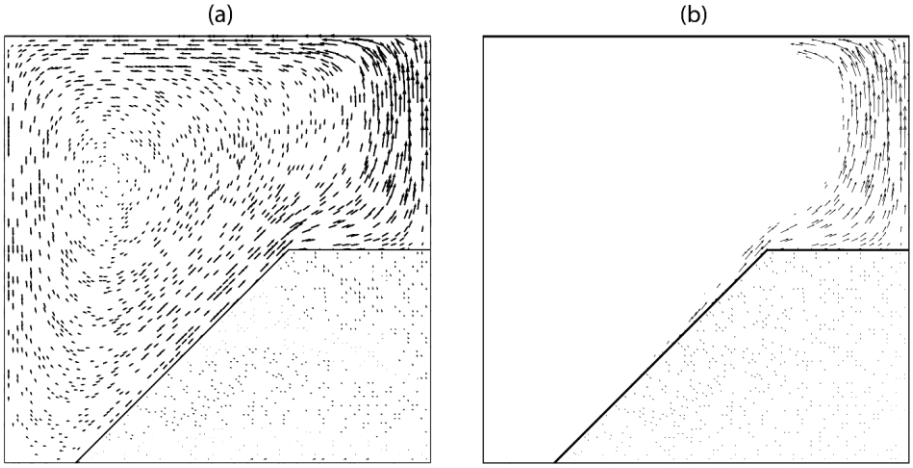

Figure 5.32 Velocity vectors of (a) liquid and (b) vapour at steady state

The consequent effect on the rise in temperature of the solid particles is shown in Figure 5.33(b). The solid temperature starts to rise rapidly due to the local dryout occurring in the initial stages. This rise is sustained in case of the enclosure wall at saturation temperature with the solid temperature increasing by ~26K in 500 s. The rise in temperature, in case of the subcooled walls, stop as the liquid saturation starts to increase and ultimately reaches a steady value close to the saturation temperature. The evolution of solid temperature with time is shown in Figure 5.35 for different wall temperatures.

The total mass of vapour generated, as shown in Figure 5.33(c), indicates that vapour continues to be generated due to dryout and accumulated within the enclosure in case of the wall maintained at saturation temperature. This can also be visualised by comparing the liquid saturation distribution at different time instances in Figure 5.34 for the saturated wall. As time progresses, the vapour generation continues and ultimately almost the entire enclosure gets filled with vapour. This is, however, not the case for the enclosure walls maintained at a subcooled temperature since continuous heat removal at the walls ensure that vapour accumulation does not take place in spite of continuous vapour generation.

Figures 5.33(d) and 5.33(e) represent the average heat fluxes at the top and side walls of the enclosure, respectively. As expected, negligible heat transfer takes place at the either cold wall in if the walls are maintained at the saturation temperature. This results in only an insignificant amount of heat being removed from the enclosure leading to dryout of the debris bed. Maintaining the temperature of the walls below the saturation

temperature creates a finite temperature difference between the bulk fluid and the wall allowing significant heat transfer, as can be seen in case of the subcooled walls. The initial occurrence of dryout in case of the subcooled walls and the consequent vapour generation leads to enhanced heat transfer in the initial stages after which the heat transfer decreases and becomes almost steady.

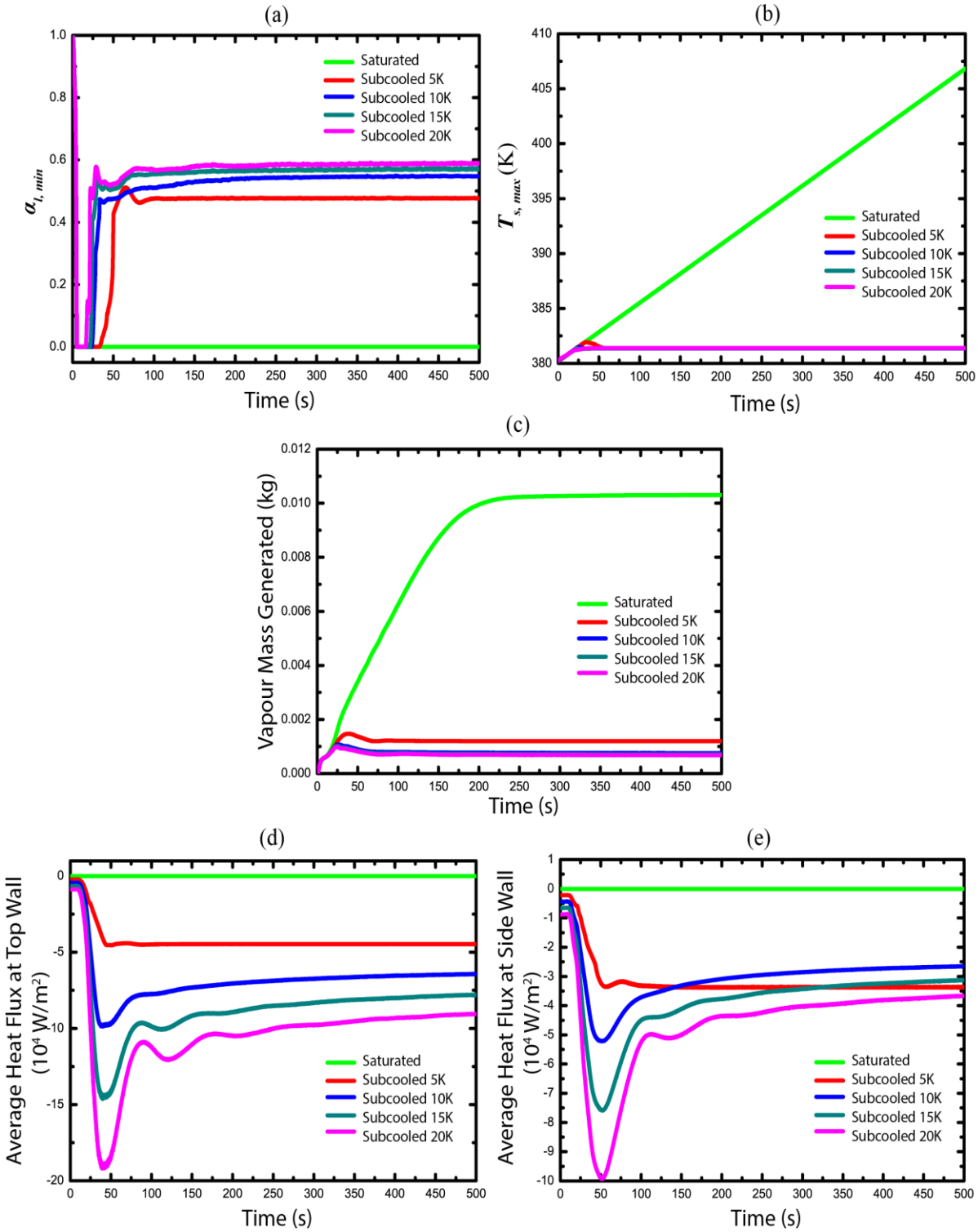

Figure 5.33 Temporal change of (a) Minimum liquid saturation (b) maximum solid temperature (c) vapour mass generated (d) average heat flux at the top wall and (e) average heat flux at the side wall for different wall temperatures

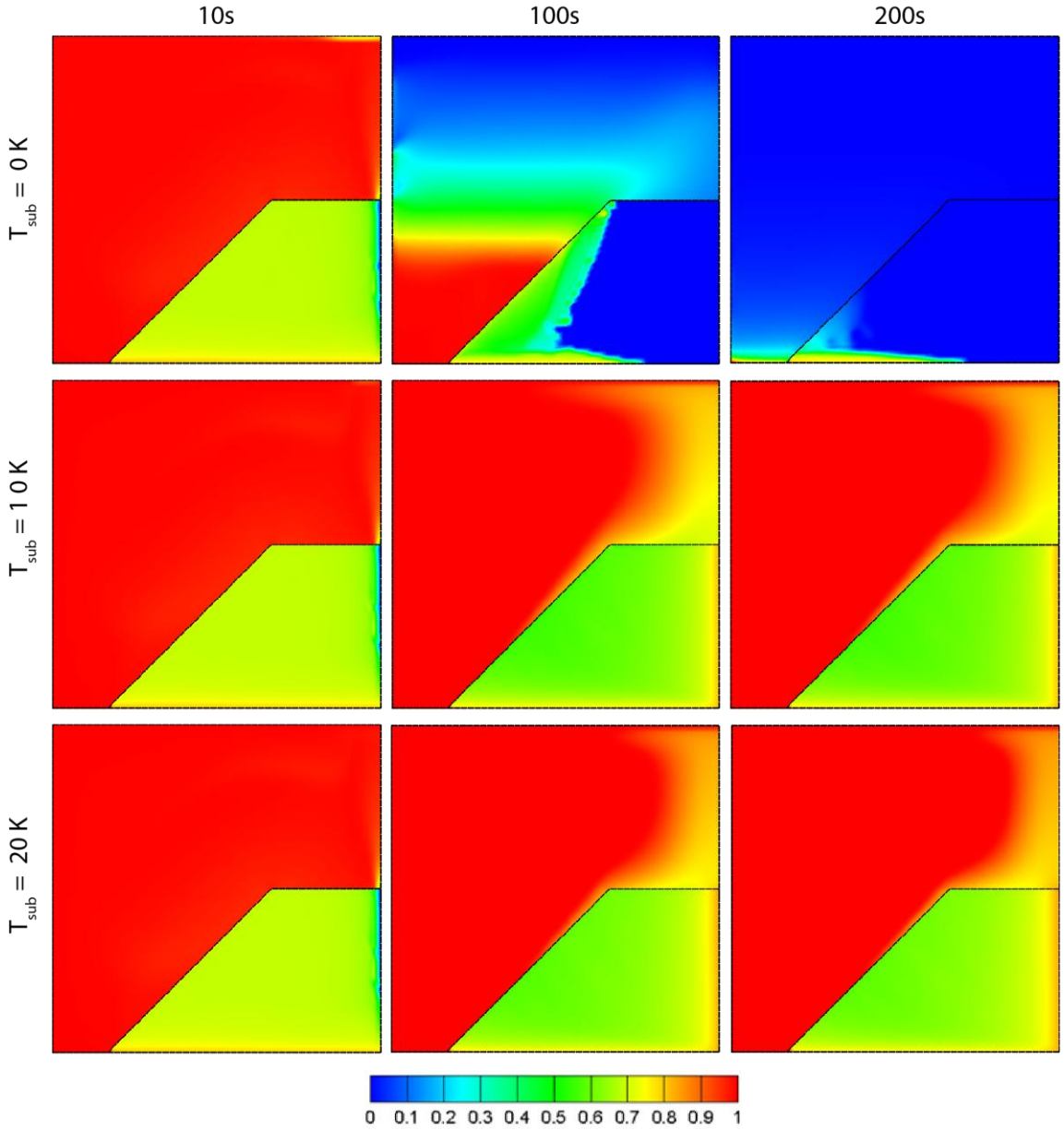

Figure 5.34 Temporal evolution of liquid saturation distribution within the enclosure

5.6 Conclusions

This chapter gives a detailed description of the computational model that has been developed for simulating multiphase flow, and associated heat and mass transfer in porous medium as well as clear fluid region. Various correlations used for achieving closure of the governing equations and the numerical assumptions made are also discussed. The numerical model is implemented in the framework of ANSYS FLUENT and is utilised to predict the occurrence of dryout in heat-generating debris beds. The model is validated with respect to pressure drop characteristics in a two-phase air-water flow through a porous bed and also with dryout data obtained from experiments. The minimum dryout power density is determined by gradual increase of the heating power from a low value in incremental steps of 1 kW until the minimum value of liquid volume

fraction stabilises at zero for a sufficient time duration (at least 100s). As a result of dryout, a rapid rise is observed in the solid phase temperature within the bed. The dryout location is determined from the liquid saturation and the corresponding solid temperature distributions in the domain.

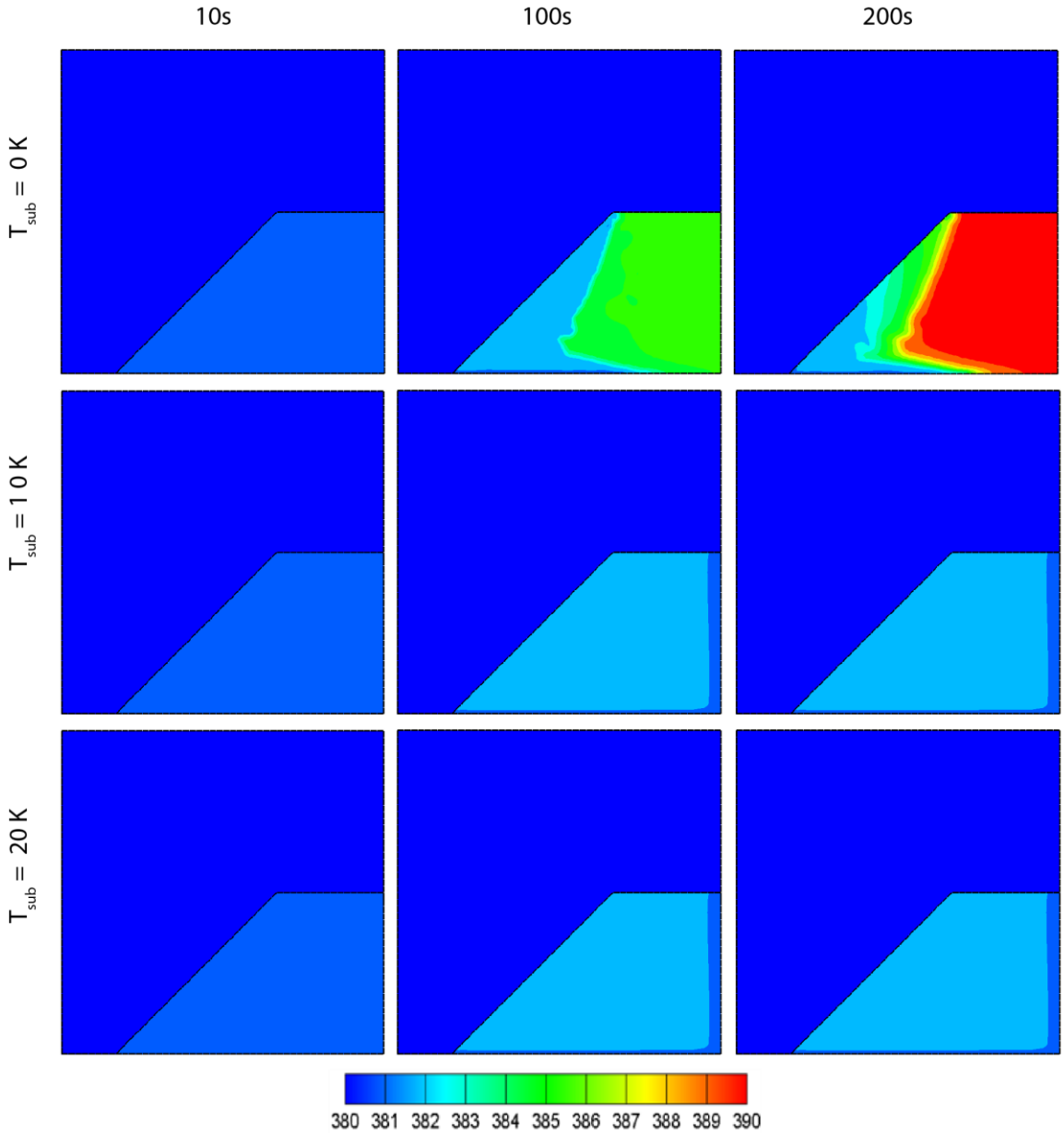

Figure 5.35 Temporal evolution of solid temperature distribution within the enclosure

A parametric analysis is carried out to with respect to bed porosity, particle size, liquid subcooling and system pressure. In addition, the effects of bed configuration and coolant flooding modes are also studied in this analysis. Results indicate that heat transfer and hence, the dryout power density is significantly influenced by porosity as well as particle size. The dryout power density increases with increase in either of these parameters due to the corresponding increase in permeability. However, the increase is not monotonic. Interestingly, the location of the dryout zone also shifts with change in bed permeability as shown in Fig. 5.36.

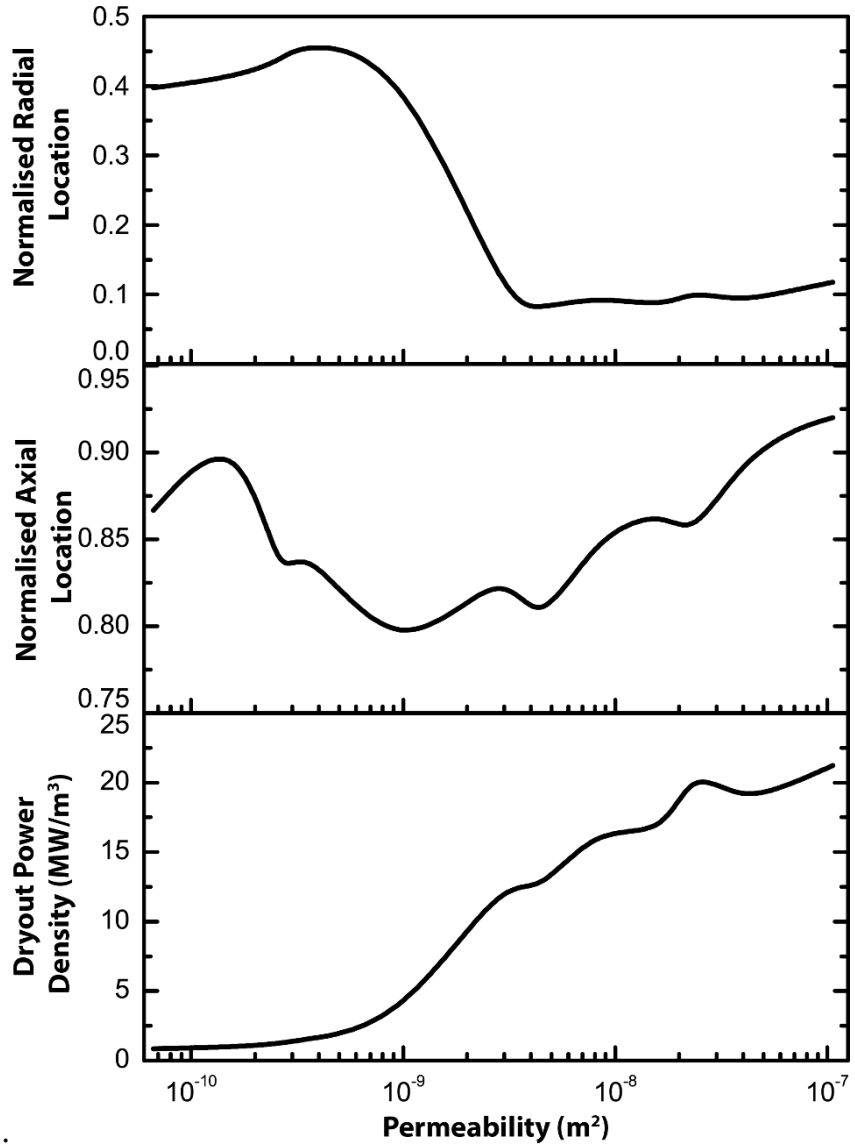

Figure 5.36 Variation in dryout power density and location of the dryout zone with change in bed permeability. Location of the dryout zone is characterised in terms of normalised axial and radial positions (with respect to bed height and bed radius, respectively) of the centre of the zone.

Liquid subcooling also affects the heat transfer dynamics and hence, the occurrence of dryout in the bed. Existence of subcooling enables greater condensation of the vapour generated and as such, a significantly higher heating power density becomes necessary for dryout to occur. In addition, it is observed that the dryout zone is formed in the inner regions of the bed when liquid subcooling is considered as evident from Fig. 5.37.

Analysis has shown that dryout occurrence in various configurations with an equivalent bed volume is mainly governed by the bed height as well as the surface area available for coolant infiltration into the bed. Experimental observations have shown that a shallow bed has a much higher dryout power density than a taller bed of the same volume. The surface area of the bed in contact with the fluid region influences the coolant infiltration within the bed and hence, affects the heat removal mechanism. It is observed in the present analysis that the truncated conical bed and the conical bed has the

maximum and minimum dryout power density, respectively. Figure 5.38 indicates the dryout zones observed in different bed configurations over a wide range of system pressure.

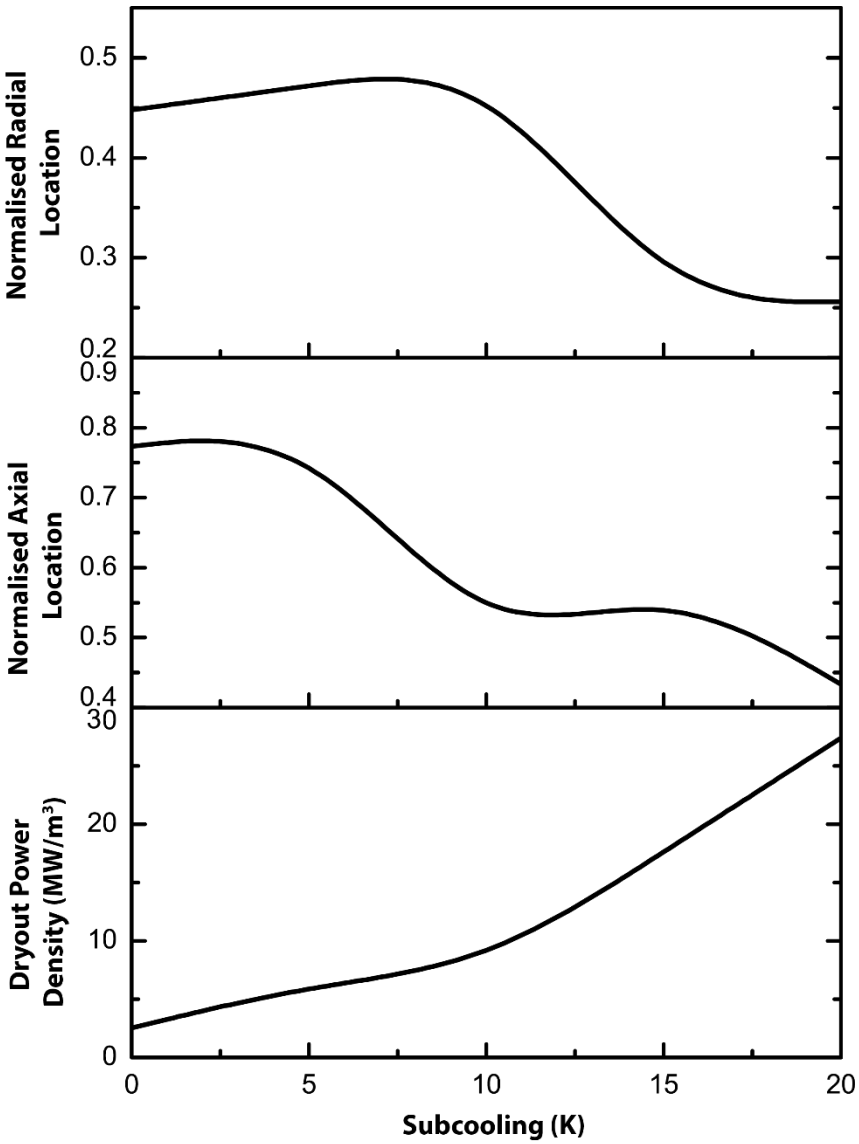

Figure 5.37 Variation in dryout power density and location of the dryout zone with change in liquid subcooling. Location of the dryout zone is characterised in terms of normalised axial and radial positions (with respect to bed height and bed radius, respectively) of the centre of the zone.

Observations also show that a multidimensional flooding approach is best suited for ensuring coolability of heat-generating debris beds. The fluid flow mechanism can be effectively modified from a counter-current mode to a co-current mode by ensuring lateral and/or bottom flooding in addition to top flooding. This resists the accumulation of vapour within the bed which is essential for causing dryout. Hence, a much higher power is required for causing dryout in such multidimensional flooding situations.

Analysis of debris bed dryout in natural convective situation indicates that the debris bed dries out and the solid temperature rises rapidly following dryout if the cold

enclosure walls are maintained at the saturation temperature. However, if the walls are maintained at a definite subcooling below the saturation temperature, the debris bed can be maintained in a coolable condition although the bed dries out initially. Thus, if the requisite amount of energy can be removed from the enclosure walls such that the walls are maintained at a subcooled temperature, dryout of a debris bed can be avoided. Hence, this mechanism of heat removal from a debris bed can be adopted as a long-term cooling strategy in post-accident situations.

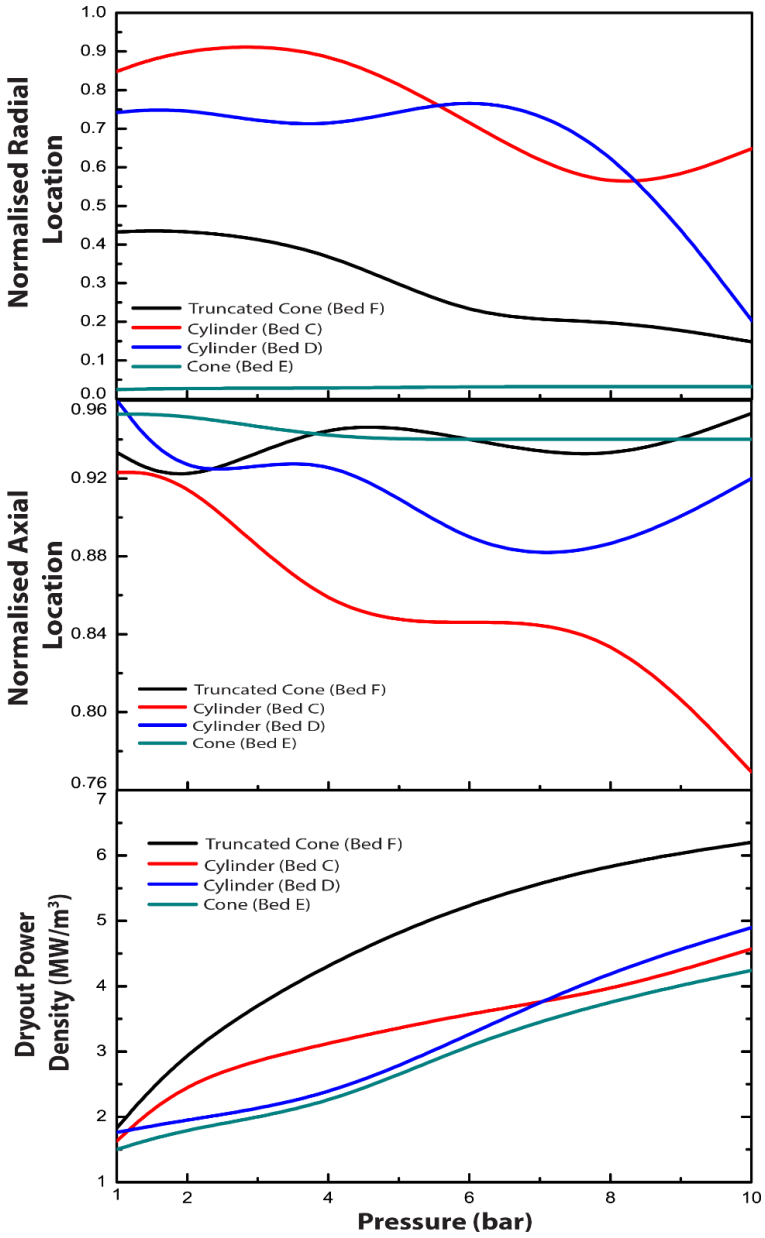

Figure 5.38 Variation in dryout power density and location of the dryout zone for different bed configurations with change in system pressure. Location of the dryout zone is characterised in terms of normalised axial and radial positions (with respect to bed height and bed radius for the respective configurations, respectively) of the centre of the zone.

.

Chapter 6

CONCLUSIONS

The present thesis addresses various thermal-hydraulic aspects of the debris coolability problem in severe accident situations of nuclear reactors. Analysis has been carried out for a heap-like, heat-generating debris bed considering single phase as well as multiphase flow situations. In this regard, a numerical model is developed and the model is implemented within the framework of the commercial CFD platform ANSYS FLUENT with extensive of user-defined functions.

In the single phase scenario, two different problems have been considered for analysis – a natural convective situation with a heat-generating debris bed placed within a fluid-filled enclosure and a mixed convective situation under the impact of coolant flooding the debris bed from its bottom. Both these problems are solved in a dimensionless manner following two different approaches of solving energy transport in porous media – local thermal equilibrium (LTE) approach and local thermal non-equilibrium (LTNE) approach. Analysis of the multiphase scenario is carried out in a dimensional manner using the LTNE approach with focus on dryout prediction in debris beds.

6.1. Contributions of the thesis towards knowledge enhancement

The major findings and contributions of the thesis are summarised below –

a. Qualitatively similar results are predicted by the LTE and LTNE models for the single phase scenarios. Heat transfer from the heat-generating debris bed to the cold walls occur by means of a buoyancy-driven counter-clockwise fluid circulation in a natural convective situation. Similar type of fluid circulation is observed in single phase as well as multiphase situations as evident from the streamlines, energy flux vectors (Figs. 3.3, 3.23) and velocity vectors (Fig. 5.32). This flow pattern gets modified on injection of coolant from the bottom of the debris bed such that maximum temperature rise is observed to occur near the top of the bed. This is in stark contrast to the natural convective situation where maximum temperature rise is found in the inner regions of the bed (see isotherm contours in Figs. 4.7 and 3.3). Further, flow spreading is observed within the debris bed near the fluid inlet in the bottom flooding situation (see streamline and energy flux vectors in Fig. 4.7).

b. Quantitative differences between the predictions of the LTE and LTNE approaches are, however, observed especially when there is appreciable convection within the debris bed ($RaDa$ > 100) and at large solid to fluid thermal conductivity ratios ($k_s/k_f > 10$) (see Tables 6.1 and 6.2). This necessitates the use of the LTNE approach in multiphase situations.

c. Additional fluid injection from the bottom of the debris bed increases heat transfer from the heat-generating debris to the coolant. It is observed from the single phase

analysis that maximum temperature rise within the debris progressively decreases as the injection strength is increased signifying enhanced heat transfer (see Table 6.3). Similar observations are obtained from the multiphase analysis. Greater heat transfer resists vapour accumulation within the debris bed and hence, a significantly larger power density is required for dryout occurrence under bottom flooding situations. The dryout power density is observed to increase from 0.78 MW/m^3 under top-flooding situation to 1.6 MW/m3 with bottom-flooding at an injection velocity of 0.05 m/s. This continues to increase with further increase in injection velocity to 3.9 MW/m^3 at 0.2 m/s (see Fig. 5.25).

Table 6.1 Comparison of maximum temperature rise with reducing bed permeability in the single phase natural convective situation

Solution approach	***Ra***	***Da***	***RaDa***	$\theta_{f,max}$	$\theta_{s,max}$
LTNE	10^{10}	10^{-6}	10^4	0.02807	0.06069
		10^{-7}	10^3	0.0618	0.06938
		10^{-8}	10^2	0.07915	0.08107
		10^{-9}	10	0.0812	0.0818
		10^{-10}	1	0.08162	0.0818
LTE	10^8	10^{-1}	10^7	0.00908	n/a
		10^{-5}	10^3	0.05619	
		10^{-8}	1	0.10845	

Table 6.2 Comparison between the LTE and LTNE approaches in terms of the predicted maximum temperature rise for the single phase mixed convective situation

Ri	***Re***	λ_s	**LTNE**		**LTE**
			$\theta_{s,max}$	$\theta_{f,max}$	θ
0.01	100	0.1	0.003323	0.002833	0.002824
		1	0.030553	0.027053	0.026304
		10	0.241422	0.21548	0.203255
		50	0.971435	0.88473	0.74999
		100	1.84147	1.68529	1.33195

d. Analysis shows that one of the main factors influencing coolability of debris beds is its permeability. Permeability determines the strength of fluid flow through porous media and hence, also affects heat transfer from porous media to the fluid phases. It is observed from the single phase analyses that a reduction in permeability lowers the heat transfer from the debris bed and leads to a larger temperature rise within the bed (see Tables 6.1 and 6.4). In the single phase natural convective situation, this is accompanied by a gradual shift in the location of the maximum temperature zone

towards the interior of the bed as the permeability reduces (see isotherm contours in Figs. 3.3, 3.23). The maximum temperature zone, in contrast, remains unaltered near the top of the debris bed with change in permeability under bottom-flooding conditions (see isotherm contours in Figs. 4.7 – 4.8). This effect of reduced heat transfer from the debris bed with decreasing permeability results in easier vapour accumulation within the bed in a multiphase flow situation. Dryout of a debris bed, therefore, occurs at a much lower power density at reduced permeabilities. The dryout power density increases from 21 MW/m^3 to 0.85 MW/m^3 when the permeability of the bed is reduced from 10^{-7} to 10^{-11} (see Fig. 5.15). Further, it is observed that the dryout zone shifts from the upper central region to upper peripheral regions of the bed as the permeability is reduced (see Figs. 5.11, 5.12, 5.36).

Table 6.3 Change in maximum bed temperature rise with increasing injection strength (in terms of *Re*)

Ri	***Gr***	***Re***	$\boldsymbol{\theta_{max}}$
0.01	10^5	3162.278	0.00205
0.1		1000	0.00562
1		316.278	0.01251
10		100	0.01508
100		31.6278	0.03204

Table 6.4 Comparison of maximum bed temperature rise with reducing bed permeability in single phase mixed convective situation

Ri	***Re***	***Da***	$\boldsymbol{\theta_{max}}$
0.01	50	10^{-1}	0.04618
		10^{-4}	0.05395
	500	10^{-1}	0.00689
		10^{-4}	0.01001

e. Bed configuration and the available fluid flow passage is observed to play a major role in determining heat transfer and hence, coolability of a debris bed. A comparison of the maximum temperature rise in natural convection situation for three different bed configurations – cylindrical, truncated conical and conical – reveals that the largest and smallest temperature rise occurs in the conical and the cylindrical configuration, respectively. The dimensionless maximum temperatures obtained for these configurations – 0.02128, 0.02341 and 0.0303 for the cylindrical, truncated conical and conical, respectively – indicate a wide variation (~ 29%) (see Table 3.6). The effect of bed configuration is more pronounced in a multiphase situation. It is observed that the availability of an additional flow passage in a laterally flooded bed modifies the fluid flow pattern within the bed and increases the dryout power density to 1.6 MW/m^3 from 0.78 MW/m^3 in a top-flooded bed (see Figs. 5.25, 5.26, 5.27). The change in dryout power density in differing bed configurations is determined by

the combined effects of available bed surface area for coolant infiltration and height of the bed. The truncated conical bed configuration, with a large coolant infiltration area and an intermediate height, is observed to have the largest dryout power density (1.8 MW/m^3 at 1 bar pressure). Interestingly, the lowest dryout power density (1.5 MW/m^3 at 1 bar) is obtained for the conical configuration which has the largest coolant infiltration area (see Fig. 5.21 and Table 5.12). This happens due to a counter-current flow mechanism existing across the lateral surface of the bed leading to easier vapour accumulation and consequent dryout of the bed.

f. Coolant subcooling is observed to significantly affect the heat transfer dynamics. Greater heat transfer takes place from the heat-generating solid phase to the coolant due to its subcooled state. This enables greater condensation of the vapour generated and as such, a significantly higher power density becomes necessary for dryout to occur. The dryout power density increases from 2.5 MW/m^3 for saturated water to 6.2 MW/m^3 for water at 5K subcooling and thereafter, increases further to 27 MW/m^3 for 20 K subcooling. In addition, it is observed that the dryout zone progressively shifts towards the inner regions of the bed when liquid subcooling is considered (see Fig. 5.37).

g. A change in system pressure is observed to have a substantial impact on dryout power density. The dryout power density increases from 1.8 MW/m^3 at 1 bar to 6.2 MW/m^3 at 10 bar for the truncated conical configuration. Similar variation in dryout power density with pressure is obtained for all bed configurations studied in this analysis (see Fig. 5.38).

h. It is observed from the analysis of natural convection in a multiphase situation that if the enclosure walls are maintained at a definite subcooling (~5 K) below the saturation temperature, the debris bed can be maintained in a coolable condition. Thus, if the requisite amount of energy can be removed from the enclosure walls such that the walls are maintained at a subcooled temperature, dryout of a debris bed can be avoided. This is especially relevant in view of long-term coolability of a debris bed.

6.1. Scope of future work

The porous debris beds considered in this thesis have been assumed to be homogeneous with uniform bed porosity and particle size. In a realistic scenario, however, the bed porosity as well as the particle size is expected to vary. Also, the solid particles constituting the porous bed have been assumed to be perfectly spherical which is far from ideal. These factors need to be accounted for in future studies.

The effects of capillarity can be studied by introducing appropriate modifications in the numerical model. The impacts of variable thermos-physical properties and non-uniform heat generation within the debris bed needs to be considered as well.

It also needs to be mentioned that the numerical model developed as a part of the thesis can also be utilised in modelling of single phase and multiphase flow in other fields involving porous media with appropriate modifications.

REFERENCES

ANSYS Inc.: *ANSYS FLUENT Theory Guide*. (2012a)

ANSYS Inc.: *ANSYS FLUENT UDF Manual*. (2012b)

Al-Amiri, A.M.: *Analysis of momentum and energy transfer in a lid-driven cavity filled with a porous medium*. Int. J. Heat Mass Transf. **43**, 3513-3527 (2000)

Atkhen, K., Berthoud, G.: *SILFIDE experiment: Coolability in a volumetrically heated debris bed*. Nucl. Eng. Des. **236**, 2126-2134 (2006)

Bachrata, A.: *Modeling of core flooding in a highly degraded reactor*. PhD Thesis, University of Toulouse, France (2012)

Bang, K.H., Kim, J.M.: *Enhancement of dryout heat flux in a debris bed by forced coolant flow from below*. Nucl. Eng. Tech. **42**(3), 297-304 (2010)

Basak, T., Roy, S., Singh, S.K., Pop, I.: *Analysis of mixed convection in a lid-driven porous square cavity with linearly heated side wall(s)*. Int. J. Heat Mass Transf. **53**, 1819-1840 (2010)

Basak, T., Pradeep, P.V.K., Roy, S., Pop, I.: *Finite element based heatline approach to study mixed convection in a porous square cavity with various wall thermal boundary conditions*. Int. J. Heat Mass Transf. **54**, 1706-1727 (2011)

Baytaş, A.C.: *Thermal non-equilibrium natural convection in a square enclosure filled with a heat-generating solid phase, non-Darcy porous medium*. Int. J. Energy Res. **27**, 975–988 (2003)

Beckermann, C., Ramadhyani, S., Viskanta, R.: *Natural convection flow and heat transfer between a fluid layer and a porous layer inside a rectangular enclosure*. J. Heat Transf. **109**, 363-370 (1987)

Bera, P., Khalili, A.: *Influence of Prandtl number on stability of mixed convective flow in a vertical channel filled with a porous medium*. Phys. Fluids **18**, 124103 (2006)

Berthoud, G.: *Models and validation of particulate debris coolability with the code MC3D-REPO*. Nucl. Eng. Des. **236**, 2135-2143 (2006)

Beukema, K.J., Bruin, S.: *Three-dimensional natural convection in a confined porous medium with internal heat generation*. Int. J. Heat Mass Transf. **26**(3), 451-458 (1983)

Bortolozzi, R.A., Deiber, J.A.: *Comparison between two- and one-field models for natural convection in porous media*. Chem. Eng. Sci. **56**, 157–172 (2001)

Bromley, L.A.: *Heat transfer in stable film boiling*. Chem. Eng. Prog. **46**, 221-227 (1950)

Buonomo, B., Lauriat, G., Manca, O., Nardini, S.: *Numerical investigation of laminar slot-jet impinging in a confined porous medium in local thermal non-equilibrium*. Int. J. Heat Mass Transf. **98**, 484-492 (2016)

Bürger, M., Buck, M., Schmidt, W., Widmann, W.: *Validation and application of the WABE code: Investigations of constitutive laws and 2D effects on debris coolability*. Nucl. Eng. Des. **236,** 2164-2188 (2006)

Bürger, M., Buck, M., Pohlner, G., Rahman, S., Kulenovic, R., Fichot, F., Ma, W., Miettinen, J., Lindholm, I., Atkhen, K.: *Coolability of particulate beds in severe accidents: Status and remaining uncertainties*. Prog. Nucl. Energ. **52**, 61-75 (2010)

Cha, J.H., Chung, M.K.: *Forced flow dryout heat flux in heat generating debris bed*. Journal of the Korean Nuclear Society **18**(4), 273-280 (1986)

Chen, Y.H., Lin, H.T.: *Natural convection in an inclined enclosure with a fluid layer and a heat-generating porous bed*. Heat Mass Transfer **33**, 247–255 (1997)

Chikhi, N., Coindreau, O., Li, L.X., Ma, W.M., Taivassalo, V., Takasuo, E., Leininger, S., Kulenovic, R., Laurien, E.: *Evaluation of an effective diameter to study quenching and dry-out of complex debris bed*. Ann. Nucl. Energy **74**, 24-41 (2014)

Chikhi, N., Clavier, R., Laurent, J.P., Fichot, F., Quintard, M.: *Pressure drop and average void fraction measurements for two-phase flow through highly permeable porous media*. Ann. Nucl. Energy **94**, 422-432 (2016)

Cho, D.H., Page, R.J., Abdulla, S.H., Anderson, M.H., Klockow, H.B., Corradini, M.L.: *Melt quenching and coolability by water injection from below: Co-injection of water and non-condensable gas*. Nucl. Eng. Des. **236**, 2296-2303 (2006)

Clavier, R., Chikhi, N., Fichot, F., Quintard, M.: *Experimental investigation on single-phase pressure losses in nuclear debris beds: Identification of flow regimes and effective diameter*. Nucl. Eng. Des. **292**, 222-236 (2015)

Clavier, R., Chikhi, N., Fichot, F., Quintard, M.: *Modeling of inertial multi-phase flows through high permeability porous media: Friction closure laws*. Int. J. Multiphase Flow **91**, 243-261 (2017)

Das, S., Sahoo, R.K.: *Effect of Darcy, fluid Rayleigh and heat generation parameters on natural convection in a porous square enclosure: a Brinkmann-extended Darcy model*. Int. Commun. Heat Mass Transfer **26**(4), 569-78 (1999)

Das, S., Morsi, Y.S.: *A non-Darcian numerical modeling in domed enclosures filled with heat generating porous media*. Numer. Heat Tr. A-Appl. **48**, 149-64 (2005)

Du, Z.G., Bilgen, E.: *Natural convection in vertical cavities with partially filled heat-generating porous media*. Numer. Heat Tr. A-Appl. **18**, 371–386 (1990)

Du, Z.G., Bilgen, E.: *Natural convection in vertical cavities with internal heat generating porous medium*. Wärme - und Stoffübertragung **27**, 149-55 (1992)

Ergun, S.: *Fluid flow through packed columns*. Chem. Eng. Prog. **48**, 89-94 (1952)

Ejlali, A., Ejlali, A., Hooman, K., Gurgenci, H.: *Application of high porosity metal foams as air-cooled heat exchangers to high heat load removal systems*. Int. Commun. Heat Mass **36**, 674–679 (2009)

Ejlali, A., Hooman, K.: *Buoyancy effects on cooling a heat generating porous medium: coal stockpile*. Transport Porous Med. **88**, 235-248 (2011)

Faghri, A., Zhang, Y.: *Transport Phenomena in Multiphase Systems*. Elsevier, Amsterdam (2006)

Fichot, F., Duval, F., Trégourès, N., Béchaud, C., Quintard, M.: *The impact of thermal non-equilibrium and large-scale 2D/3D effects on debris bed reflooding and coolability*. Nucl. Eng. Des. **236**, 2144-2163 (2006)

Fischer, M., Herbst, O., Schmidt, H.: *Demonstration of the heat removing capabilities of the EPR core catcher*. Nucl. Eng. Des. **235**, 1189-1200 (2005)

Guerroudj, N., Kahalerras, H.: *Mixed convection in a channel provided with heated porous blocks of various shapes*. Energ. Convers. Manage. **51**, 505-517 (2010)

Haajizadeh, M., Ozguc, A.F., Tien, C.L.: *Natural convection in a vertical porous enclosure with internal heat generation*. Int. J. Heat Mass Transf. **27**(10), 1893-902 (1984)

Hidaka, M., Ujita, H.: *Verification for Flow Analysis Capability in the Model of Three-Dimensional Natural Convection with Simultaneous Spreading, Melting and Solidification for the Debris Coolability Analysis Module in the Severe Accident Analysis Code 'SAMPSON'*. Journal of Nuclear Science and Technology **38**(9), 745-756 (2001)

Hooman, K.: *Energy flux vectors as a new tool for convective visualisation*. Int. J. Numer. Methods Heat Fluid Flow **20**, 240–249 (2010)

Hu, K., Theofanous, T.G.: *On the measurement of dryout in volumetrically heated coarse particle beds*. Int. J. Multiphase Flow **17**, 519-532 (1991)

Huang, Z., Ma, W.: *Validation and application of the MEWA code to analysis of debris bed coolability*. Nucl. Eng. Des. **327**, 22-37 (2018)

Huhtiniemi, I., Magallon, D.: *Insights into steam explosions with corium melts in KROTOS*. Nucl. Eng. Des. **204**, 391-400 (2001)

IAEA: *Thermophysical properties database of materials for light water reactors and heavy water reactors*. IAEA Tecdoc 1496, Vienna (2006)

Jasmin Sudha, A., Murthy, S.S., Kumaresan, M., Lydia, G., Nashine, B.K., Chellapandi, P.: *Experimental analysis of heaping and self-levelling phenomena in core debris using lead spheres*. Exp. Therm. Fluid Sci. **68**, 239-246 (2015)

Jha, B.K. Daramola, D. Ajibade, A.O.: *Role of heat generation/absorption on mixed convection flow in a vertical tube filled with porous material having time-periodic boundary condition: Steady periodic regime*. Transport Porous Med. **111**, 681-699 (2016)

Jue, T.C.: *Analysis of thermal convection in a fluid-saturated porous cavity with internal heat generation*. Heat Mass Transfer **40**, 83-9 (2003)

Kakaç, S., Kilkis, B., Kulacki, F.A., Arinç, F.: *Convective heat and mass transfer in porous media*, 1st ed. Springer, Çesme, Turkey (1991)

Kang, K.H., Park, R.J., Kim, S.B., Suh, K.Y., Cheung, F.B., Rempe, J.L.: *Simulant melt experiments on performance of the in-vessel core catcher*. Nucl. Eng. Des. **237**, 1803-1813 (2007)

Karbojian, A., Ma, W.M., Kudinov, P., Dinh, T.: *A scoping study of debris bed formation in the DEFOR test facility*. Nucl. Eng. Des. **239**, 1653-1659 (2009)

Kazachkov, I.V., Konovalikhin, M.J.: *Steam flow through the volumetrically heated particle bed*. Int. J. Thermal Sci. **41**, 1077-1087 (2002)

Khanafer, K., Chamkha, A.J.: *Mixed convection flow in a lid-driven enclosure filled with a fluid-saturated porous medium*. Int. J. Heat Mass Transf. **42**, 2465-2481 (1999)

Khanafer, K., Vafai, K.: *Double-diffusive mixed convection in a lid-driven enclosure filled with a fluid-saturated porous medium*. Numer. Heat Tr. A-Appl. **42**, 465-486 (2002)

Khanafer, K., Chamkha, A.J.: *Mixed convection within a porous heat generating horizontal annulus*. Int. J. Heat Mass Transf. **46**, 1725-1735 (2003)

Khandelwal, M.K., Bera, P.: *A thermal non-equilibrium perspective on mixed convection in a vertical channel*. Int. J. Thermal Sci. **56**, 23-34 (2012)

Kim, S.J., Choi, C.Y.: *Convective heat transfer in porous and overlying fluid layers heated from below*. Int. J. Heat Mass Transf. **39**(2), 319-329 (1996)

Kim, G.B., Hyun, J.M., Kwak, H.S.: *Buoyant convection in a square cavity partially filled with a heat-generating porous medium*. Numer. Heat Tr. A-Appl. **40**(6), 601–618 (2001)

Kim, E., Lee, M., Park, H.S., Moriyama, K., Park, J.H.: *Development of an ex-vessel corium debris bed with two-phase natural convection in a flooded cavity*. Nucl. Eng. Des. **298**, 240-254 (2016)

Krishna Murthy, S., Ratish Kumar, B.V.: *Non-Darcy mixed convection in a porous square enclosure under suction/injection effects with a non-isothermal vertical wall*. Numer. Heat Tr. A-Appl. **57**, 580-602 (2010)

Kudinov, P., Karabojian, A., Ma, W.M., Dinh, T.N.: *An experimental Study on Debris Formation with Corium Simulant Materials*. ICAPP 2008, Anaheim, CA, USA (2008)

Kumari, M., Nath, G.: *Steady mixed convection flow in a lid-driven square enclosure filled with a non-Darcy fluid saturated porous medium with internal heat generation*. Journal of Porous Media **14**(10), 893-905 (2011)

Kuznetsov, A.V., Nield, D.A.: *Local thermal non-equilibrium and heterogeneity effects on the onset of convection in an internally heated porous medium*. Transport Porous Med. **102**, 15–30 (2014)

Kuznetsov, A.V., Nield, D.A.: *Local thermal non-equilibrium effects on the onset of convection in an internally heated layered porous medium with vertical throughflow*. Int. J. Therm. Sci. **92**, 97–105 (2015)

Li, L., Ma, W.M.: *Experimental characterization of the effective particle diameter of a particulate bed packed with multi-diameter spheres*. Nucl. Eng. Des. **241,** 1736-1745 (2011a)

Li, L., Ma, W.M.: *Experimental Study on the Effective Particle Diameter of a Packed Bed with Non-Spherical Particles*. Transp. Porous Med. **89**, 35-48 (2011b)

Li, L., Ma, W.M., Thakre, S.: *An experimental study on pressure drop and dryout heat flux of two-phase flow in packed beds of multi-sized and irregular particles*. Nucl. Eng. Des. **242,** 369-378 (2012)

Li, L., Kong, L., Zou, X., Wang, H.: *Pressure drops of single/two-phase flows through porous beds with multi-sizes spheres and sands particles*. Ann. Nucl. Energy **85**, 290-295 (2015)

Li, L., Kong, L., Zou, X., Wang, H.: *Pressure drops of single/two-phase flows through porous beds with multi-sizes spheres and sands particles*. Ann. Nucl. Energy **85**, 290-295 (2015)

Li, L., Kong, L., Zou, X., Wang, H.: *Pressure losses and interfacial drag for two-phase flow in porous beds with coarse particles*. Ann. Nucl. Energy **101**, 481-488 (2017)

Li, L., Wang, H., Zou, X., Kong, L.: *Flow resistances characteristics in a particulate bed with the configurations of uniform mixture and stratification*. Ann. Nucl. Energy **112**, 62-70 (2018)

Li, L., Zou, X., Wang, H., Zhang, S., Wang, K.: *Investigations on two-phase flow resistances and its model modifications in a packed bed*. Int. J. Multiphase Flow **101**, 24-34 (2018)

Lin, S., Cheng, S., Jiang, G., Pan, Z., Lin, H., Wang, S., Wang, l., Zhang, X., Wang, B.: *A two-dimensional experimental investigation on debris bed formation behaviour*. Prog. Nucl. En. **96**, 118-132 (2017)

Lindholm, I., Holmström, S., Miettinen, J., Lestinen, V., Hyvärinen, J., Pankakoski, P., Sjövall, H.: *Dryout heat flux experiments with deep heterogeneous particle bed*. Nucl. Eng. Des. **236,** 2060-2074 (2006)

Lipinski, R.J.: *A one dimensional particle bed dryout model*. ANS Transactions, **38**, 386-387, (1981)

Lipinski, R.J.: *A coolability model for post-accident nuclear reactor debris*. Nuclear Technology **65,** 53-66 (1984)

Ma, W.M., Dinh, T.N.: *The effects of debris bed's prototypical characteristics on corium coolability in a LWR severe accident*. Nucl. Eng. Des. **240**, 598-608 (2010)

Magallon, D.: *Characteristics of corium debris bed generated in large-scale fuel-coolant interaction experiments*. Nucl. Eng. Des. **236**, 1998-2009 (2006)

Magallon, D., Huhtiniemi, I.: *Corium melt quenching tests at low pressure and subcooled water in FARO*. Nucl. Eng. Des. **204**, 369-376 (2001)

Mahapatra, P.S., Ghosh, K., Manna, N.K.: *Heat transfer partitioning model of film boiling of particle cluster in a liquid pool: implementation in a CFD code*. Heat Mass Transf. **51**, 1149-1166 (2015)

Mahapatra, P.S., Datta, P., Chakravarty, A., Ghosh, K., Manna, N.K., Mukhopadhyay, A., Sen, S.: *Molten drop to coolant heat transfer during premixing of fuel coolant interaction*, in: Basu, S., Agarwal, A., Mukhopadhyay, A., Patel, C. (Eds.), *Applications Paradigms of Droplet and Spray Transport: Paradigms and Applications*. Springer, Singapore, pp. 201-235 (2018)

Mahmoudi, Y.: *Constant wall heat flux boundary condition in micro-channels filled with a porous medium with internal heat generation under local thermal non-equilibrium condition*. Int. J. Heat Mass Transf. **85**, 524–542 (2015)

Mahmud, S., Pop, I.: *Mixed convection in a square vented enclosure filled with a porous medium*. Int. J. Heat Mass Transf. **49**, 2190-2206 (2006)

Manickam, L., Kudinov, P., Ma, W., Bechta, S., Grishchenko, D.: *On the influence of water subcooling and melt jet parameters on debris formation*. Nucl. Eng. Des. **309**, 265-276 (2016)

Manickam, Bechta, S., Ma, W.: *On the fragmentation characteristics quenched in water*. Int. J. Multiphase Flow **91**, 262-275 (2017)

Minkowycz, W.J., Haji-Sheikh, A., Vafai, K.: *On departure from local thermal equilibrium in porous media due to a rapidly changing heat source: The Sparrow number*. Int. J. Heat Mass Transf. **42**, 3373–3385 (1999)

Miscevic, M., Rahli, O., Tadrist, L., Topin, F.: *Experiments on flows, boiling and heat transfer in porous media: Emphasis on bottom injection*. Nucl. Eng. Des. **236**, 2084-2103 (2006)

Miyazaki, K., Murai, K., Ohama, T., Yamaoka, N., Inoue, S.: *Pressure dependence of the particle bed dryout heat flux*. Nucl. Eng. Des. **95,** 271-273 (1986)

Moraga, N.O., Sanchez, G.C., Riquelme, J.A.: *Unsteady mixed convection in a vented enclosure partially filled with two non-Darcian porous layers*. Numer. Heat Tr. A-Appl. **57**, 473-495 (2010)

Muthtamilselvan, M., Das, M.K., Kandaswamy, P.: *Convection in a lid-driven heat-generating porous cavity with alternative thermal boundary conditions*. Transport Porous Med. **82**, 337-346 (2010)

Nayak, A.K., Sehgal, B.R., Stepanyan, A.V.: *An experimental study on quenching of a radially stratified heated porous bed.* Nucl. Eng. Des. **236,** 2189-2198 (2006)

Nield, D.A.: *Onset of convection in a fluid layer overlying a layer of a porous medium*. J. Fluid Mech. **81**(3), 513-522 (1977)

Nield, D.A., Bejan, A.: *Convection in porous media*. 5th ed. Springer (2017)

Nishimura, T., Takumi, T., Shiraishi, M., Kawamura, Y., Ozoe, H.: *Numerical analysis of natural convection in a rectangular enclosure horizontally divided into fluid and porous regions*. Int. J. Heat Mass Transf. **29**(6), 889-898 (1986)

Nouri-Borujerdi, A., Noghrehabadi, A.R., Rees, D.A.S.: *The effect of local thermal non-equilibrium on conduction in porous channels with a uniform heat source*. Transport Porous Med. **69**, 281–288 (2007a)

Nouri-Borujerdi, A., Noghrehabadi, A.R., Rees, D.A.S.: *Onset of convection in a horizontal porous channel with uniform heat generation using a thermal nonequilibrium model*. Transport Porous Med. **69**, 343–357 (2007b)

Paladino, D., Theerthan, S.A., Sehgal, B.R.: *DECOBI: Investigation of melt coolability with bottom coolant injection.* Prog. Nucl. En. **40**(2), 161-206 (2002)

Poulikakos, D., Bejan, A.: *Natural convection in vertically and horizontally layered porous media heated from the side*. Int. J. Heat Mass Transf. **26**(112), 1805-1814 (1983)

Prasad, V.: *Thermal convection in a rectangular cavity filled with heat-generating, Darcy porous medium*. J. Heat Transf. **109**, 697-703 (1987)

Rahman, S.: *Coolability of Corium Debris under Severe Accident Conditions in Light Water Reactors*. PhD Thesis, Institute of Nuclear Technology and Energy Systems (IKE), University of Stuttgart, Germany, 2013

Ranz, W.E., Marshall, W.M.: *Evaporation from Drops*. Chem. Eng. Prog. **48**, 141–146 (1952)

Rashid, M., Kulenovic, R., Laurien, E., Nayak, A.K.: *Experimental results on the coolability of a debris bed with multidimensional cooling effects*. Nucl. Eng. Des. **241,** 4537-4543 (2011)

Rashid, M., Kulenovic, R., Laurien, E.: *Experimental results on the coolability of a debris bed with down comer configurations*. Nucl. Eng. Des. **249**, 104-110 (2012)

Ratish Kumar, B.V., Krishna Murthy, S.: *Mixed convection in a non-Darcian fluid saturated square porous enclosure under multiple suction effect*. Int. J. Heat Mass Transf. **53**, 5764-5773 (2010)

Raverdy, B., Meignen, R., Piar, L., Picchi, S., Janin, T.: *Capabilities of MC3D to investigate the coolability of corium debris beds*. Nucl. Eng. Des. **319**, 48-60 (2017)

Reddy, B.V.K., Narasimhan, A.: *Heat generation effects in natural convection inside a porous annulus*. Int. Commun. Heat Mass **37**, 607-10 (2010)

Reed, A.W.: *The effect of channeling on the dryout of heated particulate beds immersed in a liquid pool*. PhD Thesis, Massachusetts Institute of Technology, Cambridge, USA (1982)

Reed, A.W., Bergernon, E.D., Boldt, K.R., Schmidt, T.R.: *Coolability of UO2 debris beds in pressurized water pools: DCC-1 and DCC-2 experiment results*. Nucl. Eng. Des. **97**(1), 81-88 (1986)

Rees, D.A.S., Pop, I.: *Local thermal non-equilibrium in porous medium convection*. In: Ingham, D.B., Pop, I. (eds.) Transport Phenomena in Porous Media, vol. III, pp. 147–174. Elsevier, Oxford (2005)

Rhosenow, W.: *A method of correlating heat transfer data for surface boiling of liquids*. Trans. ASME **74**, 969-976 (1952)

Saeid, N.H.: *Analysis of mixed convection in a vertical porous layer using non-equilibrium model*. Int. J. Heat Mass Transf. **47**, 5619-5627 (2004)

Salman Ahmed, N.J., Badruddin, I.A., Kanesan, J., Zainal, Z.A., Nazim Ahamed, K.S.: *Study of mixed convection in an annular vertical cylinder filled with saturated porous medium, using thermal non-equilibrium model*. Int. J. Heat Mass Transf. **54**, 3822-3825 (2011)

Santosh Kumar, D., Dass, A.K., Dewan, A.: *Analysis of non-Darcy models for mixed convection in a porous cavity using a multigrid approach*. Numer. Heat Tr. A-Appl. **56**, 685-708 (2009)

Saravanan, S.: *Thermal non-equilibrium porous convection with heat generation and density maximum*. Transport Porous Med. **76**, 35–43 (2009)

Saravanan, S., Senthil Nayaki, V.P.M.: *Thermorheological effect on thermal nonequilibrium porous convection with heat generation*. Int. J. Eng. Sci. **74**, 55–64 (2014)

Schäfer, P., Lohnert, G.: *Boiling experiments for the validation of dryout models used in reactor safety*. Nucl. Eng. Des. **236,** 1511-1519 (2006)

Schäfer, P., Groll, M., Kulenovic, R.: *Basic investigations on debris cooling*. Nucl. Eng. Des. **236**, 2104-2116 (2006)

Schiller, L., Naumann, Z.: *A drag coefficient correlation*. Z. Ver. Deutsch Ing., **77**, 318-320 (1935)

Schmidt, W.: *Influence of Multidimensionality and Interfacial Friction on the Coolability of Fragmented Corium*. PhD Thesis, Institute of Nuclear Technology and Energy Systems (IKE), University of Stuttgart, Germany (2004)

Schmidt, W.: *Interfacial drag of two-phase flow in porous media*. Int. J. Multiphase Flow **33**, 638-657 (2007)

Schulenberg, T., Müller, U.: *Natural convection in saturated porous layers with internal heat sources*. Int. J. Heat Mass Transf. **27**(5), 677–685 (1984)

Schulenberg, T., Müller, U.: *An improved model for two-phase flow through beds of coarse particles*, Int. J. Multiphase Flow **13** 87-97 (1987)

Schrock, V.E., Wang, C.H., Revankar, S., Wei, L.H., Lee, S.Y.: *Flooding in particle beds and its role in dryout heat flux prediction*. In: Proceedings of The Sixth Meeting on Debris Coolability, Los Angeles, California, EPRI NP-4455, Palo Alto, California (1986)

Sehgal, B.R.: *Nuclear Accident in Light Water Reactors: Severe Accident Phenomenology*, 1st ed., Elsevier, Amsterdam, The Netherlands (2012)

Shuja, S.Z., Yilbas, B.S., Kassas, M.: *Flow over porous blocks in a square cavity: Influence of heat flux and porosity on heat transfer rates*. Int. J. Therm. Sci. **48**, 1564-1573 (2009)

Singh, N., Kulkarni, P.P., Nayak, A.K.: *Experimental investigation on melt coolability under bottom flooding with and without decay heat simulation*. Nucl. Eng. Des. **285**, 48-57 (2015)

Sivasankaran, S., Do, Y., Sankar, M.: *Effect of discrete heating on natural convection in a rectangular porous enclosure*. Transport Porous Med. **86**, 261-81 (2011)

Song, J.H., Hong, S.W., Kim, J.H., Chang, Y.J., Shin, Y.S., Min, B.T., Kim, H.D: *Insights from the recent steam explosion experiments in TROI*. Journal of Nuclear Science and Technology **40**(10), 783-795 (2003)

Squarer, D., Pieczynski, A.T., Hochreiter, L.E.: *Effect of debris bed pressure, particle size and distribution on degraded nuclear reactor core coolability*. Nucl. Sci. Eng. **80**(1), 2-13 (1982)

Starflinger, J., Buck, M., Hartmann, A., Kulenovic, R., Leininger, S., Rahman, S., Rashid, M.: *Recent numerical simulations and experiments on coolability of debris beds during severe accidents of light water reactors.* Nucl. Eng. Des. **294**, 153-160 (2015)

Taherzadeh, M., Saidi, M.S.: *Modeling of two-phase flow in porous media with heat generation*, Int. J. Multiphase Flow **69**, 115-127 (2015)

Takasuo, E., Holmström, S., Kinnunen, T., Pankakoski, P., Hosio, E., Lindholm, I.*: The effect of lateral flooding on the coolability of irregular core debris beds*. Nucl. Eng. Des. **241,** 1196-1205 (2011)

Takasuo, E., Holmström, S., Kinnunen, T., Pankakoski, P.: *The COOLOCE experiments investigating the dryout power in debris beds of heap-like and cylindrical geometries.* Nucl. Eng. Des. **250**, 687-700 (2012)

Takasuo, E., Taivassalo, V., Hovi, V.: *A study on the coolability of debris bed geometry variations using 2D and 3D models*. VTT Technical Research Centre of Finland (2014)

Takasuo, E.: *Coolability of porous core debris beds: Effects of bed geometry and multi-dimensional flooding*. PhD Thesis, VTT Technical Research Centre of Finland (2015)

Takasuo, E.: *An experimental study of the coolability of debris beds with geometry variations. Ann. Nucl. Energy* **92**, 251-261 (2016)

Thakre, S., Li, L., Ma, W.M.: *An experimental study on coolability of a particulate bed with radial stratification or triangular shape*. Nucl. Eng. Des. **276**, 54-63 (2014)

Theofanous, T.G., Saito, M.: *An assessment of class 9 (core-melt) accidents for PWR dry-containment systems*. Nucl. Eng. Des. **66**, 301–332 (1981)

Tian, L., Ye, C., Xue, S.H., Wang, G.: *Numerical investigation of unsteady natural convection in an inclined square enclosure with heat-generating porous medium*. Heat Transfer Engineering. **35**(6-8), 620-629 (2014)

Tung, V.X., Dhir, V.K.: *Quenching of debris bed having variable permeability in axial and radial directions.* Nucl. Eng. Des. **99,** 275-284 (1987)

Tung, V.X., Dhir, V.K.: *A hydrodynamic model for two-phase flow through porous media*. Int. J. Multiphase Flow **14**, 47-65 (1988)

Ujita, H., Hidaka, M.: *Model Verification of the Debris Coolability Analysis Module in the Severe Accident Analysis Code 'SAMPSON'*. Journal of Nuclear Science and Technology **38**(4), 229-241 (2001)

Umavathi, J.C., Kumar, J.P., Chamkha, A.J., Pop, I.: *Mixed convection in a vertical porous channel*. Transport Porous Med. **61**, 315-335 (2005)

Umavathi, J.C., Sultana, J.: *Mixed convection flow in a vertical channel filled with porous medium with boundary conditions of third kind with heat source/sink-Brinkman model*. International Journal of Mathematical Archive **4**(1), 294-314 (2013)

Wang, C.H., Dhir, V.K.: *An experimental investigation of multidimensional quenching of a simulated core debris bed*. Nucl. Eng. Des. **110,** 61-72 (1988)

Widmann, W., Bürger, M., Lohnert, G., Alsmeyer, H., Tromm, W.: *Experimental and theoretical investigations on the COMET concept for ex-vessel core melt retention*. Nucl. Eng. Des. **236**, 2304-2327 (2006)

Wong, K.C., Saeid, N.H.: *Numerical study of mixed convection on jet impingement cooling in a horizontal porous layer under local thermal non-equilibrium conditions*. Int. J. Thermal Sci. **48**, 860-870 (2009)

Wu, F., Wang, G., Zhou, W.: *A thermal nonequilibrium approach to natural convection in a square enclosure due to the partially cooled sidewalls of the enclosure*. Numer. Heat Tr. A-Appl. **67**, 771–790 (2015a)

Wu, F., Zhou, W., Ma, X.: *Natural convection in a porous rectangular enclosure with sinusoidal temperature distributions on both side walls using a thermal non-equilibrium model*. Int. J. Heat Mass Transf. **85**, 756–771 (2015b)

Yakush, S., Kudinov, P., Dinh, T.N.: *Modeling of two-phase natural convection flows in a water pool with a decay-heated debris bed*. Proceedings of ICAPP '08, California, USA (2008)